Propagation, manipulation and detection of magnonic spin currents in magnetic oxides and metals

Dissertation zur Erlangung des Grades
„Doktor der Naturwissenschaften“ (Dr. rer. nat.)
am Institut für Physik der
Johannes Gutenberg-Universität Mainz

Joel Cramer
geb. in Bad Ems
Mainz, 2018

JOHANNES GUTENBERG UNIVERSITÄT MAINZ

JG|U

Joel Cramer

Propagation, manipulation and detection of magnonic spin currents in magnetic oxides and metals

Dissertation, date of the oral defense: December 3, 2018

Reviewers: Aus Datenschutzgründen entfernt / Removed due to data privacy

Supervisor: Aus Datenschutzgründen entfernt / Removed due to data privacy

MAINZ supervisors: Aus Datenschutzgründen entfernt / Removed due to data privacy

Johannes Gutenberg-Universität Mainz

AG Kläui

Institute of Physics

Staudinger Weg 7

55128 Mainz

Abstract

In anticipation of faster and more energy-efficient information technology, the research field of magnon spintronics aims to interface established electronics or spintronics systems with spin wave (magnon) based computing. In this thesis, aspects of magnon spintronics are investigated on a basic science level to obtain a better understanding of spin transport and detection mechanisms in different types of materials. On the more applied side, concepts of active magnon propagation and detection manipulation as a basis for magnon logic operations are explored.

As an essential prerequisite for magnon spintronics devices, spin information exchange via magnonic spin currents is investigated in a ferrimagnetic insulator, revealing a complex interplay of multiple competing mechanisms. In a non-local transport experiment that allows one to examine both thermally (spin Seebeck effect) and electrically (spin Hall effect) induced spin currents, it is shown that the thermal signal changes sign as a function of distance and temperature, which is partly attributable to the de-localized generation of magnons. Additionally, the spin transport mechanism in a metallic antiferromagnet is probed following an increased interest in these materials due to advantages like enhanced stability compared to ferromagnets. Performing a spin transmission experiment, a strong reduction of the spin signal is observed when long-range antiferromagnetic order is established. This effect can be explained by the opening of an antiferromagnetic magnon gap, revealing notable magnonic spin transport in the material.

Since magnon spintronics aims to integrate electronics and magnonics, the efficient generation and detection of magnons by charge signals requires materials that exhibit large spin-charge interconversion. To this end, a binary alloy is developed and the spin Hall effect is studied as a function of the composition. By means of spin current injection, the alloy structure with the maximal spin Hall angle is identified. Furthermore, DC and THz spin current stimuli yield comparable results, demonstrating that existing magnon spintronics concepts can be readily transferred into the ultrafast regime.

Regarding magnon logic, the active manipulation of magnon detection is explored in different multilayer systems that include a metallic ferromagnet serving as a spin current detector. In both spin pumping and non-local transport measurements a spin valve-like effect with an amplitude of up to 120 % can be implemented, which can be used as a switch component. Finally, the impact of actively manipulating the magnon propagation in a ferrimagnetic insulator is investigated, showing an influence of Joule heating in addition to a significant signal modulation due to applied Oersted fields.

Altogether, the results and findings presented in this thesis contribute to the key requirements for the development of magnon spintronics. The complexities of magnon propagation and detection processes are revealed and new information processing schemes are suggested, pointing towards new routes in this interesting field of research.

Zusammenfassung

In Erwartung schnellerer und energieeffizienterer Informationstechnologie strebt das Feld der Magnonspintronik die Verknüpfung von etablierten elektronischen oder spintronischen Systemen mit Spinwellen (Magnon) basierter Datenverarbeitung an. In dieser Arbeit werden Aspekte der Magnonspintronik auf einer grundlegenden wissenschaftlichen Ebene erforscht, um ein besseres Verständnis der Mechanismen von Spintransport und -detektion in verschiedenen Materialien zu erhalten. Weiterhin werden anwendungsorientierte Konzepte der aktiven Manipulation von Magnonpropagation und -detektion als Basis von Magnonlogik-Operationen untersucht.
Als wesentliche Grundlage von magnonspintronischen Bauteilen wird der Spin-Informationsaustausch durch magnonische Spinströme in ferrimagnetischen Isolatoren analysiert, wobei eine komplexe Wechselwirkung verschiedener konkurrierender Mechanismen offenbart wird. In einem nicht-lokalen Transportexperiment, dass die Untersuchung thermisch (Spin Seebeck Effekt) und elektrisch (Spin Hall Effekt) induzierter Spinströme erlaubt, wird gezeigt, dass das thermische Signal als Funktion des Abstands und der Temperatur sein Vorzeichen wechselt, was teilweise der delokalisierten Magnonerzeugung zugeschrieben werden kann. Zusätzlich wird der Spintransport-Mechanismus in einem metallischen Antiferromagneten bedingt durch ein gesteigertes Interesse in diese Materialklasse wegen vorteilhafter Eigenschaften gegenüber Ferromagneten, wie z. B. eine erhöhte Stabilität, untersucht. In einem Transmissions-Experiment zeigt sich eine starke Abnahme des Spinsignals, wenn eine langreichweite antiferromagnetische Ordnung ausbildet wird. Dieser Effekt kann durch die Öffnung einer Bandlücke für antiferromagnetische Magnonen erklärt werden, was auf einen beträchtlichen magnonischen Spintransport in diesem Material hindeutet.
Da die Magnonspintronik die Verknüpfung von Elektronik und Spintronik anstrebt, werden Materialien mit hoher Spin-Ladung Interkonvertierung für die effiziente Erzeugung und Detektion von Magnonen über Ladungssignale benötigt. Hierzu wird eine binäre Legierung entwickelt und der Spin Hall Effekt als Funktion der Zusammensetzung analysiert. Durch die Injektion von Spinströmen wird die Legierungskomposition mit dem höchsten Spin Hall Winkel identifiziert. Weiterhin zeigen DC und THZ Spinstrom-Impulse vergleichbare Ergebnisse, was bedeutet, dass existierende Konzepte der Magnonspintronik auf ultraschnelle Zeitskalen übertragen werden können.
Bezüglich Magnonlogik wird die aktive Manipulation der Detektion von Magnonen in Multilagensystemen untersucht, die einen metallischen Ferromagneten als Spinstromdetektor enthalten. Sowohl in Spin Pumping als auch in nicht-lokalen Transportmessungen kann ein Spin Valve ähnlicher Effekt mit einer Amplitude von bis zu 120 % realisiert werden, der als Schaltelement eingesetzt werden kann. Abschließend wird die Wirkung der aktiven Manipulation der Magnonpropagation erforscht, die zusätzlich zu einer signifikanten Modulation des Signals durch Oerstedfelder die Beeinflussung durch Joulesche Wärme aufweisen.
Alles in allem tragen die gezeigten Resultate und Erkenntnisse zu den Grundanforderungen der Entwicklung der Magnonspintronik bei. Die Komplexität von Magnonpropagations und -detektions Prozessen wird aufgezeigt und neue Informationsverarbeitungsschemata werden vorgeschlagen, die auf neue Wege in diesem interessanten Forschungsfeld hinweisen.

Contents

List of abbreviations

AFM	Antiferromagnet
AFMI	Antiferromagnetic Insulator
AHE	Anomalous Hall Effect
AMR	Anisotropic Magnetoresistance
ANE	Anomalous Nernst Effect
CoFe	$Co_{70}Fe_{30}$
CoFeB	$Co_{60}Fe_{20}B_{20}$
CPW	Coplanar Waveguide
CuIr	$Cu_{1-x}Ir_x$
EBL	Electron Beam Lithography
FM	Ferromagnet
FMI	Ferro-/Ferrimagnetic Insulator
FMR	Ferromagnetic Resonance
GGG	Gadolinium Gallium Garnet ($Gd_3Ga_5O_{12}$)
GMR	Giant Magnetoresistance
IrMn	$Ir_{20}Mn_{80}$
ISHE	Inverse Spin Hall Effect
LPE	Liquid Phase Epitaxy
MR	Magnetoresistance
NM	Normal Metal
PMMA	Poly(methyl methacrylate)
PNE	Planar Nernst effect
Py	Permalloy ($Ni_{80}Fe_{20}$)
SHE	Spin Hall Effect
SMR	Spin Hall Magnetoresistance
SOI	Spin-orbit Interaction
SP	Spin Pumping
SQUID	Superconducting Quantum Interference Device
SR	Spin Rectification
SSE	Spin Seebeck Effect
STT	Spin Transfer Torque
VTI	Variable Temperature Insert
XRD	X-ray Diffraction
XRR	X-ray Reflectivity
YIG	Yttrium Iron Garnet ($Y_3Fe_5O_{12}$)

1 Introduction

Over the last decades, daily routines in modern society have undergone considerable changes with regard to the rapid advancement of information and communication technology capabilities. The increasing complexity of tasks as well as the general trend of an enhanced interconnection (e.g. *Internet of Things* [1]) call for steadily increasing, always accessible computing power. So far, the latter has been mainly provided by the constant downscaling of transistors as basic information units in microprocessors. This process, however, inevitably reaches its limit due to, amongst other things, a thermodynamic bottleneck whereby further decreased feature sizes entail enhanced Ohmic losses (Joule heating) [2]. Nowadays, approximately 50 % of the energy consumed by a typical data center is used up by the indispensable cooling infrastructure [3].

To overcome the limitations of conventional electronics and to improve the efficiency, alternative concepts with regard to information transport, manipulation or storage are studied within the field of *spintronics* [4, 5]. The inclusion of the electron spin degree of freedom in information technological schemes holds potential advantages such as non-volatility and reduced electric power consumption [4]. A key moment of spintronics was marked by the discovery of the giant magnetoresistance (GMR) effect nearly three decades ago [6, 7], which led to the establishment of hard disk drives for data storage. Later developments include the implementation of a magnetic random access memory (MRAM) based on reconfigurable magnetic tunnel junctions, whose magnetic states are controlled by means of spin-transfer torque (STT) switching [8, 9].

Initial concepts of spintronics such as the aforementioned GMR or STT-MRAM are based on spin transport via spin-polarized charge currents that, as the name suggests, carry both spin and charge information. In view of energy efficiency, pure spin currents that solely convey angular momentum are beneficial and therefore have been the focus of research in the last decade and a half. Generally, one can distinguish between pure spin currents that are mediated by diffusive electron motion, i.e., electrons of opposite spins move in opposite directions, or pure spin currents carried by propagating spin wave excitations in magnetic systems. Depending on the chosen approach, charge motion and thus Ohmic losses are significantly reduced or completely absent. Several methods have been developed over the years to generate and detect pure spin currents, including the spin Hall effect and its inverse [10], spin pumping [11, 12] or the spin Seebeck effect [13, 14]. The spin Hall

effect is based on spin-orbit interaction and creates a pure spin current due to the spin-dependent deflection of conduction electrons, whereas spin pumping and the spin Seebeck effect, respectively, rely on the microwave-induced or thermally activated precession of magnetic moments in ordered systems as the spin current source. On that account, the spin Seebeck effect ultimately would enable one to recover waste heat produced by external processes for spin current generation. In terms of spin current detection, the inverse spin Hall effect proved to be a valuable tool as it enables the re-conversion of a pure spin current into a measurable charge signal. Note that this detection scheme, together with the fact that electron and spin wave mediated spin currents are fully convertible, principally allows for the integration of spin current based concepts with existing electronics.

Besides mere spin information transport, the interaction of spin currents allows one to implement logic operations and thus data processing becomes feasible. With regard to spin wave mediated spin currents, corresponding research is summarized within the fields of *magnonics* [15, 16] or, when interfacing conventional electronics, *magnon spintronics* [17]. Magnons are the quasiparticles of collective spin excitations in magnetic systems and, hence, can be considered as quantized spin waves. Among other things, an immanent feature of magnonics/magnon spintronics concepts is the possibility to implement *wave-based computing*, which in coherent systems allows one to use the spin wave phase as a further information carrier. Furthermore, *insulator spintronics* becomes feasible, which refers to the ability of magnonic spin currents to propagate in magnetic dielectrics, in which Ohmic losses (Joule heating) are avoided due to the suppressed motion of electrons. For a long time, research has mainly focused on ferro- or ferrimagnetic systems such as the yttrium iron garnet $Y_3Fe_5O_{12}$. The extremely low damping of spin waves in this material permits magnons to propagate over micrometer or even centimeter distances [16]. In more recent years, however, spintronics concepts based on antiferromagnetic materials (*antiferromagnetic spintronics*) have gained increased interest regarding advantageous features such as robustness against field perturbations or ultrafast spin dynamics in the THz range [18–21].

Embedded in this framework, the experimental results and findings presented in this PhD thesis contribute to the basic requirements for the further development of magnon spintronics. The fundamental processes involved in magnonic spin current generation, transport, and detection are investigated on a fundamental level and, on the more applied side, active manipulation schemes of magnon transport and detection are explored. Focusing first on spin information transport, the generation and propagation of thermally excited magnons are examined in a comprehensive study that uses a recently introduced non-local measurement scheme. Furthermore, spin transmission experiments concerning the nature of spin transport (electronic vs. magnonic) across a metallic antiferromagnet are presented. A further crucial factor for the success of magnon spintronics applications is the efficient

detection of spin currents, which is why the inverse spin Hall effect in a binary alloy is investigated as a function of its composition. Steady state and THz spin excitation data yield matching results, revealing the universal robustness of the effect and the potential transfer of magnonic spintronics concepts into the ultrafast regime. Based on these findings and the prospect of magnon logic, different approaches regarding the active manipulation of magnonic spin current flow and detection are investigated in the second experimental part of this thesis. Besides the application of a metallic ferromagnet as spin current detector, which allows one to implement a spin valve like effect, the impact of heat and Oersted fields on magnon propagation are investigated.

The thesis is organized as follows:

Chapter 2 gives a brief introduction to the theoretical background of magnetism in condensed matter systems to provide the basic knowledge pertinent to the results presented in this thesis. To begin with, the general appearance of magnetic order in solids is discussed, followed by a review of the various energy terms defining the magnetic configuration of a sample. Eventually, fundamental excitations of magnetic systems as well as magnetization dynamics are covered.

In **chapter 3**, the diverse spin transport effects and phenomena setting the framework for this thesis are presented. Starting from the origin of the (inverse) spin Hall effect and its fundamental properties, a short summary on spin Hall magnetoresistance is given. The theoretical considerations in this thesis are completed by a discussion of the different generation schemes for magnonic spin currents employed in this thesis, which includes spin pumping, the spin Seebeck effect and finally the electrical injection of magnons due to the spin Hall effect.

Chapter 4 opens with a short description of the main features of the insulating ferrimagnet $Y_3Fe_5O_{12}$, which is the material of choice in this thesis to serve as a spin current source as well as a spin conduit. Subsequently, a brief introduction to the main experimental techniques regarding sample fabrication and characterization is provided, followed by a closing section addressing the different measurement setups and procedures employed in this thesis.

The experimental results obtained in the different projects pursued are divided into two parts, with the first of which being presented in **chapter 5**. Initially, the thermal generation and detection of magnonic spin currents in $Y_3Fe_5O_{12}$ is investigated in Sec. 5.1 using a recently introduced non-local measurement scheme [22]. Temperature, field, distance and detector material dependent measurements reveal a complex interaction of various effects that need to be taken into account to obtain a thorough understanding of the detected signal. This work was partly achieved in collaboration with the group of Prof. Dr. S. T. B. Goennenwein (Walther-Meißner-Institut in Garching, now at TU Dresden), with the results

being published in Ref. [o5]. Having established the properties of such a non-local spin Seebeck effect, thermal spin currents are used in Sec. 5.2 to examine the mechanism of spin transport across the metallic antiferromagnet $Ir_{20}Mn_{80}$. The information deduced from temperature- and thickness-dependent data together with the comparison to spin dynamics simulations performed in the theoretical physics group of Prof. Dr. U. Nowak (University of Konstanz) implies significant magnonic spin transport in the otherwise conductive system. The respective findings are presented in publication [o8]. Considering that magnon spintronics aims for the integration of electronics and magnonics, materials that exhibit a large spin-charge interconversion are required for the efficient generation and detection of magnons by charge signals. On that account, the inverse spin Hall effect in the binary alloy $Cu_{1-x}Ir_x$ is studied in the last section of chapter 5 (Sec. 5.3), revealing a complex compositional dependence with a maximum near 40 % of Ir content (see Ref. [o7]). The results of DC measurements agree with THz spin dynamics data recorded in the group of Prof. Dr. T. Kampfrath (Fritz Haber Institute of the Max Planck Society, Berlin), suggesting that existing magnon spintronics concepts principally can be transfered in the ultrafast regime [o12].

Chapter 6 comprises the experimental results targeting the active manipulation of the propagation or detection efficiency of magnonic spin currents, which may be useful in view of magnon logic operations. In the first section (Sec. 6.1), spin pumping experiments are performed in $Y_3Fe_5O_{12}$/CoO/Co multilayer systems with the essential finding that the voltage signal tapped at the Co layer strongly varies for parallel or antiparallel alignment of the $Y_3Fe_5O_{12}$ and Co magnetization. Spin dynamics simulations suggest that for the explanation of the observed valve-like effect intrinsic contributions such as a spin-dependent inverse spin Hall effect need to be considered. The work, which was conceptualized and achieved in collaboration with Prof. Dr. U. Nowak (University of Konstanz) and Prof. Dr. E. Saitoh (Tohoku University, Sendai, Japan), is summarized in Ref. [o9]. In Sec. 6.2, the concept of magnetization orientation-dependent spin detection in metallic ferromagnets is transferred to the non-local detection scheme, this time using $Co_{60}Fe_{20}B_{20}$ as spin current injector or detector. The results obtained are in rough agreement with the findings of the previous section, for which the chosen sample structure supports the model of a spin-dependent spin Hall effect. Section 6.3 finally targets the manipulation of magnon propagation via additional heat and Oersted fields applied to the system. Both an influence of Joule heating on the spin transport signal as well as a distinct voltage modulation due to the applied Oersted field are observed.

Finally, **chapter 7** summarizes the main conclusions of the different projects presented in this thesis, which includes a short outlook on potential proceeding experiments.

2 Magnetism

In the subsequent chapter, the fundamental concepts of magnetism and magnetization dynamics are briefly discussed. Starting from the basic phenomenon of long-range order in magnetic materials, the different contributions to the free energy are presented, which govern the magnetic configuration. Afterwards, spin waves, as elemental excitations of magnetic systems, are introduced, which are of major interest for the presented work. Finally, the principles of magnetization dynamics, in form of collective excitations, are discussed.

2.1 Magnetism in Solids

Magnetism in solids relates to the formation of a long-range magnetic order in crystal lattices, which, depending on the material characteristics, either requires the presence of an external magnetic field or can be sustained even in the absence of one. Generally, the magnetic response (magnetization M = magn. moment per volume) of a solid towards an external field H is quantified by the magnetic susceptibility $\chi = \partial M/\partial H$. In *diamagnetic* materials $\chi < 0$, which signifies that the induced magnetization counteracts the penetrating field in order to minimize it. Diamagnetism is of quantum mechanical origin and appears in all materials, however, it is a weak effect which is mostly dominant in atoms with no unpaired electrons [23]. In the case of partially unfilled shells, a net magnetic moment appears that tends to align along the external field ($\chi > 0$). For negligible interactions between the atoms, *paramagnetic* behavior is present, which means that, in zero field, the moments are randomized ($M = 0$). In *ferromagnetic* (FM) materials however, the magnetic moments of atoms is carried by electron spins that couple via magnetic interaction. A long-range order is established, resulting in a spontaneous magnetization M. In the case of perfect spin alignment over the whole solid, one speaks of the saturation magnetization M_s. Among other things, the direction in which the moments align is determined by the crystal structure or the sample shape.

2.2 Landau theory of phase transitions

A feasible approach to understand and describe the general appearance of long-range magnetic order is the Landau theory of phase transitions [23, 24]. The basic idea of this phe-

nomenological model is to develop the free energy $\mathcal{F}$ of a system as a function of an order parameter, which is M in the case of ferromagnets. A phase transition from a disordered to an ordered state is established, if the order parameter that minimizes $\mathcal{F}$ is zero above a critical temperature, marking the disordered state, but becomes finite for temperatures below. In case of ferromagnets, this temperature is generally known as the Curie-Temperature T_C (for $T > T_\mathrm{C}$, ferromagnets usually become paramagnetic). The model is not limited to ferromagnetism, but is also able to describe further phenomena, e.g. the superconducting phase transition.

The expansion of the free energy $\mathcal{F}$ as a function of M can be written as

$$\mathcal{F} = \mathcal{F}_0 + uM^2 + vM^4 - HM, \tag{2.1}$$

where $\mathcal{F}_0$ is the ground state energy in the paramagnetic phase and H is an external magnetic field. Since in the absence of external fields ($H = 0$) the system energy is independent of the direction of M [$\mathcal{F}(M) = \mathcal{F}(-M)$] only even powers of M are allowed.

Initially, we consider $H = 0$. To observe a phase transition, i.e. the minimum of $\mathcal{F}$ is to be found at $M = 0$ or $M = \pm M_s$ for temperatures above and below T_C, the prefactors must fulfill certain prerequisites. While v must be a positive constant, u changes its sign when crossing T_C: $u = u_0(T - T_\mathrm{C})$ with $u_0 > 0$. Graphically, the phase transition is illustrated in Fig. 2.1. Mathematically, one has to consider the first derivative of $\mathcal{F}$ to identify the ground state:

$$\partial\mathcal{F}/\partial M = 2uM + 4vM^3 \equiv 0 \tag{2.2}$$

$$\Rightarrow M = 0 \quad (T > T_\mathrm{C}) \tag{2.3}$$

$$\Rightarrow M = \pm\sqrt{\frac{u_0(T_\mathrm{C} - T)}{2v}} \quad (T \leq T_\mathrm{C}). \tag{2.4}$$

Below T_C, Eq. 2.2 would be also fulfilled for $M = 0$, however this is a metastable position as could easily be shown by taking into account $\partial^2\mathcal{F}/\partial M^2$.

In addition to the temperature dependent development of M, one can derive an expression for the magnetic susceptibility χ by taking the Zeeman term $-HM$ into account. It is useful to consider small variations δM of the order parameter, which are proportional to the field $\delta M \propto H$:

$$0 = \partial\mathcal{F}/\partial M = 2u\left(M + \delta M\right) + 4v\left(M + \delta M\right)^3 \tag{2.5}$$

$$= \underbrace{\left(2uM + 4vM^3\right)}_{\equiv 0} + \delta M\left(2u + 12vM^2\right) - H + \mathcal{O}\left(\delta M^2\right). \tag{2.6}$$

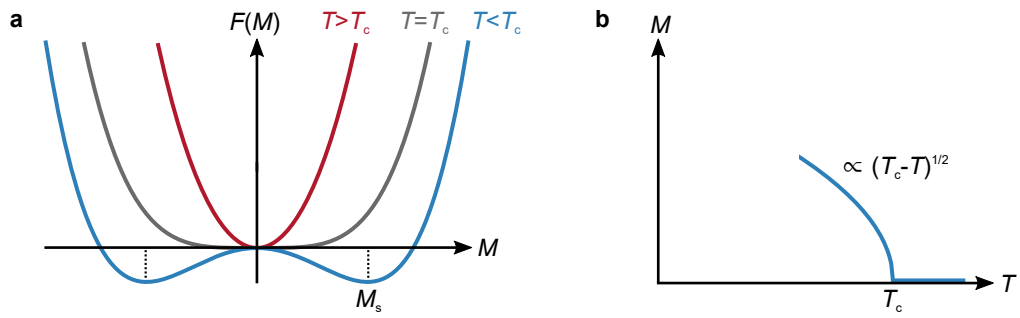

Figure 2.1: (a) Free energy $\mathcal{F}(M)$ for different temperatures above, equal to and below the phase transition temperature T_c. (b) Temperature dependence of M near the phase transition.

Using the solutions of Eq. 2.3 and Eq. 2.4, we find

$$T > T_C : \chi^+ = \frac{\delta M}{H} = \frac{1}{2u_0(T - T_c)}, \tag{2.7}$$

$$T < T_C : \chi^- = \frac{\delta M}{H} = \frac{1}{4u_0|T - T_c|}. \tag{2.8}$$

This result is known as the Curie-Weiss-Law [23] and can also be derived using a simple mean-field approach. In mean-field theories, one assumes that all magnetic moments feel the same effective field induced by external fields and also by their surrounding neighbors. For the Landau theory, a mean-field approximation is made as well. In principle, this allows one to describe general phenomena, however, fluctuations and correlations of the order parameter are neglected. These become important near the phase transition, which is why, in that region, solutions of mean-field theories have to be considered cautiously.

2.3 Magnetic free energy

The free energy of an actual magnetic solid, which eventually determines its magnetic state, comprises both intrinsic and extrinsic contributions that are of a more complex form than the power series considered in the Landau model. The fundamental energy terms, which appear in most magnetic materials, include exchange interactions that couple the atomic magnetic moments, dipolar interaction, anisotropy as well as the Zeeman energy:

$$\mathcal{F} = \mathcal{F}_{\text{exch.}} + \mathcal{F}_{\text{dip.}} + \mathcal{F}_{\text{anis.}} + \mathcal{F}_{\text{Zeeman}} + \dots \tag{2.9}$$

For some solids, additional terms (e.g. magnetostriction or magnetoelasticity) can become of importance.

2.3.1 Exchange interactions

The formation of long-range magnetic order, which means the alignment of the single magnetic moments along a specific direction, requires an interaction mechanism that allows for the magnetic moments to couple. As discussed more explicitly in Sec. 2.3.2, the intuitive dipolar interaction is not strong enough in most cases to couple spins to generate magnetic order at room temperature. Instead, actual exchange mechanisms are of quantum-mechanical nature and are based on electrostatic interactions including the Pauli exclusion principle. In the following, a quantum-mechanical expression of this process is developed according to Ref. [23].

To begin with, let us consider a simple system (e.g. H_2 molecule) comprising two spatially separated electrons a and b at the positions $\mathbf{r}_1$ and $\mathbf{r}_2$. The single electrons' states are described by wave functions that include both space coordinates ($\psi_a(\mathbf{r}_1)$, $\psi_b(\mathbf{r}_2)$) and spin coordinates ($\chi_a(\mathbf{S}_1)$, $\chi_b(\mathbf{S}_2)$ with $\mathbf{S}_i = \uparrow, \downarrow$). The total system is then described by a product of the single wave functions, where one has to bear in mind that in quantum mechanics identical particles are indistinguishable. Furthermore, with electrons being fermions, the total wave function must be antisymmetric $\Psi(1,2) = -\Psi(2,1)$. This means that in the case of a symmetric (antisymmetric) spatial function, the spin state is an antisymmetric spin singlet $S_{\mathrm{tot}} = 0$ (symmetric spin triplet $S_{\mathrm{tot}} = 1$):

$$\Psi_s = 1/\sqrt{2}\left[\psi_a(\mathbf{r}_1)\psi_b(\mathbf{r}_2) + \psi_a(\mathbf{r}_2)\psi_b(\mathbf{r}_1)\right]\chi_s, \tag{2.10}$$

$$\Psi_t = 1/\sqrt{2}\left[\psi_a(\mathbf{r}_1)\psi_b(\mathbf{r}_2) - \psi_a(\mathbf{r}_2)\psi_b(\mathbf{r}_1)\right]\chi_t, \tag{2.11}$$

with

$$\chi_s = 1/\sqrt{2}\left[|\uparrow\downarrow\rangle - |\downarrow\uparrow\rangle\right], \tag{2.12}$$

$$\chi_t = |\uparrow\uparrow\rangle\,; 1/\sqrt{2}\left[|\uparrow\downarrow\rangle + |\downarrow\uparrow\rangle\right]; |\downarrow\downarrow\rangle\,. \tag{2.13}$$

With normalized spin states, the energy of the total system described by the Hamiltonian $\mathcal{H}$, which is calculated as

$$\mathcal{E}_s = \langle\Psi_s|\mathcal{H}|\Psi_s\rangle = \int \mathrm{d}\mathbf{r}_1\mathrm{d}\mathbf{r}_2\Psi_s^*(\mathbf{r}_1,\mathbf{r}_2)\mathcal{H}\Psi_s(\mathbf{r}_1,\mathbf{r}_2), \tag{2.14}$$

$$\mathcal{E}_t = \langle\Psi_t|\mathcal{H}|\Psi_t\rangle = \int \mathrm{d}\mathbf{r}_1\mathrm{d}\mathbf{r}_2\Psi_t^*(\mathbf{r}_1,\mathbf{r}_2)\mathcal{H}\Psi_t(\mathbf{r}_1,\mathbf{r}_2), \tag{2.15}$$

$$\Rightarrow \mathcal{E}_s - \mathcal{E}_t = 2\int \mathrm{d}\mathbf{r}_1\mathrm{d}\mathbf{r}_2\psi_a^*(\mathbf{r}_1)\psi_b^*(\mathbf{r}_2)\mathcal{H}\psi_a(\mathbf{r}_2)\psi_b(\mathbf{r}_1). \tag{2.16}$$

The right side of Eq. 2.16 is called the exchange integral and is conventionally abbreviated by $J = (\mathcal{E}_s - \mathcal{E}_t)/2$. Using this and the identity $\mathbf{S}_1\mathbf{S}_2 = \left(\mathbf{S}_{\mathrm{tot}}^2 - \mathbf{S}_1^2 - \mathbf{S}_2^2\right)/2$ with $\mathbf{S}^2 =$

$S(S+1)$, one can derive the simple effective Hamiltonian

$$\mathcal{H} = \frac{1}{4}\left(\mathcal{E}_s + 3\mathcal{E}_t\right) - \underbrace{\left(\mathcal{E}_s - \mathcal{E}_t\right)}_{2J} \mathbf{S}_1\mathbf{S}_2. \tag{2.17}$$

The first term is a constant an can be neglected, whereas the second part yields the spin-dependent contribution

$$\mathcal{H}_{\text{spin}} = -2J\mathbf{S}_1\mathbf{S}_2. \tag{2.18}$$

While parallel alignment of the spins and therefore ferromagnetic order is preferred for $J > 0$, $J < 0$ favors antiparallel alignment. Expanding this to a multi-spin system, one obtains the Hamiltonian of the so-called Heisenberg model

$$\mathcal{H} = -\sum_{ij} J_{ij}\mathbf{S}_i\mathbf{S}_j, \tag{2.19}$$

where the factor 2 is omitted with regard to double counting the same pairs of spins. This model Hamiltonian is well suited for the description of systems comprising localized moments.

As mentioned above, $J < 0$ yields an antiparallel alignment of spins in the solid. For equal magnetic moments of the resulting sublattices $\mathbf{M}_1$ and $\mathbf{M}_2 = -\mathbf{M}_1$, the total magnetization vanishes ($\mathbf{M} = \mathbf{M}_1 + \mathbf{M}_2 = 0$) and the so-called *Néel*-order parameter $\mathbf{N} = \mathbf{M}_1 - \mathbf{M}_2$ is considered to describe the system. In this case, one speaks of *antiferromagnetism* (AFM). The respective ordering temperature T_N is called Néel-temperature. For unequal moments ($|\mathbf{M}_2| < |\mathbf{M}_1|$), a reduced magnetization appears, which is then called *ferrimagnetism*. The three different magnetization states are illustrated in Fig. 2.2.

Despite its simplicity, in most solids the direct exchange as discussed above is of minor importance due to the small overlap of strongly localized magnetic orbitals (e.g. 4f shell in

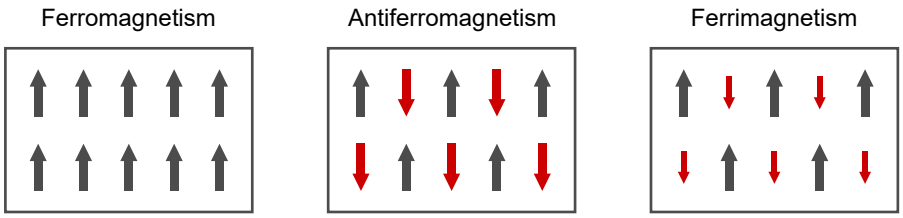

Figure 2.2: Potential magnetic states adapted by a solid for different exchange constants and sub-lattice configurations (ferromagnetism: $J > 0$; antiferromagnetism: $J < 0$, $\mathbf{M}_2 = -\mathbf{M}_1$; ferrimagnetism: $J < 0$, $\mathbf{M}_2 \neq -\mathbf{M}_1$).

rare earth elements) or the de-localization of electrons such as, for instance, in 3d metals. Consequently, magnetic order must be obtained by different mechanisms.

Superexchange

With regard to the materials investigated in this work, the exchange mechanism that is of most importance is the indirect *superexchange*. It appears in ionic solids, e.g. oxides, in which the electron orbitals of next-neighbored magnetic atoms overlap with the orbitals of a non-magnetic inter-atom. Figure 2.3a shows the demonstrative example of the cobalt monoxide $Co^{2+}O^{2-}$, where the 3d orbitals of Co hybridize with the 2p orbitals of oxygen [25]. It becomes clear from Fig. 2.3b that for ferromagnetic alignment of the Co momenta electron hopping is suppressed due to the Pauli exclusion principle, whereas antiferromagnetic alignment allows for the delocalization of electrons over the whole system. As a consequence, the total kinetic energy is reduced, rendering the antiferromagnetic state energetically favorable. Eventually, however, electron hopping increases the on-site Coulomb energy, which is why it remains virtual and antiferromagnetic oxides are mostly electrically insulating [23, 24].
In the case of unequal valency of the magnetic atoms ferromagnetic coupling may become favorable, which is then known as *double exchange* [23].

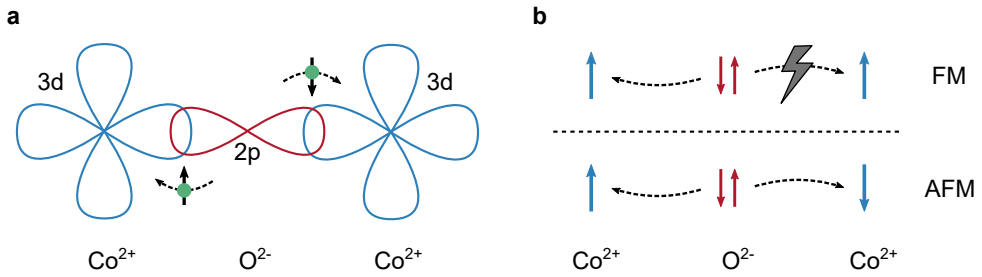

Figure 2.3: (a) Illustration of the superexchange mechanism in the cobalt monoxide. (b) Due to the Pauli exclusion principle, antiferromagnetic order is preferred. Blue arrows represent the spin orientation of the Co 3d electron spins, red arrows the oxygen 2p electron spins mediating the exchange.

Band ferromagnetism

As mentioned above, the model of localized magnetic moments does not apply for some metallic systems, in which magnetism is mediated by delocalized itinerant electrons. Instead, one needs to consider spontaneous spin-splitting of the electron bands involved. The most commonly known examples are the metallic ferromagnets Fe, Co, and Ni.

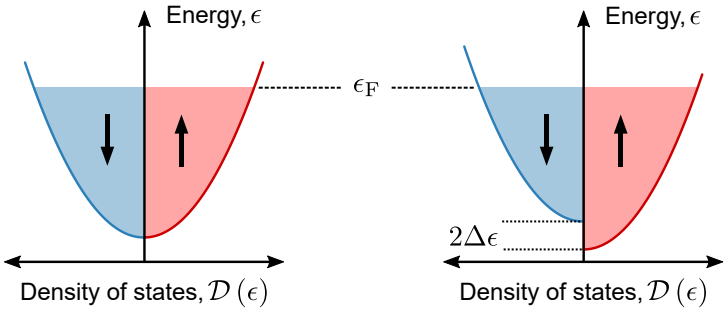

Figure 2.4: Spontaneously spin-split bands of a free electron gas. $2\Delta\epsilon$ is the effective exchange splitting energy of the two spin sub-bands.

To understand band ferromagnetism, one can consider the simplified model of a 3D free electron gas, for which the density of states is given by $\mathcal{D}(\epsilon) \propto \sqrt{\epsilon}$ (see Fig. 2.4). Due to the Pauli exclusion principle, the translation of electrons from one spin bath to the other, e.g. spin-down (minority) to spin-up (majority), is entailed by an increase of the kinetic energy of the system by $\Delta\epsilon_{\text{kin}} = 1/2\mathcal{D}(\epsilon_F)\Delta\epsilon^2$ [23]. Then, the thus induced magnetization interacts with the molecular field, yielding a further energy contribution $\Delta\epsilon_{\text{mol}} = -1/2U\mathcal{D}^2(\epsilon_F)\Delta\epsilon^2$. Here, U is a measure for the exchange and thus the Coulomb interaction.
Ferromagnetism now appears, when the second term becomes dominating and consequently the ferromagnetic states become energetically favorable. This is the case for metals which fulfill the so-called *Stoner criterion* [23]

$$U\mathcal{D}(\epsilon_F) \geq 1. \tag{2.20}$$

Accordingly, a high density of states at the Fermi level and strong Coulomb interaction are needed, which is true for the 3d electrons in Fe, Co and Ni. The heavy metal Pt is at the edge of ferromagnetism, however, it can exhibit proximity magnetization at the interface to an adjacent ferromagnet [23].

Continuum approximation

When considering real and thus sizeable systems, the quantum-mechanical treatment of single spins via the Heisenberg Hamiltonian is impractical regarding the exponentially growing Hilbert space (dimension 2^N for a system of N spin one-half particles). Therefore, a classical treatment is required, which is obtained by the *continuum approximation*. In this approximation, the local magnetization is averaged and given by $\mathbf{M}(\mathbf{r})$, which varies smoothly across the sample.
In this framework, the contribution of exchange to the free energy in Eq. 2.9 is the approx-

imation of small magnetization gradients

$$\mathcal{F}_{\text{exch.}} = \frac{A}{M_s^2} \int \mathrm{d}\mathbf{r} \left[(\nabla M_x)^2 + (\nabla M_y)^2 + (\nabla M_z)^2 \right], \tag{2.21}$$

with $A \propto J$ being the exchange stiffness and M_s the saturation magnetization of the sample [24].

2.3.2 Dipolar interaction

In addition to the Coulomb-driven exchange interaction, the magnetic moments within solids are coupled via dipolar interaction. For two distinct magnetic moments $\mathbf{m}_1$ and $\mathbf{m}_2$ that are separated by $\mathbf{r}$, the dipolar magnetostatic coupling is given by [23]

$$\epsilon = \frac{\mu_0}{4\pi r^3} \left[\mathbf{m}_1 \cdot \mathbf{m}_2 - \frac{3}{r^2} (\mathbf{m}_1 \cdot \mathbf{r}) (\mathbf{m}_2 \cdot \mathbf{r}) \right]. \tag{2.22}$$

Counterintuitively, the effective coupling is weak as compared to the exchange mechanisms discussed before. Typical values for $|\mathbf{m}_{1,2}|$ in the range of a few μ_B, detached at atomic distances, yield coupling energies corresponding to a few Kelvin [23]. This is small as compared to the Curie temperatures observed for many ferromagnets (e.g. $T_C \approx 1360\,\mathrm{K}$ for Co) and therefore, with respect to magnetic ordering, dipolar exchange is only important for materials that become ferromagnetic at low temperatures.
Notwithstanding its relatively small strength, dipolar coupling is a long-range ($\propto 1/r^3$) interaction and thus becomes relevant for the magnetic microstructure of magnetic samples [24]. The magnetic flux that penetrates a ferromagnet, $\mathbf{B} = \mu_0 (\mathbf{H} + \mathbf{M})$, includes an effective magnetic field as well as the magnetization. At the surface of the ferromagnet $\mathbf{M}$ abruptly becomes zero, whereas the divergence of the magnetic flux must always vanish according to Maxwell's second equation (Gauss's law for magnetism), i.e., $\nabla \mathbf{B} = 0$. As a consequence, the magnetic field experiences a divergence opposed to the one of the magnetization $\nabla \mathbf{H} = -\nabla \mathbf{M}$, giving rise to the so-called *demagnetizing* field [24]

$$\mathbf{H}_d = -\mathcal{N}\mathbf{M}. \tag{2.23}$$

Here, $\mathcal{N}$ is the demagnetizing tensor and depends on the shape of the magnetic body. Generally, $\mathbf{H}_d$ can be understood as the stray field of the uncompensated dipole moments at the surface. With respect to the free energy, the contribution of the stray field interacting with the sample magnetization (self-energy) essentially can be developed by rewriting Eq. 2.22 such that it gives the energy of one dipole being in the field of the other and further building the sum over all spins in the system. On the macroscopic scale, the sum is replaced

by an integral over the sample volume considering the spatial-dependent magnetization $\mathbf{M} \rightarrow \mathbf{M}(\mathbf{r})$ and the stray field distribution:

$$\mathcal{F}_{\text{dip.}} = -\frac{1}{2}\mu_0 \int \mathrm{d}\mathbf{r}\mathbf{H}_d\mathbf{M}. \tag{2.24}$$

For details, please see Ref. [24].

2.3.3 Magnetic anisotropy

The alignment direction of the sample magnetization is generally not arbitrary, but governed by several factors such as, for instance, the shape or the crystalline structure of a magnetic solid [24]. While it is energetically favorable for $\mathbf{M}$ to lie along a so-called *easy* axis, it requires an enhanced energy effort to force it into a *hard* axis direction. In the following section, several origins of magnetic anisotropy are discussed.

Shape anisotropy

Shape anisotropy arises from the previously discussed demagnetizing field. According to Eq. 2.23, the strength of $\mathbf{H}_d$ along a certain direction is determined by the demagnetizing tensor $\mathcal{N}$. Considering the example of a magnetic nanowire with a length that far exceeds its width and height ($l \gg w, h$), the magnetization prefers to align along the wire. An orthogonal alignment of $\mathbf{M}$ with respect to the long edge of the wire would imply an enhanced number of uncompensated dipole moments and, thus, an enhanced stray field [24]. This corresponds to a so-called *uniaxial* anisotropy and the self-energy in Eq. 2.24 yields [24]

$$\mathcal{F}_a = \frac{1}{4}\mu_0 V M_s^2 \sin^2\theta, \tag{2.25}$$

with $\theta = 0°$ being the long axis of the nanowire.

Magnetocrystalline anisotropy

In crystalline solids, easy and hard axes are defined by the crystallographic structure of the material. Depending on the configuration of magnetic and non-magnetic ions in the lattice, the origin of magnetocrystalline anisotropy can be given by an interplay of exchange, spin-orbit coupling, the crystal field and even dipolar interaction [25–27]. Transition metal monoxides (e.g. CoO), for instance, condense into a face-centered cubic (fcc) lattice, which can be considered as an overlap of four simple cubic (sc) sublattices. The superexchange leads to ferromagnetic alignment of the spins within the {111} planes of the sc and antiferromagnetic coupling between neighbored planes. Inter-coupling between the sublattices, however, is not provided by superexchange as 90° bonds are involved. Alternatively, it

is the dipolar interaction that yields collinear alignment of the sublattices favorable and hereby establishes so-called type II AFM order [27].
In the case of insulating ferrimagnetic oxides, which are of main interest for this work, the single ion theory is a useful tool to predict the effective anisotropy [25, 28]. In this model, the lowest energy levels regarding spin alignment are determined of the single ions at all possible crystal sites to derive the anisotropy of the whole crystal. Different anisotropy contributions need to be considered, as the magnetic d-orbitals of transition metals (f-orbitals of rare earth ions) can exhibit relatively strong (weak) crystal fields, whereas spin-orbit coupling may be weak (strong).
The general form of a uniaxial anisotropy as in Eq. 2.25 is given by

$$\mathcal{F}_{\mathrm{uni}} = VK_1^{\mathrm{uni}} \sin^2\theta + VK_2^{\mathrm{uni}} \sin^4\theta + ..., \tag{2.26}$$

with K_i^{uni} being anisotropy constants and θ the angle between the magnetization and the easy axis. In cubic crystals, for instance, the anisotropy term becomes more complex:

$$\mathcal{F}_{\mathrm{cub}} = VK_1^{\mathrm{cub}} \left(m_x^2 m_y^2 + m_y^2 m_z^2 + m_x^2 m_z^2\right) + VK_2^{\mathrm{cub}} m_x^2 m_y^2 m_z^2 + ..., \tag{2.27}$$

where m_i are the single components of the magnetization direction vector $\mathbf{m} = \mathbf{M}/M_{\mathrm{s}}$.

Exchange bias anisotropy

Another type of anisotropy can appear in artificial magnetic heterostructures including a FM/AFM bilayer, namely the so-called *exchange bias* effect [29, 30]. Considering the case with the FM ordering at higher temperatures as compared to the AFM ($T_{\mathrm{C}} > T_{\mathrm{N}}$), the antiferromagnetic order within the AFM is influenced by the FM when cooling the system down in the presence of a static magnetic field. The AFM order is established in such a way, that the exchange energy at the mutual interface is minimized. Furthermore, the AFM is unresponsive to external fields considering its vanishing magnetization and thus retains the direction of the FM magnetization during the cooling procedure. As a consequence, a *unidirectional* anisotropy is established, which shifts the FM hysteresis loop horizontally (see Fig. 2.5).
Besides this unidirectional anisotropy, exchange bias can be accompanied by a further uniaxial anisotropy that broadens the FM hysteresis. One model to explain the occurrence of this phenomenon includes the presence of individual grains in the AFM [30]. When reducing the magnetic field, which is applied in the exchange bias direction, these grains apply torques in opposite directions such that $\mathbf{M}$ locally switches by either clockwise or counterclockwise reversal nucleation. In this way a potential barrier is established, which

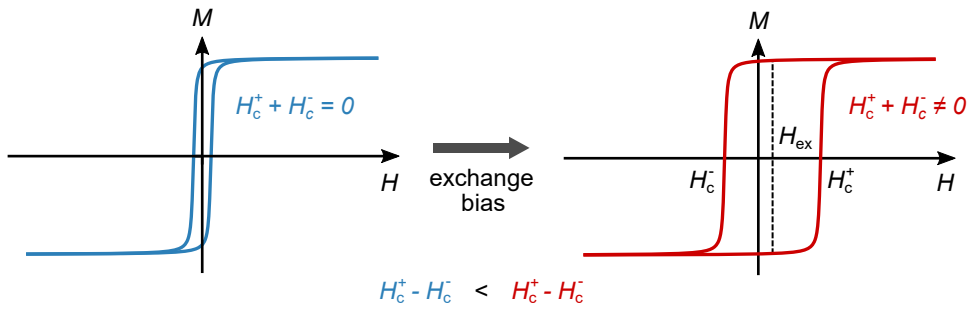

Figure 2.5: Figurative change of a magnetic hysteresis loop of a ferromagnet exposed to exchange bias. Depending on the induced anisotropy terms (unidirectional, uniaxial), the hysteresis center and width shift and increase, respectively.

yields the enhanced magnetization switching fields. If the external magnetic field is perpendicular to the exchange bias direction, however, the torques show in the same direction and the barrier is reduced, resulting in lower switching fields.

2.3.4 Zeeman energy

Eventually, the free energy of a magnetic system and consequently its magnetization are influenced by external magnetic fields $\mathbf{H}_{\text{ext}}$ via the Zeeman interaction:

$$\mathcal{F}_{\text{Zeeman}} = -\mu_0 \int \mathrm{d}\mathbf{r}\mathbf{M}\mathbf{H}_{\text{ext}}. \tag{2.28}$$

As Eq. 2.28 signifies, the lowest energy state is achieved for parallel alignment of $\mathbf{M}$ and $\mathbf{H}_{\text{ext}}$ throughout the sample volume.

2.4 Magnetic excitations

2.4.1 Magnons

For non-zero temperatures, the magnetic order within a solid is disturbed by elementary excitations of the system. These excitations are, however, not given by the flip of a single spin as the Heisenberg picture suggests. Considering a 1D chain of ferromagnetically ordered spins, flipping a single spin in the chain generates an energy cost of $k_{\text{B}}T = 2J$ according to Eq. 2.19. Then again, one obtains for the Curie temperature of the spin chain $k_{\text{B}}T_{\text{C}} = J$ according to a mean field approach [24]. The excitation energy required is, thus, too high at low temperatures.
Another mechanism must therefore be present to provide elementary excitations at low temperatures at low energy cost. In general, this is granted by dividing the spin flip into

a long wavelength rotational deflection of the spins from their equilibrium position, which propagates through the material as a *spin wave*. In this sense, the wavelength is defined by the phase difference between neighbored spins with equal rotation sense and frequency. One can furthermore, in analogy to *phonons*, consider spin waves that propagate as massless particles, so-called *magnons*. While the existence of spin waves was first discussed by F. Bloch to explain the low-temperature dependence of $\mathbf{M}$ in ferromagnets [31], the concept of magnons was introduced by Holstein and Primakoff [32] as well as Dyson [33].

When discussing spin waves, one has to keep in mind that the spins within a magnetic material are generally coupled by two fundamental interactions: the relatively weak long-range dipolar interaction (see Sec. 2.3.2) and the strong short-range exchange (see Sec. 2.3.1). Depending on the wavelength, either one or the other interaction mechanism is dominant, calling for a definition of spin wave categories [16, 34]. For wavelengths that are long as compared to the spatial separation of the spins, the phase difference and hence the relative misalignment between neighboring spins is small. According to the Heisenberg model, the impact of exchange is therefore weak and one speaks of *dipolar* or *magnetostatic waves*. In the case of short wavelengths ($\lambda \lesssim 1\,\mu\text{m}$ [17]), however, exchange becomes dominating and one considers *exchange spin waves*. Depending on the material, typical frequencies of spin waves are in the GHz regime for magnetostatic waves [16], whereas exchange modes reveal THz frequencies [35].

Since the majority of the investigated phenomena in this work deal with thermally excited exchange magnons, we initially focus on these. Reconsidering the example of a 1D spin chain, the derivation of the magnon dispersion relation in the classical picture requires the time derivative of a single spin at position n

$$\frac{\mathrm{d}\langle \mathbf{S}_n \rangle}{\mathrm{d}t} = -\frac{i}{\hbar}\langle [\mathbf{S}_n, \mathcal{H}] \rangle \tag{2.29}$$

employing the Heisenberg Hamiltonian given by Eq. 2.19. Bearing in mind that spin operators of different lattice sites commute ($[\mathbf{S}_n, \mathbf{S}_m] = 0$ for $n \neq m$) and that for the single components of a spin operator $\left[\mathbf{S}_n^i, \mathbf{S}_n^j\right] = i\varepsilon_{ijk}\mathbf{S}_n^k$ $(i, j, k = x, y, z)$ is valid, Eq. 2.29 yields

$$\frac{\mathrm{d}\langle \mathbf{S}_n \rangle}{\mathrm{d}t} = \frac{2J}{\hbar}\langle \mathbf{S}_n \times (\mathbf{S}_{n-1} + \mathbf{S}_{n+1}) \rangle\,. \tag{2.30}$$

For small deviations of the spin vector from its equilibrium position, one can assume that $\mathbf{S}_n^z \approx S = |\mathbf{S}_n|$, whereas $\mathbf{S}_n^x = \mathbf{S}_n^y \approx 0$. Introducing plane wave solutions for this coupled equation and solving the eigenvalue problem, one obtains for the dispersion relation

$$\hbar\omega = 4JS\left[1 - \cos(qa)\right]. \tag{2.31}$$

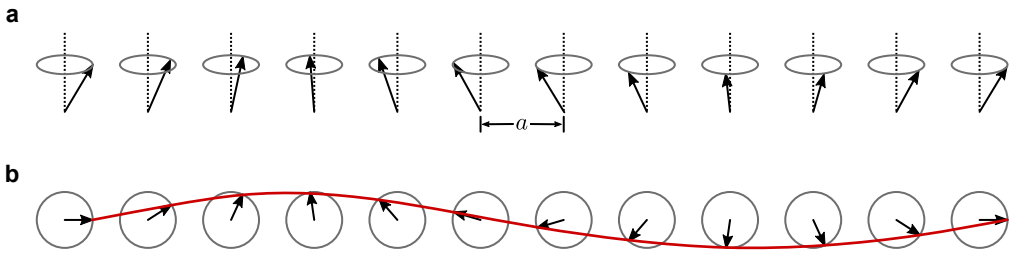

Figure 2.6: (a),(b) Illustration of a spin wave (magnon) in a 1D magnetic chain. The arrows depict the rotating magnetic moments, whose in-plane components reflect the magon wavelength (red line).

Here, a is the distance between the spins and $q = |\mathbf{q}|$ the wave vector of the magnon. One can see immediately that for small q the energy of a magnon approaches 0, which allows for it to be excited even at low temperatures [23]. However, in the presence of anisotropy or an external magnetic field, an energy gap $\Delta\epsilon \propto K_i, \mathbf{H}$ will open up at $\mathbf{q} = 0$ and therefore partially suppress the excitation of spin waves [36]. Eventually, the dispersion relation of magnons in an actual solid is more complex than the one given by Eq. 2.31 such as, for instance, further modes of acoustic or optical nature appear [35].
One of the most prominent features of magnons and the reason for the enhanced interest in them is their capability to transfer angular momentum and therefore information. Magnons are, as stated before, de-localized spin flips that carry one $\hbar$ and consequently, as being spin 1 particles, follow Bose-Einstein statistics. Within the emerging fields of *magnonics* [15, 16, 37, 38] or *magnon spintronics* [17], schemes for the exploitation of these properties for information transport and processing are conceptualized and summarized.

2.4.2 Stoner excitation

In metallic ferromagnets, a further excitation mechanism in addition to spin waves is present [24]. The transfer of electrons near the Fermi edge from the majority into the minority spin band, so-called *Stoner excitations*, lead to a supplemental reduction of the magnetization. Fulfilling the law of momentum and energy conservation, the transfer of an electron from the initial state $|\mathbf{k}, \uparrow\rangle$ to the final state $|\mathbf{k} - \mathbf{q}, \downarrow\rangle$ requires an excitation energy

$$\hbar\omega_q = \epsilon_{\text{kin}}(\mathbf{k}) - \epsilon_{\text{kin}}(\mathbf{k} - \mathbf{q}) + \Delta\epsilon. \tag{2.32}$$

Here, $\Delta\epsilon$ is the exchange splitting of the electron bands, which needs to be completely overcome at $\mathbf{q} = 0$. At finite $\mathbf{q}$, however, a broad spectrum of excitations is available (see,

for instance, Ref. [23]).

2.5 Magnetization dynamics

In the following, the dynamics of ferromagnetic magnetization in response to stimuli will be discussed. More precisely, we will consider collective excitations of the magnetic system in static and oscillatory magnetic fields, which can be considered as the special case of $\mathbf{q} = 0$ spin waves. On that account, two simplifications are adopted: (i) Employing a *macrospin* model, spatial variations of $\mathbf{M}$ are neglected such that the magnetization is uniform over the sample. (ii) Internal effects such as exchange, anisotropy, and demagnetization are considered by a net effective internal field, which together with the external field yields $\mathbf{H}_{\text{eff}} = \mathbf{H}_{\text{ext}} + \mathbf{H}_{\text{int}}$.

2.5.1 Ferromagnetic resonance

Reconsidering the discussion given in Sec. 2.3, $\mathbf{M}$ tends to align along $\mathbf{H}_{\text{eff}}$ so as to minimize the free energy of the total system. Accordingly, a torque is acting that drives a continuous precession of the magnetic moments around the effective field vector. In the absence of losses, the respective equation of motion is given by

$$\frac{\mathrm{d}\mathbf{M}}{\mathrm{d}t} = \gamma\mu_0 \left(\mathbf{M} \times \mathbf{H}_{\text{eff}}\right), \tag{2.33}$$

where $\gamma = g\mu_{\text{B}}/\hbar$ is the gyromagnetic ratio of the electron with the Landé factor $g \approx -2$ [34, 39]. Without any internal fields, the magnetization will precess with the *Larmor* eigenfrequency $\omega_{\text{L}} = \gamma\mu_0 H_{\text{ext}} \approx 2\pi \cdot 28\,\text{GHz}\,\text{T}^{-1}$. Similar to nuclear magnetic or electron spin resonance, this oscillation can be impelled by microwave (rf) fields $\mathbf{h}_{\text{rf}}(t)$ of matching frequency. The driving field $\mathbf{h}_{\text{rf}}$ is chosen to be perpendicular to the static contribution of $\mathbf{H}_{\text{ext}}$.

In ferromagnets, the internal contributions to the effective field yield a shift of the *ferromagnetic resonance* (FMR) frequency off ω_{L}. Neglecting this effect would result in values of the g-factor that are too high. The first experimental observation of FMR was reported by Griffiths [40] in 1946, followed shortly afterwards by a first theoretical description by Kittel [41, 42]. A feasible approach to derive the FMR frequency is achieved by considering a spherical coordinate system and the second derivatives of the free energy $\mathcal{F}$ (Eq. 2.9) with respect to the polar and azimuthal angle of $\mathbf{M}$ (see Fig. 2.7a) of its equilibrium position $\mathbf{M}_{\text{eq.}}$:

$$\omega_{\text{FMR}} = |\gamma| \,/\, (M_{\text{s}} \sin\theta) \left(\mathcal{F}_{\theta\theta}\mathcal{F}_{\phi\phi} - \mathcal{F}_{\theta\phi}\right), \tag{2.34}$$

where $\mathcal{F}_{xy} = \partial^2\mathcal{F}/\left(\partial x \partial y\right)$ [43]. Disregarding exchange and anisotropy ($\mathcal{F} = \mathcal{F}_{\text{dip.}} +$

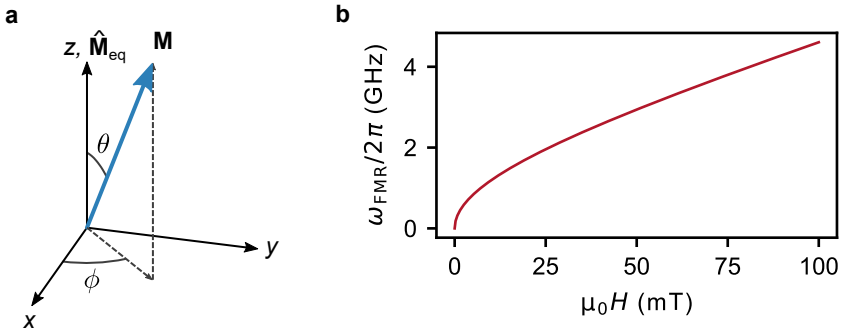

Figure 2.7: (a) Spherical coordinate system used to describe the magnetization rotation. (b) FMR frequency ω_{FMR} as a function of the external field obtained by Eq. 2.35 for a ferromagnet with $M_{\mathrm{s}} = 135.5\,\mathrm{kA\,m^{-1}}$.

$\mathcal{F}_{\mathrm{Zeeman}}$), one obtains the so-called *Kittel formula* of ferromagnetic resonance [44]

$$\omega_{\mathrm{FMR}} = \mu_0 \left|\gamma\right| \sqrt{H_{\mathrm{ext}} \left(H_{\mathrm{ext}} + M_{\mathrm{s}}\right)}. \tag{2.35}$$

In the case of uniaxial and cubic anisotropy, this expression becomes more complex:

$$\omega_{\mathrm{FMR}} = \mu_0 \left|\gamma\right| \sqrt{\left(H_{\mathrm{ext}} + H_{K_1^{\mathrm{cub}}}\right) \left(H_{\mathrm{ext}} + H_{K_1^{\mathrm{cub}}} + M_{\mathrm{s}} - H_{K_1^{\mathrm{uni}}}\right)}. \tag{2.36}$$

Here, $H_{K_1^{\mathrm{cub}}} = 2K_1^{\mathrm{cub}}/M_{\mathrm{s}}$ and $H_{K_1^{\mathrm{uni}}} = 2K_1^{\mathrm{uni}}/M_{\mathrm{s}}$ are the respective cubic and uniaxial anisotropy fields. All things considered, FMR provides a powerful tool for the investigation of intrinsic magnetic properties.

2.5.2 Landau-Lifshitz-Gilbert equation

Thus far, solely the undamped precession of $\mathbf{M}$ around $\mathbf{H}_{\mathrm{eff}}$ in view of Eq. 2.33 was discussed. This would imply that, once excited, the rotational motion of the magnetization never ceases and that $\mathbf{M}$ would never align to the direction of $\mathbf{H}_{\mathrm{eff}}$. In real systems, however, the precession of $\mathbf{M}$ is accompanied by losses due to various dissipation channels, e.g. coupling to the crystal lattice [34]. The latter can be mediated by spin-orbit interaction [34] or can be understood when considering that coherently rotating spins interact via their dipolar fields. The coupling strength depends on the distance in between the spins ($\propto 1/r^3$, see Eq. 2.22) and is therefore modulated by lattice vibrations (phonons) [34]. Further potential relaxation channels are, for instance, two-magnon scattering processes at surface and interface defects (decay of long wavelength magnons into short wavelength magnons degenerate in energy) [45], inhomogeneous microwave fields in metallic systems due to eddy currents [46], or, as discussed later, the transfer of angular momentum into adjacent heavy

metal layers [11].

Hence, the equation of motion needs to be extended in order to account for the aforementioned losses. A first approach to this topic was given by Landau and Lifshitz [47] by adding a torque to Eq. 2.33 that acts towards the effective field:

$$\frac{\mathrm{d}\mathbf{M}}{\mathrm{d}t} = \gamma\mu_0 \left(\mathbf{M} \times \mathbf{H}_{\mathrm{eff}}\right) - \frac{\lambda}{M_{\mathrm{s}}^2} \left(\mathbf{M} \times \mathbf{M} \times \mathbf{H}_{\mathrm{eff}}\right). \tag{2.37}$$

This is the so-called *Landau-Lifshitz* equation with the phenomenological damping parameter λ, which characterizes the dipolar interaction between the single magnetic moments [39].

For small damping, this phenomenological approach can be used, but it encounters problems for larger damping contributions, e.g. in the case of pulsed remagnetization of thin films [39]. Therefore, another ansatz was elaborated by Gilbert by introducing a dissipative force to a Lagrangian formulation of the problem [48]. As a result, he obtained the *Gilbert* equation

$$\frac{\mathrm{d}\mathbf{M}}{\mathrm{d}t} = \gamma\mu_0 \left(\mathbf{M} \times \mathbf{H}_{\mathrm{eff}}\right) + \frac{\alpha}{M_{\mathrm{s}}} \left(\mathbf{M} \times \frac{\mathrm{d}\mathbf{M}}{\mathrm{d}t}\right) \tag{2.38}$$

with the Gilbert damping parameter α. The Gilbert equation is numerically more challenging as it includes a recurrence relation of the time derivative of $\mathbf{M}$. However, Eq. 2.38 can easily be rewritten in the form of Eq. 2.37 by multiplying both sides with $\mathbf{M}$ and making use of vector identities, resulting in the *Landau-Lifshitz-Gilbert* (LLG) equation

$$\frac{\mathrm{d}\mathbf{M}}{\mathrm{d}t} = \gamma'\mu_0 \left(\mathbf{M} \times \mathbf{H}_{\mathrm{eff}}\right) - \frac{\gamma'\alpha\mu_0}{M_{\mathrm{s}}} \left(\mathbf{M} \times \mathbf{M} \times \mathbf{H}_{\mathrm{eff}}\right) \tag{2.39}$$

with $\gamma' = \gamma / \left(1 + \alpha^2\right)$.

In spectroscopy, FMR typically appears as a Lorentzian shaped absorption of the irradiated

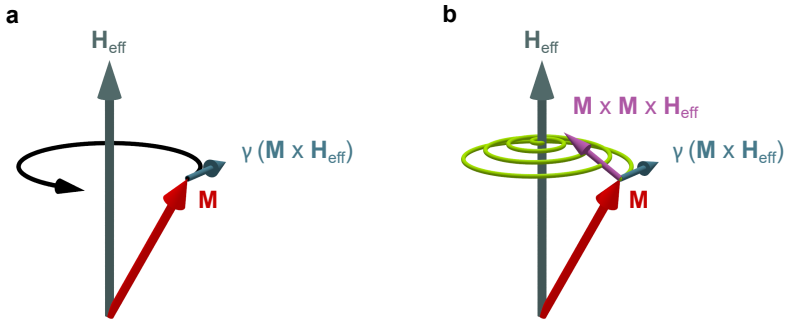

Figure 2.8: (a) Undamped and (b) damped rotation of magnetization $\mathbf{M}$ around the effective field $\mathbf{H}_{\mathrm{eff}}$. The acting torques of Eq. 2.33 and Eq. 2.37 are indicated.

microwave power. The precession lifetime is expressed as the line width of the absorption spectrum and is therefore consequently related to the different dissipation channels. For fixed excitation frequency, the full width at half maximum when sweeping the external field is given by [49]

$$\Delta H = \Delta H_0 + \frac{2\alpha}{\mu_0 \gamma} \omega_{\mathrm{FMR}}. \tag{2.40}$$

The first, constant term is referred to as *inhomogeneous broadening* and takes frequency independent effects such as, for instance, disorder or spatial fluctuations of the magnetic properties of the sample into account. The second term (*homogeneous broadening*) considers the discussed loss channels of intrinsic damping. Hence, when measuring the broadening as a function of the FMR frequency, one can extract and gain information on the Gilbert damping parameter α [49].

3 Spin transport effects and phenomena

Spintronics (spin-electronics) denotes the research field addressing the implementation of information technology concepts based on the transfer of spin angular momentum rather than electronic charge. In this chapter, a concise introduction to spintronic effects, which gained enhanced interest in recent years and which provide the basis for the experimental work reported in this thesis, will be given. Initially, the effective conversion of charge- to spin-information and vice versa via spin Hall effects is discussed, followed by a basic explanation of the closely related spin Hall magnetoresistance. With regard to spin information transport, various generation schemes of pure magnonic spin currents on the basis of ferromagnetic resonance, thermal spin pumping and electrical injection are presented.

3.1 Spin Hall effects

Within spin or magnetism related phenomena, Hall effects look back on a long history. In 1879, Hall discovered that when exposed to a magnetic field, moving electrons are deflected perpendicular to the field and propagation direction due to the Lorentz force [50]. Shortly afterwards, he demonstrated that the effect is significantly larger when observed in ferromagnetic metals [51]. The latter became known as the *anomalous Hall effect* (AHE), and is actually due to the spin-dependent, asymmetric deflection of electrons by means of spin-orbit interaction (SOI) [52].
In more recent years, a closely related effect to the AHE, namely the *spin Hall effect* (SHE), gained significant interest within the spintronics community. Without the need for applied magnetic fields or ferromagnetic order, the SHE enables the generation of pure diffusive spin currents in non-magnetic materials with large SOI. Sharing the same mechanisms with the AHE, the injection of a charge current in an SHE material results in a perpendicularly polarized, transverse spin flow due to spin-dependent, asymmetric deflection of electrons [10]. The crucial distinction from the AHE is that in non-magnetic materials conduction electrons do not exhibit spin-polarization, which is why the induced spin flow is not accompanied by an effective charge transport. In addition to the SHE, the reciprocal process (*inverse spin Hall effect*, ISHE) can occur, providing the opportunity of re-converting a spin current into a charge current and accordingly a detectable voltage [53].
The existence of the SHE was first predicted by D'yakonov and Perel, who discussed the

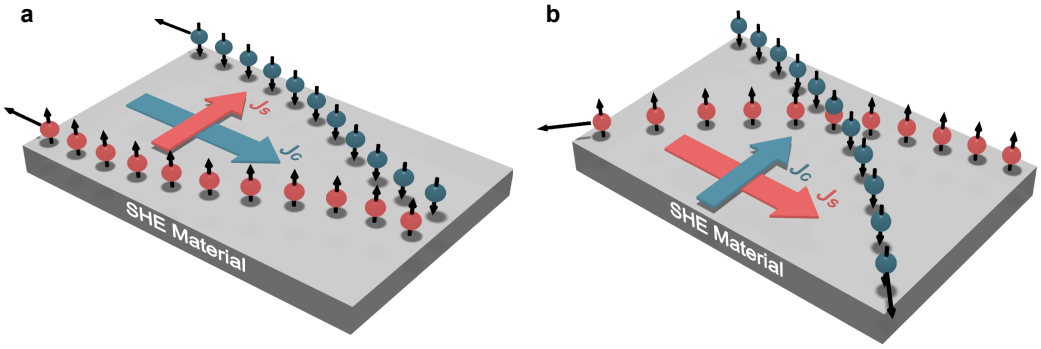

Figure 3.1: (a) Illustration of spin Hall effect: a charge current is converted into a pure spin current by the spatial separation of opposite electron spins. (b) Inverse spin Hall effect: re-conversion of a spin current into a charge current.

spatial separation of electrons with opposite spins in semiconductors [54]. This concept was picked up again later by Hirsch [55] and Zhang [56] and further expanded to paramagnetic metals. In these theoretical works, *extrinsic* effects due to Mott scattering off impurities are considered, including *skew scattering* [57] and the *side jump* mechanism [58]. Later, *intrinsic* contributions of relativistic band structures were discussed for semiconductors [59, 60] and $4d/5d$ transition metals [61]. The moving electrons gather a momentum-space Berry phase that results in a spin-dependent, anomalous velocity. Experimental demonstrations of the SHE include, for instance, measurements of the spatial separation of spin-up and spin-down electrons in semiconductors [62] or metals [63] via Kerr microscopy. In paramagnetic metals, however, initial experiments focused on the ISHE in non-local spin valve geometries [53, 64] or FMR spin pumping [12, 65] (see Sec. 3.3) for the electrical detection of spin currents.

The empirical formulae for the conversion of a charge current $\mathbf{J}_\mathrm{c} = \mathbf{J}_\uparrow + \mathbf{J}_\downarrow$ ($\mathbf{J}_{\uparrow,\downarrow}$ denotes the flow of spin-up/spin-down electrons, respectively) into a spin current $\mathbf{J}_\mathrm{s} = \mathbf{J}_\uparrow - \mathbf{J}_\downarrow$ and vice versa are given by [66]

$$\mathbf{J}_\mathrm{s} \propto \theta_\mathrm{SH} \left(\hat{\boldsymbol{\sigma}} \times \mathbf{J}_\mathrm{c}\right), \tag{3.1}$$

$$\mathbf{J}_\mathrm{c} \propto \theta_\mathrm{SH} \left(\hat{\boldsymbol{\sigma}} \times \mathbf{J}_\mathrm{s}\right). \tag{3.2}$$

Here, θ_SH is the so-called *spin Hall angle*, which quantifies the efficiency of the conversion process. For $4d/5d$ transition metals, which are of interest for this work, it was shown that the sign of θ_SH as well as its amplitude depend on the filling level of the d orbitals [61, 67]. θ_SH roughly scales with Z^4, indicating its SOI origin [68].

Despite extensive efforts, the congruent determination of θ_SH for distinct SHE materials

poses a major challenge, considering the broad spectra of θ_{SH} values reported. Taking the example of Pt, which due to its relatively large spin Hall angle became a model SHE material, θ_{SH} values in the range of approximately 0.5 % to 11 % can be found in the literature [10]. One explanation can be given by the complexity of the various measurement schemes, which require the determination or estimation of further quantities (e.g. spin mixing conductance, see Sec. 3.3) to extract θ_{SH}. Additionally, it was recently shown that the relative contribution of extrinsic and intrinsic SHE depends on the resistivity of the transition metal [69], introducing a further degree of freedom that requires consideration.
Altogether, the field of spin Hall effects is rich of physics and potential applications. The feasible generation and detection of pure spin currents provides enhanced possibilities for information transport, while it also allows one to drive the magnetization dynamics or manipulate the magnetic state of ferromagnetic layers via spin-orbit torques in multilayer systems. A comprehensive overview of the theoretical background and the various experimental schemes is provided by assorted review articles and textbook chapters [10, 66, 70].

3.2 Spin Hall magnetoresistance

Magnetoresistance (MR) describes the inherent property of metallic, magnetic systems of a manipulable electrical resistivity (longitudinal or transversal) depending on the magnetic configuration or external fields [71]. The first MR effect discovered is the so-called *anisotropic magnetoresistance* (AMR), where the resistivity depends on the relative alignment of the applied current direction and magnetization ($\rho_{\parallel} > \rho_{\perp}$). Generally, the origin of the AMR effect depends on the investigated material [72]. For transition metals or alloys the constituting mechanism is described by *s*-*d* interband scattering [73]. Due to SOI, the spin-split *d*-bands deform when re-orienting the magnetization direction, which results in larger scattering rates of the current mediating *s* electrons for $\mathbf{M} \parallel \mathbf{J}_{\mathrm{c}}$ versus $\mathbf{M} \perp \mathbf{J}_{\mathrm{c}}$.
In the course of increasing interest in spin Hall related effects, a new type of magnetoresistance was discovered, namely the *spin Hall magnetoresistance* (SMR). As one of the first reports, it was mentioned as a side finding in Ref. [74], with the resistance of a Pt film on top of the ferrimagnetic insulator (FMI) $Y_3Fe_5O_{12}$ (YIG) depending on the YIG magnetization direction. Since the electric current cannot enter the YIG film, the resistance change was initially assumed to be caused by a proximity induced magnetization of the paramagnetic Pt and thus a parasitic AMR [75]. The presence of magnetized Pt atoms, however, could later be ruled out with the aid of X-ray magnetic circular dichroism measurements [76]. Moreover, systematic studies [77–79] (including different metal layers) accompanied by a theoretical model [80] supported the validity of the SMR and provided a description

of the underlying mechanisms.

As depicted in Fig. 3.2a, the SMR is the consequence of the joint action of SHE and ISHE in the normal metal (NM) layer and an angular momentum transfer between NM and FMI. In view of the SHE, the injection of a charge current $\mathbf{J}_c$ into the NM layer induces a transverse spin current $\mathbf{J}_s$ such that a spin accumulation $\boldsymbol{\mu}_s$ builds up at the FMI/NM interface. The direction of $\boldsymbol{\mu}_s$ gives the spin polarization of the accumulated electrons. Depending on the relative alignment of $\boldsymbol{\mu}_s$ and the FMI magnetization $\mathbf{M}$, a spin-transfer torque (STT) [8, 81] and consequently spin flipping may become active. STTs generally denote the manipulation of the magnetic order in a ferromagnet by electron spin momenta and exert a torque:

$$\boldsymbol{\tau} \propto \mathbf{M} \times (\mathbf{M} \times \boldsymbol{\mu}_s)\,. \tag{3.3}$$

For parallel alignment of spin accumulation and magnetization, $\boldsymbol{\tau}$ is zero according to Eq. 3.3. As a consequence, the spin current is simply reflected and, induced by the ISHE, generates a charge current $\mathbf{J}_c^*$ flowing in the same direction as $\mathbf{J}_c$. For perpendicular alignment, however, $\boldsymbol{\tau}$ becomes finite and the reflected spin current density as well as $\mathbf{J}_c^*$ are reduced. Altogether, bearing in mind that $\boldsymbol{\mu}_s \perp \mathbf{J}_c$, this indicates an effectively enhanced (reduced) resistivity of the NM film for perpendicular (parallel) alignment of $\mathbf{J}_c$ and $\mathbf{M}$.

A method to identify the SMR are angular dependent magnetoresistance (ADMR) mea-

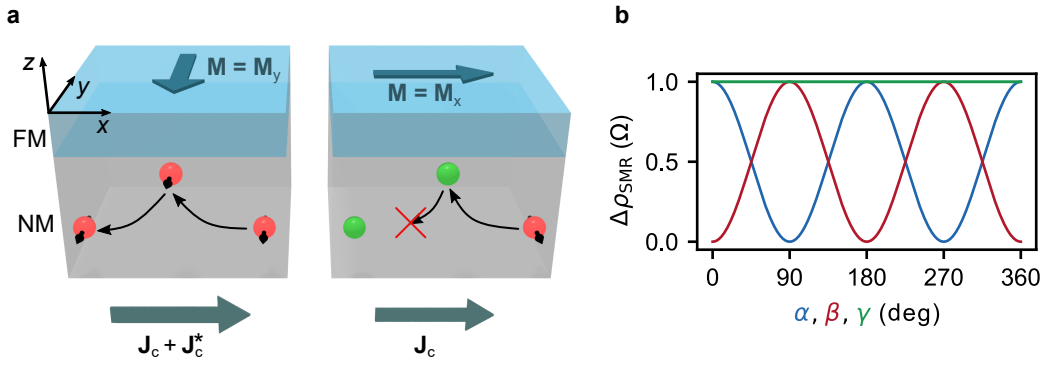

Figure 3.2: (a) Schematic representation of spin Hall magnetoresistance (SMR): In the case of parallel alignment of electron spin accumulation $\boldsymbol{\mu}_s$ and magnetization $\mathbf{M}$, the spin current is reflected and contributes to the total charge current $\mathbf{J}_c + \mathbf{J}_c^*$ (low resistive state). For $\boldsymbol{\mu}_s \perp \mathbf{M}$, the spin current is absorbed via spin-transfer torque and $\mathbf{J}_c^*$ is suppressed (high resistive state). Only one spin orientation is depicted on account of simplicity. (b) Angular dependence of $\Delta\rho_{SMR}$ in the xy-, yz-, and zx-plane. Regarding the corresponding angles, $\alpha = \beta = \gamma = 0$ signifies a magnetization alignment along the x-, y-, and z-axis, respectively.

surements, in which the external magnetic field and therefore the FMI magnetization is rotated, while capturing the longitudinal resistance of the NM film. The selection of the rotational axis allows one to distinguish potential AMR contributions, as shown in Fig. 3.2b. Whereas the field rotation within the xy-plane includes both AMR and SMR, rotating $\mathbf{M}$ in the yz-plane (zx-plane) yields the pure SMR (AMR) contribution [79]:

$$xy-\text{plane}: \quad \rho = \rho_0 + (\Delta\rho_{\text{AMR}} + \Delta\rho_{\text{SMR}})\cos^2(\alpha)\,, \tag{3.4}$$

$$yz-\text{plane}: \quad \rho = \rho_0 + \Delta\rho_{\text{SMR}}\sin^2(\beta)\,, \tag{3.5}$$

$$zx-\text{plane}: \quad \rho = \rho_0 + \Delta\rho_{\text{AMR}}\sin^2(\gamma)\,. \tag{3.6}$$

Here, $\alpha = \beta = \gamma = 0$ signify magnetization alignments along the x-, y-, and z-axis, respectively. When measuring the transversal resistance, the geometries change and in the out-of-plane measurements (yz, zx-plane) the ordinary Hall effect becomes of importance.

The effect amplitude of the SMR exhibits a complex dependence on various material-dependent parameters, as according to [80]

$$\frac{\Delta\rho_{\text{SMR}}}{\rho} = \theta_{\text{SH}}^2 \frac{\lambda_{\text{sd}}}{d_{\text{NM}}} \frac{2\lambda_{\text{sd}}\rho G_{\text{r}}^{\uparrow\downarrow}\tanh^2\left(\frac{d_{\text{NM}}}{2\lambda_{\text{sd}}}\right)}{1 + 2\lambda_{\text{sd}}\rho G_{\text{r}}^{\uparrow\downarrow}\coth\left(\frac{d_{\text{NM}}}{\lambda_{\text{sd}}}\right)}. \tag{3.7}$$

Here, θ_{SH} is the spin Hall angle introduced before, d_{NM} (λ_{sd}) the thickness (spin diffusion length) of the normal metal layer, ρ its intrinsic electric resistivity, and $G_{\text{r}}^{\uparrow\downarrow}$ the real part of the spin mixing conductance. Roughly speaking, $G_{\text{r}}^{\uparrow\downarrow}$ gives the transparency of the NM/FMI interface for spin currents and thereby affects the STT efficiency (please see Sec. 3.3 for a more detailed discussion). Experimentally, the relevance of $G^{\uparrow\downarrow}$ became apparent as the SMR amplitude depends on the NM deposition technique and therefore the interface condition [82, 83]. Temperature-dependent measurements revealed that the SMR amplitude generally reduces with decreasing temperature [84, 85], although the given interpretations of this observation partially interfere. Both Marmion *et al.* [84] and Meyer *et al.* [85] assume temperature-independent values for $G_{\text{r}}^{\uparrow\downarrow}$, however, the explanation of the signal reduction at lower temperatures is given in Ref. [84] by a temperature-independent (temperature-dependent) spin Hall angle θ_{SH} (spin diffusion length λ_{sd}), while in Ref. [85] the exact opposite behavior is reported. At high temperatures up to T_{C} the SMR amplitude reduces again (stronger decay than the magnetization) [86, 87], which is attributed to a decreasing $G_{\text{r}}^{\uparrow\downarrow}$.

The majority of SMR studies concentrated on NM/FMI bilayers. Nevertheless, the SMR also appears in fully metallic systems, in which the FMI is replaced by a metallic ferromagnet [88] and can even reveal a unidirectional behavior due to the different diffusion

properties of minority and majority spin electrons [89, 90]. More recently, it was further demonstrated that the SMR also occurs in systems including antiferromagnetic insulators (AFMI), either as a bulk crystal [o11, 91, 92] or as an interlayer between NM and FMI [93, 94]. Instead of $\mathbf{M}$, the spin accumulation in the NM couples to the Néel vector $\mathbf{N}$. This results in a 90° phase shift and is often also perceived as *negative* SMR.
In this thesis, temperature-dependent spin Hall magnetoresistance measurements were performed as a tool to probe the spin propagation mechanism (magnonic vs. electronic) of pure spin currents across metallic antiferromagnets (see Sec. 5.2 and Ref. [o8]).

3.3 Spin pumping

As already mentioned in Sec. 2.5.2, ferromagnets exhibit an enhanced Gilbert damping constant α when in contact with a normal metal layer. The explanation for this observation is the transfer of angular momentum from the precessing magnetization of the ferromagnet to the NM electron system [11, 95]. As a result, a spin current is pumped across the FM/NM interface, which in the NM is mediated by diffusive electrons. This mechanism of pure spin current generation has become known as *spin pumping* (SP) and is the reciprocal effect of the spin transfer torque discussed in the previous section. Following the notation of Ref. [11, 95], the spin current pumped into the NM is given by

$$\mathbf{I}_{\mathrm{s}}^{\mathrm{pump}} = \frac{\hbar}{4\pi}\left(\frac{\mathcal{A}_{\mathrm{r}}}{M_{\mathrm{s}}^2}\mathbf{M}\times\frac{\mathrm{d}\mathbf{M}}{\mathrm{d}t} + \frac{\mathcal{A}_{\mathrm{i}}}{M_{\mathrm{s}}}\frac{\mathrm{d}\mathbf{M}}{\mathrm{d}t}\right). \tag{3.8}$$

Referring to the Onsager's reciprocity relations [96], the interface conductance parameters $\mathcal{A}_{\mathrm{r}}$ and $\mathcal{A}_{\mathrm{i}}$ must be equivalent to the ones of the STT mechanism. They therefore correspond to the real and imaginary parts of the spin mixing conductance ($\mathcal{A}_{\mathrm{r}} = G_{\mathrm{r}}^{\uparrow\downarrow}$, $\mathcal{A}_{\mathrm{i}} = G_{\mathrm{i}}^{\uparrow\downarrow}$) that has been briefly mentioned before.
The concept of $G^{\uparrow\downarrow} = G_{\mathrm{r}}^{\uparrow\downarrow} + iG_{\mathrm{i}}^{\uparrow\downarrow}$ was first introduced in a circuit theory by Brataas *et al.* [97, 98] and describes the intermixing of spin-up and spin-down electron channels via spin rotation around the FM magnetization axis. The meaning of $G_{\mathrm{r}}^{\uparrow\downarrow}$ and $G_{\mathrm{i}}^{\uparrow\downarrow}$ can be easier understood when considering the spin current density at a FM/NM interface induced by a spin accumulation $\boldsymbol{\mu}_{\mathrm{s}}$ (STT) [80]:

$$e\mathbf{J}_{\mathrm{s}} = \frac{G_{\mathrm{r}}^{\uparrow\downarrow}}{M_{\mathrm{s}}^2}\mathbf{M}\times(\mathbf{M}\times\boldsymbol{\mu}_{\mathrm{s}}) + \frac{G_{\mathrm{i}}^{\uparrow\downarrow}}{M_{\mathrm{s}}}(\mathbf{M}\times\boldsymbol{\mu}_{\mathrm{s}}). \tag{3.9}$$

The first term on the right side characterizes a diffusive contribution, whereas the second term describes a classical precession torque [98]. In terms of SP, this signifies an enhancement of the Gilbert damping constant α due to $G_{\mathrm{r}}^{\uparrow\downarrow}$. $G_{\mathrm{i}}^{\uparrow\downarrow}$, however, affects the gyromagnetic

ratio γ and therefore manifests as a shift of the resonance frequency [11].

First-principles calculations showed that the real part of $G^{\uparrow\downarrow}$ is generally much larger than the imaginary part in systems including either metallic or insulating FMs and without insulating non-magnetic spacers [99–101]. $G_{\mathrm{i}}^{\uparrow\downarrow}$ can therefore be mostly neglected. Additionally, the initial theoretical description of the SP effect by Tserkovnyak *et al.* [11] regarded the NM as a perfect spin sink. This assumption does not hold true, however, for real systems due to finite spin relaxation channels in the NM. Typically, a spin accumulation builds up in the NM at the FM/NM interface, which, bearing in mind Onsager's reciprocity relations [96], induces a spin current back-flow into the FM. On that account, an effective spin mixing conductance $G_{\mathrm{eff}}^{\uparrow\downarrow}$ must be considered [102, 103].

Experimentally, the SP effect was first observed by Mizukami *et al.* [104, 105] in FMR measurements, in which the absorption linewidth was investigated as a function of NM layer type and thickness. Later, the inverse spin Hall effect became a useful tool for the detection of the generated spin current as it allows one to measure the ISHE voltage induced in the NM layer [12, 65, 106]. In the case of metallic ferromagnets, however, one has to be mindful of so-called *spin rectification* (SR) effects which may appear in addition to the actual SP-ISHE signal [107–110]. The electric field of the microwave driving the magnetization precession couples capacitively into the FM and induces an oscillating charge current $\tilde{\mathbf{I}}_{\mathrm{c}}(t)$. This current, together with the rotating magnetization, can result in an additional voltage due to the AMR or the AHE depending on the geometry (e.g. field direction).

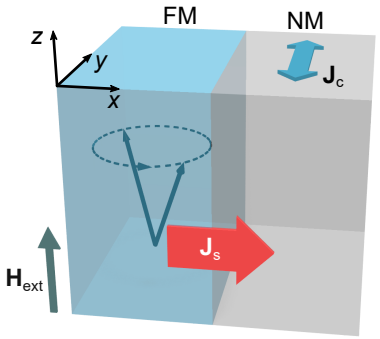

Figure 3.3: Spin pumping mechanism in a ferromagnet (FM)/normal metal (NM) bilayer system. The rotating magnetization of the ferromagnet emits a pure spin current $\mathbf{J}_{\mathrm{s}}$ into the NM via transfer of angular momentum, which is mediated by diffusive electrons. The coupling strength between the FM magnetization and the NM conduction electrons is quantified by the spin mixing conductance $G^{\uparrow\downarrow}$. If the NM exhibits the spin Hall effect, $\mathbf{J}_{\mathrm{s}}$ is conerted into a transversal charge current $\mathbf{J}_{\mathrm{c}}$.

Taking into account only the first term of Eq. 3.8, the precessing magnetization induces both a time-dependent (AC; orthogonal to equilibrium-magnetization) and constant (DC; parallel to equilibrium-magnetization) polarization component of the spin current [111]. Although the AC signal has been reported to be of larger amplitude [112, 113], the DC component is usually captured with regard to simpler detection schemes in the experiment. The DC component of the generated spin current density is [114]

$$J_\mathrm{s} = \frac{\omega\hbar}{8\pi^2 M_\mathrm{s}^2} G_\mathrm{eff}^{\mathbb{1}} \int_0^{2\pi/\omega} \left[\mathbf{M}(t) \times \frac{\mathrm{d}\mathbf{M}(t)}{\mathrm{d}t}\right]_z \mathrm{d}t, \tag{3.10}$$

where $[\cdots]_\mathrm{z}$ denotes the z-component and ω is the precession frequency. The latter typically corresponds to the FMR frequency, however, spin pumping voltages generated by parametrically pumped exchange magnons have been reported as well [115]. Similar to the SMR amplitude given in Eq. 3.7, the induced ISHE voltage is affected by several material parameters [68]:

$$V_\mathrm{ISHE}^\mathrm{SP} = \frac{-e\theta_\mathrm{SH}\lambda_\mathrm{sd} G_\mathrm{eff}^{\mathbb{1}} LP\omega}{2\pi\left(\sigma_\mathrm{N} t_\mathrm{N} + \sigma_\mathrm{F} t_\mathrm{F}\right)} \left(\frac{\gamma h_\mathrm{rf}}{2\alpha\omega}\right)^2 \tanh\left(\frac{t_\mathrm{N}}{2\lambda_\mathrm{sd}}\right). \tag{3.11}$$

Here, e gives the elementary charge, λ_sd and θ_SH are the spin diffusion length and spin Hall angle of the normal metal, σ_N (σ_F) and t_N (t_F) are the conductivity and the thickness of the normal metal (ferromagnet), and h_rf is the microwave driving field. L is the distance in between the voltage contacts and P is a correction factor considering an elliptical rather than circular magnetization precession regarding anisotropy fields.

Besides the mere generation of a spin current, spin pumping has been established as a useful tool for the investigation of material properties. For example, SP allows one to determine the interfacial spin-mixing conductance $G^{\mathbb{1}}$ by considering the additional Gilbert damping $\alpha_\mathrm{FM/NM} - \alpha_\mathrm{FM}$ [68, 116] as well as the spin diffusion length λ_sd of ISHE detection layers by measuring the SP voltage as a function of the detector thickness. Having determined both $G^{\mathbb{1}}$ and λ_sd as well as the conductivities of the single layers, one can use Eq. 3.11 to determine the spin Hall angle θ_SH [68, 116, 117]. More recently, SP has been implemented to probe spin propagation [118–121] as well as the phase transition [122, 123] of both insulating and metallic antiferromagnets.

In the work presented in this thesis, FMR spin pumping was implemented to investigate the efficiency of spin current detection in YIG/CoO/Co tri-layers. As shown in Sec. 6.1, the latter alters as a function of the relative alignment of the YIG and Co magnetization, rendering a spin-valve like behavior [o9].

3.4 Spin caloritronics

3.4.1 Classical thermoelectrics

The research field of spin-unrelated, classical thermoelectrics addresses the conversion of thermal into electrical energy and vice versa in the prospect of sustainable energy sources [124, 125]. Respective devices are, for instance, the thermoelectric generator and refrigerator based on the *Seebeck-* [126] and *Peltier effect* [127]. In terms of the former, the Seebeck effect describes the occurrence of an electric field within a conductor when exposed to a temperature gradient $\boldsymbol{\nabla} T$, see Fig. 3.4a. The induced thermovoltage is given by the varying occupation of charge carrier states around the Fermi energy ϵ_F alongside the temperature gradient. Hereby, a non-equilibrium distribution of charge carrier mean velocities is induced, resulting in a heat current $\mathbf{Q}$ mediated by charge carrier diffusion. In the open-circuit condition, the charge carriers cannot exit the conductor and an electric field parallel to the temperature gradient arises [128]:

$$\mathbf{E} = S \boldsymbol{\nabla} T. \tag{3.12}$$

S denotes the *Seebeck coefficient*, which is a material specific parameter and generally temperature-dependent. Connecting two metals with different Seebeck coefficients in series yields a so-called *thermocouple*, which, for instance, can be used as temperature sensor. Furthermore, multiple thermocouples linked in a 2D *thermopile* grid (see Ref. [125] for

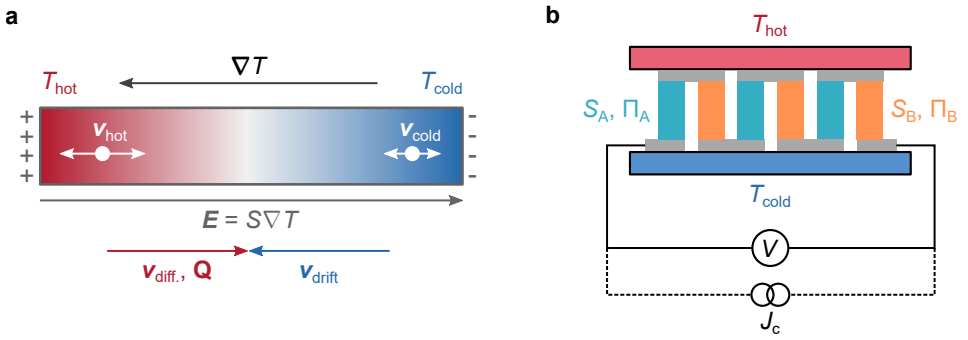

Figure 3.4: (a) Illustration of the classical Seebeck effect. Due to a thermally induced non-equilibrium distribution of electron kinetic energy, conduction electrons diffuse alongside the temperature gradient from the hot to the cold area in the metal. In the open circuit condition, the electrons cannot exit the metal but induce an electric field, which yields a reversed drift motion. Eventually, no net charge current $\mathbf{J}_\mathrm{c}$ but a heat current $\mathbf{Q}$ is flowing. (b) Multiple thermocouples connected in series to either create a thermoelectric power generator or a Peltier device.

more details) yield a thermoelectric power generator with enhanced voltage output.

Recalling Onsager's reciprocity relations [96], the Peltier effect describes the inverse mechanism to the Seebeck effect: a charge current $\mathbf{J}_\mathrm{c}$ applied to a conductor is accompanied by a heat flow [128]

$$\mathbf{Q} = \Pi \mathbf{J}_\mathrm{c} \tag{3.13}$$

with the material specific *Peltier coefficient* Π. Reconsidering the thermocouple structure in Fig. 3.4b, different heat currents $\mathbf{Q}^\mathrm{A}$ and $\mathbf{Q}^\mathrm{B}$ flow in conductor A and B. At the junctions, however, thermal equilibrium must be re-established, implying the simultaneous emission and absorption of the heat $(\Pi_\mathrm{A} - \Pi_\mathrm{B})\,\mathbf{J}_\mathrm{c}$ by the distinct junctions. As a result, one junction is cooled while the other one is heated. The respective thermopile structure is known as Peltier device.

The Seebeck and Peltier coefficient are linked by the Kelvin-Onsager relation [129]

$$\Pi = ST. \tag{3.14}$$

3.4.2 Nernst effects

Charge currents induced by thermoelectric electromotive forces instead of applied electric fields are, nonetheless, subject to the Hall and magnetoresistance effects described in Sec. 3.1 and Sec. 3.2. The thermoelectric analogue of the Hall effect, for instance, is known as the *Nernst effect* [130]. It describes the deflection of thermally activated, diffusive charge carriers within a metallic film transversal to the applied temperature gradient and magnetic field.

Maintaining a consistent notation, the thermoelectric analogue of the AHE is denoted as *anomalous Nernst effect* (ANE) [131]. Due to the scattering mechanisms discussed in Sec. 3.2, thermally induced charge motion in a metallic ferromagnet results in a thermovoltage perpendicular to the magnetization and the temperature gradient [132]:

$$\mathbf{E}_\mathrm{ANE} = -N \frac{\mathbf{M}}{M_\mathrm{s}} \times \boldsymbol{\nabla} T. \tag{3.15}$$

The proportionality factor is given by the Nernst coefficient N, which is a fraction of the Seebeck parameter S [132]. Equation 3.15 signifies a sinusoidal dependence of V_ANE on a varying angle θ between $\mathbf{M}$ and $\boldsymbol{\nabla} T$. For an out-of-plane temperature gradient, the excited thermovoltage therefore reflects the in-plane magnetization component, which lends the ANE as a useful tool for the qualitative characterization of magnetic sample properties.

With regard to in-plane temperature gradients one has to be aware of potential voltage contributions from the so-called *planar Nernst effect* (PNE) [133, 134]. It occurs in con-

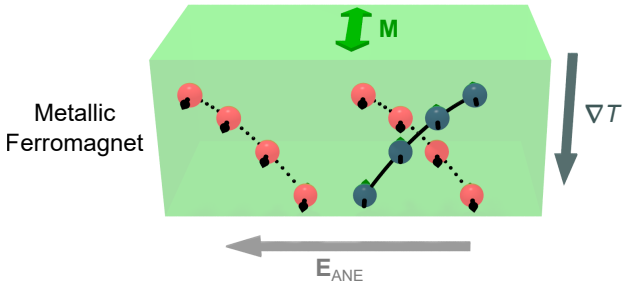

Figure 3.5: Functional principal of the anomalous Nernst effect. Electron motion is induced by a temperature gradient, at which electrons with opposite spins are deflected in opposite directions due to SOI-based extrinsic or intrinsic effects. Considering the different densities of state of minority and majority spin electrons at the Fermi level, an electric field arises.

sequence of anisotropic scattering (i.e. the thermal equivalent of the AMR) and follows an angular dependence of $V_{\mathrm{PNE}} \propto \sin(2\varphi)$, where φ is the angle between the in-plane components of $\mathbf{M}$ and $\boldsymbol{\nabla} T$.
More recently, the experimental demonstration of the thermoelectric counterpart of the SHE in normal metals, namely the *spin Nernst effect*, has been reported [135, 136]. In the same manner as the SHE, a thermally generated charge flow $\mathbf{J}_{\mathrm{c}}^{\mathrm{therm.}}$ induces a transverse spin current $\mathbf{J}_{\mathrm{s}}$. Since the direct detection of pure spin currents is unfeasible, $\mathbf{J}_{\mathrm{s}}$ was validated indirectly by means of the SMR. In a FMI/NM bilayer, the longitudinal thermovoltage generated by an in-plane temperature gradient was detected whilst rotating the FMI magnetization $\mathbf{M}$. As a result, the thermovoltage modulates as a function of the angle between the induced spin-accumulation $\boldsymbol{\mu}_{\mathrm{s}}$ at the FMI/NM interface and $\mathbf{M}$ due to an active/inactive spin-transfer torque.

3.4.3 Spin Seebeck effect

While Nernst effects consider the deflection of thermally induced charge motion in magnetic fields or through SOI scattering, the thermal activation of spin currents flowing alongside ∇T in magnetic materials is assigned to spin-equivalents of the Seebeck effect. With respect to the nomenclature, one has to be aware that depending on the spin transport mechanism and sample layout diverse notations have established [14].
In metallic ferromagnets, owing to generally different intrinsic properties of majority and minority spin electrons [5], the two spin channels exhibit distinct Seebeck coefficients $S^{\uparrow,\downarrow}$. As a result, the application of a temperature gradient leads to a spatial variation (on the length scale of the spin-diffusion length) of the spin-dependent electrochemical potentials

$\mu^{\uparrow,\downarrow}$ driving the spin current. This *spin-dependent Seebeck effect* was first observed by Slachter *et al.* making use of a lateral non-local spin valve structure [137]. Its inverse, the *spin-dependent Peltier effect*, was demonstrated in a spin-valve pillar structure directly linked to a thermocouple [138]. The *magneto-Seebeck effect*, then again, appears in magnetic tunnel junctions and denotes the magnetization alignment-dependent thermovoltage across the junction [139].

Chronological development of the spin Seebeck effect

The mechanism that is of actual interest for this thesis is the so-called *spin Seebeck effect* (SSE). At the present day, the SSE is generally understood as the thermal excitation of spin currents mediated by collective excitations [14]. Chronologically, the first claim of the SSE was reported by Uchida *et al.* in 2008, who measured a thermal signal in a $Ni_{81}Fe_{19}$ (Permalloy; Py) film with Pt wires structured on top [140]. The respective measurement geometry, which was denominated as transverse SSE, is depicted in Fig. 3.6. Following the phenomenological description given in [140], the application of an in-plane temperature gradient is supposed to generate a pure spin current owing to an imbalance between $\mu^{\uparrow}$ and $\mu^{\downarrow}$ that stretches over the whole sample. The spin current partially diffuses into the Pt stripes, where it is converted into a voltage signal by means of the ISHE. Depending on the position of the Pt stripe (hot/cold end, sample center), the ISHE voltage changes sign or disappears. Similar observations were made later for systems in which Py was replaced by the magnetic semiconductor GaMnAs [142] or the Heusler compound Co_2MnSi [143].
In conducting systems, the reported mechanism of a thermally induced spin imbalance reminds of the spin-dependent Seebeck effect. The difference, yet, is the assumption of a

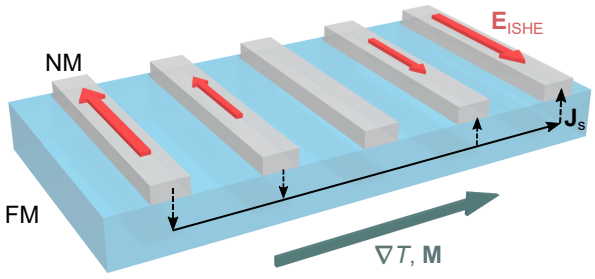

Figure 3.6: Transversal spin Seebeck geometry used in first experiments [140]. An in-plane temperature gradient shall drive a macroscopic spin current, which is detected by the ISHE in NM bars. Depending on the position (hot or cold end), opposite signs of the signal were expected.

spin imbalance over length scales ($L = 6\,\mathrm{mm}$ [140]) much larger than the spin diffusion length ($\lambda_{\mathrm{sd}}^{\mathrm{Py}} \approx 2.3\,\mathrm{nm}$ at $T = 300\,\mathrm{K}$ [144]). Doubts on the existence of such a macroscopic spin current were raised by Jaworski *et al.* [142]. In their measurements, a scratch bisecting the magnetic layer and therefore interrupting the spin current did not yield qualitative differences of the observed spin signal. Furthermore, the observation of the transversal SSE in the magnetic insulator YIG [145], in which electron motion is suppressed, questioned the overall significance of charge mediated spin transfer. Alternative explanations of the transversal SSE were given considering the spin redistribution in thermally excited systems being driven by phonons of the underlying substrate [146]. This idea was further promoted by modeling a spectral non-uniform temperature of thermal ($\hbar\omega \approx k_{\mathrm{B}}T$) and subthermal ($\hbar\omega < k_{\mathrm{B}}T$) phonons, which locally induces vertical heat and spin transport [147].
In the wake of these first reports on the transversal SSE, unsuccessful efforts were made by various research groups to reproduce the initial results using similar materials and measurement geometries [132, 134, 148–150, 141]. As an alternative, signal contributions due to the PNE were identified in metallic ferromagnets. Moreover, the comprehensive study by Meier *et al.* [141] identified the unintentional generation of out-of-plane temperature gradients depending on the employed metal contacting scheme as a further possible explanation of the transversal SSE. In the case of conducting FMs, this circumstance proposes the presence of parasitic ANE thermovoltages. Altogether, these results emphasize the complexity of the investigated phenomenon and the necessity for careful consideration and interpretation of taken measurement data.

Magnon-mediated spin Seebeck effect

Different from conductive systems, the occurrence of a thermally induced, magnetization-dependent signal in FMI/NM bilayers signified an actual spin current flow within the FMI, including spin-to-charge conversion in the NM. Since charge motion is suppressed in insulating systems, interfering Nernst contributions from the FMI itself could be excluded. However, as discussed in Sec. 3.2, the appearance of the SMR in YIG/Pt initiated a debate about a spurious proximity induced interface magnetization of Pt [75] when in contact with an FMI. This would imply potential Nernst signals generated in the Pt layer, nevertheless, systematic studies including the insertion of a thin, decoupling Cu layer in between YIG and Pt verified the validity of the SSE [151].
For one thing, the absence of parasitic Nernst signals in FMI/NM bilayers allowed for the introduction of the more robust longitudinal SSE measurement geometry [13] (see Fig. 3.7a). At the same time, the restraint of charge-mediated angular momentum transfer entailed the apparent question of the actual spin transport mechanism. In view of the established FMR spin pumping method, proposed theoretical models [152–158] consider a

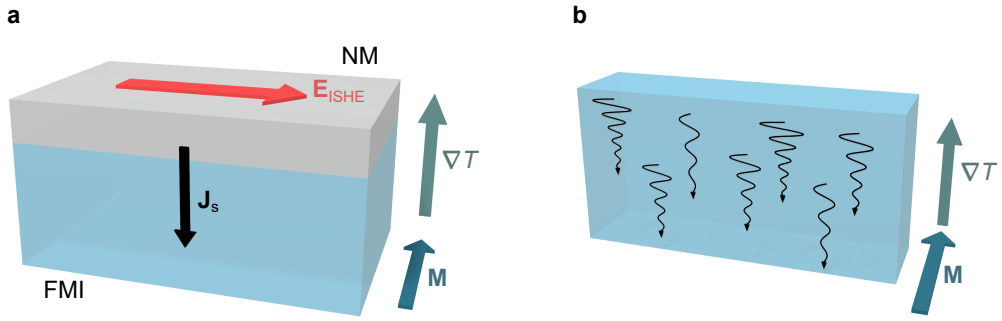

Figure 3.7: (a) Illustration of the longitudinal spin Seebeck configuration, which is applied for insulating ferromagnets. An out-of-plane temperature gradient induces a non-equilibrium distribution of magnons in the FMI, as shown in (b), yielding a diffusive spin current. The latter is transferred into an adjacent NM layer, in which it is converted into a charge signal by means of the ISHE.

magnonic origin of the SSE. Nonetheless, the suggested models exhibit distinct differences with regard to the physical processes involved. Whereas one group ([152–154]) attributes the thermally pumped spin signal to a temperature imbalance between FMI magnons (T_m) and NM conduction electrons (T_e), the second group ([155–158]) studies bulk magnon propagation (magnonic spin currents) in the FMI.

Experimental confirmation of the bulk origin of the SSE was provided by previous work preceding the results presented in this thesis [o1, o3]. When measured as a function of the FMI thickness, the SSE voltage amplitude initially increases with increasing thickness and ultimately saturates. The theoretical explanation of this behavior is based on a finite mean propagation length ξ of the thermally excited magnons. In single crystalline YIG, ξ-values from 1.2 µm to 6 µm at room temperature and low temperatures, respectively, are observed, revealing a T^{-1} dependence [o3].

Potential contributions due to an interfacial SSE were discussed in the course of ultrafast spin excitation measurements [o12, 159]. The illumination of YIG/NM bilayers by femtosecond laser pulses triggered measurable magnetic reponses in the picosecond or even femtosecond regime that are ascribed to thermal excitations. The reported argumentation includes, among other reasons, coinciding temperature dependences in comparison to conventional longitudinal SSE measurements [o12, 160]. As the observed time scales are too short for the creation of an effective temperature gradient in the bulk [159], the interfacial SSE is concluded to induce the measured signals.

The direct quantitative determination of material properties, e.g. the NM spin Hall angle, via SSE measurements is virtually impossible without any presumptions regarding the complexity of the underlying processes. In contrast to FMR, the magnetic moments of

the FMI do not rotate coherently, but the generated spin current is carried by a spectrum of incoherent spin waves. It was furthermore demonstrated that magnons of different frequencies do not contribute equally to the measured signal [o3, 36, 161]. Ultimately, the SSE reveals a complex temperature dependence concerning the interplay of magnon propagation and population as well as a magnon mode-dependent interface spin mixing conductance $G_{\mathrm{eff}}^{\mathbb{1}}$ [o3, o4]. Nevertheless, the attempt by Rezende *et al.* to capture most of the contributing factors yields the following equation for the measured ISHE voltage in a FMI/NM bilayer induced by the bulk SSE [158]:

$$V_{\mathrm{sse}} = BF\rho\frac{2e}{\hbar}wR_{\mathrm{N}}\theta_{\mathrm{SH}}\lambda_{\mathrm{sd}}\tanh\left(\frac{t_{\mathrm{N}}}{2\lambda_{\mathrm{sd}}}\right)G_{\mathrm{eff}}^{\mathbb{1}}\nabla T \tag{3.16}$$

Here, B is a factor including various integrals incorporating, for example, the energy distribution or the diffusion of magnons, while F summarizes material parameters and universal constants. The impact of a finite FMI thickness in view of the magnon propagation length is considered by ρ. R_{N}, w and t_{N} are the resistance, width and thickness of the NM with spin diffusion length λ_{sd} and spin Hall angle θ_{SH}. As mentioned earlier the large number of parameters impedes their quantitative determination. Fixing some conditions, e.g. equal bulk systems, provides nonetheless the possibility to make qualitative statements about the remaining properties of interest. In this thesis, for example, the compositional dependence of the spin-to-charge conversion process in binary copper-iridium alloys is investigated by means of SSE measurements using YIG as a spin source [o7]. While the properties of the ISHE metals vary, the spin source characteristics are kept constant by using YIG samples from the same wafer and treating the surface of each sample equally before depositing the alloy.

While the author contributed to the investigation of physical processes involved in the spin Seebeck effect [o1–o4, o12], measurements presented in this theses mainly exploit the SSE, at least in the longitudinal configuration, as a useful method for spin current generation (please see Sec. 5.2 and Sec. 5.3). Note that although the author of this thesis is the first author of Ref. [o4], the experimental results presented in this publication were mainly obtained by Er-Jia Guo (second author) such that they are not shown here. In this work, the insulating ferrimagnet YIG is considered exclusively with regard to its extraordinary properties (see Sec. 4.1) and due to the absence of undesired Nernst effect contributions. Besides YIG, however, the SSE has been investigated so far in various FMIs including further iron garnets (e.g. $Gd_3Fe_5O_{12}$ [o4, 162]) or spinel ferrites (e.g. Fe_3O_4 [163], $NiFe_2O_4$ [164], $CoFe_2O_4$ [o2, 165]). In addition, the SSE was observed in the paramagnetic $Gd_3Ga_5O_{12}$ [166] or the insulating antiferromagnets Cr_2O_3 [167] and MnF_2 [168] at low temperatures and high magnetic fields. The latter are required to bring about a sufficiently

large magnetic moment.

Referring back to Onsager's reciprocity relations [96], the injection or absorption of FMI magnon currents is entailed by a heat flow and thus heating or cooling of the magnetic system. Eventually, the respective *spin Peltier effect* has been observed experimentally in YIG/Pt bilayers [169].

3.5 Non-local spin injection

Beyond microwave induced or thermal spin pumping, the excitation and detection of spin currents in magnetic insulators can be accomplished in a fully electrical manner. In a NM1/FMI/NM2 tri-layer, the injection of a charge current through NM1 invokes a voltage response in NM2 and vice versa by means of a magnon mediated current drag. The concept was proposed theoretically by Zhang and Zhang [170, 171] and later confirmed experimentally by Cornelissen *et al.* [22] and Goennenwein *et al.* [172] in a slightly modified manner.

With regard to the concept, the current driven through NM1 stimulates a transversal spin current due to the SHE and hence a spin accumulation $\boldsymbol{\mu}_\mathrm{s}$ at the NM1/FMI interface builds up. The conduction electrons of NM1 interact with the localized magnetic moments at the FMI interface via *s-d* exchange coupling provided by the overlapping electron wave functions [170, 171, 173], thus acting as a spin bias. In contrast to the SMR [77, 80] and earlier experiments by Kajiwara *et al.* [106], angular momentum transfer by spin-transfer torques is disregarded but creation and annihilation processes of high frequency magnons ($\hbar\omega \approx k_\mathrm{B}T$) are considered here:

$$\mathcal{H}_\mathrm{sd} = J_\mathrm{sd}\sqrt{\frac{S}{2N_\mathrm{s}}}\sum_{\mathbf{k},\mathbf{k}',\mathbf{q}}\left(a_\mathbf{q}^\dagger c_{\mathbf{k}'\uparrow}^\dagger c_{\mathbf{k}\downarrow} + a_\mathbf{q} c_{\mathbf{k}'\downarrow}^\dagger c_{\mathbf{k}\uparrow}\right)\delta_{\mathbf{k}=\mathbf{k}'+\mathbf{q}} \tag{3.17}$$

Here, $a_\mathbf{q}^\dagger$ ($a_\mathbf{q}$) and $c_{\mathbf{k}^{(\prime)},\boldsymbol{\sigma}}^\dagger$ ($c_{\mathbf{k}^{(\prime)},\boldsymbol{\sigma}}$) denote the magnon and electron creation (annihilation) operators, respectively, with wave vectors $\mathbf{q},\mathbf{k},\mathbf{k}'$ and spin $\boldsymbol{\sigma} = \uparrow,\downarrow$ [171]. In this manner, a magnon non-equilibrium distribution (accumulation or depletion) is created underneath NM1, which diffuses isotropically in the FMI. At the FMI/NM2 interface, the reciprocal process occurs: the evoked magnon accumulation or depletion, which is reduced in amplitude due to magnon relaxation, spin-polarizes the conduction electrons of NM2 at the interface. The thus pumped spin current induces transversal charge motion by means of the ISHE, generating a voltage signal. Altogether, NM1 can be considered as a spin current injector, whereas NM2 acts as a detector.

The initial proposal by Zhang and Zhang examines spin current propagation in a 1D ge-

ometry [170], which has recently been demonstrated experimentally [174, 175]. In most experiments so far, however, the 2D geometry introduced by Cornelissen *et al.* [22] (see Fig. 3.8a) is used with regard to an easier sample fabrication. Instead of the envisaged tri-layer structure, which poses a major challenge regarding material growth, two parallel NM wires are structured on top of the FMI. This geometry reveals the same functionality as the tri-layer and furthermore yields the conceptual advantage that magnon propagation properties can easily be investigated by modulating the wire distance [22, 176]. In this respect, magnon propagation lengths of 0.7 µm [172] and 9.4 µm [22] were measured in YIG films of different thickness at room temperature.

According to Eq. 3.1, the sign and amplitude of the spin accumulation $\boldsymbol{\mu}_s$ and hence the induced magnonic spin current respond linearly to the charge current $\mathbf{J}_c$ applied to NM1. In addition to that, an angular dependence on the FMI magnetization orientation is expected with regard to the active spin transfer mechanism. Roughly speaking, in view of magnon creation or annihilation, the spin accumulation $\boldsymbol{\mu}_s$ couples to the magnetization component parallel to it such that the non-local signal is largest for $\mathbf{M} \parallel \boldsymbol{\mu}_s$ ($\mathbf{M} \perp \mathbf{J}_c$) and zero for $\mathbf{M} \perp \boldsymbol{\mu}_s$ ($\mathbf{M} \parallel \mathbf{J}_c$). Furthermore, in the case of $\mathbf{M} \perp \boldsymbol{\mu}_s$, the spin accumulation amplitude

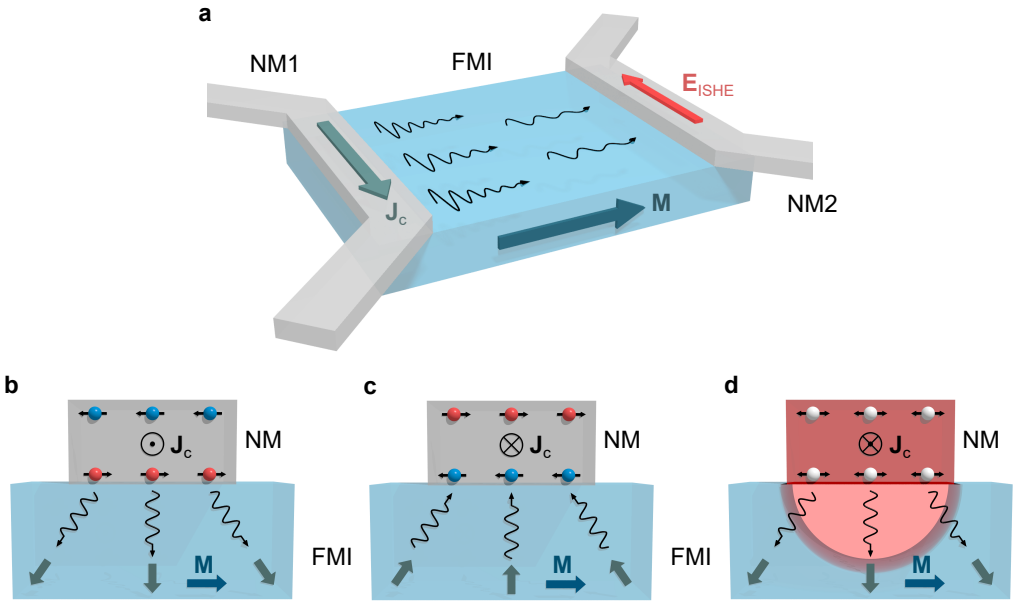

Figure 3.8: (a) Schematic of the non-local spin injection geometry. Injecting a charge current into the NM1 detector induces a magnon (a) accumulation or (b) depletion at the interface due to the SHE or (c) thermally induces the SSE. After propagating through the FMI, the spin current is re-converted into a voltage signal in the NM2 detector by the ISHE [reciprocal process of (a),(b)].

at the interface is at least reduced by the spin-transfer torque [172]. Adopting the picture of a non-local magnetoresistance provided by Goennenwein *et al.* [172], one may write for the detected spin signal:

$$V_{\mathrm{el.}}^{\mathrm{nl}} = R_{\mathrm{el.}}^{\mathrm{nl}} \cos^2(\alpha) \cdot J_{\mathrm{c}}. \tag{3.18}$$

Note that $R_{\mathrm{nl}}^{\mathrm{el.}}$ is negative when using the non-local geometry shown in 3.8 and injector and detector materials with equal sign of the spin Hall angle [172].

Beyond the electrical generation of magnon spin currents, the non-local geometry can be used to investigate the propagation of thermally excited spin waves. The injection of a charge current in NM1 entails Joule heating and therefore gives rises to a non-local spin Seebeck effect. Being tempted to draw an analogy to the previously discussed transversal SSE measurement geometry that does not allow for an easy interpretation (Fig. 3.6), one has to bear in mind that the localized temperature gradients are much larger and that the injector-detector distance is of the order of the magnon propagation length. Moreover, one needs to be careful when comparing the non-local signal with local (longitudinal) SSE measurements, considering the different magnon spectra probed [o3]. While in the local geometry all excited magnon modes (low-energy to $k_{\mathrm{B}}T$) contribute, only the low-energy, long-range magnons induced at the injector site will be captured by the displaced detector. Contrary to the electrically induced signal, the polarization of the thermal spin current is independent of the injector current sign but is given by the FMI magnetization direction. Due to its thermal origin, the non-local SSE voltage is proportional to the square of the current amplitude:

$$V_{\mathrm{sse}}^{\mathrm{nl}} = R_{\mathrm{sse}}^{\mathrm{nl}} \cos(\alpha) \cdot J_{\mathrm{c}}^2. \tag{3.19}$$

In the light of the different magnetization orientation and current dependences of the electrical and thermal signal, one can distinguish them by means of angular and current polarity-dependent measurements (see Sec. 4.3.2).

The propagation of electrically induced magnons has been studied extensively in FMIs as a function of injector-detector distance [22, 177], temperature [172], and applied magnetic field strength [178], yielding a comprehensive understanding of the fundamental effects. In this work, the non-local geometry was implemented to probe the non-local SSE as a function of temperature and wire distance (Sec. 5.1, published in [o5]). Moreover, the spin-dependent inverse spin Hall effect in $Co_{60}Fe_{20}B_{20}$ (Sec. 6.2) as well as the influence of heat and Oersted fields on the magnon propagation are studied (Sec. 6.3).

4 Experimental methods and materials

In this chapter, the experimental methodology applied in the presented work for the investigation of diverse spintronic effects is introduced. To begin with, the structural as well as magnetic properties of the insulating ferrimagnet yttrium iron garnet are briefly discussed, considering the fact that all results shown in this thesis were obtained by using this material. Subsequently, sample fabrication and characterization methods are described. Metallic thin films, which are required for the effective spin- to charge conversion via the spin Hall effect, are deposited by means of the magnetron sputtering technique and, if required, nano-patterned via electron beam lithography. The quality of deposited materials is checked by X-rays, while magnetic properties are probed by SQUID magnetometry. Amongst others, metallic thin film deposition via magnetron sputtering and electron beam lithography are described. Finally, the different setups used to perform spin transport measurements are described, which, generally speaking, allow one to probe the generation and detection of magnonic spin currents as a function of temperature, field and magnetization orientation.

4.1 Yttrium Iron Garnet

The insulating ferrimagnet $Y_3Fe_5O_{12}$ (YIG) is at the heart of the work presented in this thesis and therefore its essential properties are introduced briefly in the following. Being a garnet ferrite, YIG exhibits a complex lattice structure with a cubic unit cell (lattice parameter 12.376 Å) containing 8 formula units (160 atoms) [179]. Within the unit cell, four sub-lattices $\{c_3\}\,[a_2]\,(d_3)\,O_{12}$ can be identified with the cation occupation c=Y^{3+}, a=Fe^{3+}, and d=Fe^{3+} [25]. As depicted in Fig. 4.1, the 24 d-site iron ions are tetrahedrally coordinated by oxygen atoms, whereas the 16 a-site iron ions are surrounded by oxygen ions in an octahedral configuration.

While yttrium does not exhibit a magnetic moment, antiferromagnetic coupling of the two iron sub-lattices via superexchange provides the ferrimagnetic nature of YIG. As a result, a magnetic moment of 5 μ_B per formula unit appears ($M_s \simeq 135.51\,\mathrm{kA\,m^{-1}}$ at 300 K) with a Curie temperature $T_C \simeq 560\,\mathrm{K}$ [179]. When exchanging yttrium by other heavy rare earth atoms that posses a magnetic moment, the magnetic structure becomes more complex and characteristic phenomena, as for instance magnetic compensation ($M = 0$)

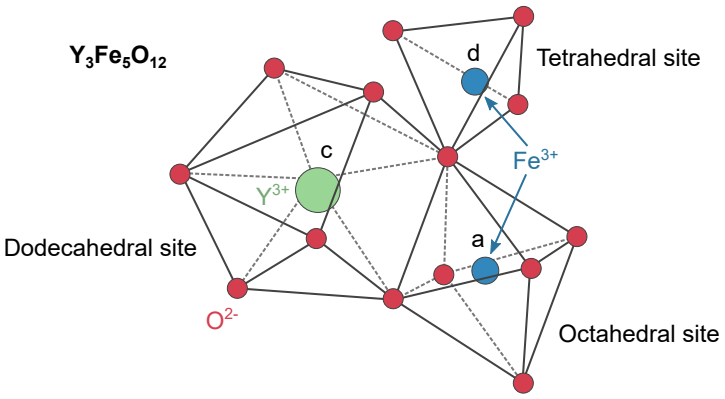

Figure 4.1: Crystal structure of yttrium iron garnet.

at specific temperatures [o4, 180], appear. With regard to its electrical properties, YIG reveals an electron band gap of $\Delta E \approx 2.68\,\mathrm{eV}$ [181].
The enhanced interest in YIG regarding magnon-based applications is grounded on its uniquely low Gilbert damping parameter [16] with reported values down to $\alpha = 8.58 \cdot 10^{-5}$ for ultra-thin films [182]. Low damping signifies reduced losses and therefore enables long distance spin transport as the magnon propagation length follows $\xi = \lambda / (\pi\alpha)$ in the low anisotropy limit [157].
Garnet ferrites do not appear in nature but need to be synthesized. Moreover, with regard to spintronic applications, thin films are preferred as compared to bulk crystals. So far, the growth of (ultra-)thin YIG films of high or even bulk-like quality has been accomplished by three different techniques: pulsed laser deposition [183], sputtering [184] or liquid phase epitaxy (LPE) [185]. In the case of LPE, the substrate (commonly $Gd_3Ga_5O_{12}$ (GGG) with a (111) surface orientation) is immersed into a molten solution of various oxides (mainly PbO, B_2O_3, Y_2O_3 and FeO) and furthermore rotated to obtain a homogeneous film thickness [186]. All YIG films used in this thesis have been grown by the LPE method and were obtained either commercially or from collaboration partners (Saitoh Lab, Tohoku University Sendai, Japan).

4.2 Sample fabrication and characterization

4.2.1 Magnetron sputtering

The normal metal thin films used in this work for spin current injection/detection were deposited by *sputtering*, which constitutes a subgroup of physical vapor deposition [187, 188]. Figure 4.2 shows the schematic view of a sputter unit. To start the sputtering process, the vacuum chamber is initially partly filled with a process gas until a predefined pressure

is reached. For the deposition of metallic films noble gases such as argon are used. An electric field between target (cathode) and substrate holder/dark shield (anode) is then applied to ignite a plasma discharge of the sputtering gas. The thus ionized gas atoms are accelerated towards the cathode and knock out both target atoms and secondary electrons. While the sputtered atoms spread out via ballistic motion and deposit on the substrate and chamber walls, the secondary electrons are attracted by the anode potential, gaining kinetic energy. This energy is transferred to further Ar atoms due to random collisions, which as a result become ionized and the discharge is sustained.

The total number of knocked out target atoms and thus the deposition rate of DC sputtering is limited by the absorption of secondary electrons, which ionize the process gas atoms, by the anode. This effect implies the need for higher gas pressures to sustain the plasma discharge, which furthermore reduces the mean free path of the sputtered atoms. To increase the efficiency of the process, one can make use of *magnetron sputtering*, in which permanent magnets underneath the target cathode establish a static magnetic field. In this way, the secondary electrons are trapped in a closed loop drift path just above the target. The enhanced collision rates with process gas atoms allow one to use lower gas pressures and therefore increase the deposition rate.

Contrary to DC sputtering, an AC electric field (common frequency $f = 13.56\,\mathrm{MHz}$) is applied to the cathode when implementing *RF sputtering*. The AC field induces additional oscillating motion of electrons within the plasma, which results in enhanced ionization rates of sputter gas atoms and therefore a higher plasma density. Moreover, RF sputtering allows one to sputter electrically insulating targets, which otherwise charge up in a static electric field.

The sputter chamber in Mainz (base pressure $3 \times 10^{-9}\,\mathrm{mbar}$) used mainly in this work

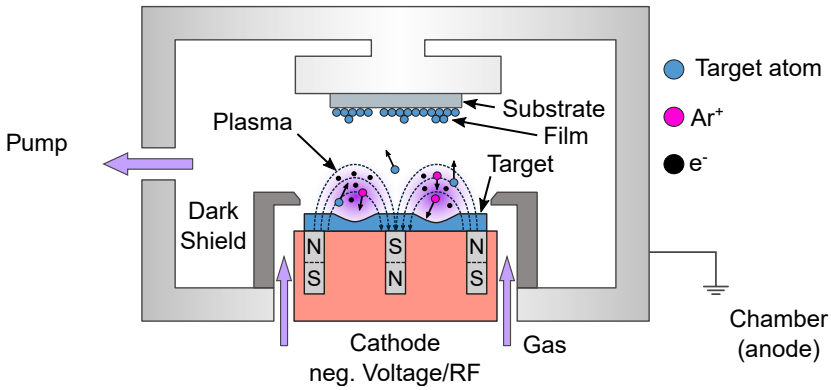

Figure 4.2: Schematic of a magnetron sputtering chamber. In the used setup, DC or RF voltages can be applied to the target cathode.

can be operated using both DC and RF sputtering. For Pt, DC sputtering is used with optimized process parameters including an argon pressure of 1×10^{-2} mbar, 10 cm target-substrate distance and an applied voltage of $\simeq 350$ V (15 mA), resulting in a growth rate of $\simeq 0.787\,\text{Å}\,\text{s}^{-1}$. In the case of W thin films, RF sputtering is implemented. An RF power of 20 W together with an Ar pressure of 2×10^{-2} mbar (same target-substrate distance) yield a sputtering rate of $\simeq 0.57\,\text{Å}\,\text{s}^{-1}$.

4.2.2 X-ray analysis

The structural characteristics of bulk materials and thin films can be determined with the aid of X-ray analysis methods. While *X-ray diffraction* (XRD) patterns allow one to investigate, among other things, lattice constants or the overall crystallographic quality of a sample, *X-ray reflectometry* (XRR) yields access to thin film properties such as thickness, interface- and surface roughness as well as material density [189]. In this work, mainly XRR measurements were performed in a Bruker D8 Discover device to examine the quality of deposited metal thin films.

X-ray diffraction

The functional principle of XRD is based on X-ray scattering off atoms confined within lattice planes periodically aligned in the crystal. Experimentally, the intensity of an X-ray beam reflected from a sample is measured as a function of the angle of incidence. For specific angles, at which Bragg's law for constructive interference

$$m\lambda = 2d_{\text{hkl}} \sin\theta \tag{4.1}$$

is fulfilled, intensity peaks may appear, generating a diffraction pattern. In Eq. 4.1, m is an integer number, d_{hkl} is the distance between lattice planes with the Miller indices (hkl), and θ is the angle of incidence between X-ray beam and lattice plane. For known crystal structures and lattice constants, the diffraction pattern therefore allows one to identify the crystal orientation. Note that Bragg's law reveals limitations as it cannot explain varying scattering intensities, for example. This information is, however, provided by the *structure factor*, which basically considers the electron distribution within the unit cell [189].

X-ray reflectometry

In XRR, the sample is irradiated by an X-ray beam that hits the sample surface under a grazing incidence angle θ [190]. Below a critical angle θ_{c}, which is proportional to the square root of the material density $\theta_{\text{c}} \propto \sqrt{\rho}$, the beam experiences total reflection. Above θ_{c}, however, the X-rays partially enter the thin layer and can be reflected multiple times

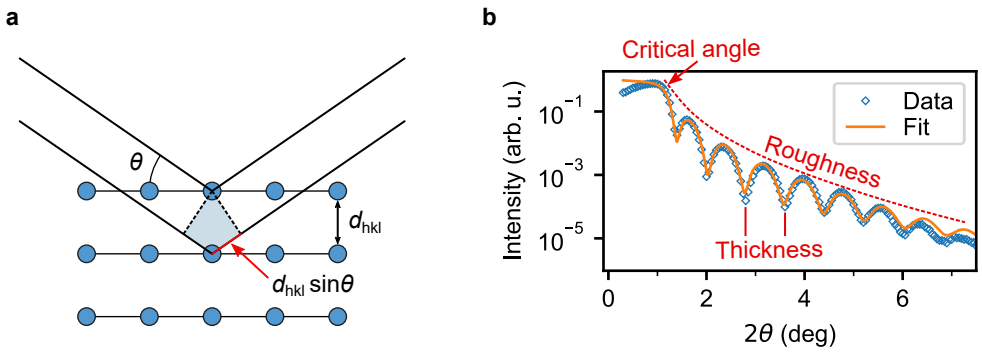

Figure 4.3: (a) Figurative depiction of X-ray reflection off a crystal lattice to deduce the Bragg condition. (b) Typical XRR scan obtained for a W film grown on a Si substrate including the respective fit function obtained by GenX. The fit reveals a W thickness of $t_{\mathrm{W}} = 10.4\,\mathrm{nm}$ with a W (Si) roughness of $\sigma_{\mathrm{rms}}^{\mathrm{W}} = 0.2\,\mathrm{nm}$ ($\sigma_{\mathrm{rms}}^{\mathrm{Si}} = 0.4\,\mathrm{nm}$).

before re-exiting. The intensity reveals an oscillating behavior when plotted as a function of θ, so-called Kiessig fringes, which are correlated to the film thickness: intensity maximums appear for constructive interference of the reflected and refracted beams, whereas the signal becomes minimum for destructive interference. Determining the oscillation frequency hence allows one to deduce the film thickness. Eventually, the height of the Kiessig fringes as well as the overall decay of the signal contain information about the roughness of the film surface and the film/substrate interface.
To obtain the aforementioned parameters, XRR data were fitted using the noncommercial software GenX, which employs the Parratt recursive method [189].

4.2.3 Electron beam lithography

Defined structures on the micro- or nanometer scale, e.g. the non-local geometry introduced in Sec. 3.5, require patterning of metal films prior or subsequent to their deposition. Conventionally, this is done by *lithography*, which denotes the transfer of a structure pattern onto a thin layer of a radiation-sensitive material called *photoresist* [191]. The minimum feature size of the designed pattern is limited by the wavelength of radiation-type employed in the process. For structures in the micrometer range, *optical lithography* with ultraviolet light is conventionally implemented in university research areas[1]. The non-local measurement geometry used in this thesis, however, requires nano-sized wires and therefore is fabricated by means of *electron beam lithography* (EBL) [191].
To begin with, the substrate is covered with a thin, homogeneously distributed layer of a

[1]Note that in current industrial semiconductor manufacturing plants structure sizes down to 14 nm are achieved [192])

polymer photoresist via spincoating, followed by a baking step to promote the evaporation of solvent residues. In EBL, the desired pattern is then transferred onto the resist by a focused electron beam scanning across the sample surface. Depending on the chemical composition of the resist polymers, the interaction with the incoming electrons commutes their reaction when brought into contact with a chemical solvent (*developer*) [193]. In the case of a *positive* tone resist, the exposed areas become soluble and therefore are removed by the developer. *Negative* resists, on the other hand, further polymerize within the exposed areas, rendering them insoluble. With regard to sample structuring, subsequent lift-off (this work) or etching processes are implemented, as depicted in Fig. 4.4.

To obtain the desired result, several parameters need to be adjusted in the EBL process. Higher acceleration voltages of the electron beam generally enable smaller feature sizes. Nonetheless, the enhanced energy and penetration depth result in secondary electron emission by the substrate that may expose the resist non-locally. Furthermore, proximity effects (unintentional exposure of areas in between close by features) may appear for maladjusted exposure doses besides under- or overexposure.

In this work, the non-local geometry discussed in Sec. 3.5 was fabricated by implementing a lift-off process. The employed photoresist polymethyl methacrylate (PMMA, acrylic glass) 950K is a positive tone resist, which when exposed to the electron beam becomes soluble in a methyl isobutyl ketone:isopropyl alcohol (MIBK:IPA with 1:3 ratio) developer. For the electron beam an acceleration voltage 10 kV was chosen together with a 15 µm aperture and an exposure dose of 115 $\mu C\,cm^{-2}$. More detailed information on the process can be found in App. B.

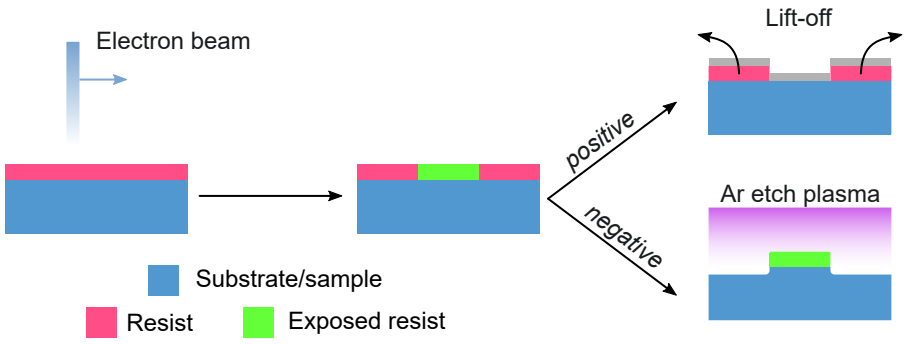

Figure 4.4: Sketch of a typical EBL process. After spin-coating the sample with the photoresist, the desired structured is patterned by a scanning electron beam. In the case of a positive (negative) resist, the exposed area becomes soluble (insoluble) in the respective developer. Subsequently, a lift-off or etching process can be implemented.

4.2.4 SQUID magnetometry

Among other methods, superconducting quantum interference device (SQUID) magnetometry has been established as a useful tool to investigate the static magnetic properties of thin films [194]. In principle, SQUIDs are superconducting loops interrupted by one (RF-SQUID) or two (DC-SQUID) Josephson junctions [194], which can only contain magnetic fluxes that are integer multiples of $\Phi_0 = h/2e$. Furthermore, the critical current above which superconductivity breaks down depends on the magnetic flux flowing through the SQUID.

Briefly summarizing the working principle of a SQUID magnetometer, the magnetized sample is moved through a pickup coil (conventionally a second order gradiometer [195]) that is placed in the center of a superconducting magnet. The magnetic moment of the sample induces an induction current, which is forwarded by superconducting wires and re-converted to a magnetic flux by a SQUID input coil. An inductively coupled feedback loop (e.g. see Ref. [195]) balances the total magnetic flux through the SQUID by means of a compensation coil to maintain the initial state. If adjusted correctly, the output voltage generated by the feedback loop is directly proportional to the magnetic moment of the sample. Considering the vast variety of concepts and implementations, please see Ref. [194] for more details.

Figure 4.5 shows an example of a magnetic hysteresis curve obtained for GGG(111)/YIG (630 nm). Depending on the substrate underneath the magnetic layer of interest, a background signal with positive (e.g. GGG) or negative (e.g. MgO) slope may appear in the raw data due to the substrate's paramagnetic or diamagnetic nature, respectively. This background signal can be eliminated by subtracting a linear function fitted to field regions

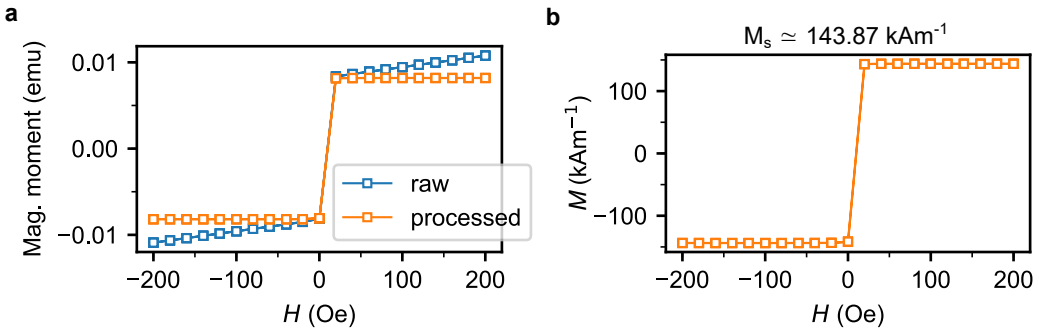

Figure 4.5: (a) Magnetic hysteresis loop of GGG(111)/YIG (630 nm) (double sided) obtained by SQUID magnetometry. Processed data are rectified by the paramagnetic background of the GGG substrate. (b) Data from (a) divided by the sample volume and multiplied by the correction factor 1.14 to obtain the sample magnetization M.

above full saturation of the ferromagnetic layer. As the output value provided by the SQUID corresponds to the total magnetic moment of the sample, it has to be divided by the sample volume to obtain the magnetization. Here, further data correction is required as the used SQUID magnetometer (Quantum Design MPMS XL) is calibrated to the stray field of a cylinder with 2.5 mm for both height and diameter [196]. Depending on the sample geometry, a correction factor thus has to be applied.

4.3 Measurement procedures

4.3.1 Local spin Seebeck effect

In this section, a brief introduction to the experimental procedures used to perform local spin Seebeck measurements in FMI/NM bilayers shall be given. The term *local* is used in the sense that the temperature gradient, which excites the SSE, is perpendicular to the FMI/NM interface and generated by heating either the FMI or the NM (longitudinal configuration). Moreover, the term shall emphasize the distinction from the non-local excitation scheme introduced by Cornelissen *et al.* [22].
The setups and measurement schemes presented hereinafter have mainly been implemented in the course of doctoral studies preceding the presented work. Therefore, the interested reader may refer to Ref. [197] for a more comprehensive description of experimental details.

Room temperature measurement setup

Local SSE measurements require the generation of a robust, homogeneous temperature gradient to induce a steady heat flow through the sample stack. While this can be achieved, for instance, by a current heating method [198] that exploits Joule heating effects, room temperature measurements presented in this work rely on an external heat generation scheme.
As depicted in Fig. 4.6, the sample is clamped in between two copper blocks that can be cooled or heated individually. The chilling effect is accomplished by cooling water flowing through the baseplate on which the setup is fixed, whereas inbuilt cartridge heaters allow one to heat up the copper blocks. A feedback loop is provided by Pt100 thermal sensors that are attached to each block and connected to Lakeshore 330 temperature controllers. Based on a PID (proportional-integral-derivative) control circuit, the controllers adjust the power applied to the cartridge heaters such that the intended set temperatures is reached and kept [197]. This way, stable temperature differences of up to 15 K between top and bottom copper block can be achieved, with the lower temperature's minimum being predefined by the cooling water temperature.

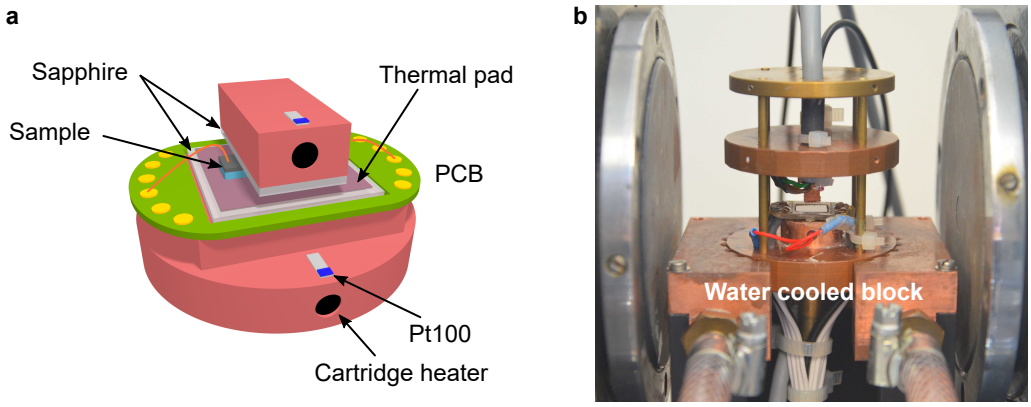

Figure 4.6: (a) Sketch and (b) photograph of the measurement setup used to perform longitudinal SSE measurements at room temperature.

The actual temperature difference across the magnetic sample, however, is most likely smaller as the set $\Delta T = T_{\mathrm{top}} - T_{\mathrm{bottom}}$. For one thing, Al_2O_3 (sapphire) substrates of 500 µm thickness are stuck on the copper blocks below and above the sample to prevent short circuiting of the NM and due to smooth surfaces. In addition, thermally conductive pads are inserted between the sapphire substrates and the sample to enhance the uniformity of the temperature gradient. The different thermal conductivities of the various materials involved alter the temperature drop across the magnetic layer, implying uncertainties in ΔT. An alternative approach by Sola *et al.* [199] therefore considers measuring the heat flux instead of the temperature difference, demonstrating reliable results. Nevertheless, careful consideration of ΔT allows one to perform qualitative measurements for relative comparison as, for instance, presented in Sec. 5.3.

The external magnetic field required for the alignment of the FMI magnetization is provided by an electromagnet, in which the SSE setup is installed. Electrical contacting of the NM layer, on the other hand, is supplied by a printed circuit board (PCB) attached to one of the copper blocks. Thin copper leads are soldered to the board and connected to the NM layer via conductive silver paste such that the thermally generated ISHE voltage can be picked up by a Keithley 2182a nanovoltmeter. All controller devices are connected to a measurement computer, which by means of the graphical programming tool Keysight Vee allows one to perform automated measurements as a function of field and ΔT.

The SSE signal (ISHE voltage) V_{sse} is typically determined with the aid of magnetic field sweeps. As the spin current polarization observed depends on the FMI magnetization direction, a voltage hysteresis loop is detected following the magnetic configuration of the FMI [200]. V_{sse} is eventually defined as half the difference between the voltage levels obtained for positive and negative magnetization saturation. Potential hysteresis offsets can

be explained by the ordinary Seebeck effect, an offset in the electrical ground connection of the setup or the nanovoltmeter calibration. When repeating the field sweep measurements for different temperature gradients, a linear dependence between V_{sse} and ΔT is observed. This is in line with the linear response of the SSE to ∇T given in Eq. 3.16. The slope of a respective linear function eventually yields the so-called SSE coefficient.

Low temperature measurement setup

For temperature-dependent measurements, which are performed in an Oxford Instruments cryostat including a superconducting magnet and a variable temperature insert (VTI), a different scheme for the temperature gradient generation is implemented considering the confined space and potential heat input. The radiated heat by a relatively hot, massive copper block, for instance, may overcome the cooling power of the system and therefore impede low temperature measurements.
Roughly speaking, the used setup is composed of a substrate stack with the magnetic sample being clamped in between a resistive heater and temperature sensor, see Fig. 4.7. The resistive heater is given by a 10 mm × 5 mm Al_2O_3 substrate, on which a Pt film of 15 nm

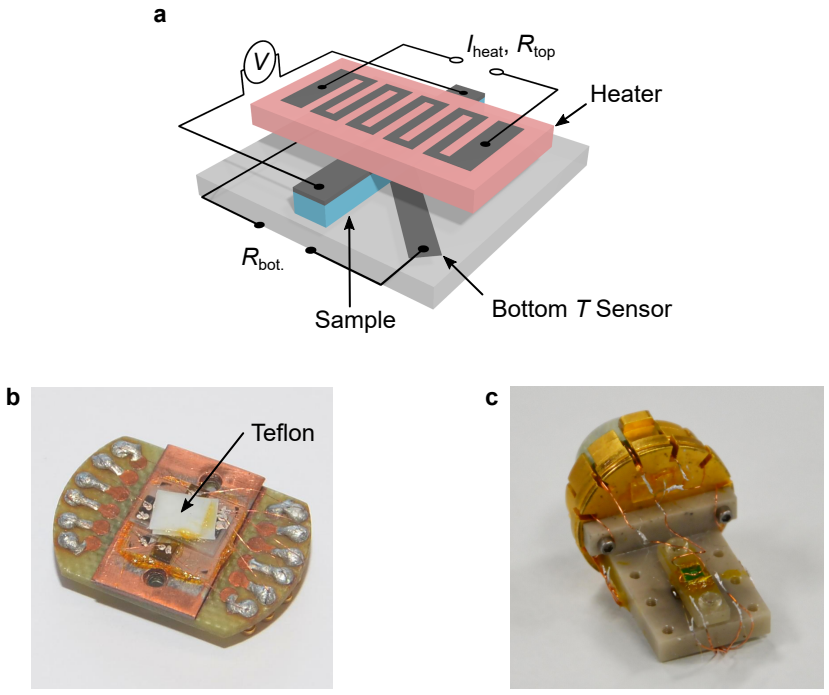

Figure 4.7: (a) Sketch and (b) photograph of the measurement setup used to perform longitudinal SSE measurements in a cryostat at various temperatures and large magnetic fields. (c) Photograph of the corresponding setup used at Tohoku University, Sendai, Japan.

thickness is deposited and structured into a meander pattern. Electric currents injected into the Pt induce Ohmic losses (Joule heating), therefore establishing a heat source. The meander pattern is chosen to obtain enhanced heating powers for equal current densities due to the increased wire resistance as well as to provide a homogeneous heat distribution. The heating area is furthermore capped by a Teflon plate to diminish heat exchange with the VTI sample space. Underneath the sample, a 10 mm × 10 mm Al_2O_3 substrate with a patterned, diagonal Pt wire is attached. The distinct temperature dependence of its electrical resistivity renders the Pt wire an effective thermometer, which is also true for the resistive heater structure. By applying an insulating GE low temperature varnish, the complete stack is glued together and furthermore attached to a copper plate on top of a PCB. The latter is required for electrical connections, whereas the copper plate acts as a heat sink when in contact with the VTI exchange gas (He^4).

Two equivalent measurement protocols are available for the investigation of the temperature dependence of the spin Seebeck effect. Implementing the first method, the VTI is stabilized at the desired temperature and, in the same manner as with the room temperature setup, V_{see} is determined via field sweep measurements. In the second approach, the magnetic field is fixed at a predefined value that guarantees full saturation of the sample, while the temperature is swept continuously. Repeating this method for positive and negative fields allows one to extract $V_{\mathrm{see}}(T)$ by the subtraction of the obtained voltage curves. While the first method provides direct information of the magnetic response at each point in temperature, obtaining a close-meshed temperature dependence is rather time-consuming. With respect to the latter, the second method is relatively faster, however, one has to take more care that during the independent temperature sweeps equal conditions, e.g. the He exchange gas pressure, are maintained.

In each measurement scheme, the resistances of both the heater and thermometer sample are logged simultaneously by the aid of Keithley 2400 sourcemeters. Performing a respective R vs. T calibration measurement then allows one to gain information about the temperature gradient applied to the sample.

During an exchange research stay of the author at the Tohoku University (Sendai, Japan), temperature-dependent SSE and ANE measurements were performed using a physical property measurement (PPMS) Dynacool system of Quantum Design, Inc. (cryogen-free refrigerator including superconducting magnet). This environment allows for temperature-dependent measurements from 10 K to 400 K, while uniaxial magnetic fields in the range of −9 T to 9 T can be applied. The measurement principle is the same as described above, but instead of Al_2O_3 substrates, aluminum nitride (AlN) components (see Fig. 4.7c) are employed due to a large thermal conductivity of 180 $\mathrm{W\,m^{-1}\,K^{-1}}$. Good thermal contact between the sample and AlN is established by the application of the thermal grease *Apiezon*

N on the top and on the bottom of the sample before clamping it in the holder. However, one needs to be aware of the fact that the specific heat of Apiezon N exhibits a distinct maximum near $T = 250\,\mathrm{K}$ [201], which can distort the measurement result. In this setup, the temperature difference is determined by a thermocouple device and predefined calibration curves.

4.3.2 Non-local spin Seebeck effect and spin injection

In view of the similarities between the underlying processes, measurement principles of the local SSE can be transferred to a great extend to the non-local geometry. For the non-local SSE, the need for an external heat source and thus the previously described substrate stack is eliminated as it is driven by Joule heat emitted by the injector. One has to bear in mind, however, that the ISHE potential drop at the detector simultaneously includes the pure electrical transport signal. Consequently, measurement protocols need to be implemented that allow for a clear distinction between the thermal and electrical contributions.
As described by Cornelissen *et al.* [22], one option to separate the signals is by implementing an alternating current (AC) measurement scheme: an oscillating current of fixed frequency is applied to the injector, whereas the voltage drop at the detector is picked up by a synchronized lock-in amplifier. According to the functional dependence of the electrical and thermal signal on the input current (Eq. 3.18 and Eq. 3.19), the respective signals appear as first and second harmonic responses. In the presented work, though, a direct current (DC) scheme is implemented. The injector stripe is biased with a constant current of fixed amplitude but switching polarity using a Keithley 2400 sourcemeter, which simultaneously captures the injector resistance (2-wire or preferably 4-wire mode). The ISHE voltage drop across the detector strip in turn is recorded by the aid of a Keithley 2182a nanovoltmeter. Revealing a proportionality to the injector current squared, the thermal signal is independent of the injector current polarity. The electrically induced signal, then again, acts in linear response to the injector current. The current direction specifies whether a magnon accumulation or depletion is induced, therefore determining the spin current direction. Hence, the electric spin transport signal can be filtered out as the difference of the ISHE voltage signals obtained for a positive and negative injector current, which furthermore eliminates the thermal contribution. At the same time, the non-local SSE signal is provided by the average of the recorded voltages, given that the electrical injection and absorption of magnons are of equal efficiency.
In addition to the injector current dependence, the validity of electrical and thermal spin signals is verified by means of angular-dependent measurements. For in-plane rotations, the former exhibits a $\cos^2(\alpha)$ dependence with regard to the angle α between magnetization direction and stripe orientation (Eq. 3.18). Thermal signals, on the other hand, modulate

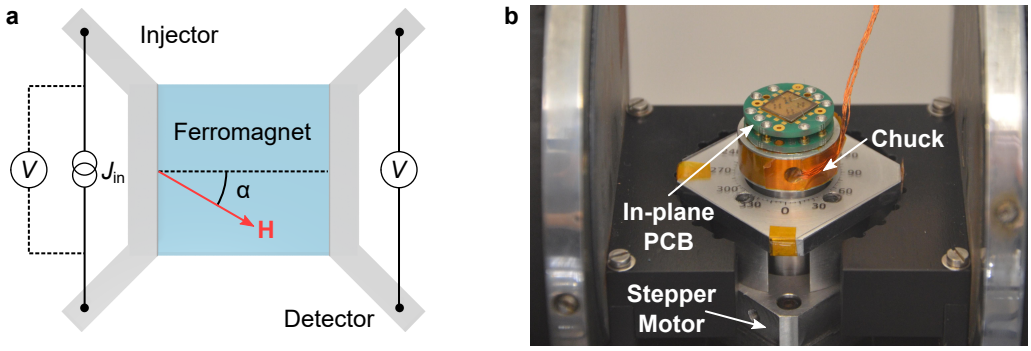

Figure 4.8: (a) Typical connection of the non-local measurement geometry to external circuitry. (b) Photograph of the rotational setup implemented to perform spin transport measurements at room temperature.

following a $\cos(\alpha)$ dependence (Eq. 3.19) as the spin signal polarity is solely defined by the magnetization direction. Consequently, non-local SSE experiments can be performed applying the previously described field sweep sequences, which has been exploited for the results presented in Sec. 5.1.

As part of the presented work, a rotational setup was constructed to enable straightforward non-local transport measurements at room temperature. The setup, see Fig. 4.8, is based on a stepper motor with 0.45° angular resolution, on top of which an aluminum chuck is mounted. A PCB provides the required electrical connections, which in the sense of a plug-in system allows one to perform in-plane and out-of-plane rotations when using different PCB equipment. The mounted system is located in the same electromagnet used for room temperature local SSE measurements. In this case, the maximum field value is limited to $\simeq 85\,\mathrm{mT}$ since the stepper motor, which is driven by electromagnetic coils, loses functionality at larger fields and might be even lifted out of its pedestal. Nonetheless, the available field values are sufficient for most applications.

4.3.3 Ferromagnetic resonance spin pumping

The presented experiments on ferromagnetic resonance spin pumping in spin valve-like structures (Sec. 6.1) were performed using a setup implemented at Tohoku University in Sendai, Japan. Principally, the setup is based on a coplanar waveguide (CPW) installed in the previously described PPMS DynaCool system by Quantum Design.

The copper-based CPW, as shown in Fig. 4.9, is short-circuit terminated and connected by a single coaxial input cable. Within the cryostat, the sample holder is arranged in such a manner that applied magnetic fields are parallel to the CPW center conductor and therefore perpendicular to RF-fields induced by injected microwaves ($H_{\mathrm{ext}} \perp h_{\mathrm{rf}}$). The

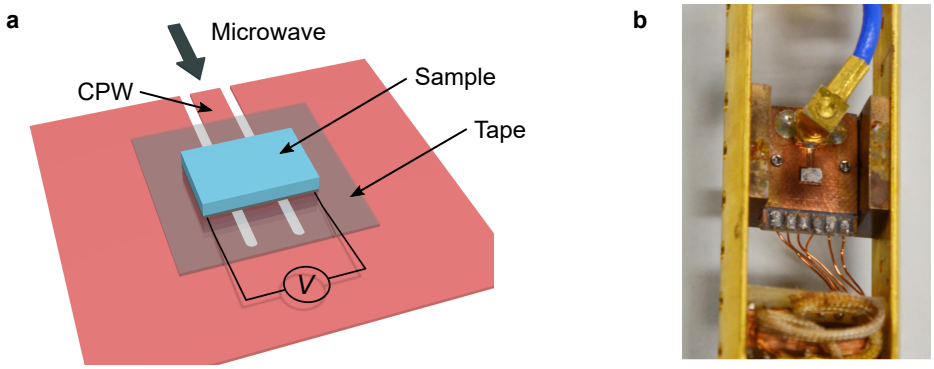

Figure 4.9: (a) Sketch and (b) photograph of the measurement setup used to perform ferromagnetic resonance spin pumping measurements at Tohoku University, Sendai, Japan.

samples, in which spin pumping is probed, are fixed face down on top of the CPW by means of a double-sided tape of 10 µm thickness to provide maximum RF-field amplitudes. At the same time, the tape ensures electrical insulation between the CPW and the spin-Hall active metallic layer required for spin current detection. For the latter, the sample holder provides electrical connections via soldering spots. Thin gold wires are attached mechanically to both the sample and the soldering spots by pressing them into previously fixed indium junctions.

Considering external circuitry, microwaves are provided by a Keysight (Agilent) RF signal generator with a maximum microwave power output of +23 dBm. Induced microwave signals pass through a coaxial cable into the CPW and become, due to the short-circuit termination, reflected. To avoid backscattering into the RF generator, a circulator is placed in-line, which forwards the reflected microwave to a Keysight Power Sensor. At ferromagnetic resonance, partial microwave absorption by the sample appears as a dip in the recorded power spectrum. With regard to the ISHE voltage detection, both AC and DC acquisition schemes are available. In the case of AC measurements, the RF generator emits pulsed microwaves and simultaneously triggers an NF LI5460 lock-in amplifier that captures the ISHE voltage. For DC measurements, a continuous microwave signal is applied to the sample and the resultant voltage is picked up by a Keithley 2182a nanovoltmeter. While the major advantage of the AC measurement principle is a significantly enhanced signal-to-noise ratio, one has to be mindful of potential phase shifts of the signal. The implemented measurement software, which enables automated control and readout of the devices, basically allows one to measure FMR spin pumping by means of field or microwave frequency sweeps.

5 Spin propagation through magnetically ordered insulators and metals

Among other fundamental tasks of magnon spintronics, the investigation of magnon propagation properties as well as efficient magnon detection schemes have been the focus of research efforts in recent years. In the following chapter, relevant experimental results obtained during the doctoral studies of the author are presented, starting with a discussion of the non-local generation and detection of thermally induced magnons in YIG. Surprisingly, the spin signal generated by such magnonic spin currents inverts sign as a function of the spatial separation between the magnon generation and detection site, which in the given system cannot be understood by assuming direct magnon transport from the injector to the detector. To uncover the origin of this effect, both temperature- and field-dependent measurements of the non-local SSE are presented and discussed.
As already mentioned in the introduction to this thesis, spin transport as well as spin-dependent effects in antiferromagnets have gained increased interest in recent years considering potential advantages of AFMs over FMs, for example the absence of stray fields. In the second section of this chapter, spin transport across the metallic antiferromagnet $Ir_{20}Mn_{80}$ is investigated, for which spin currents are generated either thermally in an underlying YIG layer or by means of the spin Hall effect in a top Pt layer. Besides the general phenomenon of spin transport across $Ir_{20}Mn_{80}$, which can be mediated by either electronic or magnonic spin currents, it is discussed which of these spin transport channels is dominating.
Finally, magnonic spin currents are employed to investigate the spin Hall effect in the binary alloy $Cu_{1-x}Ir_x$ for $0.05 \leq x \leq 0.7$. It has been shown that the use of alloys of varying compositions allows to adjust the spin-charge interconversion efficiency of SHE and ISHE, depending on the requirements. Furthermore, the results obtained for both steady and ultrafast (femtosecond) spin currents are directly compared, indicating the unbounded effectiveness of SHE and ISHE at THz speeds.

5.1 Non-local detection of thermal spin currents

The successful demonstration of the non-local magnon injection and detection scheme by Cornelissen *et al.* [22] unveiled a potential route towards low-dissipation, insulator-based

spintronic systems. For one thing, the injection of spin currents generally allows one to transport information over distances in the micrometer range, mediated by the efficient propagation of magnons. In addition, it was shown that superimposing magnonic spin currents inherently provides the possibility to implement logic operations, e.g. a majority gate [202].
As discussed in Sec. 3.5, magnon currents can be injected both electrically, exploiting the SHE, and thermally by means of the SSE. With regard to the latter, thermally induced spin current signals reveal peculiarities that indicate a more complex transport mechanism than direct magnon propagation from the injector to the detector. Mentioned first as a secondary finding in the supplemental information of Ref. [22], the sign of the non-local spin Seebeck signal changes as a function of the injector-detector distance. For small separations, local and non-local SSE exhibit the same sign (*positive*), while at larger distances the non-local voltage inverts (*negative*). Equal signs of local and non-local SSE imply equal spin current directions across the respective FMI/NM interfaces, while direct magnonic spin transport from injector to detector should yield a spin current flow in the opposite direction across the detector interface.
Altogether, the SSE signal detected in the non-local geometry reveals a complex behavior which cannot be fully explained assuming direct propagation of thermally excited magnons from the injector to the detector. To clarify the physics behind the non-local thermal signal, it has been studied as a function of strip separation and temperature. The corresponding results, which were obtained together with the experimental research group of Prof. Dr. S. T. B. Goennenwein at the Walther-Meißner-Institut (WMI) Garching (now at TU Dresden), have been summarized and published as a research article [o5]. More recent data, including interface- and field-dependence, in combination with most recent findings by other groups extend the conclusions drawn in this article.

5.1.1 Experimental details

The non-local spin Seebeck effect was investigated in two distinct series A and B comprising of bilayers of the insulating ferrimagnet YIG and the normal metals Pt and W. Series A, whose results are included in Ref. [o5], was fabricated using a commercial, single crystalline LPE-YIG film of 3.3 µm thickness grown onto a GGG (111) substrate. On top of the FMI, non-local devices with a wire width of $w = (1.00 \pm 0.25)\,\mu\text{m}$ and injector-detector distances of $(1.10 \pm 0.05)\,\mu\text{m} \leq d \leq (2.10 \pm 0.05)\,\mu\text{m}$ were patterned using electron beam lithography. Note that all distance values given in this section generally refer to center-to-center distances. In a lift-off process, the device structures were imprinted into the photoresist and, subsequently, a Pt film of 7.5 nm thickness was deposited with the aid of DC magnetron sputtering. Figure 5.1(a) shows a scanning electron microscope (SEM)

image of the patterned photoresist PMMA 950K before the deposition of the metal layer. For series B, YIG films of 1.5 µm thickness were employed, provided by the same company. Contrary to series A, non-local geometries including three instead of two nanowires were implemented, as shown in Fig. 5.1(b). This enhanced design allows for the simultaneous detection of the non-local signal at two separate detectors, which can be positioned at different distances from the injector wire in the middle. Using the EBL parameters given in Sec. 4.2.3, wire widths and separations of $w \simeq (450 \pm 25)\,\mathrm{nm}$ and $(540 \pm 50)\,\mathrm{nm} \leq d \leq (9.39 \pm 0.05)\,\mu\mathrm{m}$ (center-to-center) were produced. Besides the variation in the YIG thickness, both Pt ($d = 7.5\,\mathrm{nm}$) and W ($d = 10\,\mathrm{nm}$) wires were employed in series B to investigate potential interface effects. In addition, in this series a short Ar ion etch process of 10 s was implemented prior to the metal deposition with the purpose of cleaning the YIG surface of residuals (indicated by YIG*).

To study the temperature-dependence of the non-local SSE, the fabricated samples of series A and B were mounted on PCBs and placed in the variable temperature insert (VTI) of a superconducting magnet cryostat from Oxford Instruments. The VTI principally allows one to vary the temperature in the range of $2\,\mathrm{K} \leq T \leq 300\,\mathrm{K}$, while the magnet supplies a uniaxial magnetic field with a maximal amplitude of $\pm 12\,\mathrm{T}$. With regard to the fact that YIG saturates at field values of the order of a few mT, magnetic fields of $\pm 200\,\mathrm{mT}$ applied in regular temperature-sweep measurements were sufficient to guarantee full alignment of the YIG magnetization.

Following the measurement scheme described in Sec. 4.3.2, the injector was connected to an external, switchable current source (Keithley 2400 source meter) to supply the charge current J_{in} required for the electrical and thermal excitation of a spin current J_{s}. Typical

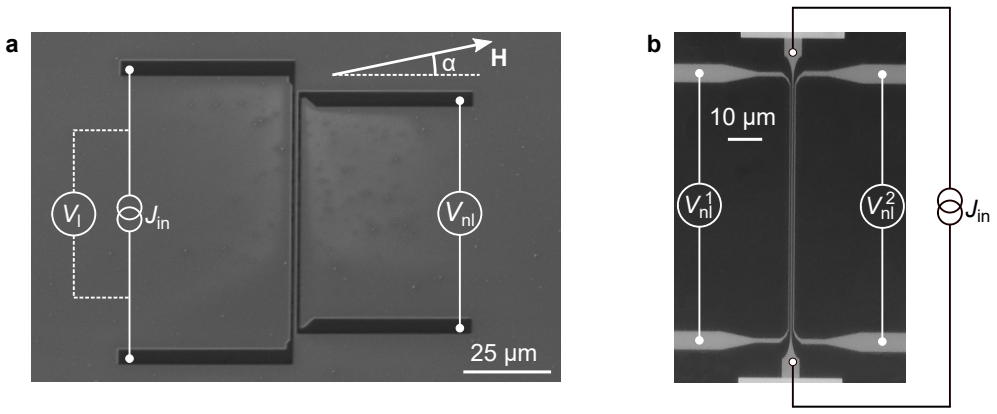

Figure 5.1: (a) Scanning electron and (b) optical micrograph of non-local device structures implemented in series A and B, respectively. In addition, the experimental wiring is indicated.

values of J_{in} are 250 µA ($j_{\mathrm{in}} \approx 3.3 \times 10^{10}\,\mathrm{A\,m^{-2}}$) in the case of series A, while for series B 350 µA ($j_{\mathrm{in}}^{\mathrm{Pt}} \approx 1.0 \times 10^{11}\,\mathrm{A\,m^{-2}}$, $j_{\mathrm{in}}^{\mathrm{W}} \approx 7.8 \times 10^{10}\,\mathrm{A\,m^{-2}}$) was applied. Note that for the temperatures probed, these current densities were well below a recently reported threshold, above which the electrical injection becomes non-linear [203]. In addition to the source meter, a Keithley 2182A nanovoltmeter could be connected in parallel to the current source to pick up the local SSE signal. For the non-local voltage, an additional nanovoltmeter was connected to the detector wire. The latter remained unbiased and electrically isolated from the injector such that solely magnon mediated spin signals, re-converted by the ISHE, should yield a voltage drop.

As mentioned in Sec. 4.3.2, the spin signal contributions (electrical or thermal) are separated by considering either the voltage difference or the average for reversed J_{in}:

$$V_{\mathrm{el.}}^{\mathrm{nl}} = V_{\Delta}^{\mathrm{nl}} = \left[V^{\mathrm{nl}}\left(+J_{\mathrm{in}}\right) - V^{\mathrm{nl}}\left(-J_{\mathrm{in}}\right)\right]/2., \tag{5.1}$$

$$V_{\mathrm{therm.}}^{\mathrm{loc./nl}} = V_{\Sigma}^{\mathrm{loc./nl}} = \left[V^{\mathrm{loc./nl}}\left(+J_{\mathrm{in}}\right) + V^{\mathrm{loc./nl}}\left(-J_{\mathrm{in}}\right)\right]/2. \tag{5.2}$$

The relation in Eq. 5.2 is only true for the non-local signal if the electrical emission and absorption of magnons at the injector is of equal probability for a fixed magnetization orientation but reversed current polarities. Considering the linear dependence of this effect on J_{in}, this assumption should hold according to Onsager's reciprocity relations [96]. To check for potential deviations of this expected behavior, which would have a noticeable impact on the reliability of the SSE signal, current sweep measurements were performed for positive and negative external fields, as shown in Fig. 5.2. According to Eq. 3.18 and Eq. 3.19, the expected voltage response is

$$V^{\mathrm{nl}} = R_{\mathrm{el.}}^{\mathrm{nl}} J_{\mathrm{in}} + R_{\mathrm{therm.}}^{\mathrm{nl}} J_{\mathrm{in}}^{2}. \tag{5.3}$$

The parabolic signal shape provided by the thermal effect, whose sign depends on the FMI magnetization orientation, becomes skewed by the linear, electrical contribution. Depending on the magnetization direction, positive and negative currents lead to magnon emission and absorption at the injector or vice versa.

In the case of equal emission and absorption probabilities, the respective linear slopes for the different current polarities should be the same. Indeed, fitting second order polynomials to the measurement data (solid lines in Fig. 5.2a,b) reveal that, while minor deviations are observed for opposite field directions, opposite current polarities yield linear responses of equal amplitude in first approximation. Figures 5.2c,d show the separated electrical and thermal voltage contribution using Eq. 5.1 and Eq. 5.2, respectively. The solid lines are fits of purely linear and quadratic functions, emphasizing the nature of the recorded signals.

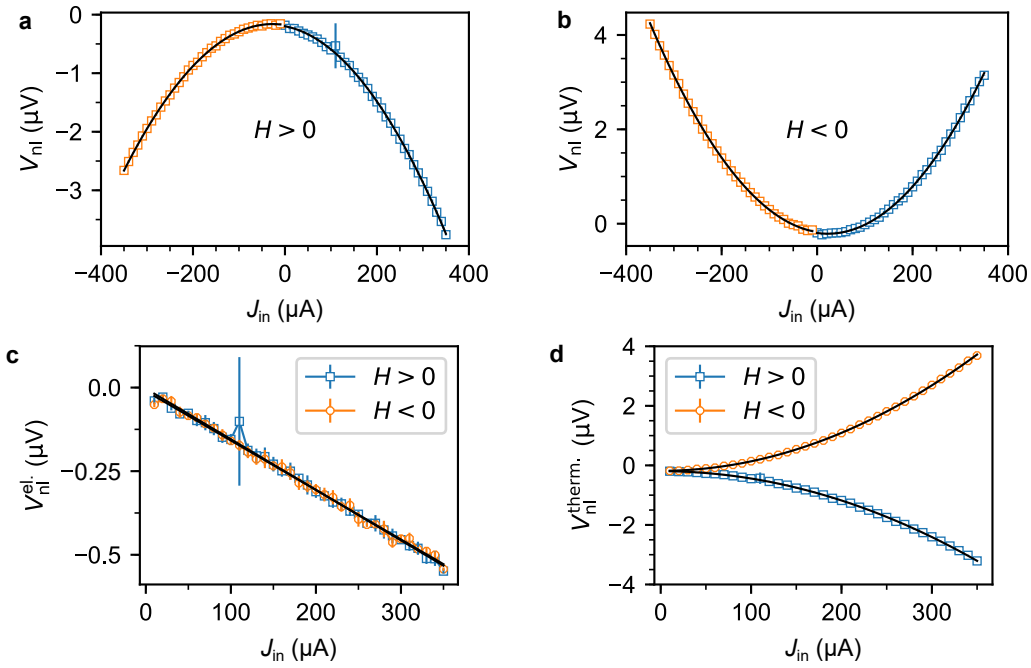

Figure 5.2: Non-local voltage as a function of the injector current for (a) positive and (b) negative external magnetic field ($\alpha = 0$) applied to a typical device of series B. The polynomial fit reveals a linear slope of (a) $R_{\text{el.}}^{\text{nl}} = (-1.39 \pm 0.12)\,\text{m}\Omega$ and (b) $R_{\text{el.}}^{\text{nl}} = (-1.48 \pm 0.10)\,\text{m}\Omega$. The extracted (c) electrical and (d) thermal signal reveal the expected linear and quadratic current dependence. Error bars represent the standard error of the recorded signal average.

Please note that the current-sweep measurements for the two field polarities were performed on different days, which most likely explains the differences in the slopes of $V_{\text{therm.}}^{\text{nl}}$ in Fig. 5.2d due to varied ambient conditions as, for instance, the room temperature of the laboratory.

As described in Sec. 4.3.1, two measurement protocols are available to determine the temperature dependence of the non-local SSE: magnetic field-sweeps at fixed temperatures or temperature-sweeps at fixed magnetic fields. Figure 5.3 provides a direct comparison of the two distinct methods. From the magnetic hysteresis loop shown in Fig. 5.3a, the SSE voltage $V_{\text{sse}}^{\text{nl}}$ is obtained by the signal height difference for positive and negative fields. In the case of temperature-sweep measurements (Fig. 5.3b), the measurement is repeated for different field polarities (blue/green data points), with the resultant voltage lines being subtracted from each other to obtain the SSE signal (red data points). Due to small variations in the fabrication process and a temperature-dependent Pt resistivity, the thermal voltage is divided by the heating power applied to the injector for a rough normalization within each measurement series and sub-series. For a thorough, quantitative comparison

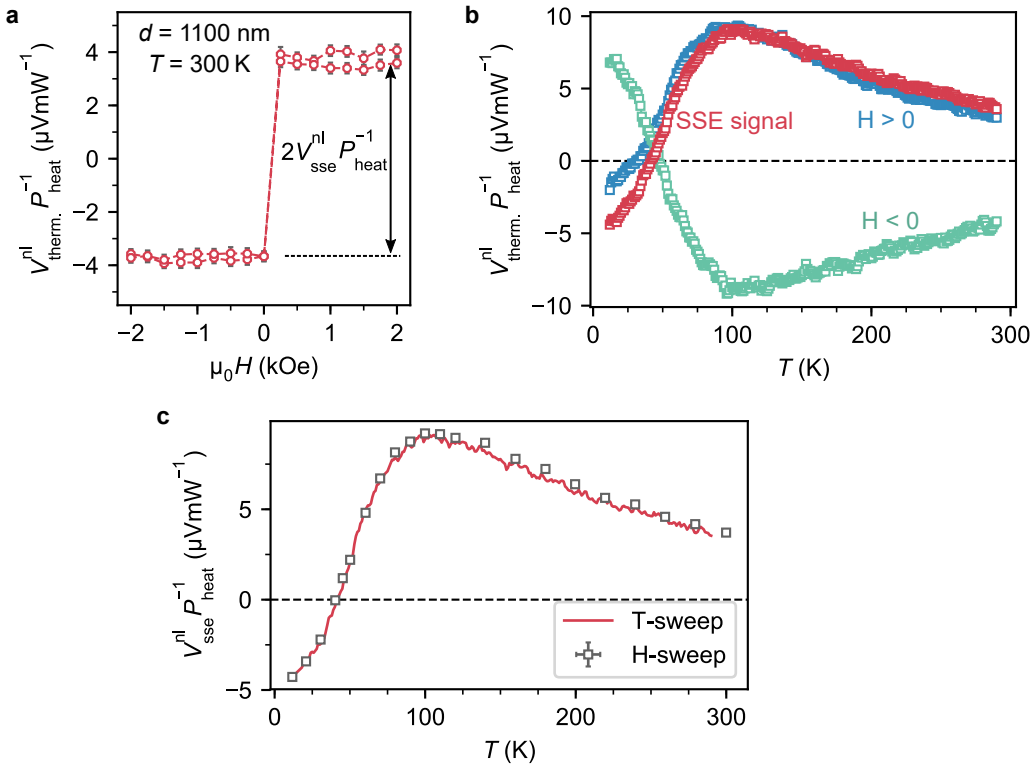

Figure 5.3: (a) Hysteresis loop of the non-local SSE voltage obtained for a device of series A with an injector-detector center-to-center distance of ≈ 1100 nm. $V_{\mathrm{sse}}^{\mathrm{nl}}$ is defined as half the hysteresis height and normalized to the applied heating power. (b) Raw thermal voltages for opposite magnetic field directions (blue/green) and calculated SSE signal (red) obtained by temperature-sweep measurements using the same sample as in (a). Considering the equal injection and absorption probabilities of magnons at the injector, the applied charge current polarity is fixed during the measurements. (c) Direct comparison of non-local SSE voltages obtained during the temperature-sweep and field-sweeps at fixed temperatures. Error bars, which are given by the standard error of the signal height, are smaller than the symbol size.

of the generated signals, which is not the aim of the presented work, a more elaborate normalization scheme needs to be implemented. Some of the parameters, which should be incorporated in such a measure, are the applied current as well as the wire resistances and geometries of both injector and detector. The equivalence of the two measurement protocols is supported by Fig. 5.3c, where temperature-dependent signals obtained by both methods are directly compared and agree well. Note that the indicated temperature on the x-axis is re-calibrated by temperature-resistance calibration curves determined for the injector.

In this work, temperature-sweeps are the generally preferred method considering a reduced

measurement time and a more detailed signal curve.

5.1.2 Results and discussion

To demonstrate the peculiar, aforementioned behavior of a sign change of the SSE voltage, a comparison of local and non-local signals at different wire separations is shown in Fig. 5.4. At room temperature, in-plane angular-dependent scans were performed on the YIG/W devices of series B, recording either the SSE voltage drop at the injector (Fig. 5.4a) or detectors at center-to-center distances of $d \approx 750\,\mathrm{nm}$ (Fig. 5.4b) and $d \approx 4220\,\mathrm{nm}$ (Fig. 5.4c). For all devices, a $\cos(\alpha)$ dependence is observed (for $\alpha = 0$, the field is perpendicular to the wire, see Fig. 5.1), as expected for the SSE, with an amplitude of the local signal that is one or two orders of magnitude larger as the non-local voltages. Besides confirming the SSE origin, the observed angular dependence emphasizes once more that field-sweeps ($\alpha = 0°, 180°$) are sufficient to obtain the SSE signal in later experiments.
To confirm the universality of this behavior and to investigate its origin, the temperature dependence of the non-local SSE has been measured as a function of temperature and strip center-to-center distance for both series A and B. Figure 5.5 provides an overview over the resulting data: Figure 5.5a,c,e respectively show the temperature dependences obtained for the devices of series A, series B/Pt and series B/W, while the corresponding distance dependences extracted at different temperatures are plotted in Fig. 5.5b,d,f. The generally opposite sign of the results obtained for the sample comprising of W wires can be easily understood with regard to the reversed sign of the spin Hall angle θ_{SHE} of W as compared to Pt [204].

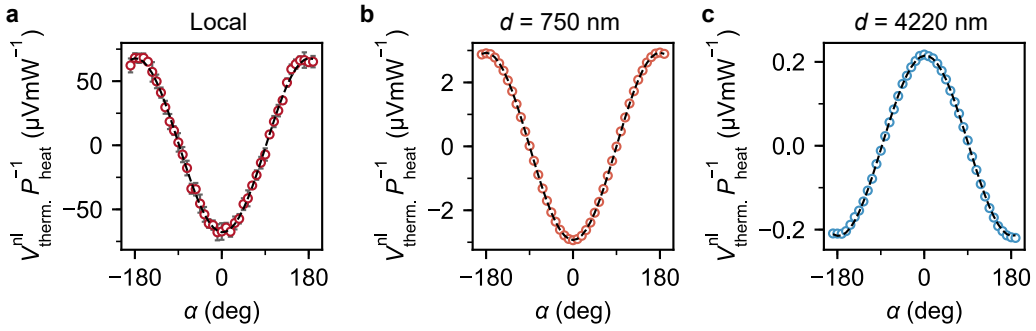

Figure 5.4: Angular-dependent measurements of (a) local and non-local SSE at injector-detector distances of (b) 750 nm and (c) 4220 nm. All signals reveal a $\cos(\alpha)$ dependence, as expected for an SSE induced spin current (e.g. see Eq. 3.19). While the local and short distance device exhibit the same sign, an inverted amplitude is observed at larger strip separations. Error bars account for the standard error of the mean of the voltage signal and the applied heating power. If not visible, they are smaller than the symbol size.

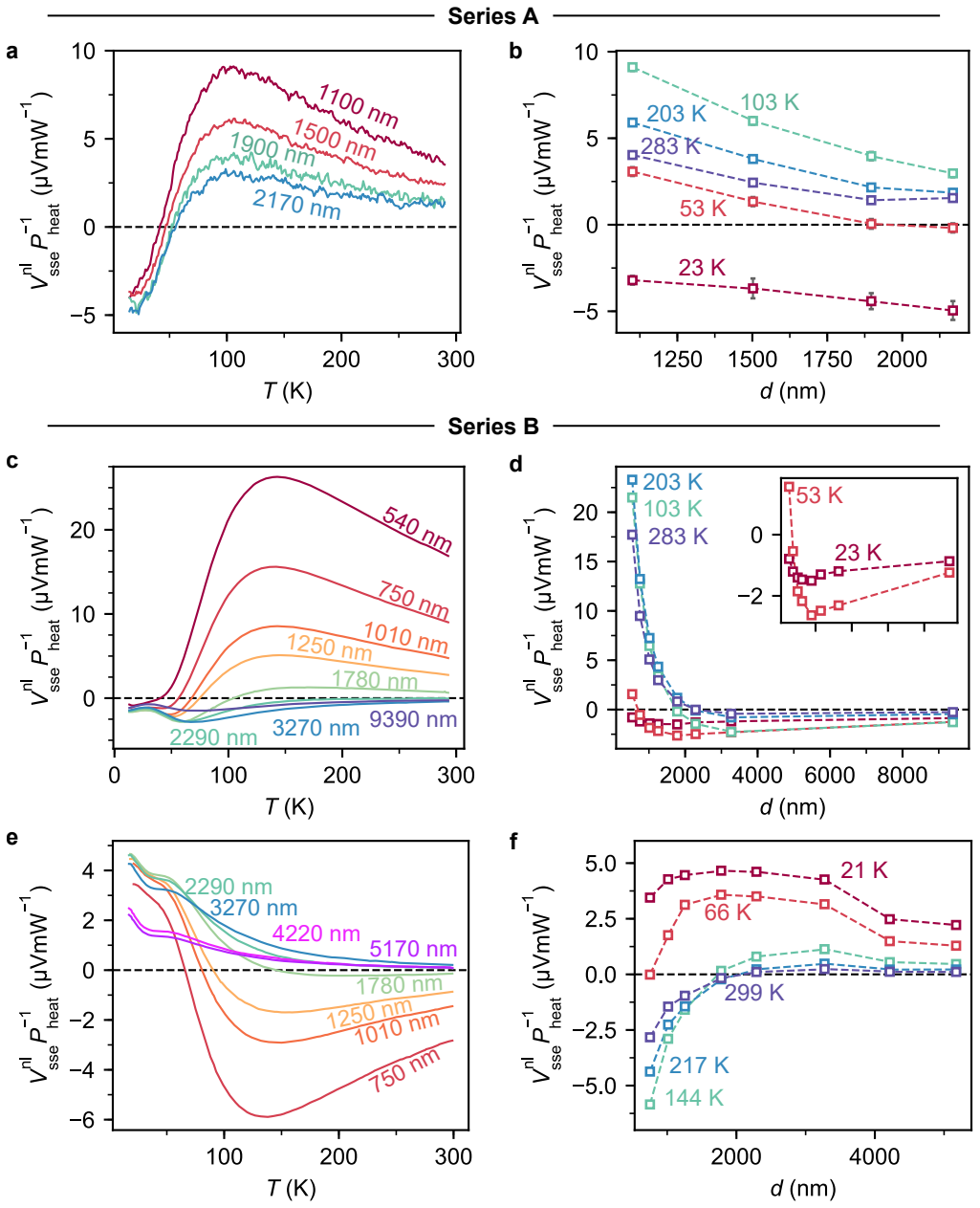

Figure 5.5: (a),(c),(e) Non-local spin Seebeck signal as a function of temperature obtained for non-local devices with varying injector-detector center-to-center distance of (a) series A, (b) series B/Pt and (c) series B/W. The inverted sign of the latter as compared to Pt based structures is due to the opposite signs of the respective spin Hall angles. (b),(d),(f) Non-local spin Seebeck signal as a function of distance for different temperatures extracted from the respective datasets shown in (a),(c) and (e). Error bars account for the standard error of the mean of the voltage signal and the applied heating power.

Considering first the temperature dependence, one observes a complex profile for all devices that start off with the same sign as local measurements (positive for Pt, negative in case of W) at high temperatures. With decreasing temperature, the signal amplitude exhibits an initial enhancement, followed by a sign reversal. The appearance of the signal peak is reminiscent of similar observations made for the local SSE by Guo *et al.* [o3], in which the peak was investigated as a function of YIG thickness. As suggested in the theoretical framework presented in Ref. [o3], the peak can be explained by a competition of magnon propagation and population. With decreasing temperature, an increase of the propagation length ξ is observed, following roughly a T^{-1} dependence [o3]. For the local SSE, this implies that the effective sample volume contributing to the magnon spin current increases, until it is limited by the finite film thickness. At the same time, the total magnon population diminishes due to a lowered thermal energy, yielding a reduction of the total spin current. In the case of non-local measurements, a similar mechanism could be considered, although the situation is more complex as lateral transport must be taken into account. The weak strip distance dependence of the peak position as well as similar peak temperatures for Pt and W wires in series B imply the bulk origin of the effect. Furthermore, lower peak temperatures observed for series A ($d_{\mathrm{YIG}} \approx 3\,\mu\mathrm{m}$) as compared to series B ($d_{\mathrm{YIG}} \approx 1.5\,\mu\mathrm{m}$), which is in line with the findings of Ref. [o3], hint at an influence of the film thickness on the in-plane spin transport.
From the temperature-dependent data of the various devices, it is apparent that the sign reversal (temperature) of the non-local SSE exhibits a strong strip separation dependence. The closer the injector and detector are, the lower the temperature of the zero crossing. In the inverted sense, which is represented by the graphs in Fig. 5.5b,d,f, the distance d_0, above which the sign opposite to the local signal is observed, decreases with decreasing temperature. While for series A the sign change as a function of distance only appears at lower temperatures, the enhanced strip separation range implemented in series B allows one to observe it in the high temperature region as well. The extracted values of d_0 for the three device series are summarized in Fig. 5.6. Note that the same qualitative behavior is observed for the samples of Ref. [o5] investigated at WMI Garching.

Origin of sign change

In the following, we first discuss the general appearance of the non-local SSE sign change and its characteristics based on a theoretical model proposed by Shan *et al.*, who investigated d_0 in YIG/Pt as a function of the YIG thickness and interface spin transmissivity at room temperature [205]. Roughly speaking, the sign inversion is attributed to the spatial distribution of thermally excited magnons $\mu_{\mathrm{m}}(\mathbf{r})$ within the YIG film, see Fig. 5.7. These are induced by Joule heating of the injector and diffuse radially towards the GGG/YIG

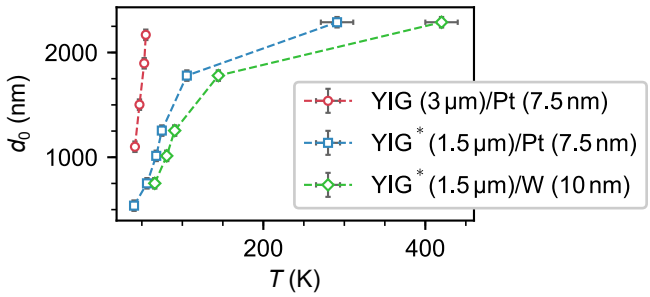

Figure 5.6: Injector-detector center-to-center distance d_0, which marks the sign change of the non-local SSE signal, of the different series and sub-series as a a function of temperature. If not visible, error bars obtained by the standard error and assumed temperature uncertainties are smaller than the symbol size. The high-temperature values ($T > 200\,\mathrm{K}$) for series B are obtained by extrapolation, indicated by an enhanced T-error.

interface and the sample edges. Following the generated temperature profile underneath the injector, this outlet of angular momentum leads to a depletion of magnons as compared to the equilibrium state ($\mu_\mathrm{m}^- < 0$). At further distances (on the range of the magnon propagation length), the magnons accumulate and $\mu_\mathrm{m}^+ > 0$. The sign of μ_m defines the spin current polarity across the YIG/NM detector interface and thus the sign of the non-local SSE, with $\mu_\mathrm{m}(d_0) = 0$. Note that this model is in agreement with previous results on thermal magnon propagation [o1], in which the distribution of magnons was captured as a local magnetization enhancement/reduction in atomistic spin dynamics simulations.

In Ref. [205], Shan *et al.* observe an increase of d_0 with increasing film thickness. Contrary to phonons, which can diffuse into the GGG substrate, vertical magnon propagation is limited such that magnons accumulate at the GGG/YIG interface. Due to a back-flow into the depleted region, the effective amplitude of both μ_m^+ and μ_m^- is reduced, resulting in a lower d_0. In thicker films, the magnon accumulation and depletion are further spatially separated, which ultimately leads to an increase of d_0. Additionally, Shan *et al.* see that, in the case of an injector interface that is opaque for spin currents, which is obtained by inserting a thin Al_2O_3 layer, d_0 becomes larger. With a similar argument as above, they explain this observation by a canceled back-flow of angular momentum from YIG into the injector, eventually enhancing the magnon depletion region.

Bearing this model in mind, both a thickness and interface effect can be recognized in Fig. 5.6. On the one hand, series A utilizing thicker YIG generally reveals larger d_0 values at fixed temperatures as compared to the devices implemented in series B, supporting the findings of Ref. [205]. At the same time, for distances $> 1500\,\mathrm{nm}$ d_0 appears at significantly enhanced temperatures for W wires in series B as compared to Pt. In other words, W reveals lower d_0 values at fixed temperatures. According to the considered model, this suggests

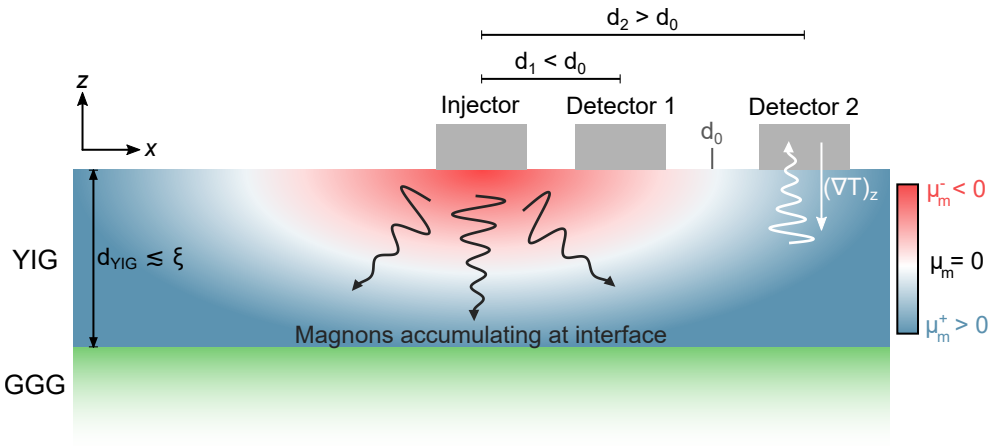

Figure 5.7: Schematic illustration of the device and magnon distribution in the YIG sample when performing non-local SSE experiments. The application of a charge current to the injector produces a radial temperature gradient that spans both the YIG and GGG substrate, giving rise to the non-local SSE. Thermally excited magnons diffuse along the generated temperature profile from hotter to colder regions, resulting in a magnon depletion $\mu_\mathrm{m}^- < 0$ zone near the injector and magnons accumulating ($\mu_\mathrm{m}^+ > 0$) at greater distances (at d_0, μ_m is zero and changes sign). If the YIG thickness is less than or comparable to the mean magnon propagation length ξ, a significant magnon accumulation builds up at the GGG/YIG interface as they cannot enter and propagate through the paramagnetic GGG. The sign of μ_m defines the spin current polarity across the YIG/detector interface such that the sign of the non-local SSE depends on the distance between injector and detector: for detector 1 (detector 2), the non-local SSE has the same (opposite) sign as compared to the local SSE at the injector. Note that the de-localized generation of spin currents, for example due to a temperature gradient across the YIG/detector interface, may also generate additional signal contributions. Inspired by [176].

a higher transparency of the YIG/W interface for spin currents, which is given by the spin-mixing conductance, as compared to that of YIG/Pt. However, it was demonstrated that YIG/W exhibits a spin mixing conductance $G_\mathrm{eff}^{\uparrow\downarrow}$ that is approximately half that of YIG/Pt [184]. This suggests that besides the absolute transparency of the interface for spin currents, further aspects like a spectral dependence of $G_\mathrm{eff}^{\uparrow\downarrow}$ as suggested in Ref. [o3] might need to be considered.

At this point, it must be noted that low temperature data ($T \lesssim 80\,\mathrm{K}$) obtained for series B must be treated with caution. While for series A the non-local SSE signal amplitude increases below the sign change with decreasing temperature, as can be seen in Fig. 5.5, the Pt devices of series B exhibit a nearly constant, and of similar magnitude, value for $V_\mathrm{sse}^\mathrm{nl}$ at all distances. This behavior can be explained by a frustration of the surface magnetization of the YIG films below the injector/detector at low temperatures, possibly induced by

the Ar etching process implemented in the sample fabrication. Similar observations for comparable conditions have been reported by Vélez *et al.* [206], who conclude that altering the stoichiometry of the YIG surface via Ar etching lead to modified magnetic interactions and eventually perpendicular coupling between YIG bulk and surface moments. For the devices investigated here, experimental evidence for a frustrated magnetization is given in Fig. 5.8a, in which a field-dependent sweep of the local and non-local ($d = 1780\,\mathrm{nm}$) SSE at $T = 18\,\mathrm{K}$ is depicted. Instead of signal saturation at low fields and a potential suppression at high fields (see Ref. [36]), for both local and non-local SSE the signal starts to saturate at fields larger than 9 T, implying that the magnetic frustration is lifted. While this finding of frustrated state is interesting and is worth further investigation, this is beyond the scope

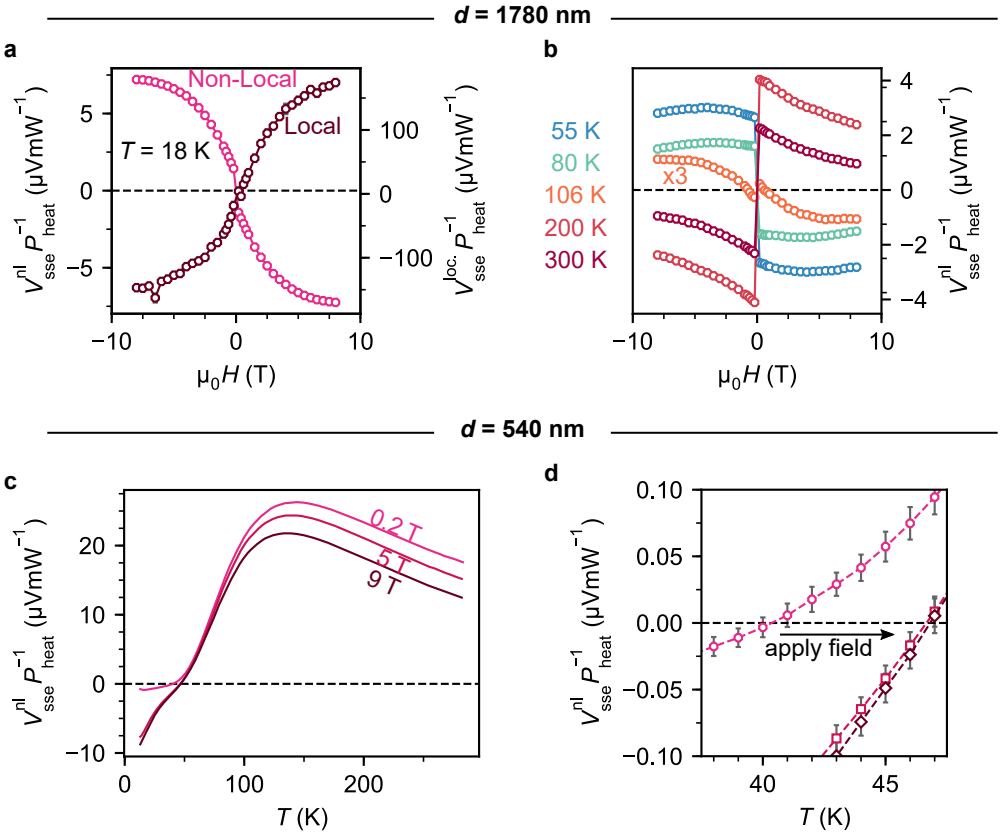

Figure 5.8: (a) Local and non-local ($d = 1780\,\mathrm{nm}$) SSE voltage as a function of magnetic field, measured simultaneously at $T = 18\,\mathrm{K}$. The absence of signal saturation indicates magnetic surface frustration (see definition in the main text). (b) Non-local SSE signal as a function of magnetic field obtained for the same device as in (a) at various fixed temperatures. (c),(d) Non-local SSE signal as a function of temperature for different applied fields. The injector-detector distance is $d = 540\,\mathrm{nm}$. Error bars represent the standard error of the mean.

of the presented work. Hereafter, only the results for $T \gtrsim 80\,\mathrm{K}$ are considered, at which *regular* behavior in line with other reports [207] is observed.
To check the impact of a frustrated interface on the temperature dependence of the non-local SSE, temperature sweeps have been repeated for series B/Pt ($d = 540\,\mathrm{nm}$) at 5 T and 9 T, as shown in Fig. 5.8c. While at high temperatures the previously reported signal suppression with increasing field [36] is observed, $V_{\mathrm{sse}}^{\mathrm{nl}}$ shows a similar trend below the zero crossing as in series A. The sign change temperature, as depicted in more detail in Fig. 5.8d, experiences a significant positive shift of $\approx 6.5\,\mathrm{K}$. This shift in temperature of d_0, i.e. a shift of d_0 to lower values at a fixed temperature, is in accordance with the model discussed above, as lifting the magnetic surface frustration at the YIG/Pt interface should effectively enhance the spin-mixing conductance (mixing vs. transmission).

Temperature dependence of non-local SSE

Finally, it is discussed whether the observed temperature dependence of the non-local SSE and consequently d_0, which is the focus of the presented work, can be fully understood in terms of the mechanism described above or whether adjustments are necessary. To do so, the various parameters governing the transfer of angular momentum across the FMI/NM interface as well as the magnon diffusion process need to be analyzed.
As already discussed above, the interface transparency for spin currents, which is described by the effective spin-mixing conductance $G_{\mathrm{eff}}^{\mathbb{1}}$, has a significant impact on the sign reversal distance d_0. In previous experiments focusing on the transport of electrically induced magnon currents in YIG/Pt heterostructures, it has been shown that the signal strength decreases with decreasing temperature [172]. The temperature profile follows a power law $V_{\mathrm{el.}}^{\mathrm{nl}} \propto T^n$ with n in the range of 1 to 1.5, which is in line with theoretical predictions of $G_{\mathrm{eff}}^{\mathbb{1}} \propto T^{3/2}$ [171, 208] for large magnon diffusion lengths. In the presented work, comparable behavior is observed for electrically induced magnon propagation in series A and B/Pt, as shown in Fig. 5.9. For series A, in which electrically induced magnon currents were only probed for a single distance of $d = 1100\,\mathrm{nm}$, an exponent $n = 1.76$ is obtained at temperatures below 100 K, similar to what has been reported before [172]. In the case of series B in the same temperature region, however, one observes n-values that decrease from 3.45 to 1.68 for an increasing injector-detector distance up to $d = 1780\,\mathrm{nm}$, followed by a slight increase again. These deviating values may be explained by the frustrated surface magnetization and the spectral dependence of the magnon propagation length, which decreases with higher energy, i.e., decreasing wavelength of the magnon [36]. Assuming that the frustrated surface highly affects short-wavelength (short-range) magnons but may be unseen by long-wavelength (long-range) magnons, one can understand the different power laws by the magnon spectra detected at the different distances: at short distances, both short- and

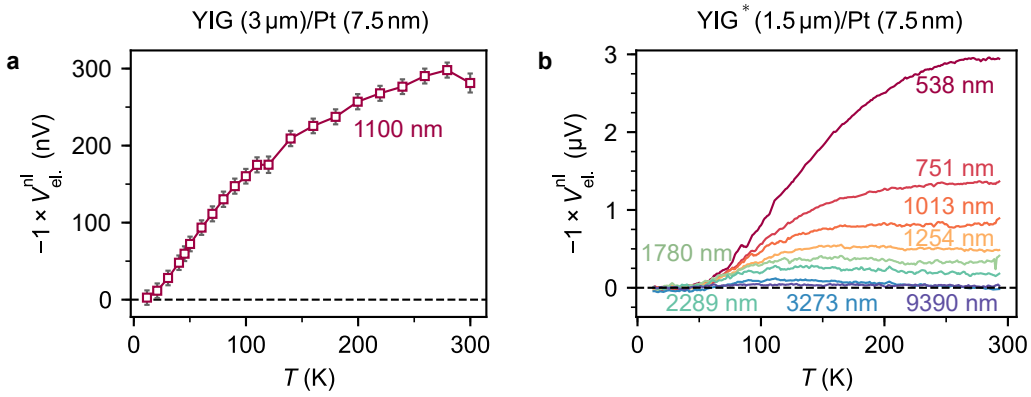

Figure 5.9: Spin transport signal of electrically induced magnons as a function of temperature obtained for (a) series A and (b) series B/Pt. While the temperature-dependent data in (a) was obtained by probing $V_{el.}^{nl}$ at fixed temperatures, temperature-sweeps at a fixed field but with opposite injector current polarity were used in (b). Error bars represent the standard error of the mean.

long-range magnons are detected, while at larger distances only long-range magnons are captured by the detector. This implies that the frustrated interface has a major impact on short distance signals, while its influence on large-distance signals is reduced. Here, this is reflected by the fact that at larger distances the theoretically expected power law [171, 208] is re-obtained. Nonetheless, according to these results, the YIG/Pt interface is becoming more opaque for spin currents with decreasing temperature, which in terms of the above described model implies an increase of d_0 due to the reduced back-flow. This is in direct contrast to the findings depicted in Fig. 5.6, signifying that the interface effect is not sufficient on its own to describe the temperature dependence of the non-local SSE. Therefore, bulk effects that affect the propagation of thermally excited magnons need to be considered.

Regarding magnon transport in the bulk, the mean magnon propagation length ξ and the magnon spin conductivity σ_m, which are interrelated [208], are decisive. However, the experimental determination of the temperature dependence of ξ is non-trivial and so far inconclusive [o3, o5, 177]. Considering first only electrically induced magnons, Cornelissen *et al.* extract constant values of ξ as a function of temperature [177], while for the samples of the related work in Ref. [o5] an increase of ξ with decreasing temperature is observed (measured at WMI Garching). The latter is roughly described by a T^{-1}-law, which is in line with the findings of Ref. [o3] for the local SSE and can be explained by the relation between ξ and a temperature-dependent Gilbert damping parameter α [157]. A qualitatively similar observation is made for ξ-values extracted from the non-local data presented in Fig. 5.9b using the coupled diffusion-relaxation equation provided by Ref. [22]. The result is depicted

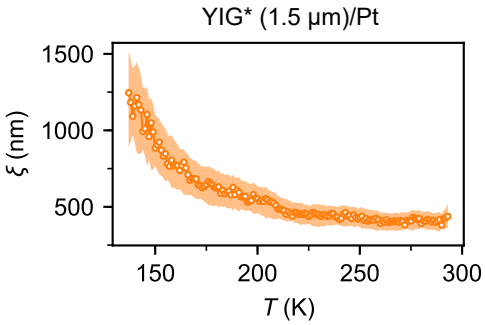

Figure 5.10: Magnon propagation length ξ in series B/Pt as a function of temperature. The values are obtained by fitting the data in Fig. 5.9 to a coupled diffusion-relaxation equation provided by Ref. [22]. The shaded area around the data points marks the fitting errors.

in Fig. 5.10, with ξ increasing from $\approx$ 400 nm at room temperature to $\approx$ 1250 nm at $T = 130\,\mathrm{K}$. Below this temperature, the fit becomes unstable. One explanation for the comparably low magnon propagation length at room temperature could be an enhanced Gilbert damping α, which by means of FMR measurements (not shown) is determined to be in the range of $5 \times 10^{-4} - 1.5 \times 10^{-3}$ for the YIG sample batch used in series B. In the case of series A, $\xi \approx 980\,\mathrm{nm}$ is found at room temperature, which agrees with the value reported in Ref. [172]. Ultimately, the direct impact of ξ on d_0 is not obvious and most likely depends on the FMI thickness. Additionally, the effect of further parameters as, for instance, the magnon spin conductivity σ_m need to be investigated in more detail [208]. Nevertheless, the qualitative variation of d_0 as a function T observed in Fig. 5.6 implies an enhanced interaction between the magnon depletion (μ_m^-) and accumulation (μ_m^+) region, which reduces d_0 [205], at lower temperatures due to the enhanced magnon propagation length ξ.

More instructive information on the general mechanism of the non-local SSE can be obtained by the distance-dependent data of the thermal voltage. As can be seen in Fig. 5.5d,f, the latter is non-trivial and exhibits a non-monotonic behavior: after the sign change, an amplitude increase is observed, followed by a signal reduction at larger distances. Indeed, more recent reports demonstrate multiple decay regimes [176, 209], suggesting the presence of various contributions to the non-local SSE voltage. To be precise, according to Giles *et al.* [209], the magnon spin current is driven by both the spatial variation of μ_m and the temperature profile in the FMI:

$$\sigma_\mathrm{m} \nabla^2 \mu_\mathrm{m}(\mathbf{r}) + \zeta \nabla^2 T(\mathbf{r}) = g \mu_\mathrm{m}(\mathbf{r}) \,. \tag{5.4}$$

Here, σ_m is the aforementioned magnon spin conductivity, ζ the intrinsic SSE coefficient, and g a parameter quantifying magnon relaxation. While short distance signals are dominated by $\nabla^2\mu_\mathrm{m}$, a local SSE provided by $\nabla^2 T$ is governing the ISHE voltage drop across the detector at larger strip separations.

For the sake of completeness, one can think of a further signal contribution induced by a heat flow from the FMI into the detector NM. This is insofar justified, as, for instance, Pt reveals an enhanced thermal conductivity as compared to YIG [209] and is furthermore in contact with the exchange gas in the VTI. Due an interfacial heat resistance, the so-called *Kapitza* resistance, the magnon temperature in the FMI and the NM conduction electron temperature are not continuous, giving rise to a potential interfacial SSE [152] at the detector site. In other works, e.g. Ref [207], this effect is neglected.

With these findings, one can try to understand the observed increase of the non-local SSE amplitude after the sign change at low temperatures (Fig. 5.5a and Fig. 5.8c) as well as the weak field dependence in that temperature region (Fig. 5.8b; Ref. [207]). Regarding the former, YIG films of micrometer thickness exhibit a peak of the phonon-mediated thermal conductivity κ near $T = 60\,\mathrm{K}$, while for further decreasing temperature κ goes to zero [210]. On that account, the temperature profile in YIG may alter, leading to a larger temperature gradient ∇T near the heat source (injector) and a larger local SSE at the detector site.

In terms of an applied magnetic field, the non-local SSE shows a strong field dependence at high temperatures, while a weak response of $V_\mathrm{sse}^\mathrm{nl}$ to large fields is observed for $T = 55\,\mathrm{K}$ and $80\,\mathrm{K}$ (see Fig. 5.8b). Similar behavior has been reported in other works [207], but has not been directly discussed. With regard to the low temperature region, the weak field dependence of $V_\mathrm{sse}^\mathrm{nl}$ reminds one of field-dependent data obtained for the local SSE in thin films [36]. Generally, the application of an external magnetic field leads to the opening of a Zeeman gap, which cuts off low energy magnons with large propagation lengths. In bulk or thick films, this leads to a reduction of the signal amplitude as these magnons contribute significantly. In thin films, however, these long-range magnons with wavelengths that are larger than the film thickness are strongly suppressed, yielding a reduced field sensitivity of the SSE. The in-plane propagation of magnons, on the other hand, is expected to reveal a higher field sensitivity. In view of Eqs. 5.4 and the distinct field trends of the non-local SSE at high and low temperatures in Fig. 5.8b, this implies a diffusion ($\nabla^2\mu_\mathrm{m}$) dominated signal at high temperatures, whereas $\nabla^2 T$ and thus the local SSE at the detector governs at low temperatures. This effect may also explain the field-induced sign change and the subsequent saturation of $V_\mathrm{sse}^\mathrm{nl}$ in Fig. 5.8b at $T = 106\,\mathrm{K}$, which is above the temperature region of magnetic frustration and also observed in Ref. [207]. By suppressing in-plane magnon propagation, the depletion region shrinks and the relative contribution of the local SSE at the detector becomes stronger. Eventually, these findings suggest that, in agreement

with Ref. [209], the non-local SSE is not given exclusively by the diffusion of magnons from the injector to detector region but that the non-local generation of magnons (e.g. local SSE at the detector) must also be considered, especially at low temperatures.

5.1.3 Conclusion

In conclusion, the non-local spin Seebeck effect has been investigated in YIG/Pt and YIG/W bilayers as a function of injector-detector distance, temperature and applied magnetic field strength. For a small strip separation, the non-local SSE shows the same sign as the local SSE at the detector, whilst a sign change is observed at larger strip separations. By means of temperature-dependent measurements, it is demonstrated that the characteristic distance d_0, at which the sign change occurs, decreases with decreasing temperature. Furthermore, it is shown that when using thicker YIG, larger values for d_0 are obtained. Considering an increasing magnon propagation length ξ with decreasing temperature, these findings can be brought in line with a theoretical model suggested by Shan *et al.* [176, 205]. This model correlates the sign change to the creation of magnon depletion and accumulation regions due to the diffusive magnon transport, which are furthermore strongly affected by the FMI thickness and the spin current transparency of the FMI/injector interface, which is described by the spin-mixing conductance. With increasing ξ, the magnon accumulation at the FMI/substrate interface interacts significantly with the depletion region under the injector, effectively reducing d_0. The importance of the interface, which is discussed in the model, becomes apparent in the case of samples with a frustrated surface magnetization. The frustration is lifted at high fields, resulting in the sign change occurring at higher temperatures. Effectively, this implies a lower value of d_0, which can be explained by an enhanced spin backflow into the injector and thus a reduced expansion of the depletion region.

Beyond that, field-dependent data reveal a weak field-dependence of the non-local SSE at low temperatures (but above temperatures exhibiting the frustrated state), while at higher temperatures a stronger impact of the field is observed. Moreover, by means of applying a field a sign change can be induced. These observations can be understood in terms of recent results [209] discussing the importance of magnon transport and local temperature gradients at the detector. Bearing this in mind, the field-dependent data suggest a transport dominated signal at higher temperatures, while at low temperatures and below the sign change the signal is governed by a non-local generation of thermal magnons near the detector. For the latter, a weak field dependence is expected for the FMI thicknesses used, which agrees with the measurement data.

5.2 Spin transmission across metallic antiferromagnets

As demonstrated in the previous section and in the literature [211], ferro(i)magnetic insulators pose an interesting medium for magnon-based information technology concepts [17] and have therefore caught notable, renewed attention in recent years. In contrast to metallic systems, spin transfer mediated by charge motion is suppressed and, consequently, Joule heating losses during the information transport are avoided. However, as already briefly mentioned in the introduction to this thesis, antiferromagnets have recently gained increased interest in terms of spintronic applications due to advantageous features such as an enhanced stability as compared to ferromagnets ore THz spin dynamics [18–21].

So far, it has been shown that antiferromagnetic insulators (AFMI) are capable of mediating spin information and, moreover, that magnon currents can be induced thermally by the spin Seebeck effect when forcing the AFM into the spin-flop state [167, 168]. With regard to magnon propagation properties, spin transfer across AFMI thin films has been investigated in FM(I)/AFMI/NM heterostructures both experimentally [68, 119, 122, 212–214] and theoretically [215–217]. Due to the fact that antiferromagnetic magnons exhibit resonance frequencies that are usually in the range of several THz, direct excitation by, for instance, microwave irradiation is impractical. On that account, experimental studies on AFMI magnon propagation commonly included indirect excitation schemes, with spin currents being generated in the FM(I) layer and pumped into the AFMI. After passing through the AFMI, the spin current is eventually detected in the NM by means of the inverse spin Hall effect. The variation of the ISHE amplitude when measured as a function of AFMI thickness or temperature allows one to infer information on the properties of AFMI magnon propagation.

Note that during the preparation of this thesis, the direct generation and detection of magnonic spin currents in a single crystal of the easy axis AFMI α-Fe_2O_3 (hematite) has been reported by Lebrun *et al.* [o13]. Utilizing the non-local geometry described in Sec. 3.5, both electrically and thermally injected AFMI magnons are observed, revealing propagation lengths of several micrometers. These values are comparable to those of YIG [22] and more than two orders of magnitude larger than the ones reported for AFMI thin films [68, 119, 212, 214]. One potential explanation for this may be given by the presence of domains in the thin films, which may impact the mode polarization. For more detailed information, please see Ref. [o13].

More recently, the application potential of metallic antiferromagnets in next-generation spintronic concepts has been examined [18, 19]. Beyond simply fixing the magnetization orientation of ferromagnetic layers in tunnel magnetoresistance devices via exchange bias, it has been verified, for instance, that the inherent SHE of metallic AFMs can be used to

implement field-free switching of ferromagnets via spin-orbit torque [218]. To explore their full potential, it is thus useful to further investigate spin-related phenomena in metallic AFMs, e.g. their ability to forward spin information. Amongst others, it has been shown that temperature-dependent FMR spin pumping measurements allow one to examine the antiferromagnetic-paramagnetic phase transition T_N of $Ir_{20}Mn_{80}$ (IrMn) thin films [123]. Near T_N, which strongly depends on the IrMn thickness, the Gilbert damping constant α of $Ni_{81}Fe_{19}$ in $Ni_{81}Fe_{19}$/Cu/IrMn trilayers reveals an enhancement. This finding can be explained by an increased absorption of the pumped spin current by the IrMn due to spin fluctuations [122, 213, 214], implying a significant coupling of the spin current to the Néel order parameter in IrMn. Using this method, one can therefore unveil details of the magnetic properties of metallic AFMs, however information on the spin propagation is indirect and limited.

To address this subject, experimental results on the propagation of spin currents in YIG/IrMn/Pt trilayers are presented in the following. First and foremost, the transmission of thermal spin currents through IrMn is investigated by means of temperature- and thickness-dependent SSE measurements. By comparing the obtained results to previous findings and theoretical models, conclusions on potentially dominating electronic or magnonic spin transmission channels are drawn. Furthermore, SMR measurements were carried out to examine whether genuine spin transport in IrMn or interface exchange coupling effects are observed. In previous measurements, the SMR effect has proven to be a useful tool to probe, for instance, the magnetic sublattice orientations in complex magnetic oxides [o6, 219]. The experimental data is eventually discussed in the context of numerical simulations targeting the transfer of angular momentum across FM/AFM interfaces.

The aforementioned results were obtained together with the research groups of Prof. Dr. U. Nowak (University of Konstanz) and Prof. Dr. E. Saitoh (Tohoku University, Sendai, Japan) and have recently been published as a research article [o8].

5.2.1 Experimental details

The sample layout used to investigate spin transmission in YIG/IrMn/Pt is illustrated in Fig. 5.11a. Single crystalline YIG of 5 µm thickness was grown epitaxially on (111)-oriented GGG substrates by means of liquid phase epitaxy. After cleaving the GGG/YIG into samples of size 2 mm × 6 mm × 0.5 mm, IrMn/Pt bilayers with varying IrMn thickness and constant Pt thickness ($d_{IrMn} = 0.8, 1.3$ nm, $d_{Pt} = 5$ nm) were deposited via magnetron sputtering from Pt and $Ir_{20}Mn_{80}$ targets. Further YIG/Pt($d_{Pt} = 5$ nm) and YIG/IrMn ($d_{IrMn} = 1.3$ nm) samples were fabricated for reference. In addition to Pt, which has become a model material with regard spin-to-charge conversion, IrMn itself exhibits a spin Hall angle [19]. The reference samples are therefore required to be able to understand and

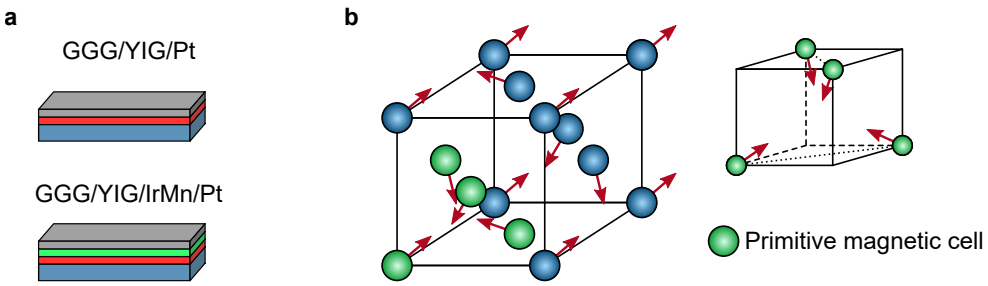

Figure 5.11: (a) Simple schematic of sample structure. (b) Crystallographic structure of $Ir_{20}Mn_{80}$: face-centered cubic without a preference of Mn or Ir to occupy each lattice site. The primitive magnetic cell determined by Kohn *et al.* [220] is depicted, with the magnetic moments being tilted away from the crystal face diagonals at an angle of 45°.

distinguish the contributions to the signal from either the IrMn or the Pt. In contrast to the non-local experiments described in the previous section, nano-structuring of the metal layer was not necessary.

The crystallographic and spin structure of $Ir_{20}Mn_{80}$ is depicted if Fig. 5.11b. If not annealed, as is the case here, it condenses into the chemically disordered γ-phase of $IrMn_3$ [220], which is a face-centered cubic structure without a preferred lattice-site occupation of either Mn or Ir. Neutron diffraction measurements have revealed that the magnetic structure of the disordered phase exhibits a cubic structure with the moments being arranged under a 45° angle from the crystal face diagonals [220]. The bulk Néel temperature of $Ir_{20}Mn_{80}$ was determined to be $T_N \simeq 680\,K$ [221], whereas this value is lower in thin films [123].

As described in Sec. 4.3.1, temperature-dependent SSE measurements were performed in a cryostat with a variable temperature insert ($2\,K \leq T \leq 300\,K$), employing the longitudinal configuration [o1, 145]. Sandwiching the samples between a top resistive heater and a bottom temperature sensor (Fig. 4.7), the measurement protocol including magnetic field sweeps at fixed temperatures was implemented. A typical hysteresis loop obtained for the thermal voltage is shown in Fig. 5.12a, in which the charge current applied to the heater is varied. Extracting half the hysteresis height and plotting it as a function of the injector current amplitude, one observes a quadratic dependence (solid line in Fig. 5.12b) as expected for a thermally induced signal. Since the different metallic layers exhibit distinct resistivities, the SSE current $J_{sse} = V_{sse}/R$ will be considered in the following. Furthermore, the data is divided by the temperature difference ΔT across the sample extracted from the simultaneous logging of the top heater- and bottom sensor resistances.

The temperature-dependent SMR measurements, on the other hand, were carried out in

a superconducting vector cryostat that allows one to align the magnetic field in arbitrary directions. The MR ratio $\Delta\rho/\rho_0$ is extracted from angular-dependent measurements of the longitudinal resistance in x-direction, in which the magnetic field H is rotated in the xy-, yz- or zx-plane (α-,β-,γ-scan). To ensure that the magnetization of the YIG follows the applied field direction, the field strength is fixed to a value of $\mu_0 H = 0.8\,\mathrm{T}$, far larger than the coercive fields of the YIG. Matching with the rotational dependences given in Eqs. 3.4-3.6, a significant resistance variation is observed in the case of H-rotation in the xy- and yz-plane (Fig. 5.12c,d), while little variation is observed in the zx-plane (Fig. 5.12e). Considering the signal deviations observed in the α- and β-scan, the small resistance variation in the γ-scan is probably due to sample misalignment, indicating that no significant AMR is present, only SMR. In later graphs, only the amplitude of the β-scans are considered for $\Delta\rho_{\mathrm{SMR}}/\rho_0$.

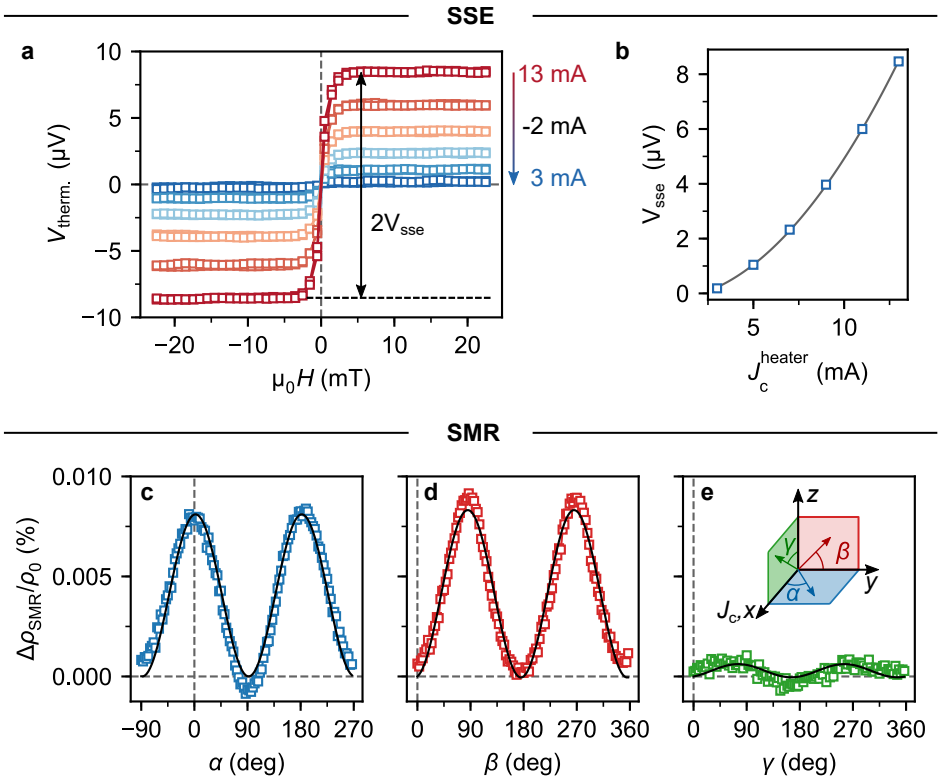

Figure 5.12: (a) Hysteresis loop of the longitudinal SSE voltage obtained for the YIG/Pt sample with various charge current amplitudes applied to the resistive heater (V_{sse} = half the hysteresis height). (b) V_{sse} as a function of the applied heat current, exhibiting the expected quadratic dependence (solid line). (c)-(e) Exemplary angular-dependent measurements of the longitudinal resistance ($\mathbf{J}_{\mathrm{c}} \parallel \mathbf{x}$) in YIG/IrMn13/Pt at $T = 285\,\mathrm{K}$. The rotation planes of $\mathbf{M}$ and respective angles are depicted in the inset of (e). Later, only the amplitude of β-scans is considered to prevent the detection of AMR effects.

5.2.2 Results and discussion

Focusing first on the SSE, the temperature-dependent $J_{\mathrm{SSE}}/\Delta T$ amplitudes obtained for the various sample stacks are shown in Fig. 5.13. The samples with and without a Pt top layer are presented separately in Fig. 5.13a and Fig. 5.13b to facilitate the readability of the graphs. While the YIG/Pt only sample (blue circles) exhibits a clear signal amplitude maximum near $T \simeq 90\,\mathrm{K}$, broad and flat maxima with deviating peak temperatures are observed for the samples that include the IrMn interlayer [$T_{\mathrm{max}}^{\mathrm{IrMn13/Pt}} \approx 150\,\mathrm{K}$, $T_{\mathrm{max}}^{\mathrm{IrMn8/Pt}} \approx 200\,\mathrm{K}$]. At low temperatures, where IrMn exhibits antiferromagnetic order, the detected SSE amplitude becomes significantly suppressed and a general IrMn thickness-dependent signal reduction is observed. At higher temperatures ($T \geq 200\,\mathrm{K}$), however, where IrMn is likely to be in the paramagnetic phase, the SSE signal amplitude observed for YIG/IrMn (0.8 nm)/Pt exceeds the one of the YIG/Pt sample. While this aspect surely is of interest, its investigation was not the focus of the presented work and further careful studies would be necessary to fully understand this phenomenon. Nevertheless, a potential explanation can be given by an enhanced effective spin-mixing conductance $G_{\mathrm{eff}}^{\Downarrow}$ of the YIG/IrMn interface as compared to the YIG/Pt interface, considering that comparable effects have been observed in similar systems [222, 223]. Eventually, when regarding the temperature-dependent SSE signal obtained for the YIG/IrMn (1.3 nm) sample without Pt capping in Fig. 5.13b, a clear signal maximum near $T = 120\,\mathrm{K}$ is observed. This temperature profile reminds one of the YIG/Pt sample in Fig. 5.13a, however, the peak is shifted and the amplitude is significantly smaller. Intriguingly, a minor but distinct shoulder effect appears at $T = 230\,\mathrm{K}$. The origin of the latter is not clear, but it may be related to the

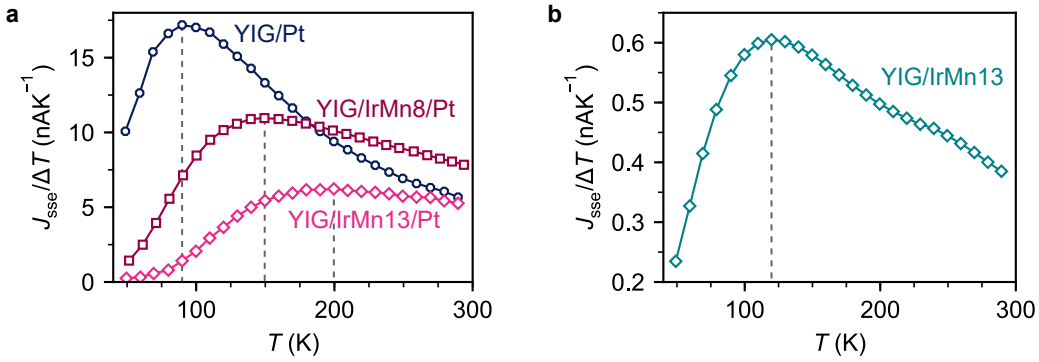

Figure 5.13: Spin Seebeck current J_{sse} divided by the temperature difference ΔT between sample top and bottom as a function of temperature for (a) YIG/Pt,YIG/IrMn (0.8 nm)/Pt, and YIG/IrMn (1.3 nm)/Pt as well as (b) YIG/IrMn (1.3 nm). The dashed lines indicate the temperatures of signal maxima. Errors of $J_{\mathrm{SSE}}/\Delta T$ are smaller than the symbol size. Adapted from [o8].

paramagnetic-antiferromagnetic phase transition of IrMn, as discussed later.

The temperature-dependent SMR amplitudes $\Delta\rho_{\mathrm{SMR}}/\rho_0$ obtained by angular-dependent measurements for the samples including the IrMn interlayer are shown in Fig. 5.14 [(light) blue circles/octagons], directly put in contrast to the ISHE current amplitude $J_{\mathrm{sse}}/\Delta T$ [red squares/pink diamonds]. This comparison is crucial as it allows one to understand and differentiate between potential interface and spin transport effects. Apart from a different amplitude ratio, both the SMR and SSE amplitude feature a similar trend in the low temperature region with an overlapping, strong signal suppression.

In the following, the results shown above are discussed in order to understand the measured signals and their different origins. To deduce information on the details of spin current transmission across IrMn, the different data sets obtained for the distinct sample stacks are analyzed and contrasted individually: Firstly, the generation and detection of magnon spin currents as a function of temperature is assessed. To do so, only the bilayers of YIG/Pt and YIG/IrMn are considered, which do not involve spin current transmission across the full IrMn layer. In YIG/Pt, as shown in Fig. 5.13a, the detected spin Seebeck current exhibits a distinct amplitude maximum near $T = 90\,\mathrm{K}$. As already discussed in the context of the non-local SSE in the previous section (Sec. 5.1), this phenomenon is explained as a consequence of an increasing magnon propagation length in YIG with decreasing temperature, which is counteracted by a reduced occupation of magnon states due to a lower thermal energy $k_{\mathrm{B}}T$ [o3]. Instead of being a pure bulk effect of the FMI, however, the temperature of the signal maximum is also affected by the employed ISHE detection layer [o3, o4]. These findings suggest a notable spectral dependence of the magnon transmission across the FMI/NM interface. In this regard, YIG/IrMn (Fig. 5.13b) shows a qualitatively similar temperature dependence as compared to YIG/Pt, but the peak position is shifted ($T = 120\,\mathrm{K}$), implying

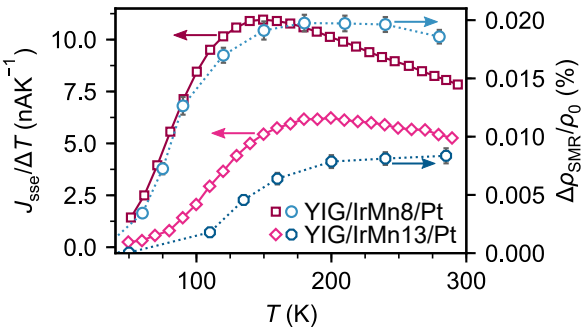

Figure 5.14: Direct comparison of temperature-dependent SMR (left y-axis) and SSE (right y-axis) amplitudes obtained for YIG/IrMn (0.8 nm)/Pt and YIG/IrMn (1.3 nm)/Pt. In the case of $\Delta\rho_{\mathrm{SMR}}/\rho_0$, error bars account for the error of the amplitude fit parameter. Errors of $J_{\mathrm{SSE}}/\Delta T$ are smaller than the symbol size. Adapted from [o8].

different magnon mode transmissions for YIG/Pt and YIG/IrMn as discussed for other detection layers in the literature [o3, o4].

In a next step, the fundamental prerequisites of spin transport in the investigated samples are determined, for which the results obtained for YIG/IrMn/Pt and YIG/IrMn stacks are compared. The significant difference in the SSE signal amplitude for YIG/IrMn and YIG/IrMn/Pt can be easily understood considering various material properties such as a reduced spin Hall angle ($\theta_{\mathrm{SH}}^{\mathrm{IrMn}} \approx 0.8\,\theta_{\mathrm{SH}}^{\mathrm{Pt}}$ [224]), a shorter spin diffusion length ($\lambda_{\mathrm{sf}}^{\mathrm{IrMn}} = 0.7\,\mathrm{nm}$ vs. $\lambda_{\mathrm{sf}}^{\mathrm{Pt}} = 2\,\mathrm{nm}$ [225, 226]) as well as an increased film resistivity ($\sigma^{\mathrm{IrMn}}/\sigma^{\mathrm{Pt}} \approx 0.15$ [224]) of IrMn as compared to Pt. Studying in detail the differences between YIG/IrMn (1.3 nm) (Fig. 5.13b) and YIG/IrMn (1.3 nm)/Pt (pink diamond, Fig. 5.13a), the much lower signal amplitude of YIG/IrMn as compared to YIG/IrMn/Pt, as well as the much lower resistance of the Pt, signify that the ISHE voltage generation in the IrMn is negligible with respect to the total signal in YIG/IrMn/Pt. Therefore, the SSE response in YIG/IrMn/Pt can be interpreted as the pure spin current stimulus transmitted from the YIG across the IrMn into the Pt, where it is converted into a detectable voltage due to the ISHE.

Comparing now the qualitative temperature dependences, one observes a clear signal maximum at $T \simeq 120\,\mathrm{K}$ for YIG/IrMn (1.3 nm), whereas in YIG/IrMn (1.3 nm)/Pt the signal amplitude is strongly suppressed at temperatures lower than 150 K. To understand this key feature of strong attenuation, the findings reported so far are reviewed: (i) From the YIG/Pt system, it is clear that the generation of spin currents in the YIG layer as well as their detection in Pt are significant below 150 K (Fig. 5.13a). (ii) The results obtained for YIG/IrMn (Fig. 5.13b) reveal that the spin transfer across the YIG/IrMn interface is large in the very same temperature region. Thus, the remaining alternative to explain the signal attenuation below 150 K in YIG/IrMn/Pt is the spin transport across the IrMn, which apparently becomes suppressed at low temperatures. In IrMn, the spin current can be mediated by both electronic and magnonic excitations. The temperature dependence of $J_{\mathrm{sse}}/\Delta T$ in YIG/IrMn/Pt hereby implies that the dominating spin channel is strongly impaired at $T < 150\,\mathrm{K}$.

Finally, it needs to be clarified whether magnonic- or electronic spin currents yield the dominating contribution. From the relatively large signal in YIG/IrMn at $T < 150\,\mathrm{K}$, one can conclude that the charge-based spin currents in IrMn required for the ISHE driven spin-to-charge conversion are still notable. As a result, the observed strong attenuation of the measured signal in the YIG/IrMn/Pt system must have its origin in the magnonic spin current transport across the IrMn layer. Additionally, bearing in mind previous findings for insulating AFMs [93, 122], the signal suppression is assumed to be correlated to the formation of antiferromagnetic order in IrMn. This conclusion is furthermore in line with the theory put forward in Ref. [o8], where a short propagation length is predicted for

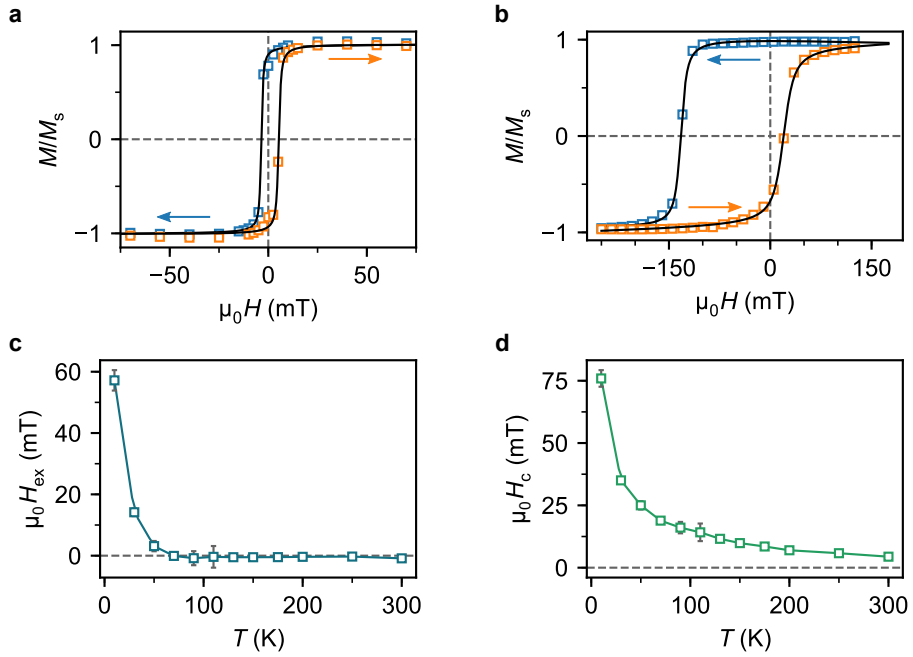

Figure 5.15: (a),(b) Magnetic hysteresis loops obtained for SiO_2/IrMn (1.3 nm)/$Co_{70}Fe_{30}$ via SQUID magnetometry at (a) $T = 300\,\mathrm{K}$ and (b) $T = 10\,\mathrm{K}$. Solid lines are fits obtained by adjusted Langevin-functions, from which the coercive- and exchange bias fields are extracted. (c) Exchange bias- and (d) mean coercive field as a function of temperature. Error bars [(c),(d)] are obtained by error propagation. If not visible, they are smaller than the symbol size.

antiferromagnetic magnons due to a reduced lifetime. More implications of this model are discussed further below.

To corroborate a potential relation between the shown experimental findings and the Néel phase transition of IrMn from the paramagnetic state into the antiferromagnetic state, temperature-dependent SQUID magnetometry measurements have been performed on a SiO_2/IrMn (1.3 nm)/$Co_{70}Fe_{30}$ (CoFe) (2 nm) reference sample. Using a reference sample was necessary as the relatively large thickness of the used YIG films hindered the assessment of T_N due to the lack of measurable exchange bias. Figures 5.15a,b show typical magnetic hysteresis curves obtained for two different temperatures $T_1 = 300\,\mathrm{K}$ (Fig. 5.15a) and $T_2 = 10\,\mathrm{K}$ (Fig. 5.15b). IrMn indeed undergoes a magnetic phase transition demonstrated by the significantly enhanced width (coercivity) as well as the horizontal shift of the CoFe hysteresis at 10 K as compared to the one recorded at room temperature, which can be explained by the exchange bias effect (see Sec. 2.3.3). From further magnetometry data, the exchange bias field $H_{ex} = (H_c^+ + H_c^-)/2$ as well as the average coercive field $H_c = (H_c^+ - H_c^-)/2$ are extracted and plotted as a function of temperature in Fig. 5.15c

and Fig. 5.15d, respectively. The exchange-bias field vanishes at the so-called blocking temperature $T_B \simeq 80\,K$, which in thin films is usually found to be smaller than T_N [227]. The coercive field, on the other hand, reveals a monotonic trend as a function of temperature, with a notable increase below $T^* \gtrsim 200\,K$. This corresponds to the temperature region, where the maximum value of the SSE amplitude is found for the respective sample (Fig. 5.13a) and in the vicinity of the signal shoulder observed for YIG/IrMn (Fig. 5.13b). According to Rinaldi *et al.* [228], T^* can be assumed to be close to T_N, which may explain the shoulder effect as a change of θ_{SH}^{IrMn} or λ_{sf}^{IrMn} across the phase transition. Note, however, that these absolute values need to be taken with care keeping in mind the compositional differences of the investigated samples. Furthermore, it is unclear if a distinct phase transition temperature can be assumed or whether spatial variations need to be considered, potentially given by finite size effects or locally varied magnetic properties of the ultra-thin IrMn films.

At this point, it must be noted that a potential exchange spring formed at the YIG/IrMn interface has no notable impact on the observed temperature dependence of $J_{sse}/\Delta T$. As demonstrated in Fig. 5.16, field cooling (FC) or zero field cooling (ZFC) measurements show no significant difference.

When drawing a direct comparison between the data obtained by the magnetometry and spin-thermoelectric measurements (Fig. 5.17), one observes that $J_{sse}/\Delta T$ starts to increase significantly just above T_B. Reconsidering the theoretical model briefly mentioned before, this characteristic behavior is recognized as a further indication for the correlation between the signal attenuation and the AFM phase transition of IrMn. Above T_N, hence in the

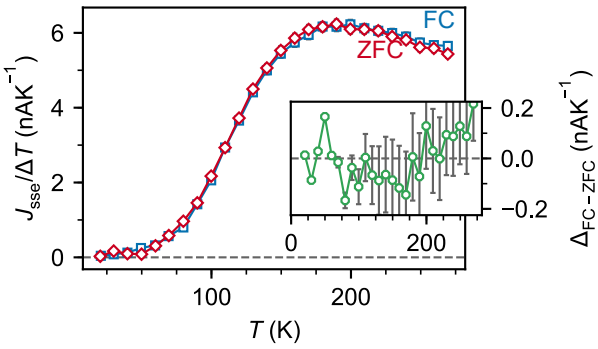

Figure 5.16: Spin Seebeck current $J_{sse}/\Delta T$ as a function of temperature in YIG/IrMn (1.3 nm)/Pt compared for a field cooled (FC, blue squares) and zero field cooled (ZFC, red diamonds) sample. The inset shows the signal difference as a function of temperature, revealing little variation around zero. Error bars are obtained by error propagation. If not visible, they are smaller than the symbol size.

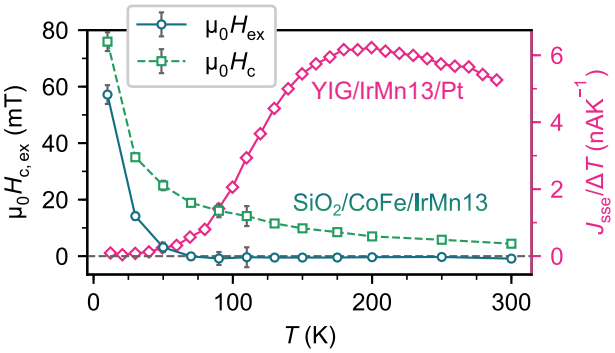

Figure 5.17: Direct comparison of $J_{\mathrm{sse}}/\Delta T$ in YIG/IrMn (1.3 nm)/Pt and the coercive- and exchange bias field in SiO_2/IrMn (1.3 nm)/$Co_{70}Fe_{30}$ as a function of temperature. Error bars of $H_{\mathrm{c,ex}}$ ar obtained by error propagation. If not visible, they are smaller than the symbol size. Errors of $J_{\mathrm{SSE}}/\Delta T$ are smaller than the symbol size. Adapted from [o8].

paramagnetic phase of IrMn, the magnonic spin current can be transported by short-range correlations [229]. Below T_{N}, however, long-range order forms and a frequency gap $\Delta\omega_{\mathrm{AFM}}$ typical of an AFM magnon dispersion relation (see theoretical discussion in Ref. [o8]) opens up and increases with further decreasing temperature. In Ref. [o8], atomistic spin dynamics simulations have been performed by the collaborators from Konstanz to investigate the excitation of spin waves and the transfer of spin angular momentum in FM/AFM bilayers. The corresponding results are shown in Fig. 5.18, studying both spin wave frequencies above (Fig. 5.18a) and below (Fig. 5.18b) the AFM magnon gap. For $\omega > \Delta\omega_{\mathrm{AFM}}$, the spin wave induced in the FM layer continues as a spin wave of equal frequency in the AFM. For $\omega < \Delta\omega_{\mathrm{AFM}}$, however, evanescent modes are excited in the AFM that decay exponentially as a function of distance from the FM/AFM interface. According to these physical processes, the strong attenuation of $J_{\mathrm{sse}}/\Delta T$ can be understood when assuming a transition from spin angular momentum transfer via precessing spin waves to evanescent waves at low temperatures.

From all the indications presented so far, it can be concluded that the spin current through IrMn is at least partially mediated by AFM magnons. This presumption is further reinforced by similar experiments performed by Saglam *et al.* [121], who document two distinct transport regimes in $Ni_{80}Fe_{20}$/FeMn/W trilayers with varying FeMn thickness. According to their observations, spin propagation is dominated by electronic transport in the short-range regime (small FeMn thickness), whereas magnonic excitations yield the leading spin transport channel in the long-range regime (larger thickness). With regard to the results presented here, note that FeMn exhibits a larger spin-diffusion length than IrMn [225]. Furthermore, Saglam *et al.* excite spin currents via FMR spin pumping ($f = 9\,\mathrm{GHz}$), while

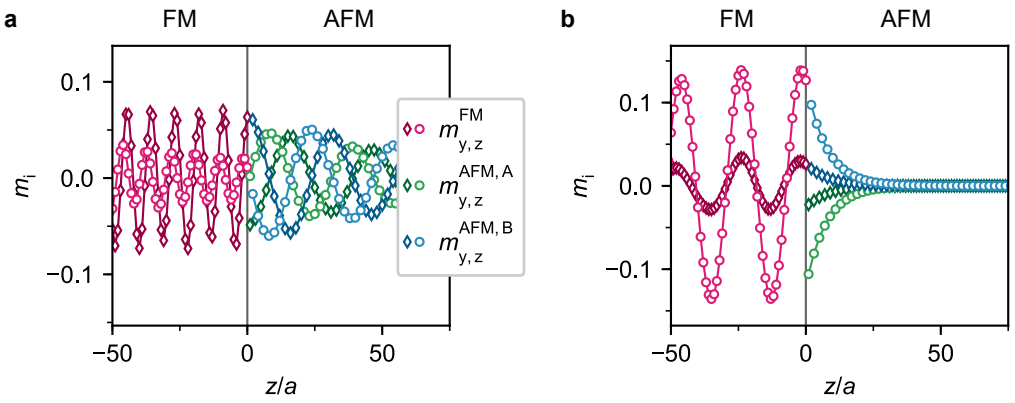

Figure 5.18: Spatial variation of the y- and z-component (diamond and circle symbols, respectively) of the magnetization for a spin wave propagating in x-direction in a two-layer FM/AFM system obtained via atomistic spin dynamics simulations. (a) Excitation frequency in the FM above the AFM magnon gap such that a spin wave of equal frequency propagates in the AFM. (b) Excitation frequency in the FM below the AFM magnon gap such that a strongly decaying evanescent wave is observed in the AFM. Data taken from [o8], to which the author would like refer the interested reader.

thermal magnons with frequencies up to the THz regime are induced in SSE experiments. The correlation between the AFM order in IrMn and corresponding spin current propagation properties becomes further apparent when comparing the trilayer samples with varying IrMn thickness. While the thickness-dependent reduction of $J_{sse}/\Delta T$ is the result of either electronic or magnonic spin diffusion, the explicit thickness dependence of the critical temperature marking the signal attenuation region is a direct indication of the paramagnetic-antiferromagnetic phase transition. In accordance with the findings by Frangou *et al.* [123], who report a positive linear dependence of T_N on the IrMn thickness due to finite size effects, the SSE amplitude suppression begins at higher temperatures for larger IrMn thicknesses.

Finally, the amplitudes of the SSE and SMR measurements are compared and discussed, revealing good agreement as shown in Fig. 5.14. In particular, coinciding low-temperature behaviors are observed, despite the conceptual differences of the underlying effects. The SMR is based on strong interface effects, bearing in mind that the pure spin current induced in the NM layer interacts (absorption/reflection) with the surface spins of the adjacent magnetic layer (Ref. [77] and Sec. 3.2). The SSE signal, on the other hand, comprises the conversion of bulk magnon spin currents into electronic spin currents at the FMI/NM interface, which are eventually converted into a charge signal by means of the ISHE. Bearing in mind the differences of thickness, conductivity and spin Hall angle of Pt and IrMn, one can assume that in the SMR experiments the SHE spin current is mainly generated in

the Pt. The angular dependence of $\Delta\rho_{\mathrm{SMR}}/\rho_0$ observed in Fig. 5.12 is in line with a *positive* SMR, which appears for spin currents interacting with the surface magnetization of FMs. In the case of AFMs, instead, the SMR couples to the Néel order parameter and a *negative* SMR [o11, 91, 92, 94] is expected. Taking this into account, it is apparent that in the SMR measurements presented here, the spin current, which is generated in the Pt, propagates across the IrMn and interacts with the YIG surface magnetization. Potential *negative* SMR contributions from the IrMn/Pt interface may appear at magnetic field values that are sufficiently large to align and rotate the Néel order parameter in the chemically disordered IrMn, however, this is not seen here. The coinciding temperature dependences of the SSE and SMR amplitudes imply a strong coupling of the electronic spin current generated in Pt to the order parameter in IrMn at the IrMn/Pt interface, assuming that the aforementioned magnonic spin transport mechanism is valid. Furthermore, this implies that the temperature dependence of the SMR amplitude in this case is dominated by the spin transport across the IrMn layer.

5.2.3 Conclusion

In conclusion, the propagation of pure spin currents across the metallic antiferromagnet $Ir_{20}Mn_{80}$ has been investigated by means of temperature-dependent SSE and SMR measurements. To deduce information on the dominating spin transport channel, which can be either of electronic or magnonic nature, the different results obtained for YIG/IrMn, YIG/Pt and YIG/IrMn/Pt heterostructures were analyzed and compared systematically. At low temperatures, where IrMn exhibits antiferromagnetic order as shown by SQUID magnetometry, the detected spin signals in YIG/IrMn/Pt are strongly suppressed, while in YIG/IrMn a notable voltage induced by a merely electronic spin current is still detected. This information emphasizes the importance of the effective spin transmission through IrMn, but also, together with theoretical considerations, implies the significance of magnonic spin information transport in the metallic antiferromagnet. The signal suppression at low temperatures is explained by the frequency gap appearing in the AFM magnon dispersion, which according to atomistic spin simulations results in spin transport via strongly decaying evanescent magnon modes. Further characteristics of the AFM state are the IrMn thickness-dependent decay of the signal at low temperature and the thickness-dependent shift of the critical temperature, below which the signal attenuation becomes active ($T_{\mathrm{N}} \propto d_{\mathrm{IrMn}}$). Ultimately, a positive SMR and a temperature dependence coinciding with that of the SSE signify the reciprocity of the process, as the spin current direction is reversed. In view of the magnonic transport, this furthermore implies a notable coupling of the electronic spin current to the Néel order parameter at the IrMn/Pt interface.

5.3 Concentration-dependent spin current detection in copper-iridium alloys

In the previous two sections, both the generation and propagation of magnonic spin currents through insulating ferrimagnets and metallic antiferromagnets have been investigated. With regard to the implementation of potential next-generation spintronic applications, these are crucial aspects for the development of novel information transmission and manipulation schemes. A further decisive key ingredient is the efficient detection of spin currents, which in view of fast data processing will need to operate at the highest possible speeds. From this perspective, as described in detail in Sec. 3.1, the spin Hall effect and its inverse are the focus of current research [10], since they allow for the interconversion of spin-charge information in normal metals with strong spin-orbit interaction. The efficiency of this conversion is quantified by the spin Hall angle θ_{SH}.

As discussed in Sec. 3.1, both intrinsic and extrinsic spin-dependent effects contribute to the SHE [10]. The extrinsic SHE is found in (dilute) alloys of normal metals with both weak and strong SOI [230–233], but can also be sizeable in pure, superclean metals [69]. As a result, the employed metal type as well as the atomic composition of the alloy are effective parameters to adjust and maximize the SHE. Remarkably, it has recently been demonstrated that the spin Hall angle of binary alloys including two normal metals with strong SOI (e.g. AuPt) can even exceed the one observed for the single alloy partners [234]. Pioneering work within this research field investigated the extrinsic SHE (skew scattering) in copper-iridium alloys [230]. However, in this study the iridium concentration was limited to an effective dilute doping of Cu with an Ir content of up to 12 %. The evolution of the SHE in this specific alloy in the higher concentration regime thus remained an open question and the maximally achievable value of θ_{SH}, obtained by an optimized alloying strategy, was unknown.

Among other methods, the efficiency of the spin-charge interconversion in a metal, i.e. θ_{SH}, can be quantified by the injection of a spin current into the NM and by gauging the resultant charge response. As described in Chap. 3, the thus required generation of spin currents can be accomplished by various techniques such as, for instance, FMR spin pumping (Sec. 3.3) or the spin Seebeck effect (Sec. 3.4.3), with the latter inducing a magnon flow along a temperature gradient. These experiments typically further involve a heterostructure composed of a magnetic insulator, such as YIG, and the ISHE-capable material under study. In the commonly established SSE measurement scheme (see Sec. 4.3.1), a static temperature gradient is induced in the FMI bulk by the application of external heat. On the ultrafast time scale, on the other hand, a step-like temperature difference across the FMI/NM interface can be generated by contact-free heating of the NM with short optical

laser pulses [o12, 159]. Recent results have demonstrated that the induced spin current flows on the femtosecond time scale and can be considered as an ultrafast version of the SSE [o12].

In the following section of this thesis, the strength of the ISHE in $Cu_{1-x}Ir_x$ (CuIr) is examined in bilayers of YIG/CuIr as a function of the atomic composition of the alloy, covering a concentration range of $0.05 \leqslant x \leqslant 0.7$. With regard to material development, this study hence goes beyond the dilute doping phase investigated in previous works [230]. Furthermore, as sketched in Fig. 5.19, two distinct generation schemes for spin current stimuli are implemented, namely the aforementioned conventional and all-optical SSE methods (a more thorough explanation of the latter is given in the experimental details). This is done, as the direct comparison of the relative changes of the signal amplitudes obtained by the two methods allows one to reaffirm the THz SSE mechanism as well as to infer qualitative information on the effectiveness of the (I)SHE with regard to THz dynamics. Bearing in mind the decisive time scales in these distinct methods, they are labelled in the following using the standard notation of electronics: the ISHE voltage due to a continuous conversion of steadily flowing spin currents in the conventional configuration is considered a DC signal, whereas the ultrafast spin response in the optical experiment is regarded as an AC effect.

The experiments have been performed in collaboration with the *Terahertz Physics Group*

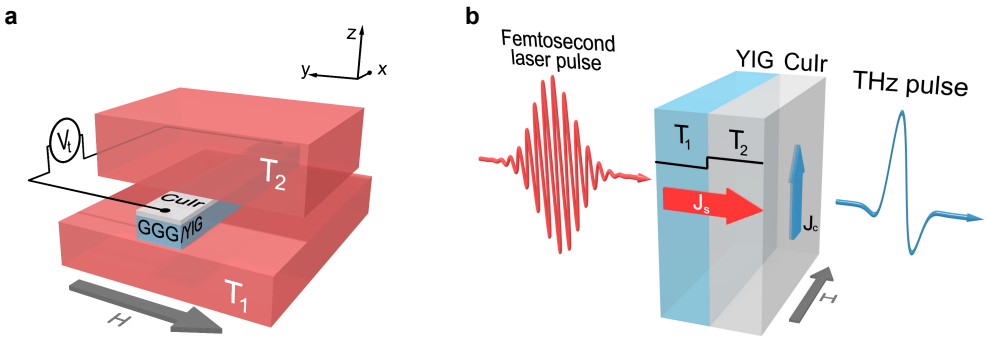

Figure 5.19: (a) Schematic DC SSE measurement setup. Individual control over the copper block temperatures T_1 and T_2 enables the application of an out-of-plane temperature gradient. An external magnetic field is applied in the sample plane and the resulting thermovoltage $V_{\text{therm.}}$ is recorded by a nanovoltmeter. (b) Schematic of the ultrafast SSE/ISHE THz measurement principle. The in-plane magnetized sample is irradiated by a laser pulse of 10 fs width, exciting a step-like temperature gradient across the YIG/$Cu_{1-x}Ir_x$ interface. The SSE-induced, sub-picosecond spin current is converted into a sub-picosecond charge current by means of the ISHE, ultimately emitting a THz electromagnetic pulse into the optical far-field. Adapted from [o7].

of Prof. Dr. T. Kampfrath at the Fritz Haber Institute of the Max Planck Society, Berlin. The work has been published as a research article [o7].

5.3.1 Experimental details

The magnetic samples used for this study are commercial YIG films of 870 nm thickness, grown epitaxially on (111)-oriented $Gd_3Ga_5O_{12}$ (GGG) substrates via LPE. Following the cutting of the GGG/YIG into samples of 2.5 mm × 10 mm × 0.5 mm dimension, $Cu_{1-x}Ir_x$ thin films (thickness $d_{CuIr} = 4$ nm) of varying composition ($x = 0.05$, 0.1, 0.2, 0.3, 0.5 and 0.7) were deposited by DC multi-source magnetron sputtering from two elemental Cu and Ir targets. During the deposition, the sputtering gas (Ar) pressure of 5×10^{-3} mbar as well as the sample temperature of ≈ 300 K were kept constant. The sputtering powers applied to the individual targets, however, were varied individually to adjust the alloy composition according to previously calibrated growth rates. Eventually, in order to prevent oxidation of the CuIr thin films, a 3 nm Al capping layer was deposited, which formed an AlO_x protection layer when exposed to air. As mentioned above, optical measurements of the THz SSE do not require electrical contacting of the sample. Moreover, in the case of DC SSE measurements, electrical contacts at the opposite sample ends (long edge) are sufficient for the detection of the thermal voltage. Therefore, structuring of the metal film is not necessary for the measurements carried out.

The quality and growth rate of the resultant CuIr films were verified by X-ray reflectometry performed on a $Si/Cu_{0.9}Ir_{0.1}$ reference sample, as shown in Fig. 5.20. Furthermore, to check for a potential phase separation of Cu and Ir during the growth process or thereafter, the XRR data has ben fit using three potential scenarios for sample configuration: Si/Cu/Ir (Fig. 5.20a), Si/Ir/Cu (Fig. 5.20b) and the desired $Si/Cu_{0.9}Ir_{0.1}$ (Fig. 5.20c). As already apparent from the plots, the best fit results were obtained for the case of homogeneously distributed Cu and Ir atoms. More specifically, the critical angles (see Sec. 4.2.2) do not coincide, which is crucial considering that these are material specific and are proportional to the square root of the material density. The fit results of Fig. 5.20c reveal, for this reference sample, a film thickness of 25 nm and a root-mean-square roughness of 0.35 nm. Simply put, these results demonstrate that the implemented growth process resulted in smooth, high quality $Cu_{1-x}Ir_x$ thin films.

The DC SSE measurements were performed in the longitudinal configuration, using the room temperature setup described in Sec. 4.3.1 and sketched in Fig. 5.19a. The required static temperature gradient was generated by clamping the sample between two copper blocks, whose temperatures can be controlled individually and are thermally connected only by the sample. For the magnetization alignment, which defines the polarization of the magnonic spin current, an external field is applied. The spin current transfers angular

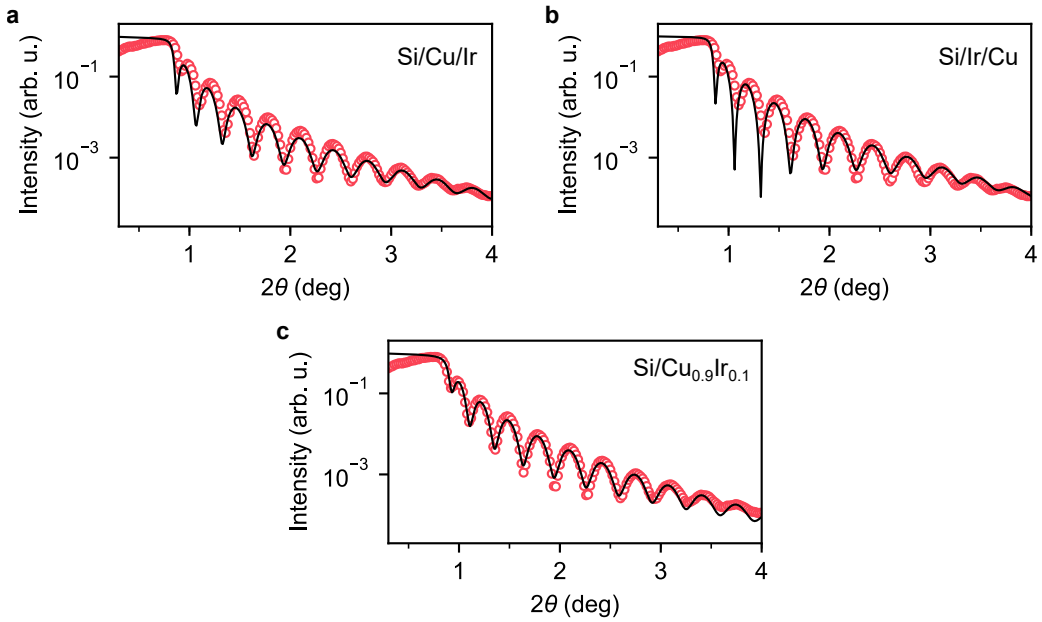

Figure 5.20: X-ray reflectometry (XRR) data obtained for a Si/$Cu_{0.9}Ir_{0.1}$ reference sample. The data is fit assuming either (a),(b) phase-separated films of Cu and Ir [(a) Si/Cu/Ir and (b) Si/Ir/Cu] or (c) an equal distribution of Cu and Ir atoms in the binary alloy. The latter fitting routine yields the best results, especially with regard to matching critical angles, corroborating the high quality of the CuIr films. For the reference sample, the fit reveals a CuIr thickness of 25.0 nm and a root-mean-square roughness of 0.35 nm. Adapted from [o7].

momentum into the $Cu_{1-x}Ir_x$ such that a spin accumulation builds up at the YIG/CuIr interface, which in turn induces spin diffusion in the metal. Eventually, this spin current is converted into a transverse charge current by means of the ISHE, resulting in a measurable voltage signal. The spin current polarization and consequently the thermal voltage change sign when the YIG magnetization is reversed. Furthermore the amplitude is linearly dependent on the temperature gradient (here, temperature difference ΔT across the sample), as demonstrated in Fig. 5.21. In the same manner as in the previous sections, the SSE voltage V_{sse} is defined as half the height of the thermal voltage hysteresis loop $V_{\mathrm{sse}} = V_{\mathrm{therm.}}^{\mathrm{sat.}}/2$.

In the case of the ultrafast SSE measurements, the very same YIG/$Cu_{1-x}Ir_x$ samples were irradiated by linearly polarized femtosecond laser pulses emitted by a Ti:sapphire laser oscillator (energy of 2.5 nJ; 10 fs pulse width; center wavelength of 800 nm, which corresponds to a photon energy of 1.55 eV; repetition rate of 80 MHz). Due to an electronic band gap of 2.6 eV [235], YIG is transparent to the wavelength of the used light. The pulses are, nevertheless, partially (approximately 50 %) absorbed by the electron system of the alloy, resulting in a non-equilibrium distribution of electrons. According to the current

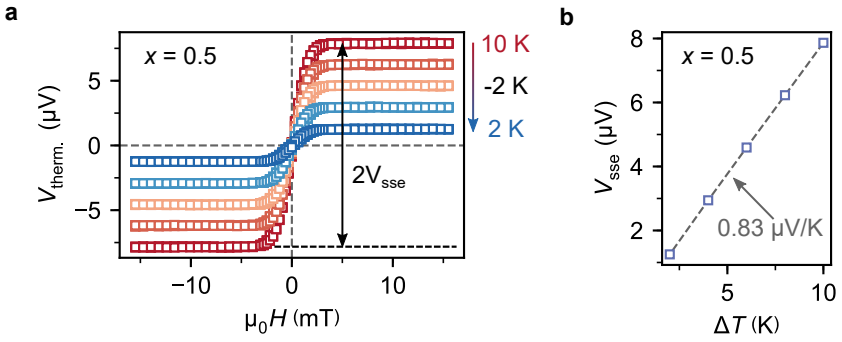

Figure 5.21: (a) DC SSE hysteresis loops obtained for varying temperature differences ΔT applied to YIG/$Cu_{0.5}Ir_{0.5}$/AlOx using the setup schematically shown in Fig. 5.19a. (b) V_{sse} obtained from the hysteresis loops in (a) as a function of ΔT. From the slope of a linear fit, the SSE coefficient is determined. Errors are smaller than the symbol size.

understanding of the effect [o12], this photoexcitation induces an additional, incoherent spin pumping process, providing the SSE on ultrafast time scales. To be more precise, the photogenerated carriers (hot electrons above the Fermi level) get multiplied during the thermalization process by electron-electron scattering, which entails enhanced rates for conduction electrons scattering off the FMI/NM interface. As stated by the theoretical model elaborated in Ref. [o12], this results in an increased random torque that is exerted on the YIG surface magnetic moments, whose rectified component yields the ultrafast transfer of spin angular momentum across the YIG/metal interface. Assuming the validity of the interfacial SSE model established by Adachi *et al.* [153], the intrinsic time scales of this new spin pumping scheme are so short such that the time-dependent spin-current density follows the quasi-static relationship

$$j_{\mathrm{s}}(t) = \zeta_{\mathrm{int.}} \cdot \left[T^{\mathrm{N}}(t) - T^{\mathrm{F}} \right]. \tag{5.5}$$

Here, $\zeta_{\mathrm{int.}}$ is the SSE coefficient of the interface, whereas $T^{\mathrm{N}}(t)$ gives the mean conduction electron temperature in the NM, whose definition can also be extended to the excitation period [o12]. T^{F}, however, describes the average magnon temperature in the FMI [14], which is only weakly affected during the experiment [o12]. In the NM layer, the sub-picosecond spin current j_{s} produces a transversal, sub-picosecond charge current by means of the ISHE. The entailed electric field yields the emission of an electromagnetic pulse into the optical far-field with a spectrum extending into the terahertz (THz) range. This THz pulse is sampled using a standard electrooptic detection scheme, making use of a ZnTe detection crystal of 1 mm thickness [236]. Eventually, the total magnetic contribution of the THz signal waveform S is determined by computing the root mean square (RMS) of

the difference of THz signals obtained for positive and negative magnetic fields.
For a more detailed insight into the THz SSE mechanism, which has been investigated in the doctoral studies of Tom Seifert at the Fritz Haber Institute, the author would like to refer the interested reader to Ref. [o12]. Please note, however, the following arguments with regard to the exclusion of alternative explanations for the emission of the THz pulse. Firstly, unlike previous observations made for semiconductor systems [237], the polarization of the pumping laser pulse (linear or circular) does not have a notable impact on the emitted THz waveform. This allows one to exclude a dominant role of a potential optical orientation (pumped spin-polarization) in the metal layer. Secondly, the THz signal amplitude was found to reflect the YIG magnetization rather than depending on the external magnetic field strength [o12]. Therefore, the Nernst effect [130] can also be excluded as a significant contribution to the emitted THz pulse.
Taken all together, the irradiation of FMI/NM systems by short laser pulses induces a thermally induced flow of spin information on the femtosecond time scale and thus joins the ranks of spin current generation schemes. Among others, the optical excitation of spin currents offers the striking benefit, in terms of experimental throughput, of contact-free measurements of the inverse spin Hall effect without the need for (time) expensive microstructuring of samples. Furthermore, the all-optical generation as well as detection of ultrafast electron spin currents [204, 238] developed as key requirements for the successful transfer of spintronic concepts into the THz range, providing a route towards ultrafast data processing [239].

5.3.2 Results and discussion

In Fig. 5.22, DC SSE hysteresis loops and corresponding THz SSE signals measured for the investigated YIG/$Cu_{1-x}Ir_x$/AlOx samples are directly compared. The Ir concentration x varies from a Cu-rich to an Ir-rich regime in ascending order. Considering first the results of the DC SSE measurement (Fig. 5.22a-f), the temperature gradient was fixed by a constant temperature difference $\Delta T = 10\,\mathrm{K}$ between sample top and bottom (base temperature of $T = 288.15\,\mathrm{K}$). In the Cu-rich phase (small x), one can observe an initial increase of the spin Seebeck voltage with increasing Ir content, exhibiting a maximum at $x = 0.3$. Intriguingly, upon further increasing x, the hysteresis height and hence V_{sse} diminishes again. Quantitative information on this behavior is provided by the spin Seebeck coefficient $\zeta = V_{\mathrm{SSE}}/\Delta T$, which is extracted as the slope of linear fits applied to $V_{\mathrm{sse}}(\Delta T)$ (see Fig. 5.21b). The respective values of ζ are stated in the single graphs of Fig. 5.22a-f, but also plotted as a function of x in Fig. 5.23a. The profile of the concentration dependence implies a maximum of ζ in the range from $x = 0.3$ to 0.5. Therefore, the first crucial result of this study is the fact that the strongest spin Hall effect is obtained in an alloying regime

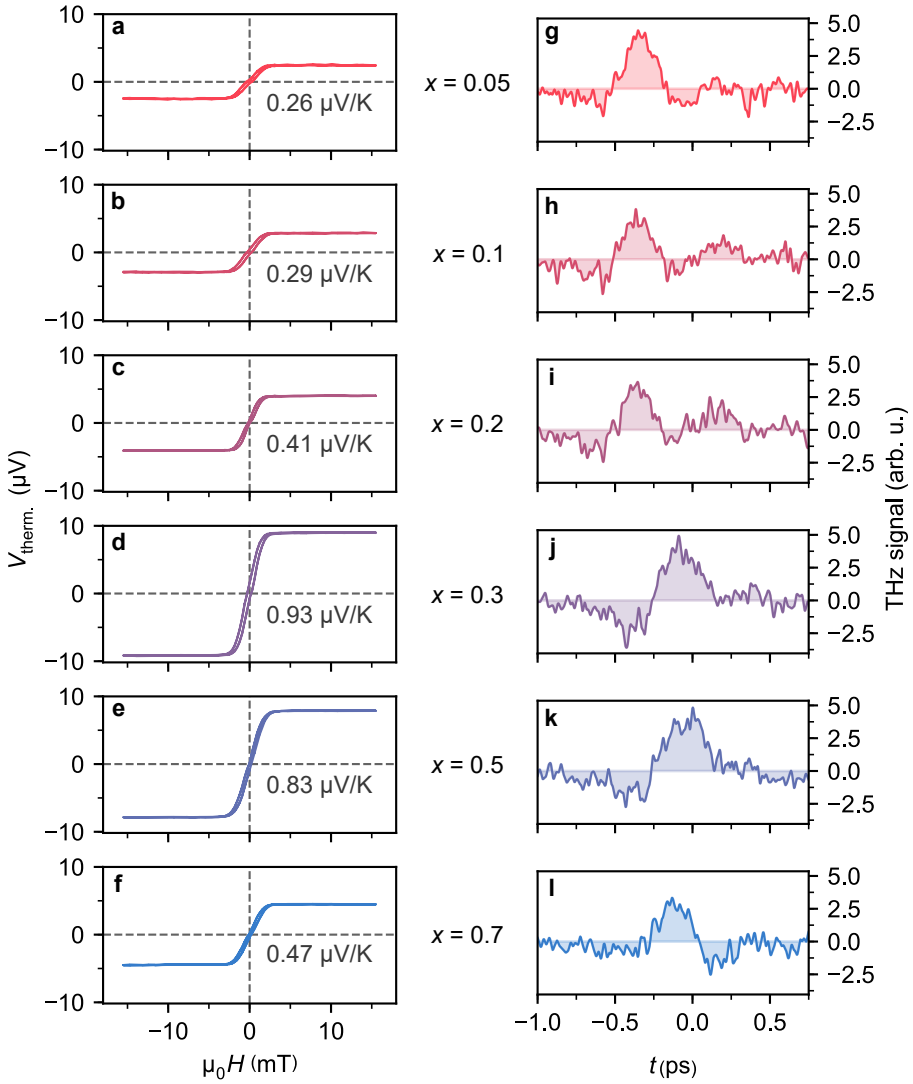

Figure 5.22: (a)-(f) Thermal voltage hysteresis loops obtained for DC measurement in YIG/$Cu_{1-x}Ir_x$/AlOx stacks with increasing Ir concentration x. Here, the temperature difference ΔT between sample top and bottom was fixed at $\Delta T = 10\,\mathrm{K}$. (g)-(l) Equivalent THz SSE signals (difference of THz pulses measured for positive and negative magnetic field) emitted from the very same samples used in (a)-(f). The shaded area signifies the evaluated strength of the signal. Adapted from [o7].

that is far beyond dilute doping and has been neglected before [230]. A further property that characterizes the alloy is its electrical resistivity $\rho = \sigma^{-1}$, which has been recorded simultaneously during the measurements and is further plotted in Fig. 5.23a. Generally, a similar trend for ρ as a function of x is observed as compared to the DC SSE signal with a

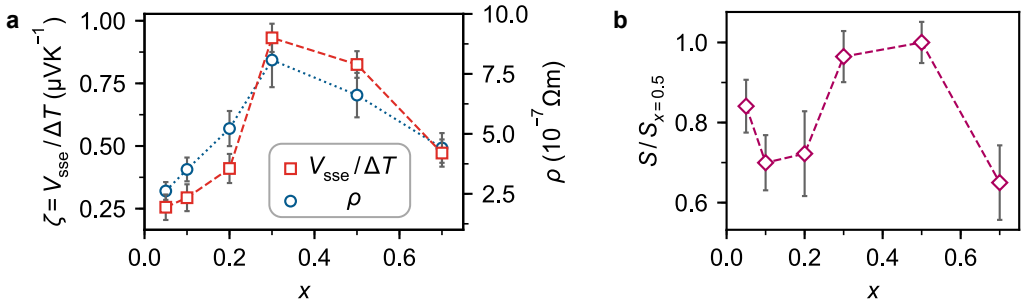

Figure 5.23: (a) SSE coefficient $\zeta = V_{\mathrm{SSE}}/\Delta T$ (red squares) and resistivity σ^{-1} (blue circles), and (b) magnetic contribution S to the THz signal (root mean square of measured pulse) as a function of Ir content x. Error bars include the standard error of the mean (voltage, resistance, signal-to-noise ratio of THz pulse) as well as inaccuracies in the set temperature difference and metal volume determination, respectively. Adapted from [o7].

maximum between $x = 0.3$ to $x = 0.5$. For different alloys, e.g. CuPt [233], the resistivity maximum has been observed for an alloy composition with equal shares of the two distinct normal metals ($x = 0.5$), which signifies a total miscibility of the alloy partners according to the Nordheim rule [233]. This implies, in turn, a limited miscibility of Cu and Ir in the investigated CuIr alloys, which is in agreement with available phase diagrams [240]. As a result, clustering and thus a spatial variation of the spin Hall angle in CuIr may be present, however, as stated before, a complete phase separation is not expected.

For the evaluation of the ultrafast SSE signal, THz pulses measured for positive and negative magnetic field polarization are subtracted from each other to extract the magnetic and thus spin current contribution. The THz transients shown in Fig. 5.22g-l were numerically low-pass filtered in the frequency domain by multiplying the Fourier transform of the measured signal with a Gaussian function centered at zero frequency and a full width at half maximum of 20 THz. The resultant spectrum is eventually transformed back into the time domain. A consistent time delay of the signal peaks in Fig. 5.22j-l as compared to the peaks in Fig. 5.22g-i is simply explained by the fact that the corresponding measurements were performed on two different days, implying a slight change in the setup calibration. The root mean square S of the THz signal (represented by shaded areas), is plotted in Fig. 5.23b as a function of x. After an initial amplitude drop in the Cu-rich phase (local minimum at $x \simeq 0.1$), the THz signal becomes larger with increasing Ir concentration with an indicated amplitude maximum between $x = 0.3$ and $x = 0.5$. A second reduction of the THz signal strength is observed when further increasing the Ir concentration.

As it is apparent from Fig. 5.23, the DC and THz SSE signal amplitudes reveal differences in their Ir concentration dependences. Considering in particular the Cu-rich region, the occurrence of a local minimum for the THz signal is distinct from the monotonic evolution

of the DC SSE amplitude as a function of x. To ascertain whether such a direct comparison of the bare signal amplitudes is anyway justified, the processes of generating the measured quantities (transient THz field, thermovoltage) are discussed in the following.

At first, directly behind the FMI/NM sample, the amplitude of the THz electric field emitted by the sample is described by a generalized Ohm's law, which includes the spin Hall driven conversion of a spin current into a charge current. As discussed in previous work of Seifert *et al.* [204], this law is given in the frequency domain by

$$\tilde{E}(\omega) \propto \theta_{\mathrm{SH}} Z(\omega) \int_0^{d_{\mathrm{CuIr}}} \mathrm{d}z \, j_{\mathrm{s}}(z,\omega) \tag{5.6}$$

with ω being the angular frequency. This equation is valid in the thin film limit, assuming that the NM layer is thin as compared to the wavelength and attenuation length of the THz pulse within the sample. The spin-current density in the metal film is integrated over the full thickness d_{CuIr}, incorporating spatial variations of $j_{\mathrm{s}}(z,\omega)$ due to spin relaxation processes and boundary conditions. The factor $Z(\omega)$ appearing in Eq. 5.6 can be understood as the effective impedance of an equivalent parallel circuit including the metal film ($\mathrm{Cu}_{1-x}\mathrm{Ir}_x$) as well as the surrounding half-spaces of the substrate (GGG/YIG) and air. As a result [204],

$$Z(\omega) = \left(\frac{n_1(\omega) + n_2(\omega)}{Z_0} + G(\omega) \right)^{-1}. \tag{5.7}$$

Here, n_1 and $n_2 \approx 1$ are the refractive indices of the substrate and air half-spaces, $Z_0 = 377\,\Omega$ is the vacuum impedance, and $G(\omega)$ is frequency-dependent sheet conductance of the $\mathrm{Cu}_{1-x}\mathrm{Ir}_x$ films. Bearing in mind the Drude-Sommerfeld model and considering an electron relaxation rate of 28 THz (room temperature) obtained for Cu as a lower boundary [241], $G(\omega)$ exhibits a weak ω-dependence [$G(\omega) \approx G(\omega = 0)$] in the investigated frequency range from 1 THz to 5 THz (predefined by the employed ZnTe detector crystal). More significantly however, is the fact that the mean conductance of the CuIr films ($G \approx 8 \times 10^{-3}\,\Omega^{-1}$) is small as compared to the shunt conductance ($[n_1(\omega) + n_2(\omega)]\,/Z_0 \approx 4 \times 10^{-2}\,\Omega^{-1}$). Hence, it can be safely neglected such that the alloying process affects the THz pulse amplitude only directly by means of the ISHE-induced, in-plane charge current flow within the metal layer.

The static thermovoltage of the DC SSE measurements, on the contrary, follows an expression that links it to the ISHE charge flow by a classical Ohm's law:

$$V_{\mathrm{sse}} \propto \theta_{\mathrm{SH}} R \int_0^{d_{\mathrm{CuIr}}} \mathrm{d}z \, j_{\mathrm{s}}(z). \tag{5.8}$$

Here, R is the Ohmic resistance of the metal area in between the electrode contacts, which

is directly proportional to the metal resistivity ρ in Fig. 5.23a, and $j_s(z)$ the density of the DC spin current continuously flowing. The latter depends on the SSE coefficient ζ and the temperature gradient applied to the sample. According to this equation, varying the alloy composition has an impact on the thermovoltage through both the efficiency of the spin-to-charge conversion process (i.e. θ_{SH}) and the NM resistivity, which in contrast to the THz data cannot be reasoned away. A direct comparison of DC and THz data is therefore justified only when considering the DC SSE current density $j_{sse} = V_{sse}/(\rho \Delta T)$, which is rectified by the compositional-dependent film resistivity, instead of the voltage.

On that account, the THz response S is depicted together with j_{sse} in Fig. 5.24 as a function of the Ir content x . The data reveal a remarkable agreement between the DC and THz SSE/ISHE amplitudes (within the error bars) across the full investigated range of compositions. Small discrepancies may arise from a variation of the optical absorptance of the near-infrared laser pump pulse, which is, however, expected to change monotonically as a function of x and only by a few percent [204]. First of all, this finding signifies that the ISHE retains its functionality from the DC regime at full volume with regard to THz dynamics, supporting the interpretations of previous reports [204]. Secondly, further support for rating the photoinduced emission of THz pulses by FMI/NM bilayers as an ultrafast version of the SSE is provided. As discussed in detail below, these findings moreover indicate that comparable alloy composition dependences of the spin-relaxation length (λ_{sd}) and spin-mixing conductance ($G^{\uparrow\downarrow}$) can be anticipated for DC and ultrafast spin currents.

For the analysis of the concentration dependences observed for the DC and THz SSE amplitudes (Fig. 5.24), Eqs. (5.6) and (5.8) are considered more thoroughly. According to

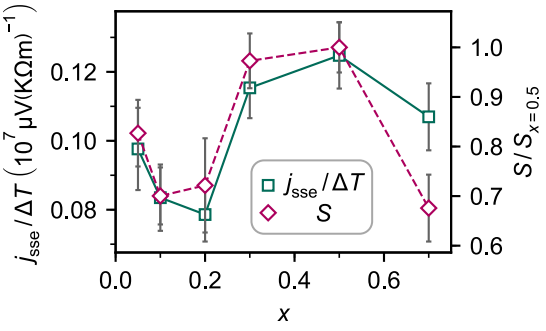

Figure 5.24: Thermal SSE charge current density (green squares) and THz signal strength (purple diamonds) as a function of the alloy composition $j_{SSE}/\Delta T$ is calculated by the voltage and resistance data displayed in Fig. 5.23a. Error bars represent the signal-to-noise ratio of the THz signal as well as errors determined by error propagation from the data in Fig. 5.23a. Adapted from [o7].

these, both the detected THz pulse amplitude and the SSE induced charge current density in CuIr are governed by two quantities: (i) the spin Hall angle θ_{SH} and (ii) the integrated spin-current density $\int_0^{d_{\mathrm{CuIr}}} \mathrm{d}z j_{\mathrm{s}}(z,\omega)$.

To address (i), the local signal minimum at the small Ir concentration of $x \simeq 0.1 - 0.15$ (dilute regime) that appears for both j_{SSE} and the THz amplitude provides crucial information as its occurrence is peculiar in nature. Instead, according to theory [242] and previous experimental works [230], one would expect a linear increase of the signal since θ_{SH} is presumed to be dominated by the skew scattering mechanism in the dilute regime. The linear dependence originates in the fact that, with increasing Ir content, an increasing density of SOI scatter centers ($\propto \rho$) is expected. However, the opposite behavior is observed, thereby suggesting that the x-dependence is governed by additional effects instead of being determined exclusively by θ_{SH}. A potential explanation can be found when examining (ii) the integrated spin-current density, more specifically the spatial variation of $\int_0^{d_{\mathrm{CuIr}}} \mathrm{d}z j_{\mathrm{s}}(z,\omega)$ that is affected by both electron momentum and spin-relaxation processes. The electron momenta and spin polarization of the diffusive spin current flowing in the metal become randomized over length scales that are specified by the mean free path ℓ and the spin diffusion length λ_{sd}. Consequently, the spin current density is reduced. Considering spin relaxation only and diverse boundary conditions (e.g. vanishing spin current at the NM/air interface), the spatial variation of the spin current density in CuIr follows [114]

$$j_{\mathrm{s}}(z) = \frac{\sinh\left[\left(d_{\mathrm{CuIr}} - z\right)/\lambda_{\mathrm{sd}}\right]}{\sinh\left[d_{\mathrm{CuIr}}/\lambda_{\mathrm{sd}}\right]} j_{\mathrm{s}}^{0}, \tag{5.9}$$

with d_{CuIr} being the thickness of the $\mathrm{Cu_{1\text{-}x}Ir_x}$ layer and $j_{\mathrm{s}}^{0} = j_{\mathrm{s}}\left(z = 0^{+}\right)$ the spin current density directly at the FMI/NM interface. The total spin current is then provided by the integrated spin current density

$$\int_0^{d_{\mathrm{CuIr}}} \mathrm{d}z j_{\mathrm{s}}(z) \propto \lambda_{\mathrm{sd}} \tanh\left(\frac{d_{\mathrm{CuIr}}}{2\lambda_{\mathrm{sd}}}\right) j_{\mathrm{s}}^{0}, \tag{5.10}$$

which directly depends on the spin diffusion length. According to the results presented by Niimi *et al.* [230], λ_{sd} varies exponentially from 30 nm at $x = 0.01$ to $\lambda_{\mathrm{sd}} \approx 5$ nm at $x = 0.12$. Regardless of this initial decay of λ_{sd} at small Ir concentration, the integrated spin current density remains approximately constant as long as the spin diffusion length exceeds the metal film thickness considering the taylor series of $\tanh(x) = x - \frac{1}{3}x^3 + \cdots$. In the Ir-rich phase (large x), λ_{sd} presumably saturates and converges to a finite value, which again results in a constant value of the total spin current amplitude. A significant decline of the integrated spin current density however, is observed for the intermediate region, where the spin diffusion length becomes of the order of the film thickness ($\lambda_{\mathrm{sd}} \approx d_{\mathrm{CuIr}}$).

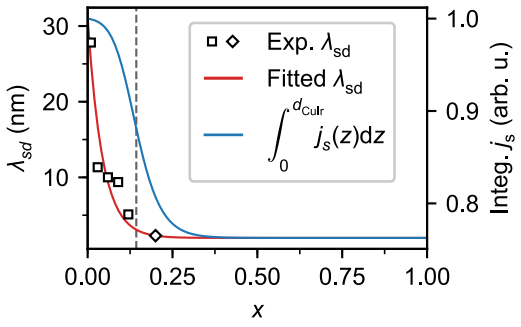

Figure 5.25: Spin diffusion length λ_{sd} (data points and red line) and integrated spin current density $\int dz j_s(z)$ (blue line) as a function or Ir concentration x. The experimental data points are extracted from Ref. [230] (black squares) and Ref. [243] (black diamond), of which the latter uses CuIr films deposited in the same chamber as in this work. At higher x, λ_{sd} is assumed to converge to a constant value. The dashed line signifies the Ir concentration, at which the integrated spin current density experiences half the decline ($x \simeq 14.33\,\%$).

Graphically, this is demonstrated in Fig. 5.25, which shows both λ_{sd} and $\int dz j_s(z)$ as a function of x. With this, on can understand the local signal minimum at small x as the spin-relaxation induced reduction of the total spin flow counteracting the presumably linear increase of θ_{SH}. On top of that, the similar trends observed for DC and THz SSE signals can be interpreted in terms of comparable concentration dependences of λ_{sd} in the DC regime and for THz dynamics. This assumption appears reasonable considering that spin-dependent and momentum scattering rates occur on the same time scale [244] (e.g. $1/36\,\text{fs} \approx 28\,\text{THz}$ for Cu [241]), which exceeds the covered bandwidth in this experiment.
Please note that the factor j_s^0 in Eq. 5.10, i.e. the spin current density at the FMI/NM interface triggered by the thermal spin pumping process, implicitly includes the spin mixing conductance $G^{\uparrow\downarrow}$, which quantifies the spin transmissivity of the interface. With regard to the DC spin Seebeck signal, an effective spin-mixing conductance $G^{\uparrow\downarrow}_{\text{eff}}$ must be considered due to the fact that the spin-accumulation in CuIr at the YIG/CuIr interface induces a spin backflow via spin transfer torque (see Sec. 3.3). In the THz measurements, however, the time scale of the spin current flow is most likely too short to build up a notable spin accumulation [244]. Arguing in the same manner as for λ_{sd}, the similar trends observed for DC and THz SSE signals when varying the alloy composition suggest that the spin mixing conductance probed by the THz SSE measurements $G^{\uparrow\downarrow}_{\text{THz}}$ and the effective spin mixing conductance probed by the DC SSE measurements $G^{\uparrow\downarrow}_{\text{eff}}$ evolve similarly with x.
As mentioned before, the integrated spin current density is influenced by momentum scattering in addition to spin relaxation. The former is determining by the metal resistivity ρ depicted in Fig. 5.23a, which demonstrates that the introduction of impurities and lattice

defects via alloying yields enhanced momentum scattering rates. When assuming that the latter increases more rapidly in the dilute phase as compared to θ_{SH}, this can be thought of as a further explanation for the local signal minimum near $x \approx 0.2$.
Finally, a brief comment is given on the subsequent development of the spin signal as a function of x. The initial increase of S and j_{sse} in the concentrated phase ($x \geq 0.2$) can be explained by a further increase of the extrinsic ISHE due to atomic disorder [232], i.e. an increase of θ_{SH}. On top of which, intrinsic ISHE contributions most likely become of importance, being mindful of the sizable intrinsic spin Hall effect of pure Ir [61, 67]. Quantifying the intrinsic ISHE requires thorough knowledge of the relativistic electron band structure, which can be obtained by calculations based on the tight-binding model [61] or the density functional theory [245], which is not done here. Ultimately, the decrease of j_{sse} and the THz Signal at $x = 0.7$ may be attributed to a loss of atomic disorder and hence a decrease of the extrinsic ISHE effect.

5.3.3 Conclusion

To conclude, the efficiency of the spin Hall driven spin-charge interconversion process in binary copper-iridium alloys has been investigated as a function of the alloy composition. In addition, the results obtained for steady-state and THz spin currents were compared. A clear maximum of the spin Hall effect is observed for alloys of about 40 % Ir concentration, which is far above the previously studied dilute doping regime. With regard to the different spin current generation schemes, distinct concentration dependences are obtained for the THz signal strength S and the DC spin Seebeck voltage, which is the often considered quantity in DC spin Seebeck measurements. Very good qualitative agreement is found when comparing the THz signal with the DC spin Seebeck current j_{sse}. This is well understood within the given model of THz emission and, furthermore, supports the interpretation of the photoinduced emission of THz pulses from FMI/NM systems as being an ultrafast version of the spin Seebeck effect. The results ultimately show that adjusting the spin Hall effect by alloying yields an unexpected, non-monotonic alloy composition dependence, which nevertheless evolves equally in the DC and THz dynamics regime. As a final remark, these findings signify that the large spin Hall effect in CuIr can be used for spintronic applications transferred to ultrafast time scales.

6 Active manipulation of spin signals from spin transport in magnetic insulators

In the last section of the previous chapter, it has been demonstrated that the efficiency of spin-charge interconversion in a binary alloy can be adapted by altering the alloy composition. While this principally allows one to customize both SHE and ISHE depending on the application requirements, this approach is infeasible in terms of real-time modulation. To address this subject, different approaches to achieve an active manipulation of spin signal generation or detection are presented in the following chapter.

To begin with, ferromagnetic resonance spin pumping measurements are performed in a spin valve like structure including a ferrimagnetic insulator, an antiferromagnetic insulator and eventually a ferromagnetic metal. A complex voltage signal is detected in the latter, which includes two different contributions, of which the spin transport signal depends on the relative alignment between the ferrimagnet's and ferromagnet's magnetization. This alignment-dependent spin signal detection is denoted as *magnon spin valve effect*.

In a second experiment, the introduced scheme of spin current detection by a metallic ferromagnet is transferred to a non-local device structure. Similar to the previous results, the detected transport signals notably varies with the orientation of the ferromagnetic moment. Furthermore, the realized device structure implies that the effect is due to a spin-dependent SHE or ISHE.

Finally, the impact of heat and Oersted fields on magnon transport in the ferrimagnetic insulator YIG is investigated. While the additional heat applied to the system results in a modulation of the transport signal, the Oersted field yields an additional voltage contribution due to a locally altered magnon generation.

6.1 Alignment dependent spin pumping in YIG/CoO/Co

Nearly three decades ago, the discovery of the GMR effect [6, 7] marked a key moment of the investigation of information processing based on spintronic concepts. As a quick reminder, spintronics denotes the inclusion of the electron spin degree of freedom in conventional electronics, which enables the implementation of logic devices with increased speed or capacity as compared to conventional electronics [4]. In view of the general framework this thesis is settled in, this approach has been successfully expanded to *magnon spintronics*

[17], which investigates magnon based information transfer and processing.

Beyond theoretical concepts and predictions, significant progress has been reported in recent years with regard to the successful experimental implementation of magnon-based logic. It was shown, for instance, that localized Oersted fields allow one to manipulate the path of magnon propagation at a bifurcation, demonstrating a de-multiplexer like behavior [246]. The amplitude of the propagating spin wave, on the other hand, could be modified when passing through a magnonic crystal, in which magnon scattering was adjusted by the injection of magnons that cannot exit the crystal. In this manner, an active spin wave attenuation scheme comparable to the functionality of a transistor was implemented [247]. More recently, the realization of a further logic module, namely a fully functional majority gate, has been reported using two similar but distinct concepts [202, 248]. In such a multi-terminal device, due to the superposition of coherent (Ref. [248]) or incoherent (Ref. [202]) magnon spin currents, the detected output signal reflects the majority of the input states. Whereas for incoherent magnons the output level voltage is decisive, both the wave amplitude and phase can be considered in the case of coherent spin waves as information carrier. In sum, these concrete realizations of magnon logic building blocks reveal the potential of this new kind of information processing scheme. Nevertheless, they also signify the necessity for further developments such that more complex operations can be performed. This includes, amongst others, the integration of a switch-like device that enables an adjustable detection efficiency of spin current signals (electrical forwarding or suppression). Unlike the magnon transistor briefly described above, which concentrates on the modulation of magnonic spin currents in their propagation phase, such a function can principally be implemented as an immanent feature of the spin current detector, which is extremely advantageous, for example, with regard to scalability.

On that account, the alignment-dependent detection of magnonic spin currents is investigated in ferroic collinear YIG/CoO/Co structures in the subsequent section. The comparison of FMR spin pumping amplitudes obtained for parallel and antiparallel alignment of the YIG and Co magnetization reveal distinct amplitude differences of up to 120 %. Regarding the origin of this effect, the experimental results are compared to observations made in atomistic spin dynamics simulations. The work was generally inspired by the concept of magnetoresistive spin valves such that the alignment-dependent detection efficiency of magnonic spin currents is referred to as *magnon spin valve effect* in the following.

The experiment has been conceptualized and performed together with the groups of Prof. Dr. U. Nowak (University of Konstanz) and Prof. Dr. E. Saitoh (Tohoku University, Sendai, Japan). The experimental work was mainly conducted in the laboratories of Prof. Saitoh during a guest research stay of Prof. Dr. M. Kläui, F. Fuhrmann and the author in Sendai, Japan, with the findings having been published in Ref. [o9].

6.1.1 Experimental details

The basic idea of the experiment as well as the sample layout are illustrated in Fig. 6.1a and Fig. 6.1b, respectively. Motivated by well-known magnetoresistive spin valve concepts (e.g. giant magnetoresistance (GMR) [6, 7]), the experiment primarily targets the question whether similar effects can be expected for the propagation or detection of magnon spin currents. Therefore, spin transmission and detection is investigated in respective multilayer systems, whose single components are able to generate, mediate and eventually detect spin currents. To be more specific, the spin current source is provided by a YIG film that is driven into ferromagnetic resonance by means of microwave irradiation. Due to the spin pumping effect (see. Sec. 3.3), the coherent rotation of the YIG magnetization emits a pure spin current into an adjacent CoO layer. The cobalt monoxide is an antiferromagnetic insulator (AFMI), which, as already briefly discussed in Sec. 5.2, forwards the pumped spin current [118–120, 122, 213] by either diffusive AFMI magnons [215, 216] or evanescent modes [217]. Besides decoupling of the ferromagnets, the choice of an AFMI as second layer has several reasons: (i) To guarantee purely magnonic spin flow until the interface to the second ferromagnet, spin transmission by conduction electrons must be forbidden (ii) AFMI magnons mediate oppositely polarized spin currents with equal probability (see discussion later) (iii) The antiferromagnetic order introduces exchange biasing of the second

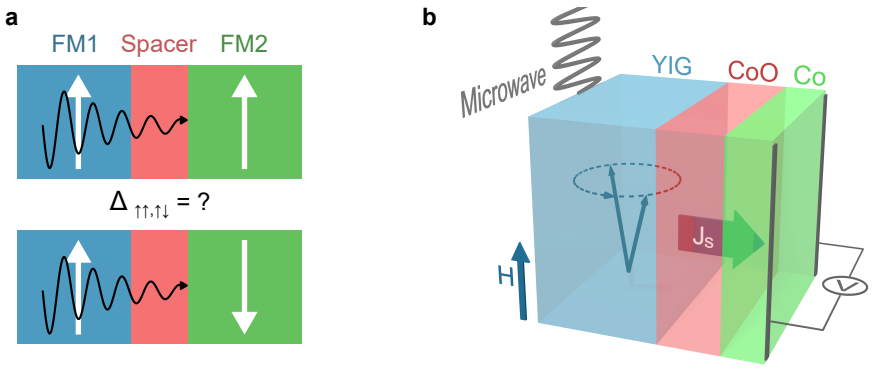

Figure 6.1: (a) Fundamental idea of the experiment, in which it shall be investigated whether the propagation or detection of magnonic spin currents is notably affected by the magnetic configuration of a spin-valve like structure. (b) Sample layout and measurement scheme implemented. By means of microwave induced ferromagnetic resonance, the rotating magnetization of the insulating ferrimagnet YIG emits a pure magnonic spin currents into the insulating antiferromagnet CoO via the spin pumping mechanism. The spin currents propagates and eventually enters the metallic ferromagnet Co, in which it is converted to a detectable voltage signal by means of the inverse spin Hall effect. Partly adapted from [o9].

ferromagnet. Eventually, the second ferromagnet in the investigated stack is the metallic ferromagnet cobalt, which acts as the active switchable layer and simultaneously is used for spin current detection. As previously reported [249, 250] and demonstrated in Sec. 5.2, magnetically ordered system as well exhibit the SHE/ISHE and thus enable spin-charge interconversion. The earlier mentioned exchange bias effect introduces both a unidirectional and uniaxial anisotropy, which shift and simultaneously broaden the magnetic hysteresis of Co [30, 251]. This is of significance, as the enhanced coercivity allows one to perform spin pumping measurements with parallel and antiparallel alignment of YIG and Co at the YIG FMR resonance field, which premises $H_{\mathrm{c}}^{\mathrm{Co}} > H_{\mathrm{FMR}}^{\mathrm{YIG}}$. Measurements revealed that for a good signal-to-noise ratio a minimum frequency of 4.5 GHz and thus $H_{\mathrm{FMR}}^{\mathrm{YIG}} \gtrsim 800\,\mathrm{Oe}$ (at $T = 120\,\mathrm{K}$) is required, which is impossible to achieve for unbiased Co thin films.

Regarding sample fabrication, single crystalline YIG of $d \approx 5\,\mu\mathrm{m}$ thickness was grown on a GGG (111) substrate via liquid phase epitaxy. To ensure equal bulk properties of the spin source, the YIG was cut into samples of size $2\,\mathrm{mm} \times 3\,\mathrm{mm}$. The YIG surface was further optimized regarding its roughness by means of a rapid thermal annealing process previous to the growth of the CoO layer (see App. C). Terrace like, smooth YIG surfaces with a root-mean-square roughness $\sigma_{\mathrm{rms}} \simeq 1.11\,\text{Å}$ were obtained, as evaluated by atomic force microscopy (see Fig. 6.2a,b). Afterwards, CoO was deposited by means of reactive magnetron sputtering from an elementary Co target in an Ar/O atmosphere, using a commercial QAM-4-STSCP (ULVAC Inc.) sputtering system. During the deposition, the substrate temperature was kept constant at 450 °C. To evaluate the the film quality, X-ray diffraction measurements were performed, as depicted in Fig. 6.2c,d. Interestingly, the XRD data reveal that for CoO, which was grown on an unannealed (as-is) YIG sample, the CoO (200) reflex appears in the spectrum, whereas CoO growth along the [111] direction is dominant on top of the annealed YIG. This further emphasizes the significance of the annealing process, as the magnetic moments in CoO align ferromagnetically within the antiferromagnetically (111) planes. Hence, the surface termination of CoO is compensated or uncompensated depending on the morphology of the YIG underneath, which may become of significance. Finally, the Co top layers were grown in-situ at room temperature by non-reactive Ar sputtering from the very same Co target. For the experiment, thickness-combinations of $d_{\mathrm{CoO}}/d_{\mathrm{Co}} = 2\,\mathrm{nm}/4\,\mathrm{nm}, 3\,\mathrm{nm}/4\,\mathrm{nm}$, and $5\,\mathrm{nm}/6\,\mathrm{nm}$ were realized, which due to simplicity are referred to as sample I, II, and III in the following.

The thermoelectric and FMR spin pumping measurements presented hereafter were performed using the setups described in Sec. 4.3.1 and Sec. 4.3.3, respectively. Generally, measurements were initialized by cooling down the samples with maximum field (either direction) applied to ensure the formation of uniform antiferromagnetic order of the CoO and thus exchange bias at low temperatures. Subsequently, measurements were performed at

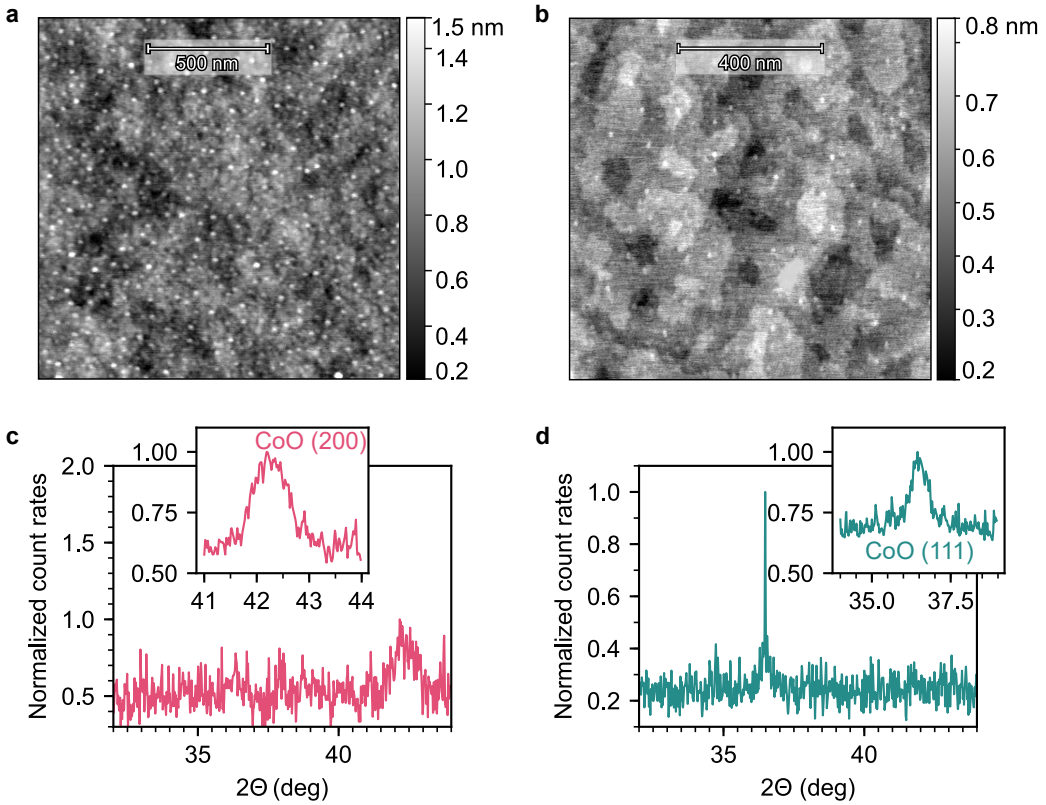

Figure 6.2: (a),(b) Atomic force microscopy data of liquid phase epitaxy grown YIG (a) directly after the growth process and (b) after modulating the YIG surface structure by means of rapid thermal annealing. (c),(d) X-ray diffraction data of YIG (5 µm)/CoO (15 nm) with the CoO being grown on (c) the untreated YIG surface and (d) a YIG sample that experienced rapid thermal annealing. While in the case of (c) YIG as-is CoO growth in the [200] direction is preferred, the (111) surface is observed for the annealed sample. The insets show more detailed scans of the respective peaks. Adapted from [o9].

fixed, increasing temperatures. High temperatures far above 300 K were avoided to prevent undesired degradation of the sample stack (especially of the metallic Co layer). For the spin-thermoelectric measurements, the samples were clamped in the sample holder depicted in Fig. 4.7c, applying the measurement schemes described in the previous result sections and in Sec. 4.3.1. In the case of spin pumping experiments, the samples were attached to the waveguide shown in Fig. 4.9. Implementing mainly the AC measurement scheme described in Sec. 4.3.3, pulsed microwaves were injected into the CPW, while a lock-in amplifier and a power sensor detected the ISHE voltage response and the microwave power absorbed by the sample, respectively.

6.1.2 Results and discussion

Sample characterization

To begin with, it needed to be verified whether the magnetic properties of the sample stacks fulfill the requirements for FMR spin pumping measurements with parallel and antiparallel alignment of YIG and Co at a sufficiently high signal-to-noise ratio. As already mentioned earlier, this especially required large coercive fields of Co ($\mu_0 H_c^{\mathrm{Co}} > \mu_0 H_{\mathrm{FMR}}^{\mathrm{YIG}} \gtrsim 80\,\mathrm{mT}$), while the YIG inevitably switches at low fields. In a first step to determine the magnetic characteristics of the stacks, SQUID magnetometry measurements have been performed, as shown in Fig. 6.3a. One clearly recognizes the switching of the YIG layer at low fields, whereas no distinct switching of the Co at higher fields is recognizable. This can be easily understood considering that the SQUID is sensitive to the total magnetic moment of the sample and the fact that the magnetic volume of the 5 µm thick YIG layer by far exceeds the one of the thin (4 nm to 6 nm) Co layers. To nevertheless obtain information about H_c^{Co}, spin-thermoelectric measurements have been performed. In the selected geometry in the experiment, the anomalous Nernst effect in Co is sensitive to its in-plane magnetization component and hence allows one to infer information on the coercive fields. A typical thermovoltage hysteresis loop is shown in Fig. 6.3b, recorded for sample I at a temperature of $T = 120\,\mathrm{K}$. The data reveal a clear switching of the thermovoltage at field values of $\mu_0 H_c^+$ [$\mu_0 H_c^-$] $\simeq 125\,\mathrm{mT}$ [$-97\,\mathrm{mT}$] (asymmetry due to exchange bias of CoO/Co), far above the YIG magnetization switching observed by SQUID in Fig. 6.3a. This signifies that the signal is exclusively given by the ANE of Co, as a thermal spin current of the YIG film generated by the SSE should invert its polarization and thus induce a voltage level change when the YIG magnetization is reversed. Such a signal change is not distinguishable within the experimental resolution, which is contrary to previous reports [213]. This might originate from different CoO structures grown on different YIG films (polycrystalline vs. single crystalline) [214] or may be explained by the reduced spin-to-charge conversion efficiency of ISHE in Co as compared to the otherwise employed Pt. Nonetheless, the absence of the SSE signal rules out pinholes in the CoO layer. The ANE origin of the thermovoltage is further corroborated by a similar signal observed for a GGG/CoO (2 nm)/Co (6 nm) reference sample, see Fig. 6.3c, in which potential contributions from a magnetic substrate are not present. The smaller switching fields can be understood considering the changed thickness ratio of AFMI/FM. Furthermore, the hysteresis loop in Fig. 6.3b exhibits an enhanced squareness with $V_{\mathrm{ANE}}^{\mathrm{H=0}}/V_{\mathrm{ANE}}^{\mathrm{sat}} \simeq 0.95$, signifying that Co switches without extensive formation of magnetic domain structures.

Having established that, in this case, spin-thermoelectrics reveals exclusive information on the magnetic properties of Co, temperature-dependent measurements were performed to

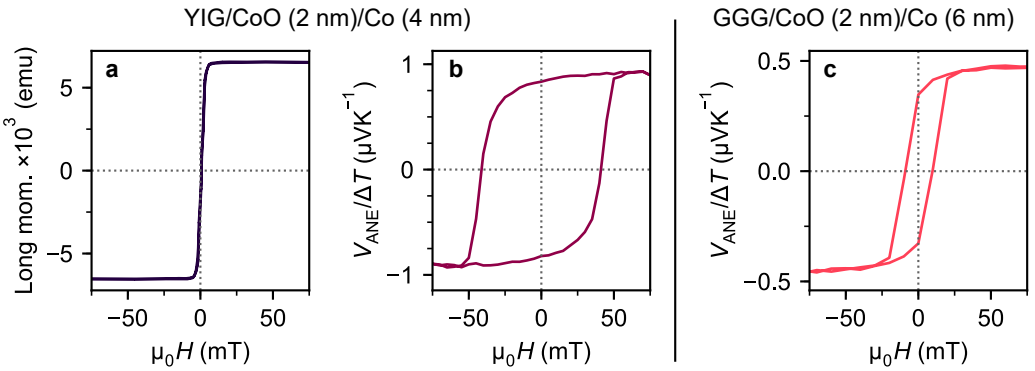

Figure 6.3: (a) SQUID magnetometry and (b) anomalous Nernst effect hysteresis loops obtained for sample I: YIG (5 µm)/CoO (2 nm)/Co (4 nm) at (a) $T = 300\,\mathrm{K}$ and (b) $T = 280\,\mathrm{K}$. (c) Anomalous Nernst effect hysteresis loop obtained for a GGG/CoO (2 nm)/Co (6 nm) reference sample without magnetic base layer.

identify the temperature region in which $H_\mathrm{c}^\mathrm{Co} > H_\mathrm{FMR}^\mathrm{YIG}\,(4.5\,\mathrm{GHz})$ is fulfilled. Exemplary ANE hysteresis loops obtained for sample I at three distinct temperatures are depicted in Fig. 6.4a-c, including solid lines marking the corresponding resonance field for $f_\mathrm{FMR} = 4.5\,\mathrm{GHz}$. As can be seen, at $T = 280\,\mathrm{K}$ the coercive fields are smaller than the resonance field value, while the opposite behavior is observed at the lower temperatures. More detailed information is contained in Fig. 6.4d,e, in which both the coercive field values $H_\mathrm{c}^\pm$ and the exchange bias field H_ex are plotted as a function of temperature. With regard to the former, the $H_\mathrm{c}^\pm$ amplitudes remain constant until $T \simeq 250\,\mathrm{K}$, followed by a monotonic increase with further decreasing temperature. Similar behavior is observed for H_ex, which initially is zero and then starts to increase. As mentioned before, this effect is to be explained by the antiferromagnetic order establishing in the CoO thin film (bulk Néel temperature $T_\mathrm{N} = 293\,\mathrm{K}$ [27]) and thus exchange bias. Bearing in mind the discussion in Sec. 5.2, the data reveals a blocking temperature $T_\mathrm{B} \approx T^* \approx 250\,\mathrm{K}$ for sample I.

Finally, the hysteresis height and hence the ANE amplitude is plotted as a function of temperature in Fig. 6.4f, revealing an initial increase with increasing temperature. The maximum at $T = 250\,\mathrm{K}$ is an artifact due to the usage of the thermal grease *Apiezon N*, whose specific heat exhibits a distinct maximum in that temperature region [201]. The actual temperature profile is assumed to be rather flat in between $T = 200\,\mathrm{K}$ and $T = 300\,\mathrm{K}$. $H_\mathrm{c}^\pm$ and H_ex are not supposed to be affected by the enhanced thermal conductivity.

Considering that the magnon spin valve effect is probed via ferromagnetic resonance spin pumping, further sample characterization by FMR measurements was carried out, as shown in Fig. 6.5. Figure 6.5a shows typical power absorption spectra obtained for sample I, II and III for microwave irradiation at a frequency of 4.5 GHz and an applied microwave power

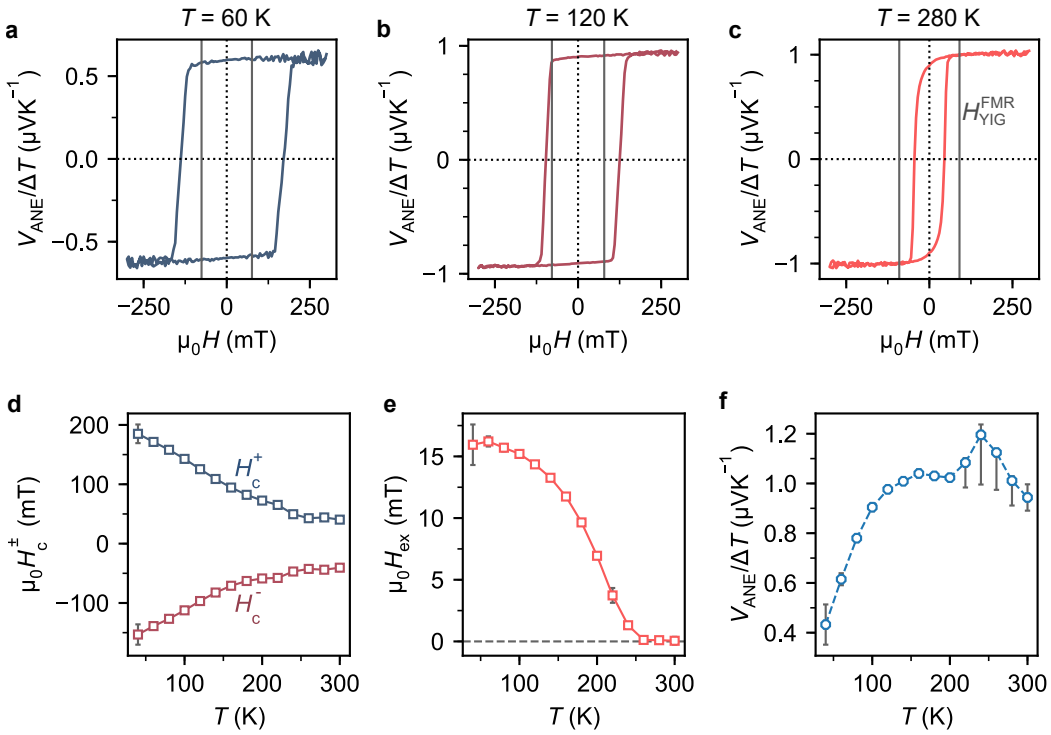

Figure 6.4: (a)-(c) Anomalous Nernst effect hysteresis loops obtained for sample I [YIG (5 µm)/CoO (2 nm)/Co (4 nm)] at different temperatures, field cooled at $\mu_0 H_{\mathrm{ext}} = +9\,\mathrm{T}$. The solid vertical lines mark the ferromagnetic resonance field of YIG for microwave irradiation at a frequency of $f_{\mathrm{FMR}} = 4.5\,\mathrm{GHz}$. (d) Coercive (switching) fields and (e) exchange bias field of Co as a function of temperature. (f) Amplitude of anomalous Nernst effect as a function of temperature. Error bars represent the standard error of the mean as well as estimated systematic errors. Partly adapted from [o9].

of 23 dBm (sample temperature $T = 120\,\mathrm{K}$). These values correspond to the settings used for most of the spin pumping measurements. While for sample I and II equal magnetic resonance fields are observed, a slight negative shift of H_{FMR} appears for sample III, which may be explained by a misalignment of the sample in the setup. To verify that the observed absorption line indeed corresponds to the ferromagnetic resonance of the YIG film, the resonance frequency f_{res} was measured as a function of field at room temperature for sample III (Fig. 6.5b). The respective fit of the Kittel formula (Eq. 2.35) yields a saturation magnetization of $M_{\mathrm{s}} = 149.83\,\mathrm{kA\,m^{-1}}$. This value is slightly above the bulk value for YIG [25], however, the saturation magnetization of Co is roughly one order of magnitude larger [24]. At a fixed frequency, the Co resonance is thus expected to appear at much lower field values. However, it could not be clearly identified in the experiment, most likely due to an enhanced Gilbert damping of the Co in the presence of exchange bias, yielding flattened

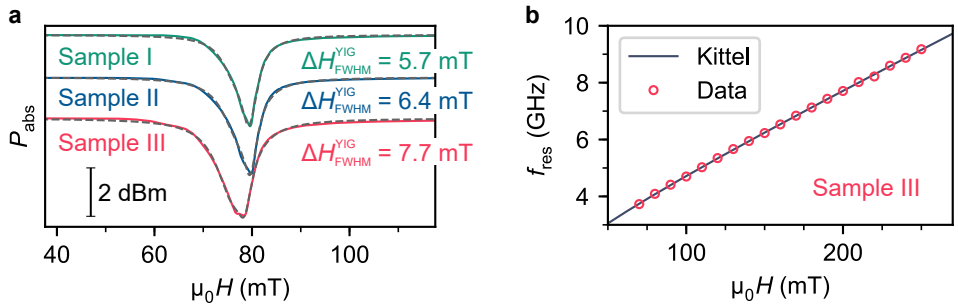

Figure 6.5: (a) Microwave absorption spectra for sample I-III, recorded for an applied microwave frequency $f = 4.5\,\mathrm{GHz}$ and power $P_{\mathrm{appl.}} = 23\,\mathrm{dBm}$ at a sample temperature of $T = 120\,\mathrm{K}$. (b) FMR dispersion relation obtained for sample III at $T = 300\,\mathrm{K}$. Fitting the data by the Kittel formula Eq. 2.35 reveals a saturation magnetization of $M_{\mathrm{s}} = 149.83\,\mathrm{kA\,m^{-1}}$. Note that error bars of f_{res} obtained from the fit routine are smaller than the symbol size. Partly adapted from [o9].

and broadened absorption peaks. As a result, the observed absorption spectrum indeed corresponds to the FMR of YIG, with the comparable resonance field values of sample I-III signifying the comparability of the YIG films with regard to their spin source properties. A remarkable feature in Fig. 6.5a is the increase of the absorption line width ΔH with increasing thickness of the CoO/Co, which is interpreted as an enhanced spin absorption by the latter and thus a larger damping of the YIG magnetization precession [11].

Note that when considering the absorption spectra in more detail, one recognizes that these are not provided by a single magnon mode but by several modes excited in the crystal. While this circumstance does not impair the previously drawn conclusions, it will become of significance for the discussion further below.

Ferromagnetic resonance spin pumping in YIG/CoO/Co

Based on the sample characterization results [determination of YIG resonance and temperature region with $H_{\mathrm{c}}^{\mathrm{Co}} > H_{\mathrm{FMR}}^{\mathrm{YIG}}\,(4.5\,\mathrm{GHz})$], ferromagnetic resonance spin pumping was investigated in YIG/CoO/Co as a function of the relative magnetization alignment of the YIG and Co layer. Typical results obtained for sample I are shown in Fig. 6.6, which shows field-dependent spin pumping voltages at $T = 120\,\mathrm{K}$, induced by microwave irradiation at a frequency of $f = 4.5\,\mathrm{GHz}$ and an input power of $P_{\mathrm{in}} = 23\,\mathrm{dBm} \simeq 199.52\,\mathrm{mW}$. During the measurements, specific field sweep sequences were implemented to create both parallel (top right, bottom left) and antiparallel (top left, bottom right) alignment of YIG and Co magnetization, covering all four possible configurations. The magnetization orientations of the single layers are indicated in each subgraph.

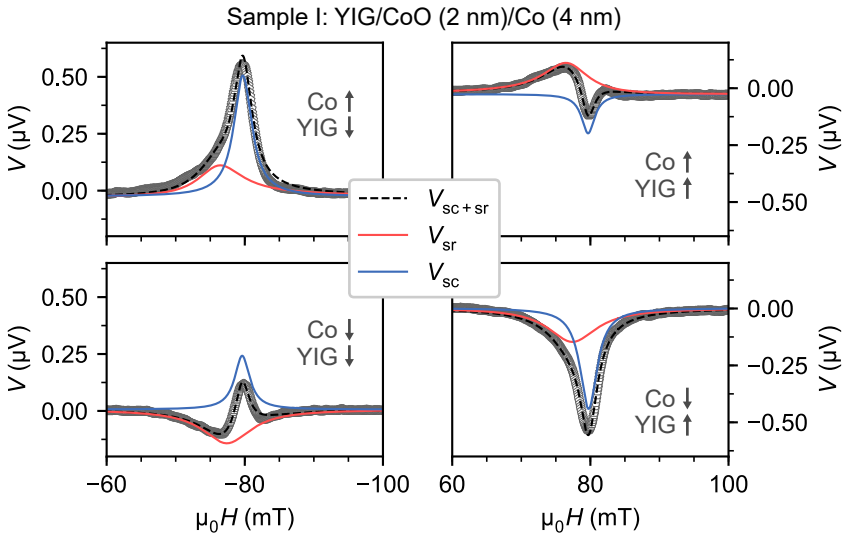

Figure 6.6: Spin pumping voltage signals as a function of field obtained for sample I ($f = 4.5\,\mathrm{GHz}$, $P_{\mathrm{appl.}} = 23\,\mathrm{dBm}$, $T = 120\,\mathrm{K}$). The magnetic configuration of the sample (parallel, antiparallel and respective polarization) is indicated by arrows in the subplots. For all cases, the total signal (data points, dashed line) is composed of two distinct signals of Lorentzian line shapes V_{sc} (blue solid line) and V_{sr} (red solid line). The sign of V_{sc} solely depends on the YIG magnetization orientation, whereas the one of V_{sr} is determined by the Co magnetization direction. Furthermore, the amplitude if the V_{sc} peak is strongly affected by the magnetic configuration of the sample ($V_{\mathrm{sc}}^{\uparrow\uparrow} < V_{\mathrm{sc}}^{\uparrow\downarrow}$), which is, in this work, referred to as *magnon spin valve effect*. Adapted from [o9].

With regard to the signal shape, a clear multi-peak voltage signal appears in the case of parallel alignment. Taking into account possible combinations of symmetric and asymmetric terms, data evaluation shows that this line shape is fitted well by two overlapping Lorentzian functions that are of opposite sign, exhibit moderately shifted peak positions as well as different line widths. At the same time, a single voltage peak with a distinct asymmetry is observed when setting antiparallel alignment of the two ferromagnets. Again, two overlapping Lorentzian functions are sufficient to fit the line shape adequately, now being of equal sign. In the subplots of Fig. 6.6, the distinct Lorentzian functions are displayed as solid lines (red and blue), while the combined signal is given by a dashed line (black). Please note that the microwave power was kept constant throughout these measurements and that the absorbed power by the sample $P_{\mathrm{abs}} \approx 48\,\mathrm{mW}$ did not alter notably (see App. C).

When comparing the four available configurations of relative magnetization alignment, one can both separate and attribute the peaks to different effects. Subject to the individual orientations of the YIG and Co magnetization, the peaks switch polarity separately and

hence can be identified as (i) the ISHE voltage of the spin current emitted by the YIG layer via FMR spin pumping (V_{sc}, blue solid lines in Fig. 6.6) and (ii) a secondary signal that solely depends on the orientation of the Co layer (V_{sr}, red solid lines in Fig. 6.6). The latter is assumed to originate from the Co layer itself, with possible explanations given by a thermally induced ANE signal due to dynamic microwave heating [252] or an AHE based spin rectification effect [107–109, 253]. In terms of the latter, the microwave driving current I_{rf} partially flows through the metallic Co layer by means of capacitive coupling. This current, in combination with the out-of-plane component of the Co magnetization precessing in the dipolar field of excited YIG magnon modes [253], results in an additional voltage drop. I_{rf} and M oscillate with the same frequency such that the spin rectification signal keeps a consistent polarity and does not average out. Although both effects are possible, the results of temperature-dependent measurements shown below suggest the SR mechanism to be dominant. In metallic ferromagnets directly driven by FMR, spin rectification yields both a symmetric and antisymmetric contribution around the resonance field:

$$\left\langle V_{\mathrm{sr}}^{\mathrm{AHE}} \right\rangle (H) = V_{\mathrm{symm.}} \frac{\Delta H^2}{(H - H_{\mathrm{FMR}})^2 + \Delta H^2} + V_{\mathrm{asymm.}} \frac{\Delta H \, (H - H_{\mathrm{FMR}})}{(H - H_{\mathrm{FMR}})^2 + \Delta H^2} \tag{6.1}$$

The asymmetric contribution originates from a phase shift between the coupled rf magnetic field of the microwave and the magnetization dynamics response [109]. Data analysis reveals that for the spin pumping data obtained here, the asymmetric term is negligible as compared to a dominating symmetric contribution and is thus neglected hereinafter. A possible explanation for the vanishing asymmetry is that the cobalt magnetization is driven off-resonance and furthermore couples towards multiple YIG magnon modes, which may lead to a weak field-dependence of the arbitrary phase between rf current and Co magnetization oscillation.

The main subject of this work is the ISHE spin detection signal induced by the spin current from the YIG layer, which can be easily distinguished from the additional stimulus generated in the Co layer, regardless its origin. The compelling observation made in this experiment is the fact that the amplitude of V_{sc} strongly depends on the magnetic configuration of the valve structure. While V_{sr} switches its polarity but otherwise retains a constant amplitude, the magnitude of V_{sc} exhibits a nearly doubled value when YIG and Co are antiparallel as compared to the parallel configuration ($V_{\mathrm{sc}}^{\uparrow\downarrow} > V_{\mathrm{sc}}^{\uparrow\uparrow}$).

Although Fig. 6.6 only shows spin pumping data obtained for sample I at $f_{\mathrm{FMR}} = 4.5\,\mathrm{GHz}$, the same qualitative behavior is observed for sample II and III and for different microwave frequencies (see App. C), which corroborates the integrity of the effect. Furthermore, when implementing a DC measurement scheme (continuous microwave irradiation instead of

pulsed microwaves), qualitative similar voltage responses are obtained, signifying that the alignment-dependent detection of spin currents is not an artifact appearing only in the AC setup (see App. C). Finally, note that changing the polarity of the external magnetic field ($\mu_0 H_{\mathrm{ext}} = \pm 9\,\mathrm{T}$) while field-cooling the sample, which as mentioned above was implemented to obtain uniform order within CoO, does not result in notable differences in both the microwave absorption and the recorded voltage line shape (see App. C). This indicates that the exchange bias field at the CoO/Co interface as well as a potential exchange spring formed at the YIG/CoO interface have negligible impact on the spin transmission across them.

Origin of V_{sc} and V_{sr} in YIG/CoO/Co

To further investigate and verify the origin of the detected signals, alignment-dependent spin pumping measurements have been repeated as a function of both temperature and applied microwave power. Considering first the temperature dependence of the signal, the respective amplitudes of $V_{\mathrm{sc}}^{\uparrow\uparrow}$, $V_{\mathrm{sc}}^{\uparrow\downarrow}$ and V_{sr} are displayed in Fig. 6.7a-c for samples I-III. While $V_{\mathrm{sc}}^{\uparrow\uparrow}$ and V_{sr} could be determined over the whole temperature range, values of $V_{\mathrm{sc}}^{\uparrow\downarrow}$ are only available up to a critical temperature $T_{\mathrm{crit.}}$. As discussed before (Fig. 6.4), for $T > T_{\mathrm{crit.}}$ the YIG resonance field is larger than the switching field of the Co layer such that parallel alignment only is possible at $H_{\mathrm{FMR}}^{\mathrm{YIG}}$. In general, this critical temperature is different for the different stack configurations studied. For the temperature region, in which antiparallel-aligned spin pumping is feasible, one always finds a larger amplitude of $V_{\mathrm{sc}}^{\uparrow\downarrow}$ as compared to the one of $V_{\mathrm{sc}}^{\uparrow\uparrow}$.

With regard to the temperature profile, the amplitude of V_{sc} generally exhibits an incipient increase with increasing temperature. For temperatures between 250 K and 300 K, signal maxima are observed for sample I and sample II. According to previous findings of Qiu *et al.* [122] and Lin *et al.* [213], this behavior can be explained by an enhanced spin conductivity of the antiferromagnetic CoO layer at its Néel temperature. In the same manner as for the IrMn thin films in Sec. 5.2, the Néel temperatures of thin CoO films T_{N} are expected to be below the bulk value of $T_{\mathrm{N}}^{\mathrm{bulk}} = 293\,\mathrm{K}$ [27] due to finite size effects. T_{N} decreases with decreasing film thickness [29, 254]. Reviewing again Fig. 6.4, the ANE measurements reveal an exchange bias blocking temperature of $T_{\mathrm{B}} \approx T^{*} \approx 250\,\mathrm{K}$ for sample I, suggesting that the phase transition occurs in between 250 K and $T_{\mathrm{N}}^{\mathrm{bulk}} = 293\,\mathrm{K}$ for this specific stack. The other multilayer stacks include thicker CoO layers such that higher T_{N} values are to be expected, which can explain the monotonic increase of V_{sc} for sample III up to 300 K.

The temperature profile of V_{sr} is significantly different to that of V_{sc}. The Co-dependent signal amplitude retains a constant value with increasing temperature before it becomes notably larger after crossing a specific temperature, revealing a nearly linear dependence.

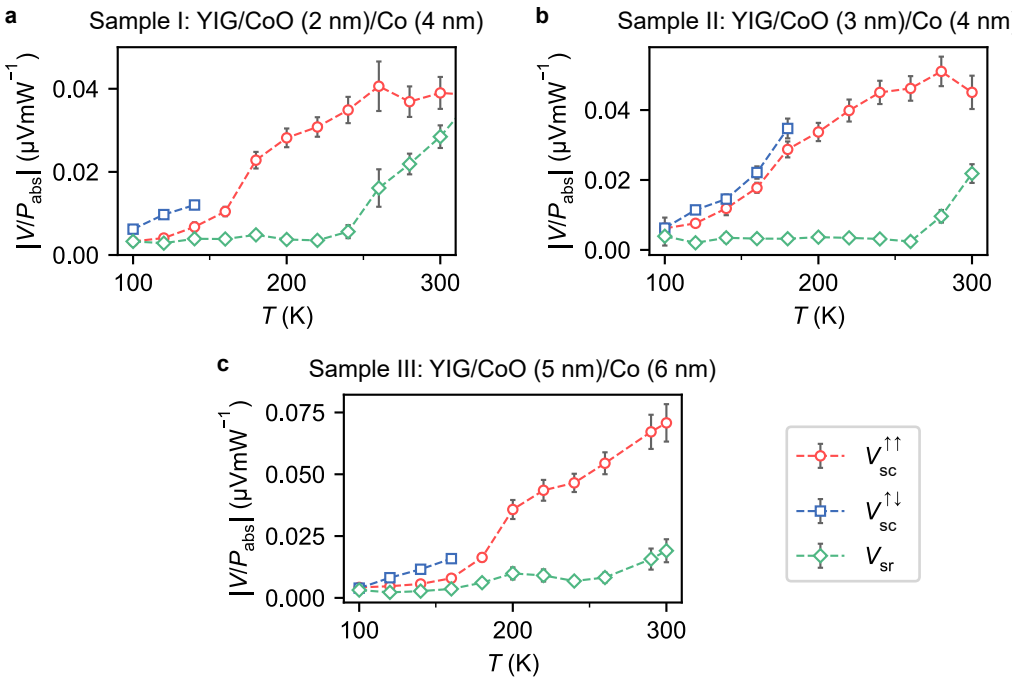

Figure 6.7: Power normalized amplitudes of $V_{\mathrm{sc}}^{\uparrow\uparrow}$, $V_{\mathrm{sc}}^{\uparrow\downarrow}$ and V_{sr} as a function of temperature for (a) sample I, (b) sample II and (c) sample III. Antiparallel alignment and thus $V_{\mathrm{sc}}^{\uparrow\downarrow}$ is observed only up to a critical, sample-dependent temperature. Below 100 K, a reduced signal-to-noise ratio hinders a clear data analysis, temperatures above 300 K were avoided to prevent sample degradation. Error bars are calculated by error propagation including errors of the sample amplitude and the absorbed microwave power. Furthermore, systematic errors estimated by the measurement device accuracy are considered. Adapted from [o9].

Depending on the sample stack, different threshold temperatures for the growth of V_{sr} are observed: with increasing CoO thickness, the temperature above which the amplitude of V_{sr} starts to increase is higher. Similar to the maxima of V_{sc} discussed above, the comparison to the spin-thermoelectric measurements shows that this threshold temperature is correlated to the blocking temperature T_{B}, above which the exchange bias induced anisotropies vanish. In view of the spin rectification mechanism, this loss of anisotropy entails a reduced Gilbert damping constant α of the Co layer such that the Co magnetization precesses at a larger cone angle [255] and hence induces a larger AHE signal. Ultimately, the sudden onset of V_{sr} corroborates the conclusion that the Co-dependent signal is not dominated by a magneto-galvanic effect, since this behavior is not expected for the ANE (e.g. Fig. 6.4f). Further information on the origin of the voltage contributions is obtained from the power dependence of the V_{sc} and V_{sr} amplitudes, as shown in Fig. 6.8. Irrespective of the implemented alignment state, the spin current transport amplitude exhibits a nonlinear power dependence. The inception of a signal saturation is noticeable at elevated microwave pow-

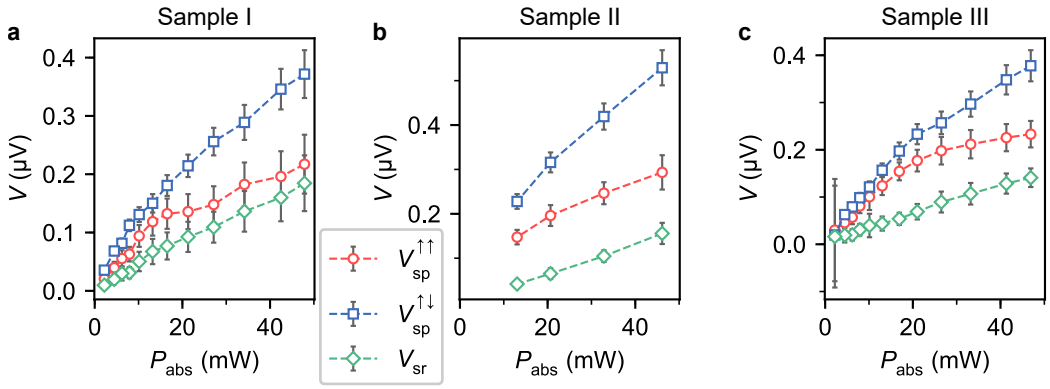

Figure 6.8: Amplitudes of $V_{sc}^{\uparrow\uparrow}$, $V_{sc}^{\uparrow\downarrow}$ and V_{sr} as a function of absorbed microwave power (a) sample I, (b) sample II and (c) sample III. Error bars are calculated by error propagation including errors of the sample amplitude and systematic errors estimated by the measurement device accuracy. Adapted from [o9].

ers, which corresponds to previously observed behavior for spin pumping in YIG/Pt structures [256]. Accordingly, V_{sc} scales with the amplitude of the spin current emitted by the YIG. The power dependence of V_{sr}, then again, does not allow for a straight-forward interpretation. According to Azevedo *et al.* [108], one expects a linear functional dependence of V_{sr} on P_{abs} as it is proportional to the dynamic field driving the Co precession. This is in line with trend displayed in Fig. 6.8, however, other possible mechanisms that also reveal a linear power dependence cannot be excluded.

With regard to the slight shift in the resonance fields of the Lorentzian functions describing V_{sc} and V_{sr}, note that this can be understood based on the underlying processes. Since spin rectification is induced by the Co magnetization precessing in the dipolar field of coupled magnon modes in the entire 5 µm thick YIG crystal, its greatest amplitude is expected at their maximum excitation [253]. The peak of V_{sc}, however, is found at the field of maximum spin current emission into the CoO by the rotating YIG magnetization and is thus dominated by the resonance at the interface. Considering potential differences between magnon modes at the surface and deep in the bulk material, the observed shift of resonance frequencies of V_{sc} and V_{sr} is not surprising.

Magnon spin valve effect

As stated above, the crucial finding of this work is the fact that the amplitude of V_{sc} strongly depends on the sample magnetization configuration. Basically, this alignment-dependent spin current detection efficiency lends itself to the implementation of a magnon spin valve. When gauging the amplitude differences between parallel and antiparallel alignment in Fig. 6.6, one extracts an effect amplitude of $\left(V_{sc}^{\uparrow\downarrow} - V_{sc}^{\uparrow\uparrow}\right)/V_{sc}^{\uparrow\uparrow} = 120\,\%$ for sample I at

$T = 120\,\mathrm{K}$. However, for the investigated structure this value is not of practical relevance considering the rather complex procedure required to obtain it: full magnetic field sweep across the resonance and fit function evaluated. In a more realistic application scheme, especially with regard to speed and the simplicity of on-chip operations, the voltage response level towards microwave irradiation would be probed at just a single fixed field value. This is illustrated in Fig. 6.9, where the voltage level directly at ferromagnetic resonance is plotted in Fig. 6.9b for repetitive back-and-forth switching of the Co magnetization direction. To do so, the external field was driven above and below the Co coercive fields $\mu_0 H_c^+ = 125\,\mathrm{mT}$, $\mu_0 H_c^- = -97\,\mathrm{mT}$) and subsequent to every switching event, the voltage response at $\mu_0 H_{\mathrm{FMR}}^{\mathrm{YIG}} = 78.8\,\mathrm{mT}$ was recorded. For sample I, an absolute voltage difference of 408 nV is obtained, which results in a total spin valve effect amplitude of

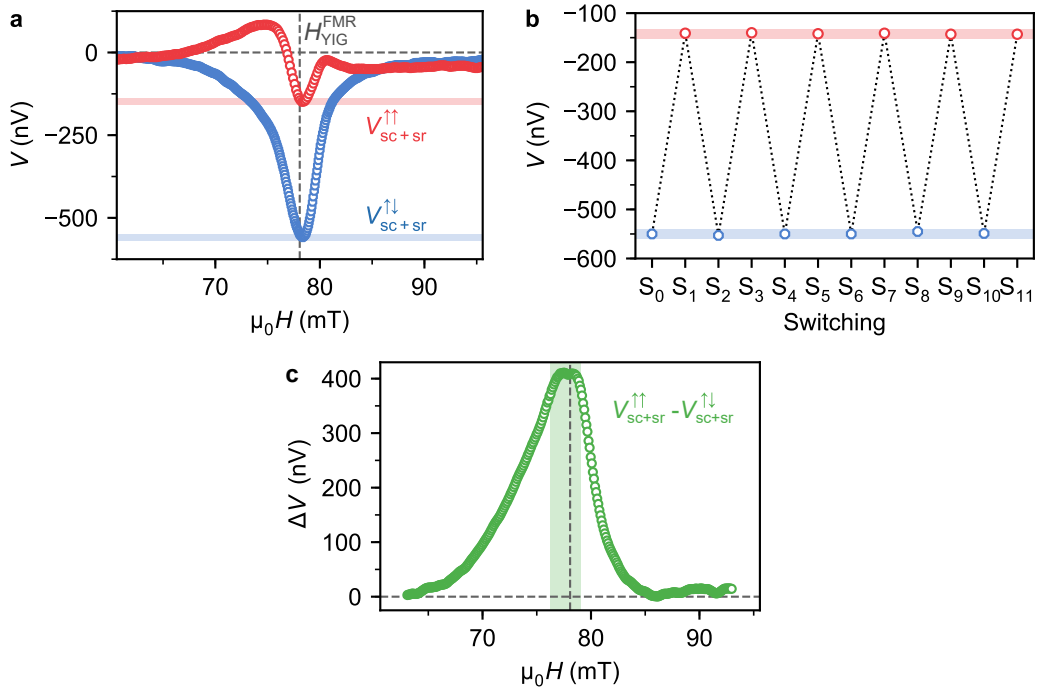

Figure 6.9: (a) Field-dependent spin pumping voltage response in sample I for parallel (red data points) and antiparallel (blue data points) alignment of YIG and Co ($f = 4.5\,\mathrm{GHz}$, $P_{\mathrm{appl.}} = 23\,\mathrm{dBm}$, $T = 120\,\mathrm{K}$). The dashed vertical line marks the ferromagnetic resonance frequency. (b) Alternating voltage levels of total signal for parallel (red data points) and antiparallel (blue data points) alignment of YIG and Co, obtained by repetitive switching of the Co layer (switching events S_i) and probing at $H_{\mathrm{FMR}}^{\mathrm{YIG}}$. The absolute voltage difference is $(408 \pm 5)\,\mathrm{nV}$, the relative change $(290 \pm 4)\,\%$. (c) Field-dependent absolute voltage difference between parallel and antiparallel state, calculated from (a). The shaded areas in (a)-(c) mark a 10 % voltage tolerance level. Partly adapted from [o9].

$\left(V_{\mathrm{sc+sr}}^{\uparrow\downarrow} - V_{\mathrm{sc+sr}}^{\uparrow\uparrow}\right)/V_{\mathrm{sc+sr}}^{\uparrow\uparrow} = 290\,\%$. Considering the field-dependent voltage difference between parallel and antiparallel alignment in Fig. 6.9c, one further sees that for a 10 % signal tolerance level (green shaded area, red and blue shaded areas in Fig. 6.9a,b), external field fluctuations in the mT regime are acceptable.
In view of the little scatter of the data points in Fig. 6.9b, the magnon spin valve effect reveals as being reliable and reproducible. The long-term operationality of potential devices is emphasized by the fact that during the performance of various experiments, no distinguishable reduction of the voltage difference (training effect) was observed over several days of continuous measurements including numerous switching events. Furthermore, the size of the signal change exhibits a weak temperature dependence such that, for optimized sample designs, it will be also visible at room temperature.

Theoretical discussion of magnon spin valve effect

In order to try to unveil the origin of the magnon spin valve effect observed in YIG/CoO/Co, (i) alignment-dependent spin current transport through the multilayer and (ii) potentially spin-dependent spin-to-charge conversion effects or (iii) even a combination of both need to be taken into account. Discussing first (i) potential impacts on the spin current transport, please recall that the FMR induced rotation of the YIG magnetization emits a magnonic spin current, which propagates across the insulating antiferromagnet. As already discussed in Sec. 5.2 and Ref. [o8], this spin transport is either mediated by antiferromagnetic magnons [215, 216] or evanescent waves [217], depending on whether the frequency is below or above the AFM magnon gap. Considering that FMR frequencies are generally found in the GHz regime as compared to AFM magnon resonances of CoO in the THz regime [257], evanescent propagation can be assumed to be dominant here. The spin current emission process at the YIG/CoO interface is of equal probability for the two possible orientations of the YIG magnetization, considering that the AFM magnon dispersion relation reveals two branches carrying opposite spin angular momentum and hence spin current polarization. This is due to the fact that the magnetic moments of the antiferromagnetically coupled sublattices precess in opposite directions, which eventually allows for an equal transmission of the pumped magnons through the CoO for both YIG orientations. At the same time, ferromagnetic magnons exhibit a unique polarization. Magnon exchange between the two ferromagnets should thus only be possible when their magnetizations are aligned in parallel. In the case of antiparallel alignment, the magnons get reflected at the interface between the connecting AFM and the second ferromagnet.
This purely magnonic spin valve effect is demonstrated in Fig. 6.10, which shows atomistic spin dynamics simulations of magnon propagation in FM/AFM/FM trilayers. For details on the simulations, which were performed by U. Ritzmann in the same manner as the ones

shown in Sec. 5.2, please see the Supporting Information of Ref. [o9]. Briefly speaking, a monochromatic spin wave is excited in the left ferromagnet FM1 by the coherent precession of magnetic moments in its first layer, which propagates to the right. In view of the FMR nature of the experiment, the frequency in the simulation chosen to to show here is below the AFM magnon gap, which results in evanescent modes in the AFM as seen in Fig. 6.10. To demonstrate the magnon spin valve effect, parallel alignment of FM1 and FM2 is simulated in Fig. 6.10a, whereas antiparallel alignment is implemented in Fig. 6.10b. Apparently, the excited spin wave continues to propagate in FM2 in Fig. 6.10a, while the transmission is blocked in the case of opposite magnetization orientations for FM1 and FM2. As a result, the aforementioned concept of a purely magnonic spin valve effects yields a larger spin current transmissivity for parallel alignment of the ferromagnets. This is, however, in contrast to the experimental findings in YIG/CoO/Co, where a larger amplitude of the spin current transport signal is observed for an antiparallel orientation of the two ferromagnets. Consequently, different mechanisms need to be considered. Note that the simulated system was kept simple and although more realistic spin models might yield different results, the real system cannot be simulated due to the structural complexity of YIG (see Sec. 4.1) and unknown YIG/CoO interface properties. Therefore, potential influences of a complex spin current spectrum in YIG [16] and spectral-dependent interface transmissivities [o3] could not be studied here.

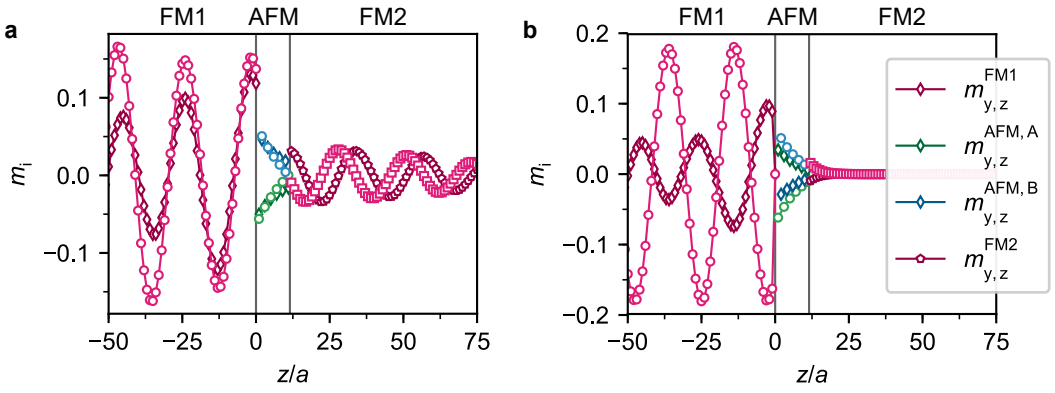

Figure 6.10: Atomistic spin dynamics simulations of magnon propagation in a FM/AFM/FM trilayer. Spin waves are excited in the left ferromagnet FM1 an propagate to the right. With regard to the ferromagnetic resonance spin pumping experiments, the spin wave frequency is below the AFM magnon gap, resulting in evanescent waves in the AFM. Depending on the magnetic orientation of the second ferromagnet FM2, the spin wave can (a) enter it when FM2 is parallel to FM1 or (b) is blocked at the interface in case of FM1 and FM2 being antiparallel. This way, a purely magnonic spin valve effect is implemented. Adapted from [o9].

In addition to the magnonic point of view, (ii) intrinsic effects such as a spin-dependent ISHE in the Co layer or a spin-dependent effective spin-mixing conductance of the CoO/Co interface need to be taken into account for a potentially better understanding of the experimental findings. Fundamentally, the magnonic spin current in CoO is pumped into the Co layer by generating a spin accumulation in the Co at the CoO/Co interface, which results in a diffusive flow of spin-up and spin-down electrons moving in opposite directions. This spin current is converted into a charge current as a result of the ISHE, which spatially separates electrons of opposite spin polarizations. While normal metals like Pt are spin-unpolarized and exhibit equal properties for electrons of both spin polarizations, this is not true for ferromagnets. The latter are spin-polarized (different density of states at the Fermi level for spin-up and spin-down electrons with $\mathcal{N}^{\downarrow}/\mathcal{N}^{\uparrow} = 2.64$ for Co [258]) and show significant differences in the intrinsic properties of the spin sub-bands. For example, Co exhibits a positive spin current polarization with $\alpha_{\mathrm{F}} = (\sigma^{\uparrow} - \sigma^{\downarrow}/(\sigma^{\uparrow} + \sigma^{\downarrow}) \approx 0.12$ [259]. One thus has to bear in mind that the measured ISHE voltage results from magnon spin currents coupling to two distinct electron channels with different properties. Ultimately, reversing the Co magnetization orientation manifests in a reversal of the roles of spin-up and spin-down electrons in the Co, which thus may result in a magnetization alignment-dependent spin-charge interconversion process.
Eventually, besides purely magnonic or electronic (intrinsic) origins of the magnon spin valve effect, one could further think of (iii) a combined action. Cheng *et al.* [260] theoretically discussed the interplay of magnon and electron spin currents, showing that an intermixing of the two via *sd*-exchange coupling can become of significance. Presupposed that the spin current pumped across the CoO/Co interface is constant regardless of the alignment configuration and that the purely magnonic spin valve effect described above is present, one could explain the experimentally observed magnon spin valve effect in the following manner: in the case of parallel alignment, the spin current can be mediated by both magnons (rotation of the localized $3d$ moments in Co) and itinerant spin transport, whereas electronic spin currents only are possible for antiparallel alignment. In spite of a potential polarization of the Co conduction electrons by the magnon spin current due to the *sd*-exchange [260], this may lead to a reduced electronic spin current flowing in the parallel aligned Co layer and hence a lower ISHE signal, giving $V_{\mathrm{sc}}^{\uparrow\downarrow} > V_{\mathrm{sc}}^{\uparrow\uparrow}$.

6.1.3 Conclusion

In conclusion, ferromagnetic resonance spin pumping measurements were performed in YIG/CoO/Co multilayers acting as spin-valve like structures. As a first experimental finding in the sample preparation process, it is shown that the morphology of YIG surfaces can be significantly improved in terms of surface roughness by means of a rapid thermal

annealing process. Furthermore, spin-thermoelectric measurements probing the anomalous Nernst effect in Co reveal a notable exchange bias exerted by the antiferromagnetic CoO. In the spin pumping experiment, the total voltage signal detected at ferromagnetic resonance of YIG is generally composed of two clearly separable contributions, which individually depend on the magnetic configuration (magnetization orientation) of YIG and Co. While the YIG-dependent signal is identified as the voltage generated by spin-to-charge conversion of the spin current emitted by the YIG layer, the experimental data suggests an anomalous Hall effect induced spin rectification origin of the Co-dependent signal. The latter is unaffected by the relative alignment of the YIG and Co magnetization, whereas the amplitude of the spin current signal is notably larger for an antiparallel magnetization configuration as compared to the parallel state. This alignment-dependent detection of spin currents is referred to as *magnon spin valve effect*. By means of this effect, together with the fact that the spin current signal switches sign when the YIG magnetization is reversed, eventually allows one to store two bits of information in the magnon valve. Ultimately, the presented data gives an insight into spin-dependent effects in magnetic multilayers and provides a switch-like element at the spin current detection site, thus providing a further building block for magnon-based logic operations.

6.2 Magnetization-orientation dependent (inverse) spin Hall effect in $Co_{60}Fe_{20}B_{20}$

In the previous section, it has been successfully demonstrated that the usage of a metallic ferromagnet for the detection of pure spin currents allows for the implementation of a spin valve like effect. For a fixed spin current polarity, the efficiency of the spin current detection in the FM strongly depends the orientation of its immanent magnetization, lending itself a useful tool for prospective logic operations [17]. While the data presented in Sec. 6.1 constitutes a proof of principle, verifying the origin of the effect requires further investigation. As discussed, potential explanations for the alignment-dependent spin-to-charge conversion can be given by both an intrinsic (spin-dependent ISHE) and magnonic (spin wave transmission or reflection) effect. The latter may indirectly affect the amplitude of the electron-mediated spin current propagating in the metallic ferromagnet. In view of this aspect, additional experiments that allow one to further specify the origin or to identify a dominating intrinsic or magnonic contribution are necessary.

Considering that the previously used method of FMR spin pumping for spin current generation sets rather high requirements in terms of circuitry design [17, 247], a different experimental approach would be beneficial. A promising alternative is given by the non-local device already implemented in Sec. 5.1, which allows one to generate and detect thermally (SSE) as well as electrically (SHE) induced magnonic spin currents in a magnetically ordered insulator [o13, 172]. The non-local design is therefore apt to investigate spin-related material properties and, so far, has already revealed its potential concerning magnon logic concepts by the implementation of a majority gate [202] or the spin current controlled modulation of magnon flow [261].

In the following section, spin-charge interconversion processes, i.e., the spin Hall effect and its inverse are probed in the metallic ferromagnet $Co_{60}Fe_{20}B_{20}$ (CoFeB) in a non-local spin transport experiment. The realized device structure includes two parallel, electrically insulated Pt and Cu/CoFeB/Ru wires deposited on top of the insulating ferrimagnet YIG. The Cu interlayer ensures that, when employed as a detector, the spin current sensed by CoFeB is exclusively mediated by electrons, which is crucial information for the later discussion of measurement data. Note that while conducting the experimental work of this study, Das *et al.* [262] reported on similar results obtained using $Ni_{80}Fe_{20}$ (permalloy, Py) instead of CoFeB, which was further directly put in contact with the YIG. Quantitative differences between these two experiments are discussed paying attention to material properties and the implemented sample configuration.

6.2.1 Experimental details

Figure 6.11 shows an optical micrograph of the fabricated device structure. As shown in the image, a non-local measurement geometry similar to that in Sec. 5.1 was fabricated, implementing parallel, spatially separated Pt and Cu/CoFeB/Ru nanowires on top of a single crystalline YIG film [$d_{\mathrm{YIG}} = 630\,\mathrm{nm}$, grown on GGG (111) via LPE]. Similar to the fabrication process in Sec. 5.1, the nanowires were produced by a lift-off procedure. In contrast to these previous experiments, however, different wire materials were implemented in a single device such that a multi-step process was implemented. To begin with, nanowires of a designed width $w = 250\,\mathrm{nm}$ were imprinted into the photoresist by electron beam lithography (recipe see App. B), followed by the deposition of a 7.5 nm thick Pt film via magnetron sputtering. After a further lithography step to structure the second nanowire, a Cu/CoFeB/Ru multilayer stack with individual layer thicknesses of $d_{\mathrm{Cu}} = 2\,\mathrm{nm}$, $d_{\mathrm{CoFeB}} = 7\,\mathrm{nm}$ and $d_{\mathrm{Ru}} = 2\,\mathrm{nm}$ was deposited. Due to a higher resistivity of the multilayer stack ($\rho_{\mathrm{Cu/CoFeB/Ru}} = (99.29 \pm 9.02)\,\mu\Omega\,\mathrm{cm}$) as compared to that Pt ($\rho_{\mathrm{Pt}} = (31.59 \pm 2.23)\,\mu\Omega\,\mathrm{cm}$), a larger wire width $w = 350\,\mathrm{nm}$ for Cu/CoFeB/Ru was chosen to avoid high absolute resistance values and hence to limit, for instance, Johnson noise [263]. The designed center-to-center distance was 1250 nm such that potential minor misalignments during the fabrication process did not result in shortcutting the wires, while the distance is small enough to provide a sufficiently large signal. In the following, the Cu/CoFeB/Ru multilayer is referred to as CoFeB for convenience.
In spite of the circuitry illustrated in Fig. 6.11, both the Pt and CoFeB wires were used as magnon injector and detector to study the charge-to-spin as well as spin-to-charge conversion in CoFeB, respectively. The application of a charge current to the injector yields either

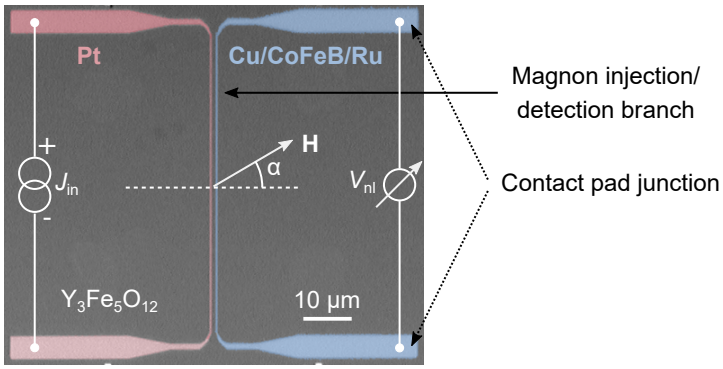

Figure 6.11: Optical micrograph of the implemented non-local device structure comprising two parallel, electrically insulated Pt (red) and Cu/CoFeB/Ru (blue) wires. The electrical wiring as well as the magnetic field direction definition are indicated. The micrograph was taken before the deposition of contact pads.

the thermal or electrical excitation of magnonic spin currents in the YIG, respectively, via the SSE or SHE. In the detector, these spin currents induce an electrical voltage response by means of the ISHE (reconsider Sec. 3.5 for details). Implementing a DC measurement scheme, the injector was connected to a Keithley 2400 source meter that provided the charge current $J_{\mathrm{in}} = \pm 300\,\mu\mathrm{A}$ ($j_{\mathrm{in}}^{\mathrm{Pt}} \approx 1.6 \times 10^{11}\,\mathrm{A\,m^{-2}}$, $j_{\mathrm{in}}^{\mathrm{CoFeB}} \approx 7.8 \times 10^{10}\,\mathrm{A\,m^{-2}}$) and simultaneously recorded the injector resistance. As shown later, magnetoresistance effects in the CoFeB hold relevant information on its magnetic configuration. The non-local spin signal was picked up by a Keithley 2182A nanovoltmeter connected to the detector. For spin transport experiments, an in-plane magnetic field $\mu_0\mathbf{H}$ was applied and both angular-dependent (sample rotation in the field, angle α) and field sweep measurements were performed. Due to technical limitations of the used setup (see Sec. 4.3.2), maximum field values of $\mu_0 H = 85\,\mathrm{mT}$ and $\mu_0 H = 175\,\mathrm{mT}$ were used during the angular-dependent and field sweep measurements, respectively. All measurements were conducted at room temperature.

Note that the metallic ferromagnet CoFeB generally exhibits, in contrast to the paramagnetic Pt, other spin-dependent effects in addition to the ISHE. Especially in terms of thermally induced signals, temperature gradients in the system can give rise to additional Nernst effects, see Sec. 3.4.2, which need to be considered. Therefore, the generalized notation for electrically and thermally induced spin signals given by Eq. 5.1 and Eq. 5.2 is used in the following:

$$V_{\Delta}^{\mathrm{nl}} = \left[V_{\mathrm{nl}}\left(+J_{\mathrm{in}}\right) - V_{\mathrm{nl}}\left(-J_{\mathrm{in}}\right)\right]/2., \tag{6.2}$$

$$V_{\Sigma}^{\mathrm{nl}} = \left[V_{\mathrm{nl}}\left(+J_{\mathrm{in}}\right) + V_{\mathrm{nl}}\left(-J_{\mathrm{in}}\right)\right]/2. \tag{6.3}$$

Here, V_{Δ}^{nl} gives the electrically induced signal, while V_{Σ}^{nl} quantifies the thermal response of the system.

6.2.2 Results and discussion

To begin with, the functionality of the non-local device was checked by means of angular-dependent measurements. Figure 6.12a,b shows V_{Δ}^{nl} and V_{Σ}^{nl} as a function of α for the two distinct configurations of either using CoFeB as injector and Pt as detector (CoFeB $\rightarrow$ Pt, Fig. 6.12a) or vice versa (Pt $\rightarrow$ CoFeB, Fig. 6.12b). Considering first the electrically induced signal, V_{Δ}^{nl} reveals for both cases the $\cos^2(\alpha)$ angular dependence expected from Eq. 3.18, with $\alpha = 0°$ signifying a positive alignment of $\mathbf{M}_{\mathrm{YIG}}$ perpendicular to the injector/detector stripes. The signal is negative and, within the error, of equal amplitude for the two configurations with $V_{\Delta}^{\mathrm{nl}}\,(\mathrm{CoFeB} \rightarrow \mathrm{Pt}) = (-202 \pm 3)\,\mathrm{nV}$ and $V_{\Delta}^{\mathrm{nl}}\,(\mathrm{Pt} \rightarrow \mathrm{CoFeB}) = (-195 \pm 6)\,\mathrm{nV}$. As a first finding, the negative sign of V_{Δ}^{nl} indicates that the ISHE charge

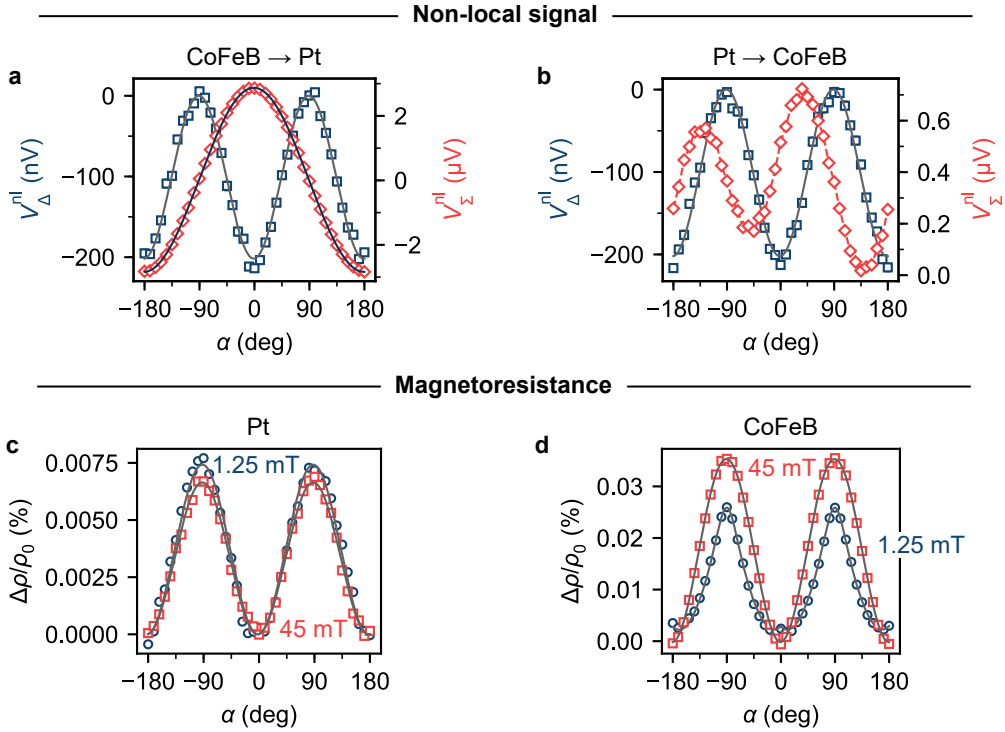

Figure 6.12: (a),(b) Angular-dependent measurements of non-local voltage induced by electrically (V_Δ^{nl}) and thermally (V_Σ^{nl}) excited spin currents. In (a) CoFeB is used as injector and Pt as detector, while results obtained for the reversed configuration are shown in (b). (c),(d) Angular-dependent magnetoresistance measurements for (c) the Pt and (d) the CoFeB wire at different external fields amplitudes. In all graphs, solid lines give the results of corresponding fit functions. If visible, error bars account for the standard error of the measurement data and device inaccuracies.

current in the detector flows in the same direction as J_{in}, meaning that the spin Hall angle of CoFeB θ_{SH}^{CoFeB} has the same sign as that of Pt [172]. Concerning its absolute value, the chosen wire structure does not allow for its direct determination as the spin current first has to cross the Cu layer, in which it is attenuated. Furthermore, the charge current generated by the ISHE presumably experiences shunting in both the Cu and Ru layer.

The thermal voltage V_Σ^{nl} picked up at the Pt detector exhibits the $\cos(\alpha)$ dependence expected for the SSE (see Eq. 3.19) with an amplitude of (3310 ± 5) nV. For the CoFeB detector, however, the symmetry of the signal notably differs, indicating the superposition of different effects. Besides SSE (Sec. 3.4.3) and ANE (Sec. 3.4.2), which both depend on the in-plane direction of the YIG or CoFeB magnetization, respectively, the angular dependence of V_Σ^{nl} in Fig. 6.12b suggests a dominating planar Nernst effect (PNE). As discussed briefly in Sec. 3.4.2, the PNE is the spin-thermoelectric equivalent of the AMR

and, in the studied non-local device, is expected to show a $\sin(2\alpha)$ dependence [133]. This can be recognized in the signal symmetry. More detailed evaluation of V_{Σ}^{nl} with regard to this aspect, however, is omitted considering that the thermal signal is not the focus of this work, but is only used to infer information on magnetic properties of the YIG and CoFeB.

As mentioned above, the resistance of the injector stripes was recorded as well during the angular-dependent measurements to quantify magnetoresistive effects that contain further information on the magnetic configuration of the system. While for YIG/Pt, given that no parasitic magnetic moment is present in Pt, only the SMR is expected to appear [79], both SMR and AMR can be observed in YIG/CoFeB. Bearing in mind their origins, the SMR depends on the YIG magnetization orientation [77], whereas the AMR is determined by the angle between the charge current flow and the magnetization direction in CoFeB [73]. Figure 6.12c shows the angular-dependent magnetoresistance data obtained for the Pt injector at two distinct external magnetic fields $\mu_0 H = 1.25\,\mathrm{mT}$ and $\mu_0 H = 45\,\mathrm{mT}$. For both field values, the signal curve reveals comparable SMR amplitudes with $\Delta\rho/\rho_0 \simeq 7.4 \times 10^{-5}$. The data further signifies that the YIG magnetization follows the external field at even low field strengths (see field sweeps in Fig. 6.14). At the same time, the shape and amplitude of the angular-dependent magnetoresistance in CoFeB (Fig. 6.12d) vary notably for the different field amplitudes applied. At low field strengths, $\Delta\rho/\rho_0$ displays a flat resistance change near $\alpha = 0°, \pm 180°$ and distinct peaks at $\alpha = \pm 90°$, whereas the $\sin^2(\alpha)$ dependence expected for either SMR or AMR in the realized device symmetry is seen at larger external fields. Regarding the fabricated wire structure, the measured resistance is dominated by the magnon injection/detection branch, see Fig. 6.11. One can thus explain the observed behavior by a uniaxial shape anisotropy, which at low external fields forces $\mathbf{M}_{\mathrm{CoFeB}}$ to align alongside the wire. At larger external fields, however, the Zeeman energy becomes dominating and $\mathbf{M}_{\mathrm{CoFeB}} \parallel \mathbf{H}$, irrespective of the field direction. Taken all together, the magnetoresistance measured in CoFeB is determined by its magnetization direction and hence the AMR.

Having shown that $\mathbf{M}_{\mathrm{YIG}}$ essentially always shows in the direction of the external field, the anisotropic magnetoresistance in CoFeB primarily signifies that $\mathbf{M}_{\mathrm{YIG}}$ and $\mathbf{M}_{\mathrm{CoFeB}}$ are exchange-decoupled by the Cu interlayer. In addition, large fields are required to achieve parallel alignment of $\mathbf{M}_{\mathrm{YIG}}$ and $\mathbf{M}_{\mathrm{CoFeB}}$ for external field components that are perpendicular to the wire, which verifies that the studied system allows one to investigate both the magnetization orientation-dependent generation as well as detection of spin currents in CoFeB. One approach to derive the angle between $\mathbf{M}_{\mathrm{YIG}}$ and $\mathbf{M}_{\mathrm{CoFeB}}$ at different external fields would be provided by solving the Stoner-Wohlfarth model [23, 24], with which, as demonstrated by the solid line in Fig. 6.12, one basically can reconstruct the angular dependence of the MR. Nevertheless, the additional magnetoresistance in the contact pad

junctions (see Fig. 6.11) of the nanowires prohibits an unambiguous quantification of the angle between $\mathbf{M}_{\mathrm{CoFeB}}$ and $\mathbf{H}$. Alternatively, the amplitude of the total MR effect in CoFeB is used to obtain at least qualitative information on the CoFeB magnetization orientation, as presented in Fig. 6.13. The resistance variation $\Delta\rho/\rho_0$, with $\Delta\rho = \rho\,(90°) - \rho\,(0°)$, initially increases with increasing field amplitude until it saturates above a critical value of $\mu_0 H_c \geq 25\,\mathrm{mT}$. Based on that finding, one can conclude that $\mathbf{M}_{\mathrm{CoFeB}}$ is fully aligned with the external field and thus $\mathbf{M}_{\mathrm{YIG}}$ for $H \geq H_c$, whereas a finite angle appears at fields below.

The effective decoupling of the two magnetic layers is further verified by linear magnetic field sweeps ($\alpha = 0°, \pm 180°$) regarding the thermally excited signal. In Fig. 6.14a, a V_{Σ}^{nl} hysteresis loop obtained for the Pt $\rightarrow$ CoFeB configuration is depicted, revealing a complex multi level voltage switching. Considering first the switching event at low fields, the comparison to the CoFeB $\rightarrow$ Pt data shown in Fig. 6.14b signifies that this is to be attributed to the YIG magnetization reversal and thus an inversion of the SSE spin current polarity. Additionally, the YIG stray field may influence the CoFeB magnetization such that the signal jump may also include an ANE voltage in the presence of a potential out-of-plane temperature gradient across the CoFeB wire. A further evident feature of the hysteresis loop, which corroborates the assumption of effective decoupling, is a second switching event that appears near $-2\,\mathrm{mT}$ and is only observed when sweeping the field from positive to negative values. The depth of this additional dip depends linearly on the applied heating power (not shown here), which indicates a thermal origin (e.g. ANE). Furthermore, the switching from a lower to a higher voltage level at $-2\,\mathrm{mT}$ implies that this additional thermal signal has a different sign than the SSE induced ISHE voltage, which is consistent with previously reported ANE data in $Co_{20}Fe_{60}B_{20}$ [264]. The asymmetry of the switching, i.e., its exclusive appearance for one field sweep direction, may be due

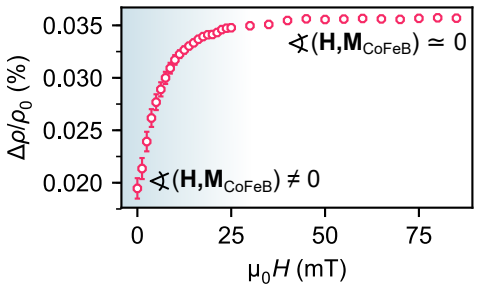

Figure 6.13: Amplitude $\Delta\rho/\rho_0$ of the angular-dependent magnetoresistance effect in the CoFeB wire (AMR dominated) as a function of magnetic field. Error bars represent the standard error of the mean.

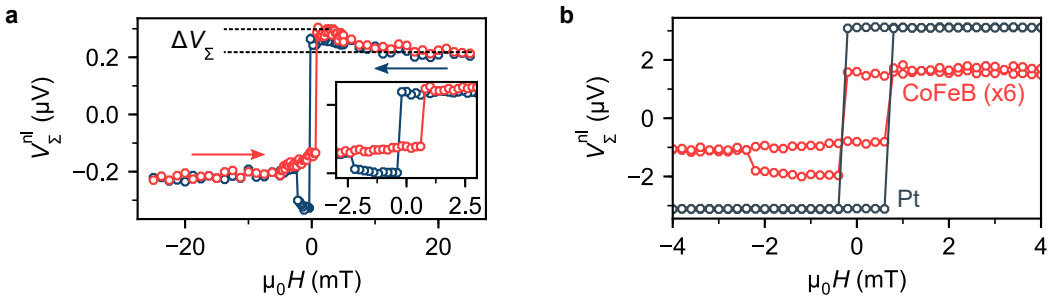

Figure 6.14: Thermal voltage hysteresis loops ($\alpha = 0°, \pm 180°$) recorded for (a),(b) the CoFeB and (b) the Pt detector. The external field is applied perpendicular to the wire. While the thermal signal at the Pt detector is induced by the SSE in YIG exclusively, ANE and PNE contributions to the CoFeB signal are likely. The arrows in (a) indicate the field sweep direction, while the inset shows a more detailed scan at low fields. Beyond the displayed field range, the signals stay constant up to the maximum achievable field values of 185 mT.

to the chosen wire structure or a localized defect breaking the inversion symmetry, which may lead to a unidirectional anisotropy in the system. A potential mechanism one could think of would be, in the case of an incomplete capping of the CoFeB by the Ru layer, a localized oxidation of the CoFeB leading to antiferromagnetic behavior and thus exchange bias [265].

Apart from that, the hysteresis in Fig. 6.14a shows for both field directions a monotonic decrease of the voltage level with increasing field, followed by a saturation level. Comparing this finding to the field dependence of $\Delta\rho/\rho_0$ in Fig. 6.13, this behavior is attributable to the CoFeB magnetization aligning along the field such that a supplementary Nernst effect emerges or disappears. Considering that the total voltage change ΔV_Σ has the same sign for both field directions, the additional signal can neither be provided by the ANE nor a spin-dependent ISHE, for which one would expect asymmetric behavior [264]. As already discussed in terms of the angular-dependent measurements, the PNE with its $\sin(2\alpha)$ symmetry [134] yields a possible explanation for ΔV_Σ. At low external fields, the CoFeB magnetization in the magnon injection/detection branch aligns along the nanowire due to the previously discussed shape anisotropy such that a finite PNE voltage appears in the presence of an in-plane temperature gradient. If one now increases the external field amplitude, $\mathbf{M}_{\mathrm{CoFeB}}$ becomes parallel to the field ($\alpha = 0°, 180°$) and the PNE contribution vanishes.

So far, the magnetic properties of the studied system have been determined as a fundamental prerequisite to the actual scope of this project, which is the magnetization orientation-dependent injection and detection of magnonic spin currents by the CoFeB

layer. As demonstrated above, the implemented non-local device allows one to probe and compare the SHE and ISHE in CoFeB for a finite angle between the YIG and CoFeB magnetization ($\mathbf{M}_{\mathrm{CoFeB}} \nparallel \mathbf{M}_{\mathrm{YIG}}$ at low fields perpendicular to the wire) and for parallel alignment ($\mathbf{M}_{\mathrm{CoFeB}} \parallel \mathbf{M}_{\mathrm{YIG}}$ at high fields perpendicular to the wire). Considering that spin-thermoelectric signals (V_{Σ}^{nl}) have revealed to be unsuited for the identification of a spin-dependent (I)SHE due to supplemental signal contributions, only the non-local voltage induced by electrically injected magnons (V_{Δ}^{nl}) is considered hereafter. To exploit the whole spectrum of available field amplitudes ($0\,\mathrm{mT} \leq \mu_0 H \leq 175\,\mathrm{mT}$), V_{Δ}^{nl} data presented in the following was obtained by magnetic field sweeps and subsequent rotation of the sample in the setup by 15°.

Figure 6.15a shows V_{Δ}^{nl} as a function of α and field amplitude in the Pt → CoFeB configuration, in which CoFeB acts as the spin current detector. As can be seen in the graphs, the

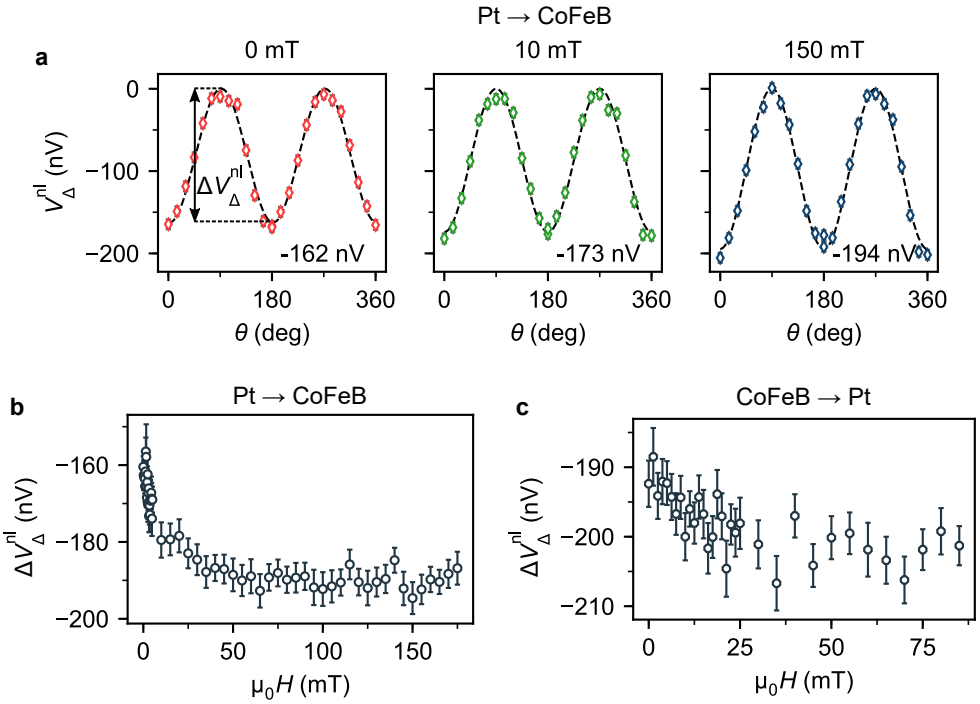

Figure 6.15: (a) Angular-dependent data at different magnetic fields obtained for the electrically induced non-local voltage V_{Δ}^{nl} using the Pt → CoFeB configuration. The data is extracted from linear field sweeps at fixed angles (15° steps) between the external field and the wire axis ($\alpha = 0°$ for field perpendicular to the wire). The dashed lines give the results of corresponding fit functions. (b),(c) Amplitude $\Delta V_{\Delta}^{\mathrm{nl}}$ of the angular-dependent non-local voltage as a function of field for (b) the Pt → CoFeB configuration and (c) the CoFeB → Pt configuration. Error bars account for (a) the standard error and measurement device inaccuracies as well as (b),(c) fit parameter errors.

amplitude $\Delta V_\Delta^{\mathrm{nl}}$ of the non-local voltage increases with increasing external field, a corresponding fit function yields $\Delta V_\Delta^{\mathrm{nl}}(0\,\mathrm{mT}) = (-162 \pm 4)\,\mathrm{nV}$, $\Delta V_\Delta^{\mathrm{nl}}(10\,\mathrm{mT}) = (-173 \pm 5)\,\mathrm{nV}$ and $\Delta V_\Delta^{\mathrm{nl}}(150\,\mathrm{mT}) = (-194 \pm 4)\,\mathrm{nV}$. The detailed field-dependence obtained for this configuration is shown in Fig. 6.15b, displaying an initially increasing signal amplitude that eventually saturates. The relative amplitude change amounts to

$$\left[\Delta V_\Delta^{\mathrm{nl}}(> 100\,\mathrm{mT}) - \Delta V_\Delta^{\mathrm{nl}}(0\,\mathrm{mT})\right] / \Delta V_\Delta^{\mathrm{nl}}(0\,\mathrm{mT}) = (-17.2 \pm 3.4)\,\%.$$

For the reversed process, i.e., CoFeB now acts as spin current injector and Pt as detector, a similar but weaker effect is observed, see Fig. 6.15c. As before, an initial voltage amplitude increase with applied field strength is identified that eventually levels off to a saturated value. Here, the relative amplitude change amounts to $(-5.3 \pm 2.6)\,\%$.

To verify whether this field-dependent modification of the electrically induced non-local signal correlates with the magnetic orientation of CoFeB and, thus, is due to a spin-dependent SHE or ISHE, the results obtained for the CoFeB detector are directly compared to the field-dependent magnetoresistance amplitude in CoFeB, as shown in Fig. 6.16. Apparently, both $\Delta\rho/\rho_0$ and $\left|\Delta V_\Delta^{\mathrm{nl}}\right|$ show the same trend as a function of field with an initial rise and a subsequent saturation above $\mu_0 H_\mathrm{c} \gtrsim 25\,\mathrm{mT}$. Since the magnetoresistance in CoFeB is dominated by the AMR and hence directly depends on the direction of $\mathbf{M}_{\mathrm{CoFeB}}$, this demonstrates that the spin-to-charge conversion efficiency in CoFeB exhibits a notable magnetization orientation dependence. Bearing in mind Onsager's recipocity relations [96], the same conclusion can be drawn for the SHE (see Fig. 6.15c), although the effect is smaller. Potential explanations for this observation are discussed further below.

The observation of a spin-dependent SHE and ISHE in CoFeB generally agrees with the findings reported in Ref. [262]. As mentioned in the introduction, Das *et al.* studied the non-local injection and detection of pure spin currents in YIG by Py, demonstrating a

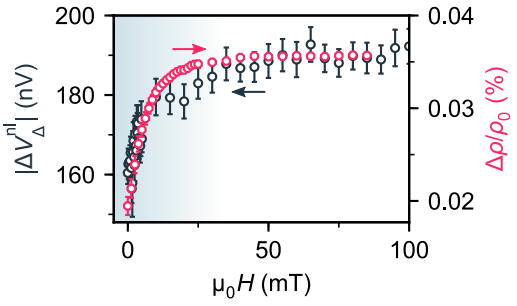

Figure 6.16: Direct comparison of $\Delta\rho/\rho_0$ (Fig. 6.13) and the non-local signal amplitude $\delta V_\Delta^{\mathrm{nl}}$ (Fig. 6.15b) in the CoFeB wire as a function of field. Error bars are given by the standard error ($\Delta\rho/\rho_0$) and by extracted fit parameter errors ($\Delta V_\Delta^{\mathrm{nl}}$).

qualitatively similar behavior as the one shown for CoFeB here. Urging a similar reasoning as compared to that in the foregoing section 6.1, Das *et al.* argue that the finite spin-polarization in metallic FMs yields an additional, spin-dependent contribution to the (I)SHE. [1] One of the differences between the experiment in Ref. [262] and this work, however, is the fact that Das *et al.* exclusively used Py as spin current injector with a second Py or Pt stripe as detector. The alignment-dependent detection of spin currents in Py was inferred indirectly by building the ratio of the voltages tapped at the Py and Pt detector. Here, when implementing the Pt $\rightarrow$ CoFeB configuration, the magnonic spin current in YIG is excited by generally spin-unpolarized conduction electrons in the Pt injector and detected by spin-polarized conduction electrons in the CoFeB detector. Therefore, the field dependence shown in Fig. 6.15b is directly attributable to a spin-dependent spin-to-charge conversion process in the CoFeB. This is further corroborated by the fact that due to the Cu interlayer a purely electronic spin current is probed. Potential magnonic effects, which have been discussed in the previous section and that may be of significance for the experiment of Das *et al.*, hence are negligible.

Despite the qualitative agreement, note that the relative amplitude change between $\mathbf{M}_{\mathrm{Py}} \nparallel \mathbf{M}_{\mathrm{YIG}}$ and $\mathbf{M}_{\mathrm{Py}} \parallel \mathbf{M}_{\mathrm{YIG}}$ reported by Das *et al.* is significantly larger than the one observed for the CoFeB wire in this work. At first glance, one may consider the different intrinsic properties of spin-up and spin-down electrons in Py and CoFeB as a potential explanation for this finding. However, previous studies showed a stronger AHE for CoFeB ($\rho_{\mathrm{AHE}}/\rho_{xx} \approx 21 \times 10^{-3}$ [266]) than for Py ($\rho_{\mathrm{AHE}}/\rho_{xx} \approx 2.7 \times 10^{-3}$ [267]). Bearing in mind that SHE and AHE share the same origin [10], one could expect a larger spin-dependent (I)SHE contribution in the CoFeB. Alternatively, as already indicated above, the reduced spin sensitivity may result from the fact that the magnonic spin currents propagating in the YIG directly couple to the Py such that one may think of a further magnonic spin valve effect [o9]. Furthermore, previous works reported on larger spin-mixing conductances $G^{\uparrow\downarrow}$ of FMI/FM interfaces as compared to FMI/NM interfaces [222, 223], which may be of importance here. One may even consider, with regard to the distinct densities of states of spin-up and spin-down electrons in metallic ferromagnets near the Fermi edge [268], a spin-dependent spin-mixing conductance of the YIG/Py interface. It may improve at larger fields ($\mathbf{M}_{\mathrm{CoFeB}} \parallel \mathbf{M}_{\mathrm{YIG}}$), while $G^{\uparrow\downarrow}$ of YIG/Cu should be field-independent. Finally, a further effect that is unavoidable and needs to be taken into account is the so-called *spin memory loss* at metallic interfaces [269], which quantifies the depolarization probability of spin currents crossing the interface For example, depolarization by up to 22 % and 60 % were

[1] Note that Das *et al.* label this supplemental term as *(inverse) spin anomalous Hall effect.* In this thesis, however, the magnetization orientation generation/detection of spin currents is referred to as spin-dependent (I)SHE to maintain a congruent notation and furthermore to comply with the classification of SHE and AHE given by Sinova *et al.* [10].

reported for Co/Cu and Co/Pt interfaces [270]. These values are material specific and most likely vary strongly for different deposition conditions and interface qualities, which would require further detailed studies to quantify spin-flip scattering at the fabricated Cu/CoFeB interface.

For the presented results, the distinct difference in the relative amplitude change for spin current detection [$(17.2 \pm 3.4)\,\%$] and spin current injection [$(5.3 \pm 2.6)\,\%$] by CoFeB, which in view of the reciprocity of SHE and ISHE intuitively would be assumed to be comparable, remains an open question. While in both cases a spin current flows perpendicularly to the Cu/CoFeB interface, an additional charge current flows through the wire when employed as injector. One may speculate whether spatially varying current densities due to different resistivities of the single Cu, CoFeB and Ru [271]) layers may affect the SHE induced spin current due to, for instance, spatially varying Oersted fields $\mathbf{H}_{\mathrm{Oe}}$ in the multilayer. In App. D, finite element simulations are performed that give both out-of-plane and in-plane Oersted field components perpendicular to the long edge of the wire. Since the exact resistivities of the single layers are unknown, reported bulk and thin film values are used as an estimate: $\rho_{\mathrm{Cu}} = 1.7 \times 10^{-8}\,\Omega\,\mathrm{m}$ [271], $\rho_{\mathrm{CoFeB}} = 2.3 \times 10^{-7}\,\Omega\,\mathrm{m}$ [272], $\rho_{\mathrm{Ru}} = 7.1 \times 10^{-8}\,\Omega\,\mathrm{m}$ [271]. The simulation data reveals that in the Cu layer notable out-of-plane Oersted field components are created near the wire edges, while in the CoFeB layer the Oersted field is insignificant in comparison. Considering now that the SHE effect generates spin currents with an in-plane spin polarization $\boldsymbol{\mu}_{\mathrm{s}}$, this out-of-plane field may alter their amplitude due to an applied torque $\boldsymbol{\tau} \propto \boldsymbol{\mu}_{\mathrm{s}} \times \mathbf{H}_{\mathrm{Oe}}$ (see Sec. 2.5.1). However, this aspect requires further investigation, which includes varying device and material configurations.

Note that, as a final remark, a direct comparison of the obtained results for CoFeB with the FMR spin pumping data in YIG/CoO/Co (Sec. 6.1) may appear tempting, however, one has to be cautious regarding the significant differences between these two experiments. For once, the sample structures including a non-magnetic metal (Cu, here) or an insulating antiferromagnet (CoO, Sec. 6.1) as interlayer exhibit fundamental differences with regard to the spin transport mechanism (electronic vs. magnonic spin currents). In addition, spin waves generated by FMR spin pumping are coherent, while in the non-local scheme spin currents are carried by incoherent magnons. Lastly, the non-local device studied here only allows to compare the cases of $\mathbf{M}_{\mathrm{CoFeB}} \nparallel \mathbf{M}_{\mathrm{YIG}}$ and $\mathbf{M}_{\mathrm{CoFeB}} \parallel \mathbf{M}_{\mathrm{YIG}}$ instead of parallel and antiparallel alignment of the ferromagnets. Nonetheless, the results presented in this sections strongly suggest a notable intrinsic contribution to the magnon spin valve effect.

6.2.3 Conclusion

In conclusion, non-local spin transport measurements were performed to probe the magnetization orientation dependent generation and detection of spin currents in the metallic

ferromagnet $Co_{60}Fe_{20}B_{20}$. The non-local device includes two spatially separated, parallel wires of Pt and Cu/CoFeB/Ru deposited on the insulating ferrimagnet YIG, which acts as a spin conduit. By means of spin-thermoelectric and magnetoresistance measurements, it is shown that the Cu interlayer leads to exchange-decoupling of YIG and CoFeB such that their magnetizations can be, to some extent, controlled individually via an external field. At low fields with a field component perpendicular to the wire, $\mathbf{M}_{\mathrm{CoFeB}}$ and $\mathbf{M}_{\mathrm{YIG}}$ are aligned at a finite angle due to shape anisotropy in the nanowire, while they are parallel at large fields. Probing electrically excited spin currents, either generated in the CoFeB and detected in the Pt or vice versa, the non-local voltage reveals a field-dependence that is correlated to the orientation of $\mathbf{M}_{\mathrm{CoFeB}}$. Since the Cu interlayer rules out direct coupling of YIG magnons to the CoFeB magnetization dynamics, this unambiguously demonstrates the spin-dependent generation and conversion of spin currents in CoFeB. However, the relative amplitude change is different for the two measurement schemes, which may be caused multilayer structure of the CoFeB wire. This aspect requires further investigation, which includes, for instance, samples that both include and exclude a decoupling layer. Otherwise, a modified device structure may allow one to achieve parallel and antiparallel alignment of $\mathbf{M}_{\mathrm{CoFeB}}$ and $\mathbf{M}_{\mathrm{YIG}}$ similar to the results shown in the previous section.

6.3 Spin signal manipulation by Joule heating and Oersted fields

The results shown in the previous two sections have demonstrated that the magnetization orientation-dependent interconversion of spin and charge information in metallic ferromagnets essentially allows one to create a spin valve-like effect. Exploiting this scheme, the magnitude of forwarded spin information signals strongly depends on the angle between the magnetization direction in the injector/detector and the polarization vector of the spin current. While this facilitates the implementation of logical gates in spin current junctions (generation/detection site), further methods to manipulate spin information exchange in magnonic devices during the magnon propagation phase would be advantageous in the prospect of complex logic operations. Previous works regarding this subject include the spin wave de-multiplexer introduced by Vogt *et al.* [246] or the magnon transistor by Chumak *et al.* [247].
More recently, Cornelissen *et al.* reported on the spin current-controlled modulation of magnon transport in the ferrimagnetic insulator YIG [261]. In a non-local device structure including three parallel, electrically insulated Pt wires, the spin information exchange between the outer wires can be altered through an additional spin current injected by the middle wire. In the upcoming section, a similar, yet essentially different approach is pursued by investigating the impact of heat and Oersted fields on magnon spin transport. To do so, non-local experiments are performed using a device structure comparable to that of Cornelissen *et al.*, however, with a different material employed for the middle wire. Instead of Pt, a non spin Hall active metal is used with the consequence that the application of a DC charge current to this wire solely results in Joule heating and static magnetic fields.

6.3.1 Experimental details

The non-local structure used in this study is schematically shown in Fig. 6.17a. The design can be considered as a multi-terminal device including three parallel, electrically insulated nanowires deposited on the insulating ferrimagnet YIG. While the outer wires are made of Pt and are used as spin current injector or detector, the middle wire, which is also referred to as manipulator, consists of aluminum oxide capped Cu. Due to its weak spin-orbit interaction, Cu does not exhibit a sizable SHE/ISHE [68], which means that the application of a charge current to the Cu manipulators does not lead to the electrical injection of magnonic spin currents into the YIG but locally heats the sample and creates a static magnetic Oersted field.
With regard to sample fabrication, the non-local devices were patterned using a lift-off process similar to that described in the previous section (see App. B). Initially, the Pt wires of 7.5 nm thickness, a designed width of 250 nm and 1.1 µm center-to-center distance

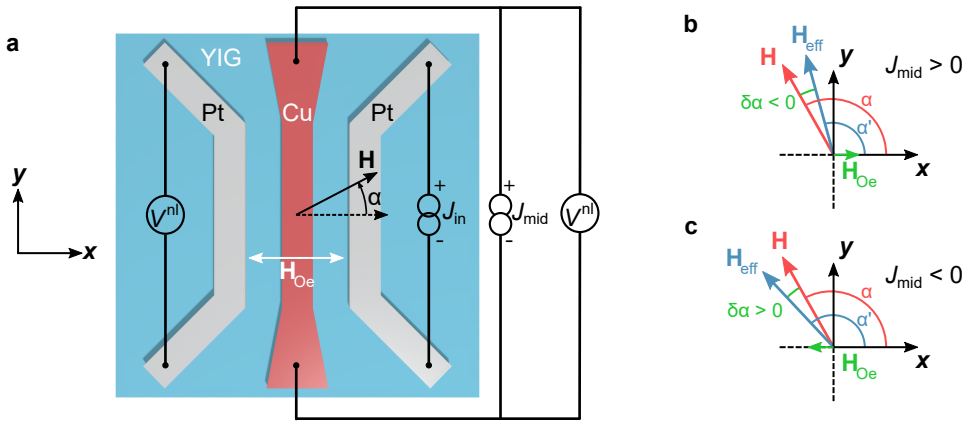

Figure 6.17: (a) Schematic view of the fabricated non-local device structure. Besides two parallel Pt wires, a third nanowire mainly comprised of Cu is positioned in the center of the device. Depending on the performed experiment, the electrical wiring changes. (b),(c) Illustration of the effective field $\mathbf{H}_{\mathrm{eff}} = \mathbf{H} + \mathbf{H}_{\mathrm{Oe}}$ and thus the angular shift $\delta\alpha$ for different charge current polarities applied to the Cu wire.

were fabricated on top of a commercial, single crystalline YIG film ($d_{\mathrm{YIG}} = 150\,\mathrm{nm}$, grown on GGG (111) by LPE). In a second fabrication step, the Cu manipulator wires of 250 nm designed width and 15 nm Cu thickness were patterned. To protect the copper of undesired long-term degradation via oxidation, it was capped by 5 nm of Al, which formed an AlOx protection layer when exposed to air.

To fully characterize the device and investigate the various signal contributions, different circuitry configurations were implemented (see Fig. 6.17a). Spin information exchange between the outer Pt stripes (Pt $\rightarrow$ Pt) was studied by connecting the right Pt wire (injector) to a Keithley 2400 source meter supplying the DC charge current $J_{\mathrm{in}} = \pm 250\,\mu\mathrm{A}$ ($j_{\mathrm{in}} \approx 1.3 \times 10^{11}\,\mathrm{A\,m^{-2}}$) used for the electrical (SHE) or thermal (SSE) excitation of magnons in the YIG. By means of the ISHE, the induced spin currents generate a voltage signal in the left Pt stripe (detector), which was picked up by a Keithley 2182A nanovoltmeter. With regard to the potential modulation of the spin current flow, the center Cu wire was connected to a Lakeshore 140 AC/DC current source, supplying a DC charge current J_{mid} of up to $\pm 1\,\mathrm{mA}$ ($j_{\mathrm{mid}} \lesssim \pm 2.29 \times 10^{11}\,\mathrm{A\,m^{-2}}$). In a different configuration, the direct response of the detector towards charge currents applied to the manipulator (Cu $\rightarrow$ Pt) was checked by connecting the latter to the source meter and leaving the Pt injector unbiased. Finally, to verify that the Cu center wire indeed reveals no spin-charge interconversion, it was connected to the nanovoltmeter while applying a charge current to the injector (Pt $\rightarrow$ Cu). In general, field or angular-dependent measurements were performed by sweeping the applied external field $\mathbf{H}$ or rotating the sample in it (in-plane

rotation angle α, see Fig. 6.17a). All measurements were conducted at room temperature. In view of the potential modulation of the magnon spin transport in the YIG, the amplitude of J_{mid} (charge current applied to the Cu manipulator) determines both the generated Joule heat and the magnitude of the Oersted field. At the same time, its polarity defines the direction of $\mathbf{H}_{\mathrm{Oe}}$. According to Ampère's law [24]

$$\oint \mathbf{H}_{\mathrm{Oe}} \mathrm{d}\mathbf{s} = J_{\mathrm{mid}}, \tag{6.4}$$

where $\oint \mathrm{d}\mathbf{s}$ integrates over a closed path around the middle wire. Considering that charge currents applied to the non-local device flow along the y-direction, $\mathbf{H}_{\mathrm{Oe}}$ exclusively exhibits an x- or z-component, of which only the former is of interest here with regard to an in-plane shape anisotropy of the relatively thin YIG film. Eventually, $J_{\mathrm{mid}} > 0$ results in a positive Oersted field underneath the Cu wire (x-component in $\alpha = 0°$ direction), whereas a negative J_{mid} yields an Oersted field component along $\alpha = 180°$. For the following discussions, it is useful to consider an effective field $\mathbf{H}_{\mathrm{eff}} = \mathbf{H} + \mathbf{H}_{\mathrm{Oe}}$ at the angle $\alpha' = \alpha + \delta\alpha$, which locally acts on the YIG magnetization. As sketched in Fig. 6.17b,c, in the range of $0° < \alpha < 180°$ the shift $\delta\alpha$ is negative for $J_{\mathrm{mid}} > 0$, while being positive for $J_{\mathrm{mid}} < 0$. For $180° < \alpha < 360°$, it is the opposite.

Finally, note that during this study it will become apparent that a simple distinction between electrically and thermally induced signals as given in Sec. 5.1 is not applicable. The generated Oersted fields induce an artificial signal contribution, which is why, as already done in the previous section, the generalized notation

$$V_{\Delta}^{\mathrm{nl}} = \left[V_{\mathrm{nl}}\left(+J\right) - V_{\mathrm{nl}}\left(-J\right)\right]/2., \tag{6.5}$$

$$V_{\Sigma}^{\mathrm{nl}} = \left[V_{\mathrm{nl}}\left(+J\right) + V_{\mathrm{nl}}\left(-J\right)\right]/2. \tag{6.6}$$

introduced in Eq. 5.1 and Eq. 5.2 is used in the following. Here, J is the charge current applied to either the Pt injector (J_{in}) or the Cu manipulator (J_{mid}), depending on the sample connection.

6.3.2 Results and discussion

To start with, the functionality of the non-local device and especially the absence of any spin-charge interconversion in the Cu wire were checked by implementing the different connection schemes described above and performing angular-dependent measurements. The results obtained for the Pt $\rightarrow$ Pt configuration, without any charge current applied to the Cu manipulator, are shown in Fig. 6.18a. In agreement with the spin current excitation model [22], the non-local voltages reveal the expected angular dependences for electrically

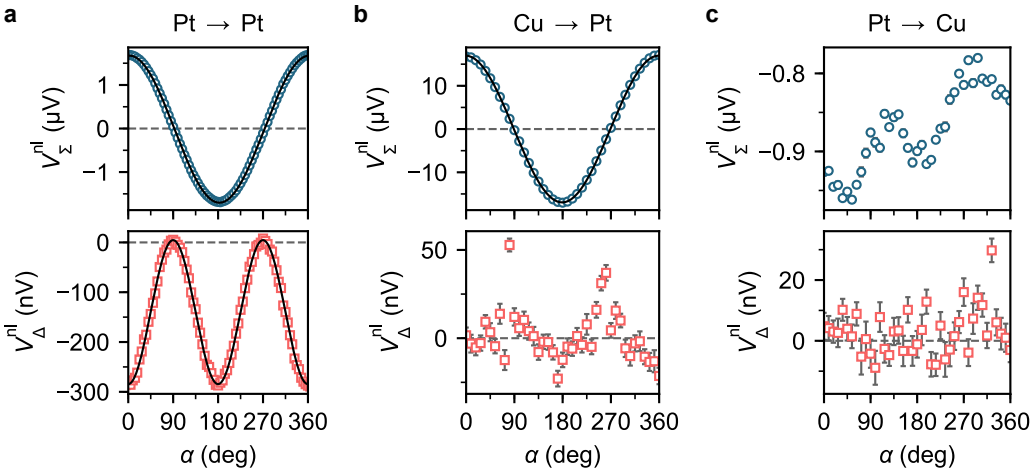

Figure 6.18: Non-local voltages due to electrical (V_Δ^{nl}) and thermal (V_Σ^{nl}) excitation of spin currents as a function of the in-plane field direction α. In (a), data obtained for Pt → Pt is shown, whereas (b) displays the results for Cu → Pt and (c) for Pt → Cu. In all graphs, solid lines give the results of corresponding fit functions. The external field amplitude is $\mu_0 H = 75\,\mathrm{mT}$. If visible, error bars give the standard error.

[$V_\Delta^{nl} \propto \cos^2(\alpha)$, see Eq. 3.18] and thermally excited magnon currents [$V_\Sigma^{nl} \propto \cos^2(\alpha)$, see Eq. 3.19]. Figure 6.18b, on the other hand, shows the non-local voltage tapped at the Pt detector when injecting a charge current into the Cu wire (Cu → Pt). As clearly visible, the dissipated Joule heat gives rise to the non-local SSE, which is captured by V_Σ^{nl}, while V_Δ^{nl} shows minor fluctuations and essentially remains zero. This matches the expectation, as Cu does not exhibit strong spin-orbit interaction and thus is not supposed to inject magnon currents by means of the SHE [68]. The higher amplitude of V_Σ^{nl} as compared to that observed in the Pt → Pt configuration is due to the smaller distance between the wires and a larger generated Joule heat ($\approx 6.40\,\mathrm{mW}$ vs. $\approx 0.73\,\mathrm{mW}$). Finally, the absence of a notable spin-to-charge conversion (ISHE) in Cu is verified by implementing the Pt → Cu configuration, see Fig. 6.18c. While V_Δ^{nl} fluctuates around zero, V_Σ^{nl} shows a finite, oscillating and slightly increasing voltage. This trend, however, does not correspond to the geometry of the non-local SSE, but is more likely due to the conventional Seebeck effect [128], which is always present. The sample temperature may not be stabilized, taking into account that the used setup was not fully isolated from the air flow in the laboratory, which is modulated by an air conditioning system.

Briefly speaking, the results shown so far demonstrate the functionality of the device with regard to the spin exchange mechanisms between the outer Pt stripes as well as the absence of any notable spin-charge conversion within the Cu wire. The latter information is crucial for the discussion of the experimental results shown in the following.

Spin signal excitation by the Cu wire

The sample characterization results presented in Fig. 6.18b reveal that when using the Cu manipulator as a spin signal generator (charge current applied to the manipulator only), solely thermal magnon currents (SSE) are excited while V_{Δ}^{nl} remains zero. This data, however, ignores the Oersted fields generated by J_{mid}, which may alter the result. The amplitude of the external field, in which the sample was rotated before, was $\mu_0 H = 75\,\mathrm{mT}$, which was presumably much larger than the magnitude of $\mathbf{H}_{\mathrm{Oe}}$ such that the additional torque of the Oersted field exerted on $\mathbf{M}_{\mathrm{YIG}}$ was negligible. Finite element simulations (see App. E) reveal that for $J_{\mathrm{mid}} = 1\,\mathrm{mA}$, a field amplitude of $\mu_0 H_{\mathrm{Oe}} \approx 1.4\,\mathrm{mT}$ (x-component) is induced at the wire center, directly underneath the YIG/Cu interface. While this gives an estimate for the order of magnitude of the Oersted field, $\mathbf{H}_{\mathrm{Oe}}$ exhibits a strong spatial variation and its amplitude decays inversely proportional with the distance to the manipulator wire according to Eq. 6.4. For that reason, the impact of the Oersted field is discussed qualitatively rather than quantitatively hereafter.

Based on that information, angular-dependent measurements in the Cu → Pt configuration were repeated at a reduced external field of $\mu_0 H = 5\,\mathrm{mT}$, which is 15 times smaller in amplitude than before but still large enough for the YIG magnetization to follow the field direction (see field-sweep measurement in Fig. 6.25a further below). Figure 6.19 displays the respective results, directly comparing the low and high field data obtained for V_{Σ}^{nl} and V_{Δ}^{nl}. In Fig. 6.19a, it shows that $\mathbf{H}_{\mathrm{Oe}}$ has insignificant impact on V_{Σ}^{nl} and thus the conventional non-local SSE signal is recorded. In terms of V_{Δ}^{nl}, which is odd in the direction of $\mathbf{H}_{\mathrm{Oe}}$, the angular dependence recorded at 5 mT however deviates significantly from the one measured at 75 mT: a finite voltage response of distinct angular dependence appears.

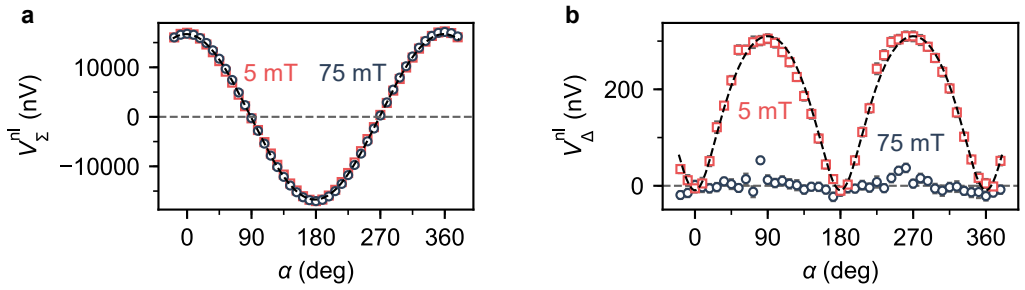

Figure 6.19: Angular dependence of (a) V_{Σ}^{nl} and (b) V_{Δ}^{nl} recorded using the Cu → Pt configuration. In each graph, the results obtained for low ($\mu_0 H = 5\,\mathrm{mT}$, blue circles) and high ($\mu_0 H = 75\,\mathrm{mT}$, red squares) external magnetic field amplitude are directly compared. Black dashed lines give the result of corresponding fit functions (please see main text). If visible, error bars give the standard error.

The symmetry of the signal does not agree with the one of electrically injected SHE spin currents, however it can be fitted by a function, whose structure will be discussed later in the text. The extracted amplitude is $(337 \pm 10)\,\mathrm{nV}$.

To deduce information on the origin of this additional signal, angular-dependent measurements covering a reduced range of angles have been repeated for different charge currents applied to the Cu wire, see Fig. 6.20. Considering first the non-local SSE, Fig. 6.20a,b shows V_Σ^{nl} as a function of α and J_{mid}, respectively. A quadratic current dependence is observed, which agrees with the thermal origin of the voltage. In the case of V_Δ^{nl}, fitting the data in Fig. 6.20c by the same function used in Fig. 6.19b and extracting the amplitude also reveals a quadratic current dependence, see Fig. 6.20d. While this indicates a thermal origin of V_Δ^{nl}, further information is required to fully understand this finding. Essentially, one has to reconsider the direction of $\mathbf{H}_{\mathrm{Oe}}$ and the induced angular shift $\delta\alpha$ as a function of

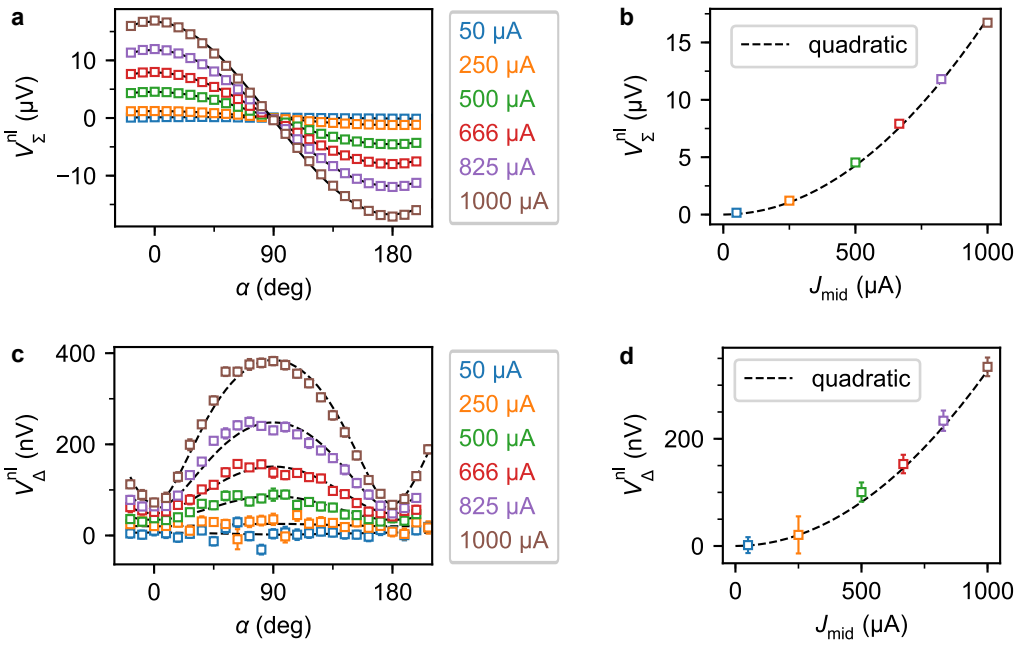

Figure 6.20: (a) V_Σ^{nl} and (c) V_Δ^{nl} as a function of the in-plane field direction α and charge current J_{mid}, recorded using the Cu $\rightarrow$ Pt configuration and an external field amplitude of $\mu_0 H = 5\,\mathrm{mT}$. Dashed lines give the result of corresponding fit functions (please see main text). (b) Non-local SSE amplitude extracted from (a) as a function of J_{mid} including a quadratic fit curve. (d) Current dependence of the V_Δ^{nl} amplitude, derived from the fit curves shown in (c). A fit function based on a quadratic (dashed line) current dependence is displayed. Error bars are (a),(c) given by the standard error as well as device inaccuracies and (b),(d) extracted from corresponding fit routines. If not visible, they are smaller than the symbol size.

the applied charge current J_{mid}. The largest $\delta\alpha$ is expected for $\alpha = 90°$, 270° (x-component of the external field is zero), whereas $\delta\alpha = 0°$ is anticipated for $\alpha = 0°, 180°$. This is verified by the data shown in Fig. 6.21, where the raw voltage tapped at the Pt detector is plotted as a function of J_{mid} at different magnetization directions. To do so, $\mathbf{M}_{\mathrm{YIG}}$ was aligned by means of the external field, which was switched off afterwards. In Fig. 6.21a ($\alpha = 0°$), one can see that V^{nl} increases symmetrically with increasing amplitude of J_{mid} and can be well fitted by a square function (red solid line). This agrees with the fact that the non-local SSE depends linearly on the generated Joule heat ($\propto J_{\mathrm{mid}}^2$) and verifies that the additional Oersted field is insignificant in this direction. For $\alpha = 90°$ in Fig. 6.21b, however, the signal is highly asymmetric, roughly following a cubic current dependence (red solid line). At this position, the positive (negative) voltage for $J_{\mathrm{mid}} > 0 \rightarrow \delta\alpha < 0$ ($J_{\mathrm{mid}} < 0 \rightarrow \delta\alpha > 0$) corresponds to a non-local SSE signal at $\alpha' < 90°$ ($\alpha' > 90°$), see Fig. 6.19a. Note that the imperfect point inversion with regard to $J_{\mathrm{mid}} = 0\,\mu\mathrm{A}$ is most likely due to a slight deviation of the equilibrium sample magnetization from $\alpha = 90°$. The relevance of $\mathbf{H}_{\mathrm{Oe}}$ becomes further evident in Fig. 6.21c,d, in which $\mathbf{M}_{\mathrm{YIG}}$ was initially aligned along $\alpha = 45°$

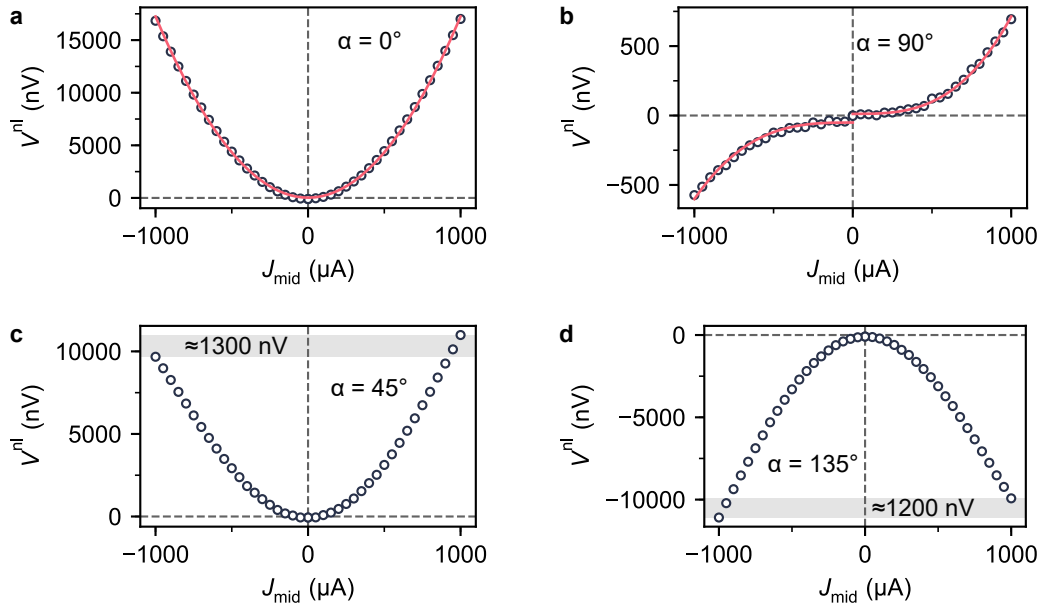

Figure 6.21: Raw voltage V^{nl} tapped at the Pt detector as a function of the charge current J_{mid} applied to the Cu manipulator. In the subgraphs, the external field is applied in different directions: (a) $\alpha = 0°$, (b) $\alpha = 90°$, (c) $\alpha = 45°$ and (d) $\alpha = 135°$. The red solid line in (a) corresponds to a quadratic fit function, whereas the one in (b) describes a cubic current dependence. The gray shaded areas in (c),(d) mark voltage level asymmetries for positive and negative polarity of J_{mid} During the measurements, the external field was shut off. Error bars accounting for the standard error ar smaller than the symbol size.

and $\alpha = 135°$, respectively. While the opposite signs of the voltages signify the reversed x-components of $\mathbf{M}_{\mathrm{YIG}}$, the inverted asymmetries with regard to the polarization of J_{mid} corroborate the Oersted field effect. For $\alpha = 45°$, a positive or negative J_{mid} applied to the Cu manipulator results in $\alpha' < 45°$ or $\alpha' > 45°$, respectively, explaining the distinct difference in amplitude (compare to Fig. 6.19a). At the same time, for $\alpha = 135°$, a positive or negative charge current through the Cu wire results in $\alpha' < 135°$ or $\alpha' > 135°$, again giving different voltage amplitudes.

With this information, one can understand the appearance of a finite V_{Δ}^{nl} at low fields and explain its functional dependence, e.g. in Fig. 6.19b. Briefly speaking, V_{Δ}^{nl} measures the difference between the x-components of thermally excited magnonic spin currents, to which the ISHE in the Pt detector is sensitive, induced under the influence of the reversed Oersted fields. While the latter have noticeable impact at low external field amplitudes ($\delta\alpha \neq 0$), V_{Δ}^{nl} becomes zero at large external fields due to $\mathbf{H}_{\mathrm{eff}} \simeq \mathbf{H}$ ($\alpha' \simeq \alpha$) for the charge current amplitudes applied to the manipulator in this work.

Based on this conclusion, the fit function used in Fig. 6.19b and Fig. 6.20c reconstructs the difference between angular-dependent, normalized x-components of the effective fields $\tilde{H}_{\mathrm{eff}}^{x} = H_{\mathrm{eff}}^{x}/H_{\mathrm{eff}}$ for positive and negative Oersted field, with the amplitude of the latter serving as a fit parameter (the external field value is known). $\tilde{H}_{\mathrm{eff}}^{x}(\alpha)$ is further multiplied by a proportionality factor, e.g. shown in Fig. 6.20d. Eventually, the Oersted field amplitude determines the shape of the signal and for $J_{\mathrm{mid}} = 1\,\mathrm{mA}$, a value of $(2.68 \pm 0.10)\,\mathrm{mT}$ is extracted. While this value roughly agrees with what is obtained from the finite element simulations, for such large Oersted fields as compared to the external field one calculates at $\alpha = 90°$ an angular shift of $\delta\alpha \approx \pm 28°$. According to Fig. 6.19a, at first view one would thus expect a V_{Δ}^{nl} amplitude of several µV instead of a few hundred nV, which complies with a significantly smaller angular shift of $\delta\alpha \approx \pm 0.6°$. The observed amplitude deviation can be understood when considering that the Oersted field effect is restricted to a limited sample volume as compared to that which provides the non-local SSE captured by V_{Σ}^{nl}.

Furthermore, the conclusion that V_{Δ}^{nl} is given by thermal spin currents allows one to understand the cubic functional dependence of V^{nl} on J_{mid} in Fig. 6.21b. Reviewing Eq. 3.19, the non-local voltage induced by SSE spin currents is proportional to the Joule heat generated ($\propto J_{\mathrm{mid}}^2$) and to the x-component of $\mathbf{M}_{\mathrm{YIG}}$:

$$V_{\mathrm{nl}}^{\mathrm{therm.}} \propto \cos(\alpha') \cdot J_{\mathrm{mid}}^2. \tag{6.7}$$

At $\alpha = 90°$, this can be written as

$$V_{\mathrm{nl}}^{\mathrm{therm.}} \propto \sin(\delta\alpha) \cdot J_{\mathrm{mid}}^2 \approx \delta\alpha J_{\mathrm{mid}}^2 \tag{6.8}$$

for small $\delta\alpha$. This assumption appears reasonable when comparing the amplitudes of V^{nl} for $J_{\mathrm{mid}} = \pm 1\,\mathrm{mA}$ at $\alpha = 0°$ and $\alpha = 90°$ in Fig. 6.21a,b ($\approx 17\,500\,\mathrm{nV}$ vs. $\approx \pm 700\,\mathrm{nV}$). As mentioned before, at $\alpha = 90°$ a finite x-component of $\mathbf{M}_{\mathrm{YIG}}$ is solely provided by $\mathbf{H}_{\mathrm{Oe}}$ such that, according to Eq. 6.4, $\delta\alpha \propto J_{\mathrm{mid}}$. Consequently, Eq. 6.8 yields

$$V_{\mathrm{nl}}^{\mathrm{therm.}} \propto J_{\mathrm{mid}}^{3}. \tag{6.9}$$

Among other things, the proportionality factor is eventually determined by the amplitude of $\mathbf{H}$.

Taken all together, the results presented so far demonstrate that even when using a metal wire with weak spin orbit interaction, a finite V_{Δ}^{nl} can appear. Here, this voltage is not generated due to SHE induced spin currents, but is given by the different x-components of thermal spin currents generated in the presence of reversed Oersted fields.

Spin transport modulation by heat and Oersted fields

As described in the introduction, the non-local device sketched in Fig. 6.17 was actually realized to probe whether the Cu manipulator wire allows one to tune the spin information exchange in between the outer Pt stripes. In previous works by Cornelissen *et al.* [261], it was demonstrated that when employing a heavy metal such as Pt as the manipulator material, additional spin currents injected via the SHE alter the magnon spin conductivity σ_{m} and hence the amplitude of the detected signal. In this study, however, due to the absence of the SHE in Cu, solely the impact of the previously discussed Oersted fields as well as of Joule heating, i.e., additional SSE currents flowing in the YIG or a locally reduced YIG magnetization, is investigated.

Focusing first on the potential effect of Joule heating, angular-dependent measurements implementing the Pt $\rightarrow$ Pt configuration (see Fig.6.18a) were repeated for $J_{\mathrm{mid}} = 0\,\mathrm{mA}$ and $J_{\mathrm{mid}} = +1\,\mathrm{mA}$. Furthermore, the sample was rotated in an external field of $\mu_0 H = 75\,\mathrm{mT}$ to suppress any influence by the Oersted field component. As can be seen in Fig. 6.22a, the variation of V_{Σ}^{nl} due to J_{mid} is trivial considering a merely enhanced amplitude caused by the supplemental heat applied to the system. This data further emphasizes that, due to its definition, V_{Σ}^{nl} is given by magnonic spin currents that are excited thermally near both the injector and manipulator. Instructive information of the spin transport mechanism between the Pt wires, which is this study's focus, is hence only given by V_{Δ}^{nl}, which averages out the manipulator's contribution. On that account, V_{Σ}^{nl} will be disregarded hereafter except for required characterization measurements.

Figure 6.22b now shows the angular-dependent data obtained for V_{Δ}^{nl}, for which, at first glance, it seems that switching on the charge current flow through the Cu wire yields no

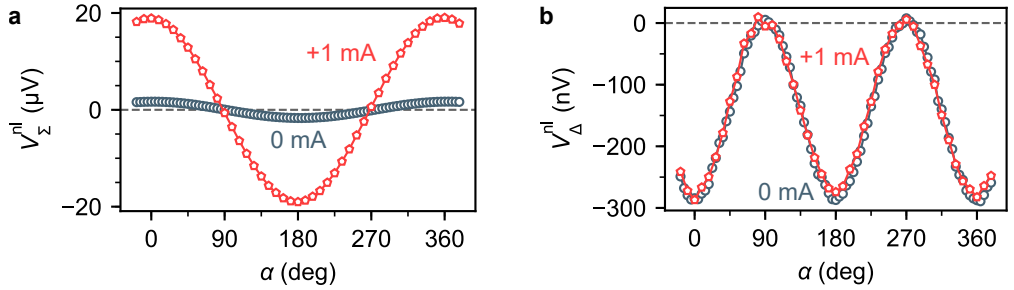

Figure 6.22: Angular dependence of (a) V_Σ^{nl} and (b) V_Δ^{nl} recorded using the Pt → Pt configuration and directly compared for different charge currents applied to the Cu manipulator ($J_{mid} = 0\,mA$, $+1\,mA$). The amplitude of the external field is $\mu_0 H = 75\,mT$.

striking modification of the spin transport signal. For both $J_{mid} = 0\,mA$ and $J_{mid} = +1\,mA$, the expected $\cos^2(\alpha)$ angular dependence is observed and similar signal amplitudes are obtained: $V_\Delta^{nl}(0\,mA) = (-282 \pm 5)\,nV$ and $V_\Delta^{nl}(+1\,mA) = (-280 \pm 4)\,nV$. To nonetheless identify potential deviations from the conventional mechanism of electrically induced spin transport, which may not be significant, the experimental data was fitted using $V_\Delta^{nl} \propto \cos^2(\alpha)$ and the resultant curve was subtracted from the data. The calculated residuals are displayed in Fig. 6.23. While for zero applied charge current (Fig. 6.23a) the residuals fluctuate around 0 V without significant variation as a function of α, one can perceive an angular-dependent alteration of $V_\Delta^{nl,res}$ for $J_{mid} = +1\,mA$ (Fig. 6.23b). Assuming the symmetry of the signal, the data can be fitted phenomenologically by a cosine function, with the fit routine giving an amplitude of $(3.68 \pm 0.78)\,nV$. The goodness of the fit is

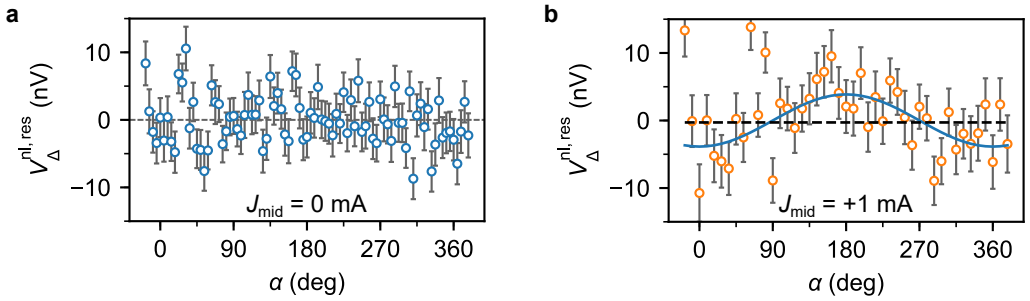

Figure 6.23: Residuals of the electrically induced non-local voltages V_Δ^{nl} from Fig. 6.22b for (a) $J_{mid} = 0\,mA$ and (b) $J_{mid} = +1\,mA$. The residuals are calculated by fitting the data in Fig. 6.22b by a corresponding function ($V_\Delta^{nl} \propto \cos^2(\alpha)$) and subtracting the resultant curve from the raw data. Displayed error bars are provided by error propagation the standard error of the original measurement data and fitting errors. In (b), the blue solid line gives a phenomenological fit curve ($V_\Delta^{nl,res} \propto \cos(\alpha)$), while the black dashed line considers no signal modulation (mean value).

checked by the *reduced* χ^2 method [273], which allows one to evaluate whether the data are consistent with the proposed model (null hypothesis) or whether the null hypothesis is to be rejected. For the cosine function, a reduced chi-squared of $\chi^2_{\mathrm{red}} \approx 0.98$ is obtained, which means that the data is well described by the function [273]. In addition, an alternative hypothesis of no signal modulation is tested, which is described by a horizontal line given by the mean value of the measurement data. Here, a reduced chi-squared of $\chi^2_{\mathrm{red}} \approx 2.71$ is obtained such that the alternative hypothesis can be rejected [273]. Altogether, this means that the observed signal modulation is significant. One may thus speculate that the diffusive SSE current, whose polarization depends on the direction of $\mathbf{M}_{\mathrm{YIG}}$ and thus rotates as a function of α, may interact with electrically induced magnon currents flowing. Note that the enhanced YIG temperature due to Joule heating entails a local reduction of the magnetization [179]. One would assume that this leads to a general decrease of the signal amplitude that further would be independent of α, which is not observed here. To obtain a better understanding of this effect and to explain the observed angular dependence quantitatively, theoretical considerations are required.

As a next step, the potential influence of the created Oersted fields on magnonic spin information transport was investigated. Following a similar strategy as in the first part of this study, angular-dependent measurements were repeated at, in relation to H_{Oe}, high and low external magnetic fields at a fixed $J_{\mathrm{mid}} = +1\,\mathrm{mA}$. In Fig. 6.24a, V^{nl}_{Δ} is shown as a function of α and the applied field amplitude. Both signals reveal similar angular dependences and for $\alpha = 0°$, 180° and 360°, at which the external field shows in x-direction, they further exhibit equal amplitudes. For $\alpha = 90°$ and $\alpha = 270°$ (**H** parallel to the Pt

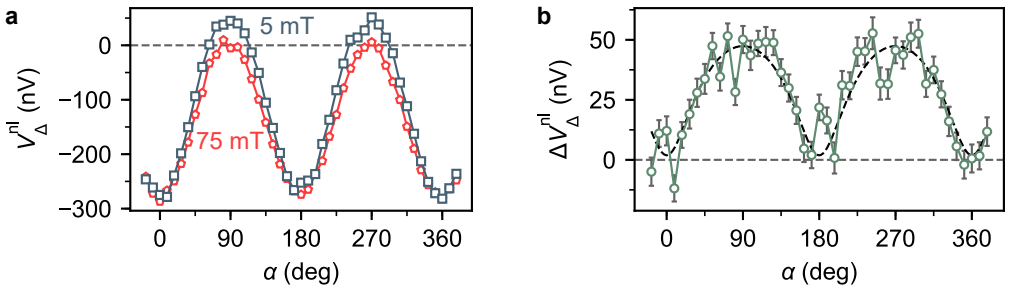

Figure 6.24: (b) Electrically induced non-local voltage V^{nl}_{Δ} obtained for the Pt → Pt configuration as a function of the in-plane field direction α. A charge current $J_{\mathrm{mid}} = +1\,\mathrm{mA}$ is applied to the Cu manipulator and the results for low ($\mu_0 H = 5\,\mathrm{mT}$, blue squares) and high ($\mu_0 H = 75\,\mathrm{mT}$, red pentagons) external magnetic field amplitude are compared. (b) Differential signal $\Delta V^{\mathrm{nl}}_{\Delta} = V^{\mathrm{nl}}_{\Delta}(5\,\mathrm{mT}) - V^{\mathrm{nl}}_{\Delta}(75\,\mathrm{mT})$ as a function of α, error bars are obtained by error propagation. The dashed black line corresponds to the adjusted fit function already used in Fig. 6.19b.

stripes), however, the non-local spin signals differ as V_Δ^{nl} is zero at 75 mT and exhibits a finite, positive value at 5 mT. The differential signal $\Delta V_\Delta^{\mathrm{nl}} = V_\Delta^{\mathrm{nl}}(5\,\mathrm{mT}) - V_\Delta^{\mathrm{nl}}(75\,\mathrm{mT})$ is shown in Fig. 6.24b. At first thought, this result seems to suggest that the generation of Oersted fields indeed alters the conductance of the YIG for detectable magnon spin currents. In a simple picture based on the findings discussed above, one may assume that $\mathbf{H}_{\mathrm{Oe}}$ cants $\mathbf{M}_{\mathrm{YIG}}$ away from the $\alpha = 90°, 270°$ directions, at which no magnons can be injected or detected by the Pt stripes via SHE or ISHE. If $\mathbf{H}_{\mathrm{Oe}}$ would be strong enough to induce a finite x-component of $\mathbf{M}_{\mathrm{YIG}}$ even underneath injector and detector, this would render these processes possible again. Nevertheless, the positive sign of $\Delta V_\Delta^{\mathrm{nl}}$ in Fig. 6.24b contradicts this assumption. Just as for the signal induced at large external fields, such an artificially created ISHE voltage ought to be negative and not positive. Consequently, $\Delta V_\Delta^{\mathrm{nl}}$ must be of different origin.

To obtain information on the source of $\Delta V_\Delta^{\mathrm{nl}}$, field and current sweep measurements were performed at different angles. Starting with the field dependence, Fig. 6.25a,b shows V_Σ^{nl} as a function of H and J_{mid} for $\alpha = 0°$ and $\alpha = 90°$. In Fig. 6.25a, spin-thermovoltage hysteresis loops can be seen with larger voltage amplitudes for $J_{\mathrm{mid}} = \pm 1$ mA as compared

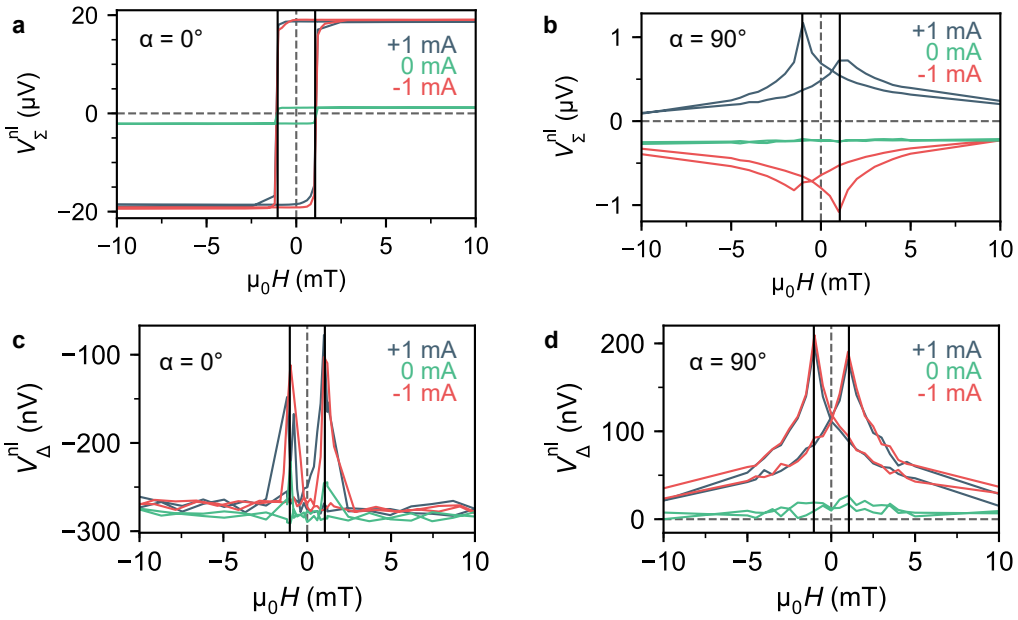

Figure 6.25: Linear field sweep of the (a),(b) thermally (V_Σ^{nl}) and (c),(d) electrically (V_Δ^{nl}) induced non-local voltage signal for different charge currents $J_{\mathrm{mid}} = 0\,\mathrm{mA}, \pm 1\,\mathrm{mA}$ applied to the Cu manipulator. In (a),(c), the (positive) field is aligned along $\alpha = 0°$, while in (b),(d) it shows in the $\alpha = 90°$ direction. The black vertical lines mark the coercive field values of the YIG film.

to $J_{\mathrm{mid}} = 0\,\mathrm{mA}$ due to the increased heat applied to the system. Since the signal reflects the in-plane magnetization of the YIG, the voltage switching fields correspond to the coercive fields $H_{\mathrm{c}}^{\pm}$ of the YIG layer. In the graphs of Fig.6.25, $\mu_0 H_{\mathrm{c}}^{\pm} \simeq \pm 1\,\mathrm{mT}$ is marked by black vertical lines. Figure 6.25b now shows V_{Σ}^{nl} at $\alpha = 90°$, for which no thermal signal should appear. The finite voltage for $J_{\mathrm{mid}} = 0\,\mathrm{mA}$ is most likely due to an imperfect alignment of the sample in the field or the conventional Seebeck effect. The different signs of V_{Σ}^{nl} obtained for finite charge currents applied to the Cu manipulator, on the other hand, are the result of the generated Oersted fields, which yield a negative ($J_{\mathrm{mid}} = +1\,\mathrm{mA}$) or positive ($J_{\mathrm{mid}} = -1\,\mathrm{mA}$) angular shift $\delta\alpha$ at $\alpha = 90°$.

For V_{Δ}^{nl}, which essentially should not include thermal spin current information from the manipulator, the field dependence looks qualitatively different. At $\alpha = 0°$, the non-local voltage is mostly independent of J_{mid}, as already discussed for Fig. 6.24a. The signal peaks near $H_{\mathrm{c}}^{\pm}$ are due to the YIG magnetization reversal and the associated formation of magnetic domains, which impede the spin transport due to random magnetization alignment. For finite J_{mid}, the peaks are broader and of larger amplitude, which signifies a more pronounced domain formation, at least near the manipulator, in the presence of the Oersted field. More significant information is obtained when considering $\alpha = 90°$ in Fig 6.25d. In the case of $J_{\mathrm{mid}} = 0\,\mathrm{mA}$, the non-local voltage basically is zero except for a small positive deflection at low fields. At the same time, $J_{\mathrm{mid}} = \pm 1\,\mathrm{mA}$ results in distinct voltage amplitude that become largest at the coercive fields of the YIG layer. In contrast to the thermal signal in Fig. 6.25b, however, the voltage is exclusively positive, irrespective of the polarity of J_{mid} and, hence, the direction of $\mathbf{H}_{\mathrm{Oe}}$. On that account, in contrast to the findings reported in the first part of this work, V_{Δ}^{nl} cannot be directly given by the SSE current generated near the Cu wire. Nevertheless, the distinct field dependence implies a general correspondence between V_{Δ}^{nl} and the absolute amplitude of $\mathbf{H}_{\mathrm{Oe}}$.

Checking further the dependence of V_{Δ}^{nl} on the amplitude and the direction of the generated Oersted field, Fig. 6.26 shows V_{Δ}^{nl} as a function of J_{mid} for different angles α and external fields (large vs. no field). Please recall that J_{mid} is the current applied to the manipulator and therefore has no direct impact on the magnitude of the electrically excited spin current in the Pt injector. In agreement with the results shown above, V_{Δ}^{nl} exhibits no distinct change for J_{mid} at relatively large external fields ($\mu_0 H = 75\,\mathrm{mT}$) for all magnetization directions, which also holds for low fields and $\alpha = 0°$ (Fig. 6.26a). At $\alpha = 90°$ V_{Δ}^{nl}, however, V_{Δ}^{nl} exhibits a symmetric increase with increasing current amplitude, see Fig. 6.26b. Without further presumptions, the resultant data is well fitted by a quadratic function (black solid line), which points out a thermal origin of the signal. For $\alpha = 45°$ and $\alpha = 135°$ in Fig. 6.26c,d the signals also increase, however, the growth is asymmetric and furthermore inverted for the different angles.

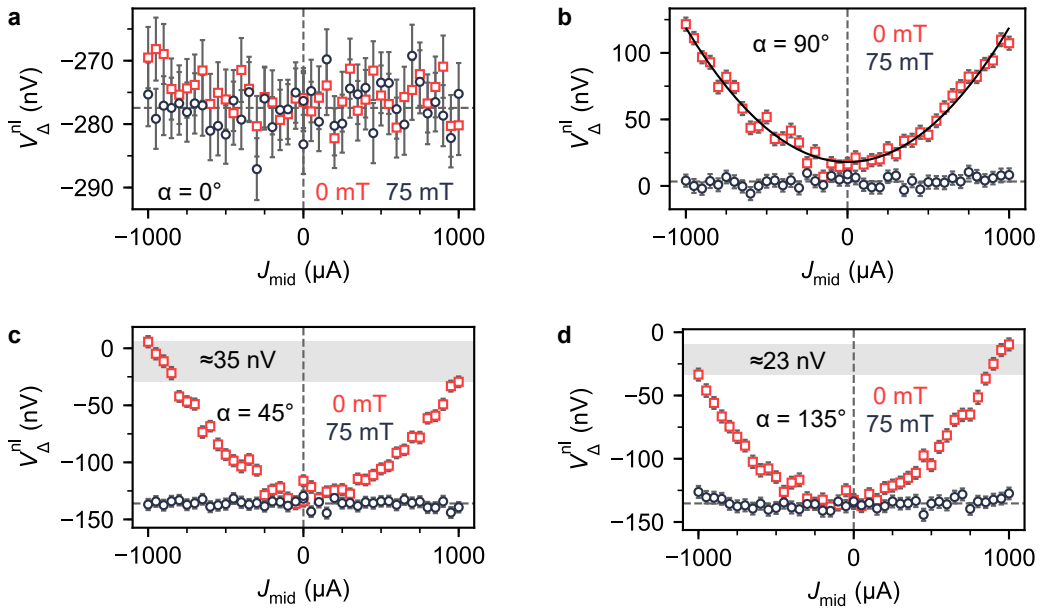

Figure 6.26: Current (J_{mid}) dependence of the electrically induced non-local voltage V_Δ^{nl} for different external field directions [(a) $\alpha = 0°$, (b) $\alpha = 90°$, (c) $\alpha = 45°$ and (d) $\alpha = 135°$]. Furthermore, the results obtained for zero applied field (red squares) and an external field amplitude of $\mu_0 H = 75\,\mathrm{mT}$ (blue circles) are directly compared. The black solid line in (b) corresponds to a quadratic fit function, while the gray shaded areas in (c),(d) mark voltage level asymmetries for positive and negative polarity of J_{mid}. Error bars are given by the standard error.

Taken all together, one can develop a model to explain the observed signal modulation $\Delta V_\Delta^{\mathrm{nl}}$ (Pt $\rightarrow$ Pt configuration) at low fields and finite charge currents J_{mid} applied to the Cu wire. To begin with, one has to bear in mind that the Joule heat generated in the Cu wire does not act locally but diffuses in the sample. Since the phonon propagation length in YIG is in the range of several hundred micrometer [274], this means that the thermal equilibrium of the system is also strongly disturbed underneath the Pt injector (and detector). Considering now that the charge current J_{in} applied to the injector as well is entailed by localized Oersted fields, on can anticipate that $\Delta V_\Delta^{\mathrm{nl}}$ is due to a difference between the x-components of thermally excited magnonic spin currents underneath the injector. It thus shares a similar origin with the non-local differential signal observed in the first part of this study (Cu $\rightarrow$ Pt configuration), which is further corroborated by the fact that V_Δ^{nl} in Fig. 6.19b and $\Delta V_\Delta^{\mathrm{nl}}$ shown in Fig. 6.24b reveal a comparable angular dependence.

Besides the heat provided by the Cu manipulator, its Oersted field can be used to explain the asymmetries of V_Δ^{nl} with regard to the sign of J_{mid} in Fig. 6.26c,d. Please note that the

observed asymmetry is opposite to that of V^{nl} in Fig. 6.21c,d, however, this is due to the different signal types shown (bare vs. differential voltage). Regarding first $\alpha = 45°$, one has to recall that $J_{\mathrm{mid}} > 0$ corresponds to a negative angular shift, i.e., $\alpha' = \alpha + \delta\alpha < 45°$, whereas $\alpha' > 45°$ for $J_{\mathrm{mid}} < 0$. This angular shift is either strengthened or weakened by the local Oersted field generated by the Pt injector, depending on polarity of J_{in}. Considering now that V_{Δ}^{nl} is a differential voltage signal, the slope of the original non-local SSE voltage at α' is decisive. The non-local SSE follows a $\cos(\alpha')$ symmetry such that

$$\mathrm{abs}\left(\partial V_{\Sigma}^{\mathrm{nl}}/\partial\alpha'\right)\Big|_{\alpha'=45°-} < \mathrm{abs}\left(\partial V_{\Sigma}^{\mathrm{nl}}/\partial\alpha'\right)\Big|_{\alpha'=45°+}.$$

As visualized in Fig. 6.27, one therefore expects a larger amplitude of V_{Δ}^{nl} for $J_{\mathrm{mid}} < 0$ as compared to $J_{\mathrm{mid}} > 0$, which agrees with what is observed in Fig. 6.26c. An analogous argumentation can be used to explain the inversed asymmetry for $\alpha = 135°$ (Fig. 6.26d).

As a final remark, please note that in recent work reported an exponentially decreasing electrical resistivity of YIG when exposed to strong local heating during non-local measurements [185]. YIG behaves like a large gap semiconductor such that at elevated temperatures ($T \gg 300\,\mathrm{K}$) parasitic, electrically transmitted voltages may interfere with the magnon mediated signals. One thus has to be careful, as this effect can become of significance when applying large current densities and thus creating enhanced Joule heating in non-local devices. However, the current densities applied here ($\approx 2.29 \times 10^{11}\,\mathrm{A\,m^{-2}}$) are significantly smaller as compared to given critical values in Ref. [185] and, furthermore, the distinct field and angular dependences observed in this work cannot be explained by this effect.

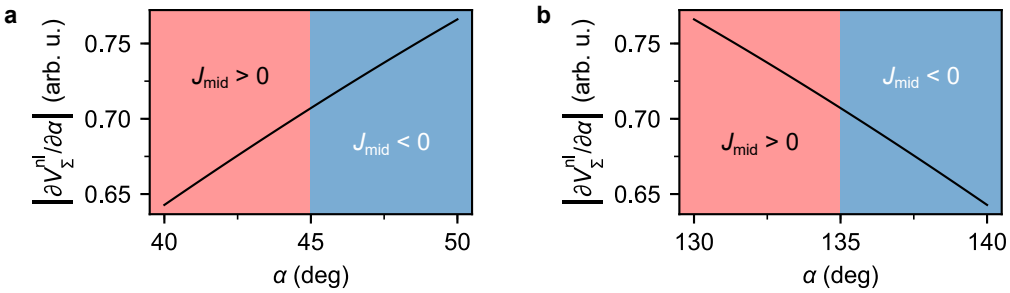

Figure 6.27: First derivative of $V_{\Sigma}^{\mathrm{nl}} \propto \cos(\alpha)$ near (a) $\alpha = 45°$ and (b) $\alpha = 135°$ in arbitrary units to visualize the origin of the asymmetry in Fig. 6.26c,d for $J_{\mathrm{mid}} \gtrless 0$.

6.3.3 Conclusion

To conclude, spin-transport experiments were performed in a modified non-local device structure to study the impact of heat and local Oersted fields on the magnonic spin transport mechanism in YIG. In addition to two Pt stripes, which are used as spin current injector and detector, the device comprises a third nanowire (mainly constituted of Cu) placed in the center, which is denoted as manipulator. Due to the absence of significant spin-charge interconversion by means of the SHE or its inverse, applying a charge current to this wire only results in Joule heating and the generation of local Oersted fields.
In a first experiment, non-local measurements were performed, during which a charge current was exclusively applied to the Cu manipulator while leaving the Pt injector unbiased. In that manner, spin signals directly generated by the manipulator were investigated and identified. Besides the conventional non-local SSE, see Sec. 5.1, a finite amplitude of V_{Δ}^{nl} is observed at low external magnetic fields similar in magnitude as compared to the generated Oersted field. Regarding its angular and current dependence, this signal is concluded to originate from thermal spin currents excited at slightly different YIG magnetization orientations underneath the manipulator.
In a second experiment, the impact of the additional heat and Oersted fields provided by the manipulator on the spin transport between the outer Pt stripes was investigated. Since the sum signal V_{Σ}^{nl} comprises various thermal contributions, only the differential signal V_{Δ}^{nl} was considered. Checking first the influence of heat, angular dependent measurements were performed at enhanced external fields and the results obtained for zero and finite charge current applied to the manipulator were compared. In the presence of supplemental Joule heat, the signal residuals reveal an angular-dependent variation, which may indicate a spin current modulation due to thermally excited magnons propagating in the YIG. To obtain a better as well as quantitative understanding of this effect, further theoretical and experimental investigations are required. Regarding the experiment, this may involve a modified device structure with a displaced manipulator at different positions or, potentially, a wide Cu gate spreading over the Pt wires. In addition to the heating effect, the impact of the Oersted field generated by the manipulator was examined by comparing non-local data obtained at high and low external fields. An angular-dependent modulation of V_{Δ}^{nl} is observed, whose origin is similar to that of V_{Δ}^{nl} when using the Cu manipulator as injector, namely the difference of thermal spin currents excited at slightly different YIG magnetization orientations underneath the Pt injector. One can thus conclude that the created Oersted field is sufficient to generate a spin current signal without the need for external fields. To increase the impact of the Oersted field, thinner YIG samples might be considered.

7 Conclusion and outlook

Conclusion

In this thesis, fundamental aspects of magnon spintronics such as the propagation, manipulation and detection of pure spin currents have been investigated. The presented results suggest new routes to follow in this complex field of research, while revealing at the same time some of the remaining challenges that need to be overcome for the large-scale implementation of magnonic devices.

Focusing first on spin transport, the non-local generation and detection of thermal magnon currents, i.e., the non-local spin Seebeck effect (SSE) has been investigated in the ferrimagnetic insulator yttrium iron garnet (YIG). When measured as a function of temperature and distance, a sign change of the non-local SSE is observed, which can be explained by the formation of magnon depletion and accumulation regions in the YIG in combination with a temperature-dependent magnon propagation length ξ. Additionally, an interface dependence of d_0 (the critical distance at which the sign change appears) is revealed by both studying different injector/detector materials and exploiting the formation of a frustrated YIG surface magnetization. Field-dependent data supports the assumption of competing signal contributions due to spin transport and the de-localized generation of spin currents given in other works. Altogether, the obtained results and findings show that, in terms of prospective magnon spintronics applications, both the device structure and fabrication process need to be designed carefully when implementing spin information transport via thermally excited magnons. Not only the signal amplitude, but also the magnon type probed strongly depend on various parameters such as the total sample thickness, the injector-detector distance or the interface structure. Additionally, the de-localized generation of spin currents must be taken into account, which could become problematic considering that, in a potential device, multiple non-local structures would need to be located in close proximity to each other in order to obtain a high information density.

After exploring the basic principles of non-local spin information exchange via thermal spin currents, the latter were used in a further, differently conceptualized spin transmission experiment to probe the mechanism of spin transport (electronic vs. magnonic) across the metallic antiferromagnet $Ir_{20}Mn_{80}$. More recent advances in the field of antiferromagnetic spintronics have generated an enhanced interest in this material class regarding advantageous features such as an insensitivity towards field perturbations or the lack of stray

fields. Regarding $Ir_{20}Mn_{80}$, the comparison of temperature-dependent measurement results obtained for various sample configurations and spin dynamics simulations performed at the University of Konstanz shows that magnonic spin transport is significant. In the temperature region in which antiferromagnetic order is established, spin transport across $Ir_{20}Mn_{80}$ is strongly suppressed, which is explained by an emerging antiferromagnetic magnon frequency gap. It is thus shown that metallic antiferromagnets could, in principle, find application in high frequency spin wave concepts considering their ability to forward information by antiferromagnetic magnons and, at the same time, the fact that they can interconvert spin and charge information by means of the (inverse) spin Hall effect [(I)SHE]. Regarding the concept of a potential magnonic spin valve, they could furthermore be used to exert additional exchange bias on adjacent ferromagnetic layers.

One of the main challenges of magnon spintronics, in terms of being a reasonable supplement or replacement of conventional electronics, is the efficient generation and detection of magnonic spin currents by charge signals. In this regard, the ISHE in binary copper-iridium alloys of varying composition has been investigated using both steady state and ultrafast SSE stimuli. For both cases, a matching complex compositional dependence is observed with a maximum near 40 % of Ir content, which is explained by the presence of intrinsic and extrinsic SHE contributions and a varying spin diffusion length in the alloy. Thus, one can actively tune and optimize the spin-charge interconversion efficiency in the alloy by its composition. Furthermore, the equal evolution of the ISHE in the DC and THz dynamics regimes signifies that the investigated material can be readily used in existing spintronic applications that have been transferred to ultrafast time scales.

A distinct feature of magnon-based data handling is the ability to perform logic operations, as recently demonstrated by the successful realization of a majority gate. The performance of complex operations requires a sufficiently large set of different gates, which must be scalable. Inspired by this, spin pumping experiments have been performed in YIG/CoO/Co multilayers in the prospect of creating a spin valve or switch-like effect. The spin current emitted by the YIG layer at ferromagnetic resonance is detected by the ISHE in Co, for which the exchange bias exerted by the CoO layer enables both parallel and antiparallel alignment relative to the YIG magnetization. Along with a secondary signal due to spin rectification, the experimental results indeed reveal a magnetization orientation-dependent spin current detection in Co with an ISHE signal that is approximately 120 % larger in the antiparallel state as compared to the parallel state. This *magnon spin valve effect* essentially can be seen as a further building block of magnon logic, as it allows one to implement a switch-like device that either permits or suppresses the forwarding of spin information by charge signals.

Depending on the design of a prospective magnon spintronics device, ferromagnetic res-

onance spin pumping may be unfeasible in terms of magnonic spin current generation. Furthermore, for the explanation of the observed magnon spin valve effect both an intrinsic and magnonic origin can be considered, which requires further clarification. To this end, non-local spin transport experiments have been conducted using two parallel metallic wires, one comprised of paramagnetic Pt and the other of a multilayer stack including the ferromagnet $Co_{60}Fe_{20}B_{20}$, deposited on YIG, which acts as a spin conduit. A Cu interlayer between YIG and CoFeB exchange decouples the ferromagnets and ensures electronic spin transport to and from the CoFeB such that the aforementioned magnonic origin can be neglected. Field-dependent measurements, in which the angle between the YIG and CoFeB magnetization is varied, demonstrate that the generation and detection efficiency of pure spin currents in CoFeB depends on its magnetization direction. This finding generally supports the validity of the magnon spin valve effect and, in view of the electronic spin transport to and from CoFeB, affirms the existence of a spin-dependent (inverse) spin Hall effect in the investigated metallic ferromagnets. Furthermore, the implementation of an alignment-dependent spin current detection in a non-local transport structure promotes the usage of the magnon spin valve effect in future magnon spintronics applications.
Targeting a different approach to create magnon logic, potential methods to manipulate the transport of magnons and thus information transmission in YIG have been investigated in the last project presented in this thesis. In a non-local device, spin information exchange between two Pt wires has been modulated by means of large charge currents applied to a third manipulatore wire in the center, which was mainly comprised of non spin Hall active Cu and thus solely provided additional heat and Oersted fields. At reduced external field amplitudes, the impact of the created Oersted fields is expressed as a supplemental signal, which can be explained by the induced tilting of the polarization vectors of thermal magnon currents that are generated near the Pt injector or the Cu manipulator. Consequently, on can thus use Oersted fields to generate an additional spin transport signal without the need for external fields alongside the charge-spin conversion in the injector due to the spin Hall effect. Beyond the Oersted field effect, an angular-dependent variation of the spin transport signal via additional Joule heating is observed, which allows one to modulate the transmitted spin signal to some extent. At last, together with the magnon spin valve effect these results demonstrate that various approaches can be pursued in order to realize magnon logic operations.

Outlook

While the presented work contributes to the ongoing progress of magnon spintronics research, various open questions and challenges remain in the field to accomplish the ultimate aim of magnon spintronics of spin wave based computing.

As discussed in this thesis, one of the crucial factors for the success of magnon spintronics is a thorough understanding of spin current propagation mechanisms in magnetic oxides or conductors. The presented results on the non-local SSE shed light on the complexity of thermal magnon generation and propagation in YIG. However, they call for further experiments at the same time. To verify the relevance of the de-localized generation of thermal magnon currents, for instance, field-dependent measurements at low temperatures and for varying YIG thicknesses would be necessary.
In terms of data processing, demanding but at the same time exciting tasks need to be fulfilled by the community to realize comprehensive magnon logic schemes. Regarding the presented work, the magnon spin valve effect as a proof-of-principle is presented, however, the chosen materials, device structures and spin current generation techniques limit the effect to either low temperatures or large external fields. By means of optimized material parameters, e.g. exchanging CoO by another antiferromagnetic insulator with a higher Néel temperature (e.g. NiO [24]), one may establish a spin pumping driven magnon spin valve that is operative even at room temperature. Such a device could be integrated with the concept of the logic majority gate [248] to allow more versatile operations. In the non-local scheme, on the other hand, a different wire design may (e.g. zig-zag wire) enable the examination of spin current detection for stable parallel and antiparallel magnetization alignment of spin current conduit and detector, without the need for external fields.
Finally, regarding the last project discussed, a different device design may help to increase the impact of Joule heating and Oersted fields on magnon transport in YIG or comparable magnetic oxides. In addition to thinner samples, an extended, gate-like structure that covers both injector and detector as well as the magnon propagation area in between might be helpful, as it would allow one to heat the sample more homogeneously and at the same time modulate the magnetization by the Oersted field on a larger scale. To ensure electrical insulation, this would require the additional deposition of an oxide layer (MgO or AlOx) to separate the different conductive structures. Finally, bearing in mind the recent discovery of long-range magnon transport in antiferromagnetic oxides [o13], such concepts could also be transferred to antiferromagnetic systems. However, due to the lack of a finite magnetization and spin-flop fields that are out of reach for such localized Oersted fields [o13], solely a signal modulation by Joule heating may appear.

Own and contributed work

o1. Kehlberger, A., Ritzmann, U., Hinzke, D., Guo, E.-J., Cramer, J., Jakob, G., Onbasli, M. C., Kim, D. H., Ross, C. A., Jungfleisch, M. B., Hillebrands, B., Nowak, U. & Kläui, M. Length Scale of the Spin Seebeck Effect. *Phys. Rev. Lett.* **115,** 096602 (2015).

o2. Guo, E.-J., Herklotz, A., Kehlberger, A., Cramer, J., Jakob, G. & Kläui, M. Thermal generation of spin current in epitaxial CoFe2O4 thin films. *Appl. Phys. Lett.* **108,** 022403 (2016).

o3. Guo, E.-J., Cramer, J., Kehlberger, A., Ferguson, C. A., MacLaren, D. A., Jakob, G. & Kläui, M. Influence of Thickness and Interface on the Low-Temperature Enhancement of the Spin Seebeck Effect in YIG Films. *Phys. Rev. X* **6,** 031012 (2016).

o4. Cramer, J., Guo, E.-J., Geprägs, S., Kehlberger, A., Ivanov, Y. P., Ganzhorn, K., Coletta, F. D., Althammer, M., Huebl, H., Gross, R., Kosel, J., Kläui, M. & Goennenwein, S. T. B. Magnon Mode Selective Spin Transport in Compensated Ferrimagnets. *Nano Lett.* **17,** 3334–3340 (2017).

o5. Ganzhorn, K., Wimmer, T., Cramer, J., Schlitz, R., Geprägs, S., Jakob, G., Gross, R., Huebl, H., Kläui, M. & Goennenwein, S. T. B. Temperature dependence of the non-local spin Seebeck effect in YIG/Pt nanostructures. *AIP Advances* **7,** 085102 (2017).

o6. Dong, B.-W., Cramer, J., Ganzhorn, K., Yuan, H. Y., Guo, E.-J., Goennenwein, S. T. B. & Kläui, M. Spin Hall magnetoresistance in the non-collinear ferrimagnet GdIG close to the compensation temperature. *J. Phys.: Condens. Matter* **30,** 035802 (2017).

o7. Cramer, J., Seifert, T., Kronenberg, A., Fuhrmann, F., Jakob, G., Jourdan, M., Kampfrath, T. & Kläui, M. Complex Terahertz and Direct Current Inverse Spin Hall Effect in YIG/Cu_{1-x}Irx Bilayers Across a Wide Concentration Range. *Nano Lett.* **18,** 1064–1069 (2018).

o8. Cramer, J., Ritzmann, U., Dong, B.-W., Jaiswal, S., Qiu, Z., Saitoh, E., Nowak, U. & Kläui, M. Spin transport across antiferromagnets induced by the spin Seebeck effect. *J. Phys. D: Appl. Phys.* **51,** 144004 (2018).

o9. Cramer, J., Fuhrmann, F., Ritzmann, U., Gall, V., Niizeki, T., Ramos, R., Qiu, Z., Hou, D., Kikkawa, T., Sinova, J., Nowak, U., Saitoh, E. & Kläui, M. Magnon detection using a ferroic collinear multilayer spin valve. *Nat. Commun.* **9,** 1089 (2018).

o10. Baldrati, L., Schneider, C., Niizeki, T., Ramos, R., Cramer, J., Ross, A., Saitoh, E. & Kläui, M. Spin transport in multilayer systems with fully epitaxial NiO thin films. *Phys. Rev. B* **98,** 14409 (2018).

o11. Baldrati, L., Ross, A., Niizeki, T., Schneider, C., Ramos, R., Cramer, J., Gomonay, O., Filianina, M., Savchenko, T., Heinze, D., Kleibert, A., Saitoh, E., Sinova, J. & Kläui, M. Full angular dependence of the spin Hall and ordinary magnetoresistance in epitaxial antiferromagnetic NiO(001)/Pt thin films. *Phys. Rev. B* **98,** 024422 (2018).

o12. Seifert, T. *et al.* Femtosecond formation dynamics of the spin Seebeck effect revealed by terahertz spectroscopy. *Nat. Commun.* **9,** 2899 (2018).

o13. Lebrun, R., Ross, A., Bender, S. A., Qaiumzadeh, A., Baldrati, L., Cramer, J., Brataas, A., Duine, R. A. & Kläui, M. Electrically controlled long-distance spin transport through an antiferromagnetic insulator. *arXiv (accepted for publication in Nature).* eprint: `1805.02451v1` (2018).

Bibliography

1. Atzori, L., Iera, A. & Morabito, G. The Internet of Things: A survey. *Comput. Networks* **54,** 2787–2805 (2010).
2. Pop, E., Sinha, S. & Goodson, K. E. Heat generation and transport in nanometer-scale transistors. *Proc. IEEE* **94,** 1587–1601 (2006).
3. Dayarathna, M., Wen, Y. & Fan, R. Data Center Energy Consumption Modeling: A Survey. *IEEE Commun. Surv. Tutorials* **18,** 732–794 (2016).
4. Wolf, S. A., Awschalom, D. D., Buhrman, R. A., Daughton, J. M., Von Molnar, S., Roukes, M. L., Chtchelkanova, A. Y. & Treger, D. M. Spintronics: a spin-based electronics vision for the future. *Science* **294,** 1488–1495 (2001).
5. Žutić, I., Fabian, J. & Sarma, S. D. Spintronics: Fundamentals and applications. *Rev. Mod. Phys.* **76,** 323–410 (2004).
6. Baibich, M., Broto, J., Fert, A., Van Dau, F. N., Petroff, F., Etienne, P., Creuzet, G., Friederich, A. & Chazelas, J. Giant magnetoresistance of (001) Fe/(001) Cr magnetic superlattices. *Phys. Rev. Lett.* **61,** 2472 (1988).
7. Binasch, G., Grünberg, P., Saurenbach, F. & Zinn, W. Enhanced magnetoresistance in layered magnetic structures with antiferromagnetic interlayer exchange. *Phys. Rev. B* **39,** 4828(R) (1989).
8. Slonczewski, J. Current-driven excitation of magnetic multilayers. *J. Magn. Magn. Mater.* **159,** L1–L7 (1996).
9. Ikeda, S., Miura, K., Yamamoto, H., Mizunuma, K., Gan, H., Endo, M., Kanai, S., Hayakawa, J., Matsukura, F. & Ohno, H. A perpendicular-anisotropy CoFeB–MgO magnetic tunnel junction. *Nat. Mater.* **9,** 721–724 (2010).
10. Sinova, J., Valenzuela, S. O., Wunderlich, J., Back, C. H. & Jungwirth, T. Spin Hall effects. *Rev. Mod. Phys.* **87,** 1213–1260 (2015).
11. Tserkovnyak, Y., Brataas, A. & Bauer, G. E. W. Enhanced gilbert damping in thin ferromagnetic films. *Phys. Rev. Lett.* **88,** 117601 (2002).
12. Saitoh, E., Ueda, M., Miyajima, H. & Tatara, G. Conversion of spin current into charge current at room temperature: Inverse spin-Hall effect. *Appl. Phys. Lett.* **88,** 182509 (2006).

13. Uchida, K.-i. I., Adachi, H., Ota, T., Nakayama, H., Maekawa, S. & Saitoh, E. Observation of longitudinal spin-Seebeck effect in magnetic insulators. *Appl. Phys. Lett.* **97,** 172505 (2010).

14. Bauer, G. E. W., Saitoh, E. & van Wees, B. J. Spin caloritronics. *Nat. Mater.* **11,** 391–399 (2012).

15. Kruglyak, V. V., Demokritov, S. O. & Grundler, D. Magnonics. *J. Phys. D: Appl. Phys.* **43,** 264001 (2010).

16. Serga, A. A., Chumak, A. V. & Hillebrands, B. YIG magnonics. *J. Phys. D: Appl. Phys.* **43,** 264002 (2010).

17. Chumak, A. V., Vasyuchka, V. I., Serga, A. A. & Hillebrands, B. Magnon spintronics. *Nat. Phys.* **11,** 453–461 (2015).

18. Jungwirth, T., Marti, X., Wadley, P. & Wunderlich, J. Antiferromagnetic spintronics. *Nat. Nanotechnol.* **11,** 231–241 (2016).

19. Baltz, V., Manchon, A., Tsoi, M., Moriyama, T., Ono, T. & Tserkovnyak, Y. Antiferromagnetic spintronics. *Rev. Mod. Phys.* **90,** 015005 (2018).

20. Kampfrath, T., Sell, A., Klatt, G., Pashkin, A., Mährlein, S., Dekorsy, T., Wolf, M., Fiebig, M., Leitenstorfer, A. & Huber, R. Coherent terahertz control of antiferromagnetic spin waves. *Nat. Photonics* **5,** 31–34 (2011).

21. Bhattacharjee, N., Sapozhnik, A. A., Bodnar, S. Y., Grigorev, V. Y., Agustsson, S. Y., Cao, J., Dominko, D., Obergfell, M., Gomonay, O., Sinova, J., Kläui, M., Elmers, H.-J., Jourdan, M. & Demsar, J. Néel Spin-Orbit Torque Driven Antiferromagnetic Resonance in Mn_2Au Probed by Time-Domain THz Spectroscopy. *Phys. Rev. Lett.* **120,** 237201 (2018).

22. Cornelissen, L. J., Liu, J., Duine, R. A., Youssef, J. B. & van Wees, B. J. Long-distance transport of magnon spin information in a magnetic insulator at room temperature. *Nat. Phys.* **11,** 1022–1026 (2015).

23. Blundell, S. *Magnetism in condensed matter* (AAPT, 2003).

24. Coey, J. M. *Magnetism and magnetic materials* (Cambridge University Press, 2010).

25. Dionne, G. F. *Magnetic oxides* (Springer, 2009).

26. Spaldin, N. A. *Magnetic materials: fundamentals and applications* (Cambridge University Press, 2010).

27. Duò, L., Finazzi, M. & Ciccacci, F. *Magnetic Properties of Antiferromagnetic Oxide Materials: Surfaces, Interfaces, and Thin Films* (John Wiley & Sons, 2010).

28. Pearson, R. Magnetocrystalline Anisotropy of RareEarth Iron Garnets. *J. Appl. Phys.* **33,** 1236 (1962).

29. Nogués, J. & Schuller, I. K. Exchange bias. *J. Magn. Magn. Mater.* **192,** 203–232 (1999).

30. Stiles, M. & McMichael, R. Model for exchange bias in polycrystalline ferromagnet-antiferromagnet bilayers. *Phys. Rev. B* **59,** 3722–3733 (1999).

31. Bloch, F. Zur Theorie des Ferromagnetismus. *Z. Phys.* **61,** 206–219 (1930).

32. Holstein, T. & Primakoff, H. Field dependence of the intrinsic domain magnetization of a ferromagnet. *Phys. Rev.* **58,** 1098–1113 (1940).

33. Dyson, F. J. General theory of spin-wave interactions. *Phys. Rev.* **102,** 1217–1230 (1956).

34. Stancil, D. D. & Prabhakar, A. *Spin Waves: Theory and Applications* (Springer, 2009).

35. Barker, J. & Bauer, G. E. W. Thermal spin dynamics of yttrium iron garnet. *Phys. Rev. Lett.* **117,** 217201 (2016).

36. Ritzmann, U., Hinzke, D., Kehlberger, A., Guo, E.-J., Kläui, M. & Nowak, U. Magnetic field control of the spin Seebeck effect. *Phys. Rev. B* **92,** 174411 (2015).

37. Lenk, B., Ulrichs, H., Garbs, F. & Münzenberg, M. The building blocks of magnonics. *Phys. Rep.* **507,** 107–136 (2011).

38. Demokritov, S. & Slavin, A. *Magnonics: From Fundamentals to Applications* (Springer Berlin Heidelberg, 2012).

39. Von Sovskii, S. *Ferromagnetic Resonance: The Phenomenon of Resonant Absorption of a High-Frequency Magnetic Field in Ferromagnetic Substances* (Elsevier Science, 2016).

40. Griffiths, J. Anomalous high-frequency resistance of ferromagnetic metals. *Nature* **158,** 670–671 (1946).

41. Kittel, C. Interpretation of anomalous Larmor frequencies in ferromagnetic resonance experiment. *Phys. Rev.* **71,** 270 (1947).

42. Kittel, C. On the theory of ferromagnetic resonance absorption. *Phys. Rev.* **73,** 155 (1948).

43. Baselgia, L. and Warden, M. and Waldner, F. and Hutton, S. L. and Drumbeller, J. E. and He, Y. Q. and Wigen, E. and Marysko, M. Derivation of the resonance from the free energy of ferromagnets. *Phys. Rev. B* **38,** 2237 (1988).

44. Neudecker, I., Woltersdorf, G., Heinrich, B., Okuno, T., Gubbiotti, G. & Back, C. H. Comparison of frequency, field, and time domain ferromagnetic resonance methods. *J. Magn. Magn. Mater.* **307,** 148–156 (2006).

45. Arias, R. & Mills, D. L. Extrinsic contributions to the ferromagnetic resonance response of ultrathin films. *Phys. Rev. B* **60,** 7395–7409 (1999).

46. Van De Riet, E. & Roozeboom, F. Ferromagnetic resonance and eddy currents in high-permeable thin films. *J. Appl. Phys.* **81,** 350 (1997).

47. Landau, L. & Lifshitz, L. On the Theory of the Dispersion of Magnetic Permeability in Ferromagnetic Bodies. *Phys. Z. Sowjetunion* **8,** 153–164 (1935).

48. Gilbert, T. A Phenomenological Theory of Damping in Ferromagnetic Materials. *IEEE Trans. Magn.* **40,** 3443–3449 (2004).

49. Beaujour, J. M., Ravelosona, D., Tudosa, I., Fullerton, E. E. & Kent, A. D. Ferromagnetic resonance linewidth in ultrathin films with perpendicular magnetic anisotropy. *Phys. Rev. B* **80,** 180415 (2009).

50. Hall, E. H. On a New Action of the Magnet on Electric Currents. *Am. J. Math.* **2,** 287–292 (1879).

51. Hall, E. H. On the rotational coefficient in nickel and cobalt. *Philos. Mag.* **12,** 157–172 (1881).

52. Nagaosa, N., Sinova, J., Onoda, S., MacDonald, A. H. & Ong, N. P. Anomalous Hall effect. *Rev. Mod. Phys.* **82,** 1539–1592 (2010).

53. Kimura, T., Otani, Y., Sato, T., Takahashi, S. & Maekawa, S. Room-temperature reversible spin hall effect. *Phys. Rev. Lett.* **98,** 156601 (2007).

54. Dyakonov, M. I. & Perel, V. I. Current-induced spin orientation of electrons in semiconductors. *Phys. Lett. A* **35,** 459–460 (1971).

55. Hirsch, J. E. Spin Hall Effect. *Phys. Rev. Lett.* **83,** 1834 (1999).

56. Zhang, S. Spin hall effect in the presence of spin diffusion. *Phys. Rev. Lett.* **85,** 393 (2000).

57. Smit, J. The spontaneous Hall effect in ferromagnetics II. *Physica* **24,** 39–51 (1958).

58. Berger, L. Side-jump mechanism for the hall effect of ferromagnets. *Phys. Rev. B* **2,** 4559–4566 (1970).

59. Murakami, S., Nagaosa, N. & Zhang, S. Dissipationless quantum spin current at room temperature. *Science* **301,** 1348–1351 (2003).

60. Sinova, J., Culcer, D., Niu, Q., Sinitsyn, N. A., Jungwirth, T. & MacDonald, A. H. Universal intrinsic spin Hall effect. *Phys. Rev. Lett.* **92,** 126603 (2004).

61. Tanaka, T., Kontani, H., Naito, M., Naito, T., Hirashima, D. S., Yamada, K. & Inoue, J. Intrinsic spin Hall effect and orbital Hall effect in 4d and 5d transition metals. *Phys. Rev. B* **77,** 165117 (2008).

62. Kato, Y. K., Myers, R. C., Gossard, A. C. & Awschalom, D. D. Observation of the Spin Hall Effect. *Science* **306,** 1910–1913 (2004).

63. Stamm, C., Murer, C., Berritta, M., Feng, J., Gabureac, M., Oppeneer, P. M. & Gambardella, P. Magneto-Optical Detection of the Spin Hall Effect in Pt and W Thin Films. *Phys. Rev. Lett.* **119,** 087203 (8 2017).

64. Valenzuela, S. O. & Tinkham, M. Direct electronic measurement of the spin Hall effect. *Nature* **442,** 176–179 (2006).

65. Azevedo, A., Vilela Leão, L. H., Rodriguez-Suarez, R. L., Oliveira, A. B. & Rezende, S. M. dc effect in ferromagnetic resonance: Evidence of the spin-pumping effect? *J. Appl. Phys.* **97,** 10C715 (2005).

66. *Spin Current* 2nd ed. (eds Maekawa, S., Valenzuela, S., Saitoh, E. & Kimura, T.) (Oxford University Press, 2017).

67. Morota, M., Niimi, Y., Ohnishi, K., Wei, D. H., Tanaka, T., Kontani, H., Kimura, T. & Otani, Y. Indication of intrinsic spin Hall effect in 4d and 5d transition metals. *Phys. Rev. B* **83,** 174405 (2011).

68. Wang, H. L., Du, C. H., Pu, Y., Adur, R., Hammel, P. C. & Yang, F. Y. Scaling of spin Hall angle in 3d, 4d, and 5d metals from $Y_3Fe_5O_{12}$/metal spin pumping. *Phys. Rev. Lett.* **112,** 197201 (2014).

69. Sagasta, E., Omori, Y., Isasa, M., Gradhand, M., Hueso, L. E., Niimi, Y., Otani, Y. & Casanova, F. Tuning the spin Hall effect of Pt from the moderately dirty to the superclean regime. *Phys. Rev. B* **94,** 060412 (2016).

70. Jungwirth, T., Wunderlich, J. & Olejník, K. Spin Hall effect devices. *Nat. Mater.* **11,** 382–390 (2012).

71. Heiliger, C., Zahn, P. & Mertig, I. Microscopic origin of magnetoresistance. *Mater. Today* **9,** 46–54 (2006).

72. Fuhr, J. D., Granada, M., Steren, L. B. & Alascio, B. Anisotropic magnetoresistance in manganites: Experiment and theory. *J. Phys. Condens. Matter* **22,** 146001 (2010).

73. Mcguire, T. R. & Potter, R. I. Anisotropic Magnetoresistance in Ferromagnetic 3D Alloys. *IEEE Trans. Magn.* **11,** 1018–1038 (1975).

74. Weiler, M., Althammer, M., Czeschka, F. D., Huebl, H., Wagner, M. S., Opel, M., Imort, I. M., Reiss, G., Thomas, A., Gross, R. & Goennenwein, S. T. Local charge and spin currents in magnetothermal landscapes. *Phys. Rev. Lett.* **108,** 106602 (2012).

75. Huang, S. Y., Fan, X., Qu, D., Chen, Y. P., Wang, W. G., Wu, J., Chen, T. Y., Xiao, J. Q. & Chien, C. L. Transport magnetic proximity effects in platinum. *Phys. Rev. Lett.* **109,** 107204 (2012).

76. Geprägs, S., Meyer, S., Altmannshofer, S., Opel, M., Wilhelm, F., Rogalev, A., Gross, R. & Goennenwein, S. T. Investigation of induced Pt magnetic polarization in $Pt/Y_3Fe_5O_{12}$ bilayers. *Appl. Phys. Lett.* **101,** 262407 (2012).

77. Nakayama, H., Althammer, M., Chen, Y. T., Uchida, K., Kajiwara, Y., Kikuchi, D., Ohtani, T., Geprägs, S., Opel, M., Takahashi, S., Gross, R., Bauer, G. E. W., Goennenwein, S. T. B. & Saitoh, E. Spin Hall Magnetoresistance Induced by a Nonequilibrium Proximity Effect. *Phys. Rev. Lett.* **110,** 206601 (2013).

78. Hahn, C., De Loubens, G., Klein, O., Viret, M., Naletov, V. V. & Ben Youssef, J. Comparative measurements of inverse spin Hall effects and magnetoresistance in YIG/Pt and YIG/Ta. *Phys. Rev. B* **87,** 174417 (2013).

79. Althammer, M. *et al.* Quantitative study of the spin Hall magnetoresistance in ferromagnetic insulator/normal metal hybrids. *Phys. Rev. B* **87,** 224401 (2013).

80. Chen, Y.-T., Takahashi, S., Nakayama, H., Althammer, M., Goennenwein, S., Saitoh, E. & Bauer, G. Theory of spin Hall magnetoresistance. *Phys. Rev. B* **87,** 144411 (2013).

81. Berger, L. Emission of spin waves by a magnetic multilayer traversed by a current. *Phys. Rev. B* **54,** 9353–9358 (1996).

82. Vlietstra, N., Shan, J., Castel, V., Van Wees, B. J. & Ben Youssef, J. Spin-Hall magnetoresistance in platinum on yttrium iron garnet: Dependence on platinum thickness and in-plane/out-of-plane magnetization. *Phys. Rev. B* **87,** 184421 (2013).

83. Jungfleisch, M. B., Lauer, V., Neb, R., Chumak, A. V. & Hillebrands, B. Improvement of the yttrium iron garnet/platinum interface for spin pumping-based applications. *Appl. Phys. Lett.* **103,** 022411 (2014).

84. Marmion, S. R., Ali, M., McLaren, M., Williams, D. A. & Hickey, B. J. Temperature dependence of spin Hall magnetoresistance in thin YIG/Pt films. *Phys. Rev. B* **89,** 220404(R) (2014).

85. Meyer, S., Althammer, M., Geprägs, S., Opel, M., Gross, R. & Goennenwein, S. T. B. Temperature dependent spin transport properties of platinum inferred from spin Hall magnetoresistance measurements. *Appl. Phys. Lett.* **104,** 242411 (2014).

86. Wang, S., Zou, L., Zhang, X., Cai, J., Wang, S., Shen, B. & Sun, J. Spin Seebeck effect and spin Hall magnetoresistance at high temperatures for a Pt/yttrium iron garnet hybrid structure. *Nanoscale* **7,** 17812 (2015).

87. Uchida, K. I., Qiu, Z., Kikkawa, T., Iguchi, R. & Saitoh, E. Spin Hall magnetoresistance at high temperatures. *Appl. Phys. Lett.* **106,** 052405 (2015).

88. Kim, J., Sheng, P., Takahashi, S., Mitani, S. & Hayashi, M. Spin Hall Magnetoresistance in Metallic Bilayers. *Phys. Rev. Lett.* **116,** 097201 (2016).

89. Avci, C. O., Garello, K., Ghosh, A., Gabureac, M., Alvarado, S. F. & Gambardella, P. Unidirectional spin Hall magnetoresistance in ferromagnet/normal metal bilayers. *Nat. Phys.* **11,** 570–575 (2015).

90. Yin, Y., Han, D. S., De Jong, M. C., Lavrijsen, R., Duine, R. A., Swagten, H. J. & Koopmans, B. Thickness dependence of unidirectional spin-Hall magnetoresistance in metallic bilayers. *Appl. Phys. Lett.* **111,** 232405 (2017).

91. Hoogeboom, G. R., Aqeel, A., Kuschel, T., Palstra, T. T. & van Wees, B. J. Negative spin Hall magnetoresistance of Pt on the bulk easy-plane antiferromagnet NiO. *Appl. Phys. Lett.* **111,** 052409 (2017).

92. Fischer, J., Gomonay, O., Schlitz, R., Ganzhorn, K., Vlietstra, N., Althammer, M., Huebl, H., Opel, M., Gross, R., Goennenwein, S. T. B. & Geprägs, S. Spin Hall magnetoresistance in antiferromagnet/heavy-metal heterostructures. *Phys. Rev. B* **97,** 014417 (2018).

93. Lin, W. & Chien, C. L. Electrical Detection of Spin Backflow from an Antiferromagnetic Insulator/$Y_3Fe_5O_{12}$ Interface. *Phys. Rev. Lett.* **118,** 067202 (2017).

94. Hou, D., Qiu, Z., Barker, J., Sato, K., Yamamoto, K., Vélez, S., Gomez-Perez, J. M., Hueso, L. E., Casanova, F. & Saitoh, E. Tunable Sign Change of Spin Hall Magnetoresistance in Pt/NiO/YIG Structures. *Phys. Rev. Lett.* **118,** 147202 (2017).

95. Tserkovnyak, Y., Brataas, A., Bauer, G. E. W. & Halperin, B. I. Nonlocal Magnetization Dynamics in Ferromagnetic Hybrid Nanostructures. *Rev. Mod. Phys.* **77,** 1375–1421 (2005).

96. Onsager, L. Irreversible processes. *Phys. Rev.* **37,** 405 (1931).

97. Brataas, A., Nazarov, Y. U. & Bauer, G. E. Finite-element theory of transport in ferromagnet-normal metal systems. *Phys. Rev. Lett.* **84,** 2481–2484 (2000).

98. Brataas, A., Nazarov, Y. & Bauer, G. Spin-transport in multi-terminal normal metal-ferromagnet systems with non-collinear magnetizations. *Eur. Phys. J. B* **22,** 99–110 (2001).

99. Xia, K., Kelly, P. J., Bauer, G. E., Brataas, A. & Turek, I. Spin torques in ferromagnetic/normal-metal structures. *Phys. Rev. B* **65,** 220401(R) (2002).

100. Zwierzycki, M., Tserkovnyak, Y., Kelly, P. J., Brataas, A. & Bauer, G. E. W. First-principles study of magnetization relaxation enhancement and spin transfer in thin magnetic films. *Phys. Rev. B* **71,** 064420 (2005).

101. Jia, X., Liu, K., Xia, K. & Bauer, G. E. W. Spin transfer torque on magnetic insulators. *EPL (Europhys. Lett.)* **96,** 17005 (2011).

102. Tserkovnyak, Y., Brataas, A. & Bauer, G. E. W. Spin pumping and magnetization dynamics in metallic multilayers. *Phys. Rev. B* **66,** 224403 (2002).

103. Brataas, A., Tserkovnyak, Y., Bauer, G. E. W. & Halperin, B. I. Spin battery operated by ferromagnetic resonance. *Phys. Rev. B* **66,** 060404(R) (2002).

104. Mizukami, S., Ando, Y. & Miyazaki, T. Ferromagnetic resonance linewidth for NM/80NiFe/NM films (NM=Cu, Ta, Pd and Pt). *J. Magn. Magn. Mater.* **226,** 1640–1642 (2001).

105. Mizukami, S., Ando, Y. & Miyazaki, T. Effect of spin diffusion on Gilbert damping for a very thin permalloy layer in Cu/permalloy/Cu/Pt films. *Phys. Rev. B* **66,** 104413 (2002).

106. Kajiwara, Y., Harii, K., Takahashi, S., Ohe, J., Uchida, K., Mizuguchi, M., Umezawa, H., Kawai, H., Ando, K., Takanashi, K., Maekawa, S. & Saitoh, E. Transmission of electrical signals by spin-wave interconversion in a magnetic insulator. *Nature* **464,** 262–266 (2010).

107. Gui, Y. S., Mecking, N., Zhou, X., Williams, G. & Hu, C. M. Realization of a room-temperature spin dynamo: The spin rectification effect. *Phys. Rev. Lett.* **98,** 107602 (2007).

108. Azevedo, A., Vilela-Leão, L. H., Rodríguez-Suárez, R. L., Lacerda Santos, A. F. & Rezende, S. M. Spin pumping and anisotropic magnetoresistance voltages in magnetic bilayers: Theory and experiment. *Phys. Rev. B* **83,** 144402 (2011).

109. Chen, H., Fan, X., Zhou, H., Wang, W., Gui, Y. S., Hu, C. M. & Xue, D. Spin rectification enabled by anomalous Hall effect. *J. Appl. Phys.* **113,** 17C732 (2013).

110. Bai, L., Hyde, P., Gui, Y. S., Hu, C. M., Vlaminck, V., Pearson, J. E., Bader, S. D. & Hoffmann, A. Universal method for separating spin pumping from spin rectification voltage of ferromagnetic resonance. *Phys. Rev. Lett.* **111,** 217602 (2013).

111. Jiao, H. & Bauer, G. E. Spin backflow and ac voltage generation by spin pumping and the inverse spin hall effect. *Phys. Rev. Lett.* **110,** 217602 (2013).

112. Wei, D., Obstbaum, M., Ribow, M., Back, C. H. & Woltersdorf, G. Spin Hall voltages from a.c. and d.c. spin currents. *Nat. Commun.* **5,** 3768 (2014).

113. Weiler, M., Shaw, J. M., Nembach, H. T. & Silva, T. J. Phase-sensitive detection of spin pumping via the ac inverse spin Hall effect. *Phys. Rev. Lett.* **113,** 157204 (2014).

114. Ando, K., Takahashi, S., Ieda, J., Kajiwara, Y., Nakayama, H., Yoshino, T., Harii, K., Fujikawa, Y., Matsuo, M., Maekawa, S. & Saitoh, E. Inverse spin-Hall effect induced by spin pumping in metallic system. *J. Appl. Phys.* **109,** 103913 (2011).

115. Sandweg, C. W., Kajiwara, Y., Chumak, A. V., Serga, A. A., Vasyuchka, V. I., Jungfleisch, M. B., Saitoh, E. & Hillebrands, B. Spin pumping by parametrically excited exchange magnons. *Phys. Rev. Lett.* **106,** 216601 (2011).

116. Mosendz, O., Pearson, J. E., Fradin, F. Y., Bauer, G. E. W., Bader, S. D. & Hoffmann, A. Quantifying spin Hall angles from spin pumping: experiments and theory. *Phys. Rev. Lett.* **104,** 046601 (2010).

117. Mosendz, O., Vlaminck, V., Pearson, J. E., Fradin, F. Y., Bauer, G. E. W., Bader, S. D. & Hoffmann, A. Detection and quantification of inverse spin Hall effect from spin pumping in permalloy/normal metal bilayers. *Phys. Rev. B* **82,** 214403 (2010).

118. Wang, H., Du, C., Hammel, P. C. & Yang, F. Antiferromagnonic spin transport from $Y_3Fe_5O_{12}$ into NiO. *Phys. Rev. Lett.* **113,** 097202 (2014).

119. Hahn, C., de Loubens, G., Naletov, V. V., Ben Youssef, J., Klein, O. & Viret, M. Conduction of spin currents through insulating antiferromagnetic oxides. *Europhys. Lett.* **108,** 57005 (2014).

120. Moriyama, T., Takei, S., Nagata, M., Yoshimura, Y., Matsuzaki, N., Terashima, T., Tserkovnyak, Y. & Ono, T. Anti-damping spin transfer torque through epitaxial nickel oxide. *Appl. Phys. Lett.* **106,** 162406 (2015).

121. Saglam, H., Zhang, W., Jungfleisch, M. B., Sklenar, J., Pearson, J. E., Ketterson, J. B. & Hoffmann, A. Spin transport through the metallic antiferromagnet FeMn. *Phys. Rev. B* **94,** 140412(R) (2016).

122. Qiu, Z., Li, J., Hou, D., Arenholz, E., N'Diaye, A. T., Tan, A., Uchida, K., Sato, K., Okamoto, S., Tserkovnyak, Y., Qiu, Z. Q. & Saitoh, E. Spin-current probe for phase transition in an insulator. *Nat. Commun.* **7,** 12670 (2016).

123. Frangou, L., Oyarzún, S., Auffret, S., Vila, L., Gambarelli, S. & Baltz, V. Enhanced Spin Pumping Efficiency in Antiferromagnetic IrMn Thin Films around the Magnetic Phase Transition. *Phys. Rev. Lett.* **116,** 077203 (2016).

124. Riffat, S. B. & Ma, X. Thermoelectrics: A review of present and potential applications. *Appl. Therm. Eng.* **23,** 913–935 (2003).

125. Hamid Elsheikh, M., Shnawah, D. A., Sabri, M. F. M., Said, S. B. M., Haji Hassan, M., Ali Bashir, M. B. & Mohamad, M. A review on thermoelectric renewable energy: Principle parameters that affect their performance. *Renew. Sustain. Energy Rev.* **30,** 337–355 (2014).

126. Seebeck, T. J. Ueber die magnetische Polarisation der Metalle und Erze durch Temperaturdifferenz. *Ann. Phys.* **82,** 133–160 (1826).

127. Peltier, J. Nouvelles expériences sur la caloricité des courants électrique. *Ann. Chim. Phys* **56,** 371–386 (1834).

128. Gross, R. & Marx, A. *Festkörperphysik* (Oldenbourg Wissenschaftsverlag GmbH, München, 2012).

129. Callen, H. B. The application of onsager's reciprocal relations to thermoelectric, thermomagnetic, and galvanomagnetic effects. *Phys. Rev.* **73,** 1349–1358 (1948).

130. Ettingshausen, A. v. & Nernst, W. Ueber das Auftreten electromotorischer Kräfte in Metallplatten, welche von einem Wärmestrome durchflossen werden und sich im magnetischen Felde befinden. *Ann. Phys.* **265,** 343–347 (1886).

131. Nernst, W. Ueber die electromotorischen Kräfte, welche durch den Magnetismus in von einem Wärmestrome durchflossenen Metallplatten geweckt werden. *Ann. Phys.* **267,** 760–789 (1887).

132. Huang, S. Y., Wang, W. G., Lee, S. F., Kwo, J. & Chien, C. L. Intrinsic spin-dependent thermal transport. *Phys. Rev. Lett.* **107,** 216604 (2011).

133. Ky, V. D. The Planar Nernst Effect in Permalloy Films. *physica status solidi (b)* **17,** K207–K209 (1967).

134. Schmid, M., Srichandan, S., Meier, D., Kuschel, T., Schmalhorst, J. M., Vogel, M., Reiss, G., Strunk, C. & Back, C. H. Transverse spin seebeck effect versus anomalous and planar nernst effects in permalloy thin films. *Phys. Rev. Lett.* **111,** 187201 (2013).

135. Meyer, S., Chen, Y. T., Wimmer, S., Althammer, M., Wimmer, T., Schlitz, R., Geprags, S., Huebl, H., Kodderitzsch, D., Ebert, H., Bauer, G. E., Gross, R. & Goennenwein, S. T. Observation of the spin Nernst effect. *Nat. Mater.* **16,** 977–981 (2017).

136. Sheng, P., Sakuraba, Y., Lau, Y. C., Takahashi, S., Mitani, S. & Hayashi, M. The spin Nernst effect in tungsten. *Sci. Adv.* **3,** e1701503 (2017).

137. Slachter, A., Bakker, F. L., Adam, J.-P. & van Wees, B. J. Thermally driven spin injection from a ferromagnet into a non-magnetic metal. *Nat. Phys.* **6,** 879–882 (2010).

138. Flipse, J., Bakker, F. L., Slachter, A., Dejene, F. K. & Van Wees, B. J. Direct observation of the spin-dependent Peltier effect. *Nat. Nanotechnol.* **7,** 166–168 (2012).

139. Walter, M., Walowski, J., Zbarsky, V., Münzenberg, M., Schäfers, M., Ebke, D., Reiss, G., Thomas, A., Peretzki, P., Seibt, M., Moodera, J. S., Czerner, M., Bachmann, M. & Heiliger, C. Seebeck Effect in Magnetic Tunnel Junctions. *Nat. Mater.* **10,** 742–746 (2011).

140. Uchida, K., Takahashi, S., Harii, K., Ieda, J., Koshibae, W., Ando, K., Maekawa, S. & Saitoh, E. Observation of the spin Seebeck effect. *Nature* **455,** 778–781 (2008).

142. Jaworski, C. M., Yang, J., MacK, S., Awschalom, D. D., Heremans, J. P. & Myers, R. C. Observation of the spin-Seebeck effect in a ferromagnetic semiconductor. *Nat. Mater.* **9,** 898–903 (2010).

143. Bosu, S., Sakuraba, Y., Uchida, K., Saito, K., Ota, T., Saitoh, E. & Takanashi, K. Spin Seebeck effect in thin films of the Heusler compound Co_2MnSi. *Phys. Rev. B* **83,** 224401 (2011).

144. Sagasta, E., Omori, Y., Isasa, M., Otani, Y., Hueso, L. E. & Casanova, F. Spin diffusion length of Permalloy using spin absorption in lateral spin valves. *Appl. Phys. Lett.* **111,** 082407 (2017).

145. Uchida, K., Xiao, J., Adachi, H., Ohe, J., Takahashi, S., Ieda, J., Ota, T., Kajiwara, Y., Umezawa, H., Kawai, H., Bauer, G. E., Maekawa, S. & Saitoh, E. Spin Seebeck insulator. *Nat. Mater.* **9,** 894–897 (2010).

146. Jaworski, C. M., Yang, J., MacK, S., Awschalom, D. D., Myers, R. C. & Heremans, J. P. Spin-seebeck effect: A phonon driven spin distribution. *Phys. Rev. Lett.* **106,** 186601 (2011).

147. Tikhonov, K. S., Sinova, J. & Finkel'stein, A. M. Spectral non-uniform temperature and non-local heat transfer in the spin Seebeck effect. *Nat. Commun.* **4,** 1945 (2013).

148. Avery, A. D., Pufall, M. R. & Zink, B. L. Observation of the planar nernst effect in permalloy and Nickel thin films with in-plane thermal gradients. *Phys. Rev. Lett.* **109,** 196602 (2012).

149. Bui, C. T. & Rivadulla, F. Anomalous and planar Nernst effects in thin films of the half-metallic ferromagnet La2/3Sr1/3MnO3. *Phys. Rev. B* **90,** 100403(R) (2014).

150. Soldatov, I. V., Panarina, N., Hess, C., Schultz, L. & Schäfer, R. Thermoelectric effects and magnetic anisotropy of Ga1-xMnxAs thin films. *Phys. Rev. B* **90,** 104423 (2014).

141. Meier, D., Reinhardt, D., van Straaten, M., Klewe, C., Althammer, M., Schreier, M., Goennenwein, S. T. B., Gupta, A., Schmid, M., Back, C. H., Schmalhorst, J.-M., Kuschel, T. & Reiss, G. Longitudinal spin Seebeck effect contribution in transverse spin Seebeck effect experiments in Pt/YIG and Pt/NFO. *Nat. Commun.* **6,** 8211 (2015).

151. Kikkawa, T., Uchida, K., Shiomi, Y., Qiu, Z., Hou, D., Tian, D., Nakayama, H., Jin, X. F. & Saitoh, E. Longitudinal spin seebeck effect free from the proximity nernst effect. *Phys. Rev. Lett.* **110,** 067207 (2013).

152. Xiao, J., Bauer, G. E. W., Uchida, K.-c., Saitoh, E. & Maekawa, S. Theory of magnon-driven spin Seebeck effect. *Phys. Rev. B* **81,** 214418 (2010).

153. Adachi, H., Uchida, K.-i., Saitoh, E. & Maekawa, S. Theory of the spin Seebeck effect. *Rep. Prog. Phys.* **76,** 036501 (2013).

154. Schreier, M., Kamra, A., Weiler, M., Xiao, J., Bauer, G. E. W., Gross, R. & Goennenwein, S. T. B. Magnon, phonon, and electron temperature profiles and the spin Seebeck effect in magnetic insulator/normal metal hybrid structures. *Phys. Rev. B* **88,** 094410 (2013).

155. Hinzke, D. & Nowak, U. Domain Wall Motion by the Magnonic Spin Seebeck Effect. *Phys. Rev. Lett.* **107,** 027205 (2011).

156. Hoffman, S., Sato, K. & Tserkovnyak, Y. Landau-Lifshitz theory of the longitudinal spin Seebeck effect. *Phys. Rev. B* **88,** 064408 (2013).

157. Ritzmann, U., Hinzke, D. & Nowak, U. Propagation of thermally induced magnonic spin currents. *Phys. Rev. B* **89,** 024409 (2014).

158. Rezende, S. M., Azevedo, A. & Rodríguez-Suárez, R. Magnon diffusion theory for the spin Seebeck effect in ferromagnetic and antiferromagnetic insulators. *J. Phys. D: Appl. Phys.* **51,** 174004 (2018).

159. Kimling, J., Choi, G.-M., Brangham, J. T., Matalla-Wagner, T., Huebner, T., Kuschel, T., Yang, F. & Cahill, D. G. Picosecond Spin Seebeck Effect. *Phys. Rev. Lett.* **118,** 057201 (2017).

160. Uchida, K.-i., Kikkawa, T., Miura, A., Shiomi, J. & Saitoh, E. Quantitative Temperature Dependence of Longitudinal Spin Seebeck Effect at High Temperatures. *Phys. Rev. X* **4,** 041023 (2014).

161. Kikkawa, T., Uchida, K.-i., Daimon, S., Qiu, Z., Shiomi, Y. & Saitoh, E. Critical suppression of spin Seebeck effect by magnetic fields. *Phys. Rev. B* **92,** 064413 (2015).

162. Geprägs, S. *et al.* Origin of the spin Seebeck effect in compensated ferrimagnets. *Nat. Commun.* **7,** 10452 (2016).

163. Ramos, R., Kikkawa, T., Uchida, K., Adachi, H., Lucas, I., Aguirre, M. H., Algarabel, P., Morellón, L., Maekawa, S., Saitoh, E. & Ibarra, M. R. Observation of the spin Seebeck effect in epitaxial Fe_3O_4 thin films. *Appl. Phys. Lett.* **102,** 072413 (2013).

164. Meier, D., Kuschel, T., Shen, L., Gupta, A., Kikkawa, T., Uchida, K., Saitoh, E., Schmalhorst, J.-M. & Reiss, G. Thermally driven spin and charge currents in thin $NiFe_2O_4$/Pt films. *Phys. Rev. B* **87,** 054421 (2013).

165. Niizeki, T., Kikkawa, T., Uchida, K. I., Oka, M., Suzuki, K. Z., Yanagihara, H., Kita, E. & Saitoh, E. Observation of longitudinal spin-Seebeck effect in cobalt-ferrite epitaxial thin films. *AIP Adv.* **5,** 053603 (2015).

166. Wu, S. M., Pearson, J. E. & Bhattacharya, A. Paramagnetic spin seebeck effect. *Phys. Rev. Lett.* **114,** 186602 (2015).

167. Seki, S., Ideue, T., Kubota, M., Kozuka, Y., Takagi, R., Nakamura, M., Kaneko, Y., Kawasaki, M. & Tokura, Y. Thermal Generation of Spin Current in an Antiferromagnet. *Phys. Rev. Lett.* **115,** 266601 (2015).

168. Wu, S. M., Zhang, W., KC, A., Borisov, P., Pearson, J. E., Jiang, J. S., Lederman, D., Hoffmann, A. & Bhattacharya, A. Antiferromagnetic spin Seebeck Effect. *Phys. Rev. Lett.* **116,** 097204 (2015).

169. Flipse, J., Dejene, F. K., Wagenaar, D., Bauer, G. E., Youssef, J. B. & Van Wees, B. J. Observation of the spin peltier effect for magnetic insulators. *Phys. Rev. Lett.* **113,** 027601 (2014).

170. Zhang, S. S.-L. & Zhang, S. Magnon Mediated Electric Current Drag Across a Ferromagnetic Insulator Layer. *Phys. Rev. Lett.* **109,** 096603 (2012).

171. Zhang, S. S. L. & Zhang, S. Spin convertance at magnetic interfaces. *Phys. Rev. B* **86,** 214424 (2012).

172. Goennenwein, S. T. B., Schlitz, R., Pernpeintner, M., Ganzhorn, K., Althammer, M., Gross, R. & Huebl, H. Non-local magnetoresistance in YIG/Pt nanostructures. *Appl. Phys. Lett.* **107,** 172405 (2015).

173. Bender, S. A., Duine, R. A. & Tserkovnyak, Y. Electronic Pumping of Quasiequilibrium Bose-Einstein-Condensed Magnons. *Phys. Rev. Lett.* **108,** 246601 (2012).

174. Li, J., Xu, Y., Aldosary, M., Tang, C., Lin, Z., Zhang, S., Lake, R. & Shi, J. Observation of magnon-mediated current drag in Pt/yttrium iron garnet/Pt(Ta) trilayers. *Nat. Commun.* **7,** 10858 (2016).

175. Wu, H., Wan, C. H., Zhang, X., Yuan, Z. H., Zhang, Q. T., Qin, J. Y., Wei, H. X., Han, X. F. & Zhang, S. Observation of magnon-mediated electric current drag at room temperature. *Phys. Rev. B* **93,** 060403(R) (2016).

176. Shan, J., Cornelissen, L. J., Liu, J., Youssef, J. B., Liang, L. & Van Wees, B. J. Criteria for accurate determination of the magnon relaxation length from the nonlocal spin Seebeck effect. *Phys. Rev. B* **96,** 184427 (2017).

177. Cornelissen, L. J., Shan, J. & van Wees, B. J. Temperature dependence of the magnon spin diffusion length and magnon spin conductivity in the magnetic insulator yttrium iron garnet. *Phys. Rev. B* **94,** 180402(R) (2016).

178. Cornelissen, L. J. & van Wees, B. J. Magnetic field dependence of the magnon spin diffusion length in the magnetic insulator yttrium iron garnet. *Phys. Rev. B* **93,** 020403(R) (2016).

179. Gilleo, M. A. & Geller, S. Magnetic and Crystallographic Properties of Substituted Yttrium-Iron Garnet, $3Y_2O_3 \cdot xM_2O_3 \cdot (5-x)Fe_2O_3$. *Phys. Rev.* **110,** 73–78 (1958).

180. Geller, S., Remeika, J., Sherwood, R., Williams, H. & Espinosa, G. Magnetic study of the heavier rare earth iron garnets. *Phys. Rev.* **137,** 1034–1038 (1965).

181. Shinagawa, K., Sato, H., Saito, T. & Tsushima, T. Charge transfer transitions in yttrium iron garnet. *J. Magn. Magn. Mater.* **104-107,** 443–444 (1992).

182. Chang, H., Li, P., Zhang, W., Liu, T., Hoffmann, A., Deng, L. & Wu, M. Nanometer-Thick Yttrium Iron Garnet Films with Extremely Low Damping. *IEEE Magn. Lett.* **5,** 6700104 (2014).

183. Onbasli, M. C., Kehlberger, A., Kim, D. H., Jakob, G., Kläui, M., Chumak, A. V., Hillebrands, B. & Ross, C. A. Pulsed laser deposition of epitaxial yttrium iron garnet films with low Gilbert damping and bulk-like magnetization. *APL Mater.* **2,** 106102 (2014).

184. Wang, H. L., Du, C. H., Pu, Y., Adur, R., Hammel, P. C. & Yang, F. Y. Large spin pumping from epitaxial $Y_3Fe_5O_{12}$ thin films to Pt and W layers. *Phys. Rev. B* **88,** 100406(R) (2013).

185. Thiery, N. *et al.* Electrical properties of epitaxial yttrium iron garnet ultrathin films at high temperatures. *Phys. Rev. B* **97,** 064422 (2018).

186. Giess, E. A., Kuptsis, J. D. & White, E. A. D. Liquid-Phase Epitaxial-Growth of Magnetic Garnet Films By Isothermal Dipping in a Horizontal Plane With Axial Rotation. *J. Cryst. Growth* **16,** 36–42 (1972).

187. Wasa, K. & Hayakawa, S. *Handbook of sputter deposition technology : principles, technology, and applications* 304 (Noyes Publications, 1992).

188. *Handbook of thin film deposition* 2nd ed. (ed Seshan, K.) (William Andrew Publishing, 2002).

189. Als-Nielsen, J. & McMorrow, D. *Elements of Modern X-ray Physics* (John Wiley & Sons, Inc., 2011).

190. Birkholz, M. *Thin Film Analysis by X-Ray Scattering* (Wiley-VCH Verlag GmbH & Co. KGaA, 2005).

191. *Nanotechnology and Nanoelectronics* (ed Fahrner, W. R.) (Springer-Verlag Berlin Heidelberg, 2005).

192. Natarajan, S. *et al. A 14nm logic technology featuring 2nd-generation FinFET, air-gapped interconnects, self-aligned double patterning and a 0.0588 μm^2 SRAM cell size* in *2014 IEEE International Electron Devices Meeting* (2014), 3.7.1–3.7.3.

193. *Photolithography. Theory and Application of Photoresists, Etchants and Solvents.* Microchemicals GmbH (Ulm, 2012).

194. *The SQUID Handbook: Fundamentals and Technology of SQUIDs and SQUID Systems* (eds Clarke, J. & Braginski, A. I.) (Wiley-VCH Verlag GmbH & Co. KGaA, 2005).

195. Drung, D. High-T_c and low-T_c dc SQUID electronics. *Supercond. Sci. Technol.* **16,** 1320–1336 (2003).

196. QuantumDesign & Note, M. S. *Effects of Magnetic Field Uniformity on the Measurement of Superconducting Samples* (2000).

197. Kehlberger, A. *Origin of the spin Seebeck effect* (Univ., Mainz, 2015).

198. Schreier, M., Roschewsky, N., Dobler, E., Meyer, S., Huebl, H., Gross, R. & Goennenwein, S. T. B. Current heating induced spin Seebeck effect. *Appl. Phys. Lett.* **103,** 242404 (2013).

199. Sola, A., Bougiatioti, P., Kuepferling, M., Meier, D., Reiss, G., Pasquale, M., Kuschel, T. & Basso, V. Longitudinal spin Seebeck coefficient: Heat flux vs. temperature difference method. *Sci. Rep.* **7,** 46752 (2017).

200. Kehlberger, A., Jakob, G., Onbasli, M. C., H. Kim, D., Ross, C. A. & Kläui, M. Investigation of the magnetic properties of insulating thin films using the longitudinal spin Seebeck effect. *J. Appl. Phys.* **115,** 17C731 (2014).

201. Bunting, J., Ashworth, T. & Steeple, H. The specific heat of Apiezon N grease. *Cryogenics* **9,** 385–386 (1969).

202. Ganzhorn, K., Klingler, S., Wimmer, T., Geprägs, S., Gross, R., Huebl, H. & Goennenwein, S. T. B. Magnon-based logic in a multi-terminal YIG/Pt nanostructure. *Appl. Phys. Lett.* **109,** 022405 (2016).

203. Thiery, N. *et al.* Nonlinear spin conductance of yttrium iron garnet thin films driven by large spin-orbit torque. *Phys. Rev. B* **97,** 060409 (2018).

204. Seifert, T. *et al.* Efficient metallic spintronic emitters of ultrabroadband terahertz radiation. *Nat. Photonics* **10,** 483–488 (2016).

205. Shan, J., Cornelissen, L. J., Vlietstra, N., Youssef, J. B., Kuschel, T., Duine, R. A. & van Wees, B. J. Influence of yttrium iron garnet thickness and heater opacity on the nonlocal transport of electrically and thermally excited magnons. *Phys. Rev. B* **94,** 174437 (2016).

206. Vélez, S., Bedoya-Pinto, A., Yan, W., Hueso, L. E. & Casanova, F. Competing effects at Pt/YIG interfaces: Spin Hall magnetoresistance, magnon excitations, and magnetic frustration. *Phys. Rev. B* **94,** 174405 (2016).

207. Cornelissen, L. J., Oyanagi, K., Kikkawa, T., Qiu, Z., Kuschel, T., Bauer, G. E. W., van Wees, B. J. & Saitoh, E. Nonlocal magnon-polaron transport in yttrium iron garnet. *Phys. Rev. B* **96,** 104441 (2017).

208. Cornelissen, L. J., Peters, K. J. H., Bauer, G. E. W., Duine, R. A. & van Wees, B. J. Magnon spin transport driven by the magnon chemical potential in a magnetic insulator. *Phys. Rev. B* **94,** 014412 (2016).

209. Giles, B. L., Yang, Z., Jamison, J. S., Gomez-Perez, J. M., Vélez, S., Hueso, L. E., Casanova, F. & Myers, R. C. Thermally driven long-range magnon spin currents in yttrium iron garnet due to intrinsic spin Seebeck effect. *Phys. Rev. B* **96,** 180412(R) (2017).

210. Euler, C., Hołuj, P., Langner, T., Kehlberger, A., Vasyuchka, V. I., Kläui, M. & Jakob, G. Thermal conductance of thin film YIG determined using Bayesian statistics. *Phys. Rev. B* **92,** 094406 (2015).

211. Althammer, M., Goennenwein, S. T. B. & Gross, R. Magnetically Ordered Insulators for Advanced Spintronics. *arXiv.* eprint: `1712.08517v1` (2017).

212. Wang, H., Du, C., Hammel, P. C. & Yang, F. Spin transport in antiferromagnetic insulators mediated by magnetic correlations. *Phys. Rev. B* **91,** 220410(R) (2015).

213. Lin, W., Chen, K., Zhang, S. & Chien, C. L. Enhancement of Thermally Injected Spin Current through an Antiferromagnetic Insulator. *Phys. Rev. Lett.* **116,** 186601 (2016).

214. Prakash, A., Brangham, J., Yang, F. & Heremans, J. P. Spin Seebeck effect through antiferromagnetic NiO. *Phys. Rev. B* **94,** 014427 (2016).

215. Rezende, S. M., Rodríguez-Suárez, R. L. & Azevedo, A. Diffusive magnonic spin transport in antiferromagnetic insulators. *Phys. Rev. B* **93,** 054412 (2016).

216. Chen, K., Lin, W., Chien, C. L. & Zhang, S. Temperature Dependence of Angular Momentum Transport Across Interfaces. *Phys. Rev. B* **94,** 054413 (2016).

217. Khymyn, R., Lisenkov, I., Tiberkevich, V. S., Slavin, A. N. & Ivanov, B. A. Transformation of spin current by antiferromagnetic insulators. *Phys. Rev. B* **93,** 224421 (2016).

218. Fukami, S., Zhang, C., Duttagupta, S., Kurenkov, A. & Ohno, H. Magnetization switching by spin-orbit torque in an antiferromagnet-ferromagnet bilayer system. *Nat. Mater.* **15,** 535–541 (2016).

219. Ganzhorn, K., Barker, J., Schlitz, R., Piot, B. A., Ollefs, K., Guillou, F., Wilhelm, F., Rogalev, A., Opel, M., Althammer, M., Geprägs, S., Huebl, H., Gross, R., Bauer, G. E. W. & Goennenwein, S. T. B. Spin Hall magnetoresistance in a canted ferrimagnet. *Phys. Rev. B* **94,** 94401 (2016).

220. Kohn, A., Kovács, A., Fan, R., McIntyre, G. J., Ward, R. C. C. & Goff, J. P. The antiferromagnetic structures of IrMn3 and their influence on exchange-bias. *Sci. Rep.* **3,** 2412 (2013).

221. Yamaoka, T., Mekata, M. & Takaki, H. Neutron Diffraction Study of γ-Phase Mn-Ir Single Crystals. *J. Phys. Soc. Japan* **36,** 438 (1974).

222. Kikuchi, D., Ishida, M., Uchida, K., Qiu, Z., Murakami, T. & Saitoh, E. Enhancement of spin-Seebeck effect by inserting ultra-thin $Fe_{70}Cu_{30}$ interlayer. *Appl. Phys. Lett.* **106,** 82401 (2015).

223. Yuasa, H., Tamae, K. & Onizuka, N. Spin mixing conductance enhancement by increasing magnetic density. *AIP Adv.* **7,** 055928 (2017).

224. Mendes, J. B. S., Cunha, R. O., Alves Santos, O., Ribeiro, P. R. T., Machado, F. L. A., Rodríguez-Suárez, R. L., Azevedo, A. & Rezende, S. M. Large inverse spin Hall effect in the antiferromagnetic metal $Ir_{20}Mn_{80}$. *Phys. Rev. B* **89,** 140406(R) (2014).

225. Zhang, W., Jungfleisch, M. B., Jiang, W., Pearson, J. E., Hoffmann, A., Freimuth, F. & Mokrousov, Y. Spin Hall effects in metallic antiferromagnets. *Phys. Rev. Lett.* **113,** 196602 (2014).

226. Isasa, M., Villamor, E., Hueso, L. E., Gradhand, M. & Casanova, F. Temperature dependence of spin diffusion length and spin Hall angle in Au and Pt. *Phys. Rev. B* **91,** 24402 (2015).

227. Van der Zaag, P., Ijiri, Y., Borchers, J. A., Feiner, L., Wolf, R., Gaines, J., Erwin, R. & Verheijen, M. Difference between blocking and Néel temperatures in the exchange biased Fe_3O_4/CoO system. *Phys. Rev. Lett.* **84,** 6102 (2000).

228. Rinaldi, C., Baldrati, L., Loreto, M. D., Asa, M., Bertacco, R. & Cantoni, M. Blocking Temperature Engineering in Exchange-Biased CoFeB/IrMn Bilayer. *IEEE Trans. Magn.* **54,** 4800107 (2018).

229. Chatterji, T., McIntyre, G. & Lindgard, P.-A. Antiferromagnetic phase transition and spin correlations in NiO. *Phys. Rev. B* **79,** 172403 (2009).

230. Niimi, Y., Morota, M., Wei, D. H., Deranlot, C., Basletic, M., Hamzic, A., Fert, A. & Otani, Y. Extrinsic spin Hall effect induced by iridium impurities in copper. *Phys. Rev. Lett.* **106,** 126601 (2011).

231. Niimi, Y., Kawanishi, Y., Wei, D. H., Deranlot, C., Yang, H. X., Chshiev, M., Valet, T., Fert, A. & Otani, Y. Giant Spin Hall Effect Induced by Skew Scattering from Bismuth Impurities inside Thin Film CuBi Alloys. *Phys. Rev. Lett.* **109,** 156602 (2012).

232. Zou, L. K., Wang, S. H., Zhang, Y., Sun, J. R., Cai, J. W. & Kang, S. S. Large extrinsic spin Hall effect in Au-Cu alloys by extensive atomic disorder scattering. *Phys. Rev. B* **93,** 014422 (2016).

233. Ramaswamy, R., Wang, Y., Elyasi, M., Motapothula, M., Venkatesan, T., Qiu, X. & Yang, H. Extrinsic spin hall effect in $Cu_{1-x}Pt_x$. *Phys. Rev. Appl.* **8,** 024034 (2017).

234. Obstbaum, M., Decker, M., Greitner, A. K., Haertinger, M., Meier, T. N. G., Kronseder, M., Chadova, K., Wimmer, S., Ködderitzsch, D., Ebert, H. & Back, C. H. Tuning Spin Hall Angles by Alloying. *Phys. Rev. Lett.* **117,** 167204 (2016).

235. Metselaar, R. & Larsen, P. K. High-temperature electrical properties of yttrium iron garnet under varying oxygen pressures. *Solid State Commun.* **15,** 291–294 (1974).

236. Leitenstorfer, A., Hunsche, S., Shah, J., Nuss, M. & Knox, W. Detectors and sources for ultrabroadband electro-optic sampling: Experiment and theory. *Appl. Phys. Lett.* **74,** 1516–1518 (1999).

237. Nastos, F., Newson, R., Hübner, J., van Driel, H. & Sipe, J. Terahertz emission from ultrafast optical orientation of spins in semiconductors: Experiment and theory. *Phys. Rev. B* **77,** 195202 (2008).

238. Kampfrath, T., Battiato, M., Maldonado, P., Eilers, G., Nötzold, J., Mährlein, S., Zbarsky, V., Freimuth, F., Mokrousov, Y., Blügel, S., Wolf, M., Radu, I., Oppeneer, P. M. & Münzenberg, M. Terahertz spin current pulses controlled by magnetic heterostructures. *Nat. Nanotechnol.* **8,** 256–260 (2013).

239. Walowski, J. & Münzenberg, M. Perspective: Ultrafast magnetism and THz spintronics. *J. Appl. Phys.* **120,** 140901 (2016).

240. *Binary Alloy Phase Diagrams* (ed Massalski, T. B.) (ASM International, 1990).

241. Gall, D. Electron mean free path in elemental metals. *J. Appl. Phys.* **119,** 085101 (2016).

242. Fert, A. & Levy, P. M. Spin Hall effect induced by resonant scattering on impurities in metals. *Phys. Rev. Lett.* **106,** 157208 (2011).

243. Seifert, T., Tran, N. M., Gueckstock, O., Rouzegar, S. M., Nadvornik, L., Jaiswal, S., Jakob, G., Temnov, V. V., Muenzenberg, M., Wolf, M., Klaeui, M. & Kampfrath, T. Terahertz spectroscopy for all-optical spintronic characterization of the spin-Hall-effect metals Pt, W and $Cu_{80}Ir_{20}$. *arXiv, accepted for publication in J. Phys. D: Appl. Phys.* eprint: `1805.02193v1` (2018).

244. Stern, N. P., Steuerman, D. W., Mack, S., Gossard, A. C. & Awschalom, D. D. Time-resolved dynamics of the spin Hall effect. *Nat. Phys.* **4,** 843 (2008).

245. Guo, G. Y., Murakami, S., Chen, T. W. & Nagaosa, N. Intrinsic spin hall effect in platinum: First-principles calculations. *Phys. Rev. Lett.* **100,** 096401 (2008).

246. Vogt, K., Fradin, F. Y., Pearson, J. E., Sebastian, T., Bader, S. D., Hillebrands, B., Hoffmann, A. & Schultheiss, H. Realization of a spin-wave multiplexer. *Nat. Commun.* **5,** 3727 (2014).

247. Chumak, A. V., Serga, A. A. & Hillebrands, B. Magnon transistor for all-magnon data processing. *Nat. Commun.* **5,** 4700 (2014).

248. Fischer, T., Kewenig, M., Bozhko, D. A., Serga, A. A., Syvorotka, I. I., Ciubotaru, F., Adelmann, C., Hillebrands, B. & Chumak, A. V. Experimental prototype of a spin-wave majority gate. *Appl. Phys. Lett.* **110,** 152401 (2017).

249. Miao, B. F., Huang, S. Y., Qu, D. & Chien, C. L. Inverse spin hall effect in a ferromagnetic metal. *Phys. Rev. Lett.* **111,** 066602 (2013).

250. Tian, D., Li, Y., Qu, D., Jin, X. & Chien, C. L. Separation of spin Seebeck effect and anomalous Nernst effect in Co/Cu/YIG. *Appl. Phys. Lett.* **106,** 212407 (2015).

251. Ambrose, T., Sommer, R. & Chien, C. L. Angular dependence of exchange coupling in ferromagnet/antiferromagnet bilayers. *Phys. Rev. B* **56,** 83 (1997).

252. Schultheiss, H., Pearson, J. E., Bader, S. D. & Hoffmann, A. Thermoelectric detection of spin waves. *Phys. Rev. Lett.* **109,** 237204 (2012).

253. Tee, W., Tay, Z. J., Yakovlev, N. L., Peng, B. & Ong, C. K. Influence of static and dynamic dipolar fields in bulk YIG/thin film NiFe systems probed via spin rectification effect. *J. Magn. Magn. Mater.* **426,** 563–568 (2017).

254. Ambrose, T. & Chien, C. L. Finite-size effects and uncompensated magnetization in thin antiferromagnetic CoO layers. *Phys. Rev. Lett.* **76,** 1743 (1996).

255. Guan, Y., Bailey, W. E., Vescovo, E., Kao, C. C. & Arena, D. A. Phase and amplitude of element-specific moment precession in $Ni_{81}Fe_{19}$. *J. Magn. Magn. Mater.* **312,** 374–378 (2007).

256. Jungfleisch, M. B., Chumak, A. V., Kehlberger, A., Lauer, V., Kim, D. H., Onbasli, M. C., Ross, C. A., Kläui, M. & Hillebrands, B. Thickness and power dependence of the spin-pumping effect in $Y_3Fe_5O_{12}$/Pt heterostructures measured by the inverse spin Hall effect. *Phys. Rev. B* **91,** 134407 (2015).

257. Satoh, T., Iida, R., Higuchi, T., Fujii, Y., Koreeda, A., Ueda, H., Shimura, T., Kuroda, K., Butrim, V. I. & Ivanov, B. A. Excitation of coupled spin-orbit dynamics in cobalt oxide by femtosecond laser pulses. *Nat. Commun.* **8,** 638 (2017).

258. Batallan, F., Rosenman, I. & Sommers, C. B. Band structure and Fermi surface of hcp ferromagnetic cobalt. *Phys. Rev. B* **11,** 545–557 (1975).

259. Villamor, E., Isasa, M., Hueso, L. E. & Casanova, F. Temperature dependence of spin polarization in ferromagnetic metals using lateral spin valves. *Phys. Rev. B* **88,** 184411 (2013).

260. Cheng, Y., Chen, K. & Zhang, S. Interplay of magnon and electron currents in magnetic heterostructure. *Phys. Rev. B* **96,** 024449 (2017).

261. Cornelissen, L., Liu, J., van Wees, B. & Duine, R. Spin-Current-Controlled Modulation of the Magnon Spin Conductance in a Three-Terminal Magnon Transistor. *Phys. Rev. Lett.* **120,** 097702 (2018).

262. Das, K. S., Schoemaker, W. Y., Van Wees, B. J. & Vera-Marun, I. J. Spin injection and detection via the anomalous spin Hall effect of a ferromagnetic metal. *Phys. Rev. B* **96,** 220408(R) (2017).

263. Johnson, J. B. Thermal Agitation of Electricity in Conductors. *Phys. Rev.* **32,** 97 (1928).

264. Wu, S. M., Hoffman, J., Pearson, J. E. & Bhattacharya, A. Unambiguous separation of the inverse spin Hall and anomalous Nernst effects within a ferromagnetic metal using the spin Seebeck effect. *Appl. Phys. Lett.* **105,** 092409 (2014).

265. Gandha, K., Chaudhary, R. P., Mohapatra, J., Koymen, A. R. & Liu, J. P. Giant exchange bias and its angular dependence in Co/CoO core-shell nanowire assemblies. *Phys. Lett. A* **381,** 2092–2096 (2017).

266. Tsukahara, A., Ando, Y., Kitamura, Y., Emoto, H., Shikoh, E., Delmo, M. P., Shinjo, T. & Shiraishi, M. Self-induced inverse spin Hall effect in permalloy at room temperature. *Phys. Rev. B* **89,** 235317 (2014).

267. Zhang, Y., Mi, W., Wang, X. & Guo, Z. Scaling of anomalous Hall effect in amorphous CoFeB films with accompanying quantum correction. *Solid State Commun.* **215-216,** 5–11 (2015).

268. Petrovykh, D. Y., Altmann, K. N., Höchst, H., Laubscher, M., Maat, S., Mankey, G. J. & Himpsel, F. J. Spin-dependent band structure, Fermi surface, and carrier lifetime of permalloy. *Appl. Phys. Lett.* **73,** 3459 (1998).

269. Belashchenko, K. D., Kovalev, A. A. & Van Schilfgaarde, M. Theory of spin loss at metallic interfaces. *Phys. Rev. Lett.* **117,** 207204 (2016).

270. Rojas-Sánchez, J. C., Reyren, N., Laczkowski, P., Savero, W., Attané, J. P., Deranlot, C., Jamet, M., George, J. M., Vila, L. & Jaffrès, H. Spin pumping and inverse spin hall effect in platinum: The essential role of spin-memory loss at metallic interfaces. *Phys. Rev. Lett.* **112,** 106602 (2014).

271. *CRC handbook of chemistry and physics* (ed Haynes, W. M.) (CRC press, 2005).

272. Seemann, K., Freimuth, F., Zhang, H., Blügel, S., Mokrousov, Y., Bürgler, D. & Schneider, C. Origin of the planar Hall effect in nanocrystalline $Co_{60}Fe_{20}B_{20}$. *Phys. Rev. Lett.* **107,** 086603 (2011).

273. Hughes, I. & Hase, T. *Measurements and their uncertainties: a practical guide to modern error analysis* (Oxford University Press, 2010).

274. Boona, S. R. & Heremans, J. P. Magnon thermal mean free path in yttrium iron garnet. *Phys. Rev. B* **90,** 064421 (2014).

Appendices

A List of contributors

In the following, detailed information is given on direct (presented) contributions of experimental and theoretical work to the different studies shown in this thesis by co-workers in Mainz or collaborating researchers.

Non-local detection of thermal spin currents

- Patterning and scanning electron microscopy of series A devices by Stefan Kauschke (JGU Mainz).
- Own contributions: Patterning and optical micrograph of series B devices, deposition of Pt and W films, angular-/temperature-/strip separation-/field-dependent measurements of non-local SSE and electrical induced spin currents in series A and B, data evaluation.

Spin transmission across metallic antiferromagnets

- Yttrium iron garnet growth by Z. Qiu (Tohoku University Sendai)
- IrMn, Pt, IrMn/Pt and SiO_2/IrMn/CoFe growth by S. Jaiswal (JGU Mainz)
- Spin hall magnetoresistance measurements by B. Dong (JGU Mainz at the time)
- Atomistic spin dynamics simulations by U. Ritzmann (University of Konstanz at the time)
- Own contributions: Thickness- and temperature-dependent measurements of spin Seebeck effect, SQUID magnetometry measurements, data evaluation.

Concentration-dependent spin current detection in copper-iridium alloys

- CuIr growth by A. Kronenberg (JGU Mainz)
- THz spin Seebeck measurements by T. Seifert (Fritz Haber Institute Berlin)
- Own contributions: DC spin Seebeck measurements, data evaluation.

Alignment-dependent spin pumping in YIG/CoO/Co

- Yttrium iron garnet growth by Z. Qiu (Tohoku University Sendai), together with F. Fuhrmann (JGU Mainz) and M. Kläui (JGU Mainz)
- CoO/Co and CoO/Pt growth, atomic force microscopy and X-ray spectroscopy by F. Fuhrmann (JGU Mainz) and the author, supported by T. Niizeki (Tohoku University Sendai)
- Spin-thermoelectric measurements (SSE, ANE) by F. Fuhrmann (JGU Mainz) and the author, supported by R. Ramos (Tohoku University Sendai)
- Spin-pumping measurements by F. Fuhrmann (JGU Mainz) and the author, supported by D. Hou (Tohoku University Sendai)
- Atomistic spin dynamics simulations by U. Ritzmann (University of Konstanz at the time)
- Own contributions: see above, SQUID magnetometry, data evaluation.

(Inverse) spin Hall effect in $Co_{60}Fe_{20}B_{20}$

- Cu/CoFeB/Ru growth by S. Jaiswal (JGU Mainz)
- Own contributions: Patterning of non-local devices, Pt deposition, field-dependent non-local and magnetoresistance measurements, data evaluation.

Signal manipulation by heating and Oersted field

- Cu growth by M. Vafaee (JGU Mainz)
- Own contributions: Patterning of non-local devices, Pt deposition, non-local measurements, data evaluation.

B Sample fabrication recipes

In this appendix, recipes of different sample fabrication steps are provided that were mainly performed at the Johannes Gutenberg University Mainz by the author of this thesis.

B.1 Lift-off process used for fabrication of non-local structures

The following process, including the used EBL parameters, was mainly implemented by A. Pfeiffer and S. Kauschke.

Sample cleaning

1. Immerse sample in acetone for 60 s
2. Immerse sample in isopropyl alcohol (IPA) for 60 s
3. Immerse sample in purified water for 60 s
4. Blow dry with nitrogen
5. Put sample on hot plate ($T > 120\,°C$) for 60 s for water desorption

If case of strong contamination, put sample in ultrasonic bath while immersed in a solvent.

Spin coating

The following table gives the spin-coating parameters used for both the actual structure fabrication and contact pad patterning. The used resist is *PMMA 950k A4* and spin-coated on the sample in two steps, yielding a resist thickness of $\approx 200\,nm$.

Step	Time	Speed	Acceleration
1 (Prespin)	2 s	500 rpm	500 rpm/s
1 (Main)	60 s	4000 rpm	4000 rpm/s

After spin-coating, pause for 5 min and soft-bake the sample on the hot plate at 180 °C for 90 s and pause for 5 min. In case of dielectric substrates, a conductive resist is deposited in a second step to avoid charging during the electron beam lithography. Deposited on PMMA, the used resist is *Electra 92 AR-PC5090*.

Step	Time	Speed	Acceleration
1 (Main)	60 s	3000 rpm	3000 rpm/s

After spin-coating and 2 min, the conductive resist is soft-baked at 90 °C for 2 min.

Electron beam lithography

During electron beam lithography, the following parameters were used:

Step	Acceleration voltage	Aperture size	Dose	Working distance
Structure	10 kV	15 µm	115 µC cm^{-2}	9 mm
Contacts	10 kV	60 µm	115 µC cm^{-2}	10 mm

Resist development

1. Immerse sample in purified water for 30 s to remove conductive resist
2. Blow dry with nitrogen
3. Immerse sample in methyl isobutyl ketone:isopropyl alcohol (MIBK:IPA with 1:3 ratio) for 45 s
4. Immerse sample in isopropyl alcohol for 30 s to stop development
5. Blow dry with nitrogen

B.2 Deposition of metal thin films

At Mainz, Pt and W thin films were deposited by the author via magnetron sputtering, using the following growth parameters evaluated by A. Kehlberger (Pt) and the author of this thesis (W):

Material	Gas	Pressure	Power	Distance	Growth rate
Pt	Ar	1×10^{-2} mbar	DC: 15 mA/300 V	10 cm	0.79 Å s^{-1}
W	Ar	2×10^{-2} mbar	RF: 20 W	10 cm	0.57 Å s^{-1}

The base pressure of the used chamber was approximately 3×10^{-9} mbar.

B.3 Rapid thermal annealing of YIG films

For the spin pumping experiments in YIG/CoO/Co multilayers presented in Sec. 6.1, the surface morphology of the used YIG samples was modified by means of a rapid thermal annealing process to achieve an optimized surface roughness. In an infrared furnace, YIG samples were arranged pairwise with their surfaces touching (face-to-face) and heated up to 900 °C at a rate of 50 K s^{-1}. Having reached the set temperature, the latter was kept for 30 min, before shutting down quickly the heating power applied by the furnace. After approximately one hour, the samples reached room temperature again.

C Supporting Information *Alignment dependent spin pumping in YIG/CoO/Co*

C.1 Microwave absorption in the parallel and the antiparallel state

Figure C1a,b shows the absolute absorbed microwave power by sample I compared for parallel and antiparallel alignment of the YIG and Co magnetization at positive and negative external magnetic fields. The ambient temperature is $T = 120\,\mathrm{K}$, while the frequency and power of the applied microwave are $f = 4.5\,\mathrm{GHz}$ and $P_{\mathrm{appl.}} = 23\,\mathrm{dBm} \simeq 200\,\mathrm{mW}$. As visible from the data, no notable impact on the maximum absorbed power and line width by the alignment state are observed, which signifies a constant precession of the YIG magnetization regardless of the spin-valve configuration. This becomes also apparent when subtracting the absorption lines for parallel and antiparallel alignment from each other, as shown in Fig. C1c,d. The maximum difference between them is about 1%, which is negligible as compared to the amplitude change of $V_{\mathrm{sc}} = 120\,\%$ observed for sample I in Sec. 6.1. In addition, these small changes can easily result from a small mismatch of the

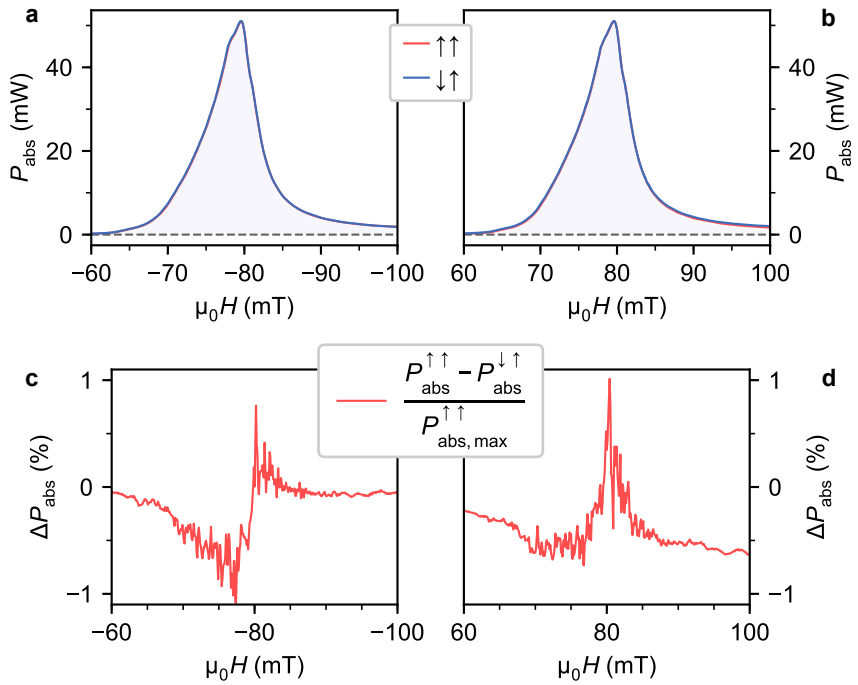

Figure C1: (a),(b) Microwave power absorbed by YIG in sample I [YIG (5 µm)/CoO (2 nm)/Co (4 nm)] for both parallel and antiparallel alignment of YIG and Co magnetization as well as both positive and negative magnetic fields ($f = 4.5\,\mathrm{GHz}$, $P_{\mathrm{appl.}} = 23\,\mathrm{dBm}$, $T = 120\,\mathrm{K}$). (c),(d) Difference between microwave absorption spectra obtained for parallel and antiparallel alignment of YIG and Co, calculated from (a),(b). Adapted from [o9].

applied magnetic field based on the employed field step resolution.

C.2 Magnon spin valve effect in sample II and sample III

In Sec. 6.1, most of the main results shown were obtained for sample I. To demonstrate the universality and integrity of the magnon spin valve effect, corresponding data obtained for sample II and sample III under equal experimental conditions is presented here in Fig. C2 and Fig. C3. Comparing these results to the ones shown in Fig. 6.6, it is apparent that qualitatively similar signals are obtained with the signal being composed of two distinct Lorentzian shaped signals V_{sc} (blue solid line) and V_{sr} (red solid line), with V_{sc} exhibiting a strong alignment dependence.

C.3 Magnon spin valve effect at different frequencies

Spin pumping results shown so far were limited to an FMR excitation frequency of 4.5 GHz. This frequency is above the threshold for a sufficiently good signal-to-noise ratio, while the relatively low resonance field allows one to measure the alignment-dependent detection of magnonic spin currents in a maximum wide temperature range. In Fig. C4, spin pumping voltages detected in sample III at $T = 120\,\mathrm{K}$ are shown for different excitation frequencies, with the microwave power kept constant for all cases. The data shows that up to

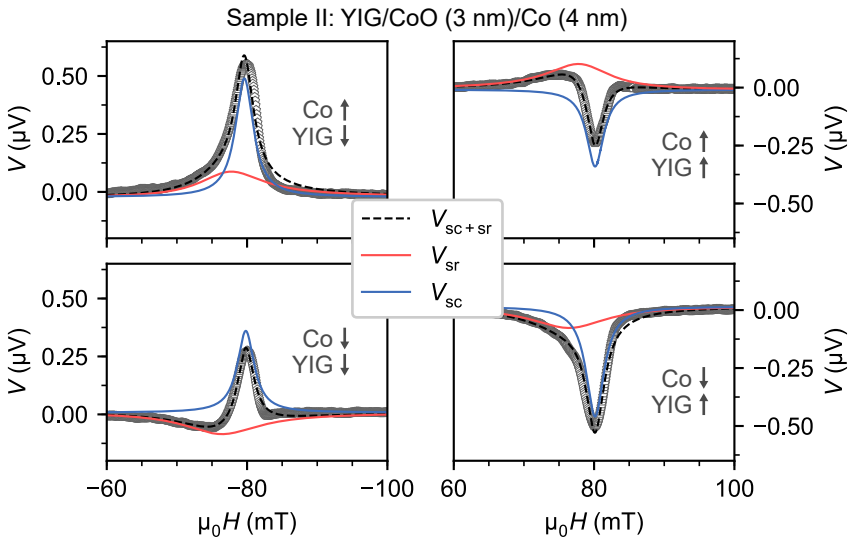

Figure C2: Spin pumping voltage responses as a function of field obtained for sample II ($f = 4.5\,\mathrm{GHz}$, $P_{\mathrm{appl.}} = 23\,\mathrm{dBm}$, $T = 120\,\mathrm{K}$). The magnetic configuration of the sample (parallel, antiparallel and respective polarization) is indicated by arrows in the subplots. Adapted from [o9].

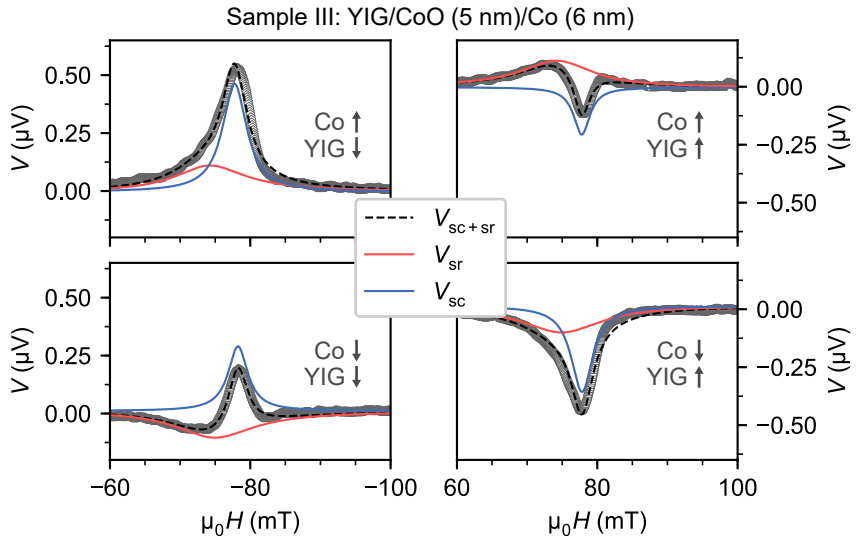

Figure C3: Spin pumping voltage responses as a function of field obtained for sample III ($f = 4.5\,\mathrm{GHz}$, $P_{\mathrm{appl.}} = 23\,\mathrm{dBm}$, $T = 120\,\mathrm{K}$). The magnetic configuration of the sample (parallel, antiparallel and respective polarization) is indicated by arrows in the subplots. Adapted from [o9].

6 GHz, qualitatively similar results are obtained for both parallel (Fig. C4a) and antiparallel (Fig. C4b) alignment. At 7 GHz, the resonance field apparently is above the switching field of the Co layer, since only the parallel behavior is observed. However, the signal for an antiparallel magnetization initialization is significantly smaller, suggesting that the Co has not switched completely and that magnetic domains are present. The explanation of

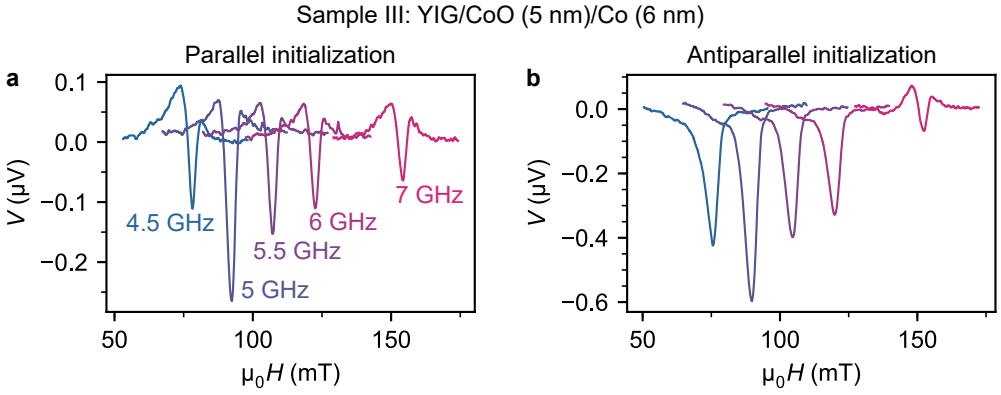

Figure C4: Spin pumping voltage response measured in sample III as a function of field and for different excitation frequencies $f = 4.5\,\mathrm{GHz}$ to 7 GHz ($P_{\mathrm{appl.}} = 23\,\mathrm{dBm}$, $T = 120\,\mathrm{K}$). In (a), the sample is initialized to exhibit parallel alignment of YIG and Co, while for (b) antiparallel alignment is set.

the frequency-dependent signal height, on the other hand, requires further investigation.

C.4 Comparison of AC and DC measurement scheme

In this work, spin pumping voltages were mainly recorded implementing an AC measurement scheme due to an enhanced signal to noise ratio. As described in Sec. 4.3.3, pulsed microwaves are injected into the waveguide and the voltage response is detected by a synchronized lock-in detector. When implementing the DC measurement scheme, the microwave is injected continuously and the spin pumping voltage is recorded by a nanovoltmeter. To verify that the magnon valve effect measured in Sec. 6.1 is not an artifact of the AC setup, alignment-dependent measurements were repeated for sample I using the DC scheme, as shown in Fig. C5. The red data points are the voltage responses in case of parallel alignment, whereas the blue data points give the antiparallel signals. As can be seen, qualitatively comparable behavior is observed for the DC scheme, however, the signal amplitudes are roughly four times larger as compared to the AC data and the difference of the total signal at resonance is smaller.

C.5 Comparison of field cooling directions

To check whether the unidirectional anisotropy in CoO/Co due to exchange bias (see the thermoelectric ANE measurements in Fig. 6.4) has a notable impact on the magnon valve effect, FMR spin pumping measurements were repeated for sample I with opposite magnetic fields $\mu_0 H_{\mathrm{ext}} \pm 9\,\mathrm{T}$ applied during the field cooling procedure. Changing the direction of the external field results in a reversal of the unidirectional anisotropy field at the CoO/Co interface and thus of a potential exchange spring at the YIG/CoO interface. The results

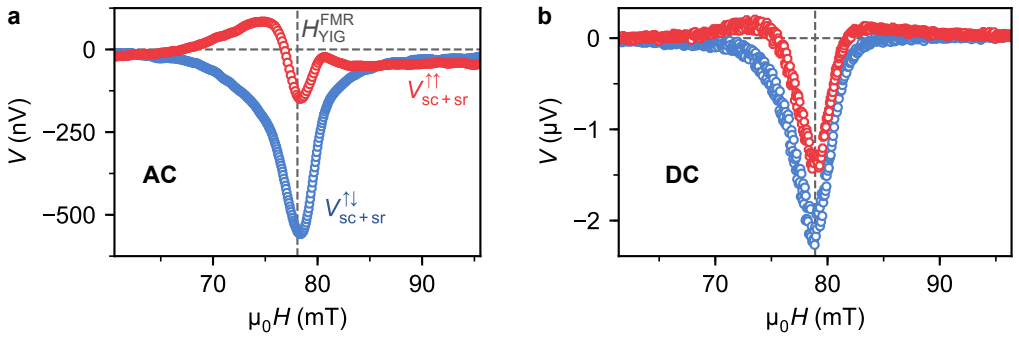

Figure C5: Spin pumping voltage response as a function of field obtained for sample I employing both (a) the AC and (b) and DC measurement scheme described in Sec. 4.3.3 ($f = 4.5\,\mathrm{GHz}$, $P_{\mathrm{appl.}} = 23\,\mathrm{dBm}$, $T = 120\,\mathrm{K}$). For both measurement schemes, qualitatively comparable results are obtained.

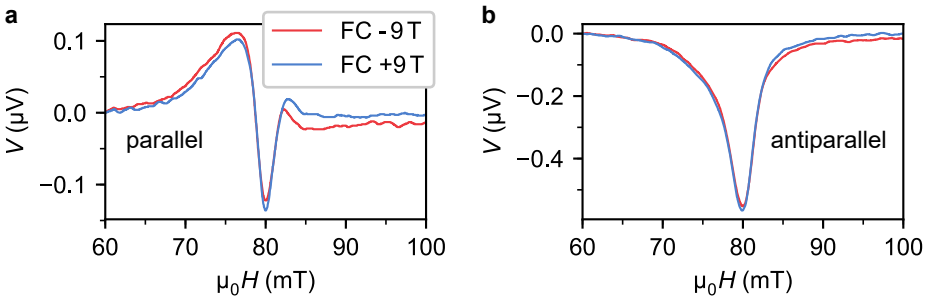

Figure C6: Spin pumping voltage response measured in sample I as a function of field for different directions of the external field applied when cooling down the sample [field cooling (FC)] ($f = 4.5\,\mathrm{GHz}$, $P_{\mathrm{appl.}} = 23\,\mathrm{dBm}$, $T = 120\,\mathrm{K}$). In (a), the sample is initialized to exhibit parallel alignment of YIG and Co, while for (b) antiparallel alignment is set. Similar results are obtained, irrespective of the field cooling direction.

are depicted in Fig. C6, showing no significant change of the qualitative signal for the two distinct field cooling procedures. As a result, the observed magnon spin valve effect cannot be explained by an uncompensated surface magnetization of the CoO layer.

D Supporting Information *Magnetization-orientation dependent (inverse) spin Hall effect in $Co_{60}Fe_{20}B_{20}$*

D.1 Finite element simulation of Oersted field distribution

Figure D1 shows the result of a finite element simulation regarding the spatial variation of the generated Oersted field components when applying a charge current to the Cu/CoFeB/Ru wire in Sec. 6.2 when used as a spin current injector. The x- [Figure D1(a), in-plane and perpendicular to the long edge of the wire] and $y-$components [Figure D1(b), out-of-plane] of the Oersted field are shown, just below and above the Cu/CoFeB interface: blue solid lines give the field amplitude in the Cu layer, whereas orange dashed line gives the field in the CoFeB. The simulation was performed by means of the freely accessible software Agros2D[1]. In the simulation, a total current of 300 µA was applied to the wire, with the current amplitudes flowing through the single Cu, CoFeB or Ru layers being estimated by the thicknesses and bulk/thin-film resistivities of the distinct layers ($\rho_{\mathrm{Cu}} = 1.7 \times 10^{-8}\,\Omega\,\mathrm{m}$ [271], $\rho_{\mathrm{CoFeB}} = 2.3 \times 10^{-7}\,\Omega\,\mathrm{m}$ [272], $\rho_{\mathrm{Ru}} = 7.1 \times 10^{-8}\,\Omega\,\mathrm{m}$ [271]). Since no reliable information could be found on the magnetic permeability of $Co_{60}Fe_{20}B_{20}$, an arbitrary value of $\mu_r = 1000$ was chosen, which is of the order of magnitude as typical values reported for metallic ferromagnets [271].

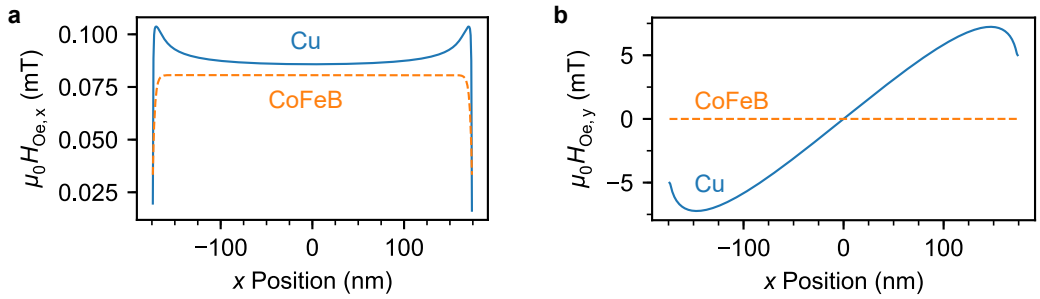

Figure D1: (a) x-component (in-plane, perpendicular to the long edge of the wire) and (b) y-component (out-of-plane) of the Oersted field generated in the Cu/CoFeB/Ru nanowire used in Sec. 6.2 to investigate the spin-dependent spin-charge interconversion in CoFeB. Blue solid lines show the field in the Cu near the Cu/CoFeB interface, while the orange dashed line shows the field in the CoFeB.

[1]Karban, P., Mach, F., Kůs, P., Pánek, D., Doležel, I. Numerical solution of coupled problems using code Agros2D. *Computing* **95**, 381-408 (2013).

E Supporting Information *Spin signal manipulation by Joule heating and Oersted fields*

E.1 Finite element simulation of Oersted field distribution

Figure E1 shows the result of a finite element simulation regarding the spatial variation of the Oersted field that is generated when applying a charge current to the Cu manipulator in the non-local device described in Sec. 6.3. The simulation was performed by means of the freely accessible software Agros2D, which was used already in App. D. In the simulation, a current density of $2 \times 10^{11}\,\mathrm{A\,m^{-2}}$ was implemented, which corresponds to a charge current of 1 mA applied to the manipulator. The plot exclusively shows the x-component of the field.

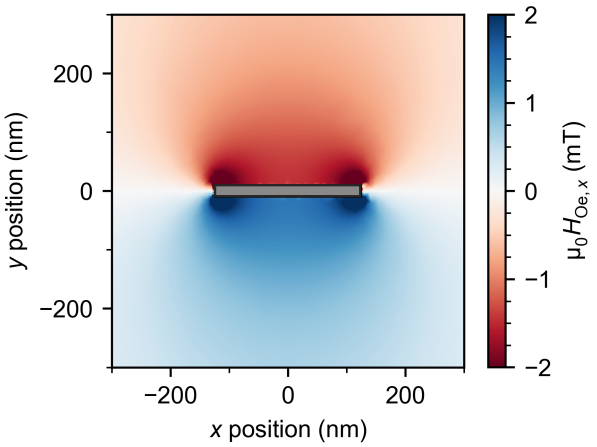

Figure E1: Spatial variation of the x-component of the Oersted field created by the manipulator, mimicking a charge current $J_{\mathrm{mid}} = 1\,\mathrm{mA}$ flowing into the drawing plane.

Acknowledgments

Aus Datenschutzgründen entfernt / Removed due to data privacy

Curriculum Vitae

Aus Datenschutzgründen entfernt / Removed due to data privacy

Eidesstattliche Erklärung

Hiermit erkläre ich an Eides statt, dass ich meine Dissertation selbständig und ohne fremde Hilfe verfasst und keine anderen als die von mir angegebenen Quellen und Hilfsmittel zur Erstellung meiner Dissertation verwendet habe. Die Arbeit ist in vorliegender oder ähnlicher Form bei keiner anderen Prüfungsbehörde zur Erlangung eines Doktorgrades eingereicht worden.

Mainz, den Joel Cramer